ADHESION OF NANO-OBJECTS TO CHEMICALLY MODIFIED SURFACES

A Dissertation
Presented to
The Academic Faculty

by

Kane McKinney Barker

In Partial Fulfillment
of the Requirements for the Degree
Analytical Chemistry in the
School of Chemistry and Biochemistry

Georgia Institute of Technology
December 2009

ADHESION OF NANO-OBJECTS TO CHEMICALLY MODIFIED SURFACES

Approved by:

Dr. Lawrence A. Bottomley, Advisor
School of Chemistry and Biochemistry
Georgia Institute of Technology

Dr. Robert L. Whetten
School of Chemistry and Biochemistry
Georgia Institute of Technology

Dr. Jean-Luc Brédas
School of Chemistry and Biochemistry
Georgia Institute of Technology

Dr. Aldo A. Ferri
School of Mechanical Engineering
Georgia Institute of Technology

Dr. L. Andrew Lyon
School of Chemistry and Biochemistry
Georgia Institute of Technology

Date Approved: July 27, 2009

ACKNOWLEDGEMENTS

I would like to thank my wife Jana. She has offered constant support and encouragement. I could not have completed this journey without her at my side. I am very thankful for my daughter, Mara Kate, who joined Jana and me early in this journey. Watching her develop curiosity for the world around her has deepened my desire to examine and understand it.

I am very grateful for my family who has supported me as I have continued my education. They have been there for every step and were instrumental in helping me stay on the path.

I owe Dr. Lawrence Bottomley unending gratitude for providing the environment to allow me to grow as a scientist. I am more thankful for the opportunity to fail than for the chance to succeed. He ensured that I always strive for that "invisible bar."

I am deeply indebted to Dr. Al Ferri for his guidance in helping me understand the mechanics of the systems presented herein. Without his help, I would most likely still be pouring over textbooks comparing the clamped-hinged versus clamped-pinned boundary conditions. His provision of the appropriate models ensured that my work has impact.

I am very grateful to Dr. Brian McRae, my undergraduate advisor. Under his recommendation, I applied to graduate school at Georgia Tech. Even though his duty

passed with my undergraduate graduation, he has continued to serve as a mentor all through my journey.

I am thankful for my officemate, Jabulani Barber. As iron sharpens iron, our back and forth discussions helped me better understand the AFM. I am also thankful for Nicole Marotta, who significantly improved the group dynamic and worked extra hours in the cleanroom so that my projects could go forward. I am indebted to Mark Poggi who pioneered MPFS, and although our time together was short, I benefited from his knowledge and example. I also thank all the other students who have passed through the Bottomley group during my tenure: Kelsey Beavers, Otonye Braide, Benedetta Carlotti, Andria Davis, David Futur, Karen Goeders, Eric Horowitz, Scott Hoy, Nathan Ives, Robert Ko, Meg Morris, Joe Parker, Charles Song, and Luigi Tarpani. Each of them added their own personal touch on my journey. I am also appreciative for several graduate students across campus for helpful discussions and friendship that have left an impact: James Bradshaw, Brett Brotherson, Matija Crne, Christina Hampton, Rob Lowe, Arti Navare, Catherine Santai, and Cameron Thompson.

I am also indebted to Yolande Berta (EM Center) and Joel Pikarsky (FIB^{2}Center) for their tireless efforts of keeping their respective instrumentation up and running.

My deepest gratitude falls to God for creating this beautifully ordered universe, and giving me the passion and ability to explore a very small part of it.

TABLE OF CONTENTS

LIST OF TABLES

LIST OF FIGURES

LIST OF SYMBOLS

A_{cr}	Cross-sectional Area
A_{DC}	Base-Amplitude
$<A^2>$	Mean-Square Amplitude
C_0	Amplitude of White Noise
C_1	Amplitude Coefficient of 1/*f* Noise
C_2	Damping Coefficient of 1/*f* Noise
d	Displacement
E	Elastic Modulus
F	Force
F_f	Force of Friction
F_N	Normal Force
f	Frequency
f_0	Resonance Frequency
G	Gain
G_{adh}	Adhesive Fracture Energy
I	Area Moment of Inertia
k	Spring Constant
k_B	Boltzmann's Constant
m	Mass
m	Angular Chiral Vector
n	Lateral Chiral Vector
P_H	Horizontal Load
P_V	Vertical Load

Q	Beam Quality Factor
R, r	Radius
s	Arc Length
s	Slope of the Deflection-Distance Curve
S_A	Surface Area
t	Time
T	Temperature
U_{dis}	Dissipated Energy
U_{str}	Energy Stored by Strain
χ	Number of Molecules per Unit Area
ε	Potential Well Depth
ε	Strain
γ	Amplitude Scaling Factor
π	Pi
σ	Distance of Zero Potential
θ	Angle
ω	Frequency

LIST OF ABBREVIATIONS

A	Ampere
ADC	Analog to Digital Converter
AFM	Atomic Force Microscope
CCNT	Coiled Carbon Nanotube
CFM	Chemical Force Microscopy
CFS	Chemical Force Spectroscopy
CNT	Carbon Nanotube
CVD	Chemical Vapor Deposition
DAC	Digital to Analog Converter
DAQ	Data Acquisition Card
DFS	Dynamic Force Spectroscopy
DFT	Discrete Fourier Transform
DNA	Deoxyribonucleic Acid
DSA	Dynamic Signal Analyzer
FC	Force Curve
FIB	Focused Ion Beam
GPa	Gigapascal
GPC	Gel Permeation Chromatography
HOPG	Highly Oriented Pyrolytic Graphite
hr	Hour
K	Kelvin
m	Meter
Mal	Maleimide

MEMS	Microelectromechanical Systems
MPFS	Multi-parameter Force Spectroscopy
MWNT	Multiwalled Carbon Nanotube
N	Newton
NI	National Instruments
NHS	*N*- hydroxysuccinimide
NEMS	Nanoelectromechanical Systems
OA	Oscillation Amplitude
ODE	Ordinary Differential Equation
PMMA	Poly(methyl methacrylate)
PEG	Poly(ethylene glycol)
PSD	Position Sensitive Detector
PSD	Power Spectral Density
RAFT	Reversible Addition–fragmentation Chain Transfer
RF	Radio Frequency
RMS	Root Mean Square
SAM	Self Assembled Monolayer
s	second
sec	second
SEM	Scanning Electron Microscope
SHO	Simple Harmonic Oscillator
ssDNA	Single Stranded Deoxyribonucleic Acid
STM	Scanning Tunneling Microscope
SWNT	Small Walled Carbon Nanotube
TEM	Transmission Electron Microscope

TPa	Terapascal
V	Volt
Vpp	Peak-to-peak Voltage
WF	Waterfall
µm	Micrometer
°C	Degrees Celsius

SUMMARY

Nano-scaled devices continue to draw interest from the science community at large. One of the major hurdles in creating these devices is understanding their mechanical and adhesive interactions at the molecular level.

The Atomic Force Microscope (AFM) is an instrument that is capable of imaging at the atomic scale. It is also capable of measuring intermolecular forces between single molecules. This makes it an ideal tool for the measurement and characterization of single molecules.

Carbon nanotubes have high electrical and thermal conductivity. Additionally, they have been shown to have elastic and shear moduli that exceed any known material. Their properties make them ideal for incorporation in nano-scaled devices. Little is known about their interfacial properties.

Multi-Parameter Force Spectroscopy (MPFS) is a technique that enables the acquisition of force curves and thermal resonance of the system under investigation. With proper interpretative models, this technique can shed light on the mechanical behavior at the molecular level. Recent improvements to MPFS have enhanced its sensitivity over background noise.

The work presented herein investigates the mechanical and interfacial properties of three carbon nanostructures: long nanotubes, nanocoils, and nanoloops. Different types of adhesion are encountered, measured and discussed: friction, rupture, and peeling. The results lead to a better understanding of the mechanical and tribological properties of the carbon nanostructures.

CHAPTER 1

INTRODUCTION

1.1 Motivation

In his famous lecture entitled *There's Plenty of Room at the Bottom*, Richard Feynman challenged the science community to begin working at the single molecule level. He stated that the goal of this endeavor was to design, create, and control devices at the molecular, and perhaps, atomic level. The value added from this endeavor is best illustrated by the miniaturization of electronic components. In the late 1950's, a single transistor in an integrated circuit occupied an area that was measured in square millimeters. Today, transistors occupy areas measured in square nanometers.[1-4] In response to Feynman's challenge, physicists and electrical engineers worked together to develop new electronic devices with performance characteristics and capabilities unimaginable at the time he presented his lecture.

Years after Feynman's challenge, K. Eric Drexler issued a more detailed challenge to the scientific community for the development of molecular machinery and manufacturing.[5] Drexler envisioned a world where nano-assemblers are used to fabricate other nanoelectromechanical devices. Before the specific challenge of nano-assemblers can be met, a broad challenge of better understanding the intra and intermolecular forces must be met. This challenge is currently being answered by chemists and materials scientist with research that focuses on understanding and controlling the chemistry and material properties at the molecular level.

A current focus involves the design, creation and testing of nanomechanical devices. One would expect the lessons learned from miniaturization of electronics should be applicable to other nanotechnologies, such as actuators or composite materials.

Largely, however, commercially successful products based on nanomechanical devices have not yet been realized. The primary challenge in manufacturing nanomechanical devices lies in positioning and affixing molecules in desired locations using a technology that enables mass production of these devices. The ability to measure, position, sculpt, and build at the molecular scale is well published but is applicable to the manufacture of prototypes and has not yet been realized for mass production.[6-13] Although success has been met in the field of academic research in terms of molecular arrangement, there are still few applications.

The remaining challenge is the ability to hold molecules in place. At the macro-scale, this can be accomplished through physical means, e.g. nuts and bolts, and chemical means, e.g. adhesives. Adhesives, however, can still be used even at the molecular level. Adhesives hold objects together through the strength of intermolecular forces. Adhesives and adhesion is therefore a physical chemistry problem.[14] Most of the methods used to measure adhesion and interfacial energy are bulk methods. These methods rely are averaging the forces over a unit area. These surface averaging methods assume homogeneity and uniform coverage. These assumptions are unacceptable at the molecular level because any local heterogeneity may significantly affect the adhesive interactions.

Precursors to the development of molecular-scale devices are an improved understanding of intermolecular forces and tools to measure them. The advantage to using adhesion over covalent bonding is that molecular building blocks can be assembled and held in place by intermolecular forces.[15, 16] This reduces the complexity associated with forming bonds between each block. New insights into intermolecular forces and energies between single molecules will come from accurate measurement of these forces. From these insights, nanomechanical devices can be designed and constructed from the molecular level. Only then will Feynman's challenge be achieved!

1.2 Research Aims

Measuring adhesive and mechanical properties at the molecular level is the overarching goal of the work presented herein. The atomic force microscope (AFM) is the ideal instrument to perform these measurements. It is capable of applying and measuring forces of a few piconewtons and manipulation in the x, y, and z directions over the range from a few micrometers down to several angstroms. The measurement of piconewton forces is regularly achieved. [17]

The adhesive interactions of interest in this work are chemically modified surfaces. The chemical modification occurs by self-assembly. In self-assembly, molecules form an ordered arrangement on the surface. Applications for self-assembled molecules include lubricants for nanomechanical systems. Additionally, self-assembled molecules enable control of the surface chemistry.

This work also focuses on high aspect ratio carbon nanostructures. These were chosen because of their wide range of potential applications in nanoelectromechanical systems, artificial muscles, and lightweight/high-strength composite materials.[18-26] As carbon nanostructures are mechanically deformable, measuring intermolecular forces is convoluted with their mechanical response. Successful measurements of the intermolecular forces must be able to distinguish between the force of adhesion and the mechanical forces that deform the nanostructure. Incorporation of carbon nanostructures into future applications requires that their mechanical and interfacial properties be well understood.

The specific aims of this investigation are: 1) deconvolute mechanical and adhesive forces acting on the carbon nanostructures; 2) quantify the tribological properties, i.e. rupture, friction, and/or peeling, of carbon nanotubes on chemically modified surfaces; 3) quantify the mechanical properties of the carbon nanostructures. Conventional AFM is unable to deconvolute the mechanical and adhesive forces. Multi-parameter force spectroscopy (MPFS), first introduced in 2004[27, 28], provides additional

data that aids in separating the contributions from mechanical deformation and adhesive interaction. A corollary to the work presented herein is to improve and communicate the fundamental understanding required for analysis of data acquired by MPFS.

This dissertation is organized in the following manner. Chapter 2 presents an overview of the AFM. Details of the primary components of the instrument are provided. Applications of the AFM in both microscopy and force spectroscopy are discussed using examples from modern research. Chapter 3 provides an overview of carbon nanotubes. Their unique structure is discussed along with different methods of fabrication. Current and proposed applications from literature are reviewed. Efforts to measure the physical properties of carbon nanotubes are also discussed. Chapter 4 contains a detailed discussion of MPFS. Each parameter and how it is acquired is discussed. Models used to interpret the data are presented. Improvements in the understanding and instrumentation of MPFS are presented. Finally, the methods and materials used in this investigation are introduced. Chapter 5 is a direct application of MPFS to measuring the mechanical properties of long, straight carbon nanotubes. Discussion of critical buckling forces is included along with a parametric study of the effects of compression and tension. Finally, by applying an elastica model to the results, the static coefficient of friction is estimated. Chapter 6 details the measurement of adhesion and mechanical response of a carbon nanocoil at large contact angles. An important conclusion distinguishing MPFS over dynamic force spectroscopy is made. Chapter 7 contains the results and conclusions of investigating carbon nanoloops. A distinction between rupture and peeling is made, along with quantification of the adhesive forces. Chapter 8 summarizes the results. New areas of interest for measuring adhesion of single molecules are suggested and improvements to MPFS are proposed.

CHAPTER 2

ATOMIC FORCE MICROSCOPE

2.1 History

The atomic force microscope (AFM) was invented in 1986 by Binnig, Quate, and Gerber.[6] The primary impetus for the AFM was measuring small forces. They predicted that with improvement of the instrumentation, the AFM would be capable of detecting forces as small as 10^{-18} N. With that limit of detection, the AFM could detect even the weakest of intermolecular forces. One of the immediate benefits of the AFM is its ability measure forces and obtain topographic images on insulators. The scanning tunneling microscope (STM), invented by Binnig, Rohrer, Gerber and Weibel in 1982, had achieved atomic resolution in three dimensions.[29] It, however, was limited to imaging conductive substrates. The AFM overcame this limitation.[30]

Since the invention of the AFM, it has become ubiquitous for a wide range of fields.[31] The AFM has been used to both image and measure forces in biology,[32-37] biochemistry,[38-48], spectroscopy,[49-51] electrochemistry,[52-55] lithography,[56-58] and surface science.[31, 52, 53, 59-71] There is broad applicability of the AFM for microscopy and force spectroscopy.

2.2 Instrument Overview

The atomic force microscope measures the motion of a microfabricated probe. The probe is a cantilever with a tip on the end. The probe is brought into contact with a surface. The cantilever deflects upon contact with the surface. As the cantilever is rastered across the surface, a feedback loop maintains a constant deflection of the cantilever by adjusting the height of the surface. A topographic map of the surface can

be generated by recording the x, y, and z coordinates. A typical setup of an AFM is presented in Figure 2.1. In this particular setup, the substrate is rastered using a piezo scanner while the cantilever is fixed in space. Other experimental setups have the cantilever raster over a fixed surface. The location of the scanner has no effect on the measurements. The diagram displays the necessary components of an AFM: cantilever, scanner, detector, and computer controller.

2.2.1 AFM Cantilever

The first AFM cantilever was a thin piece of aluminum with a diamond tip attached to it.[6] Now, cantilevers are batch fabricated using silicon micromachining techniques.[72] These techniques allow cantilevers to be made of many materials, but typical cantilevers are made from single crystal silicon or silicon nitride.

There is a broad selection of commercially available cantilevers, each designed for different applications. Cantilever geometry can be either rectangular or triangular. Rectangular cantilevers are sensitive to torsional movement during scanning whereas triangular cantilevers are resistant to this motion. Cantilevers can be made with or without tips during fabrication. The selection of physical properties of the cantilever depend on the intended application; all cantilevers should have a resonance frequency greater than 1 kHz to reduce coupling from building vibrations and greater than 20 kHz to reduce coupling with acoustic noise. Cantilevers are commercially available with spring constants that range from 0.01 to 40 N/m. Cantilevers with spring constants on the lower end of the range are more sensitive to forces and are therefore better suited to imaging soft samples or for force measurements. Stiff cantilevers resist surface forces and have a higher resonance frequency, and are therefore better suited for intermittent contact mode imaging.

The tip geometry is of utmost importance in AFM imaging. The shape and size of the apex of the tip is typically the limiting factor in lateral resolution. Early tips were

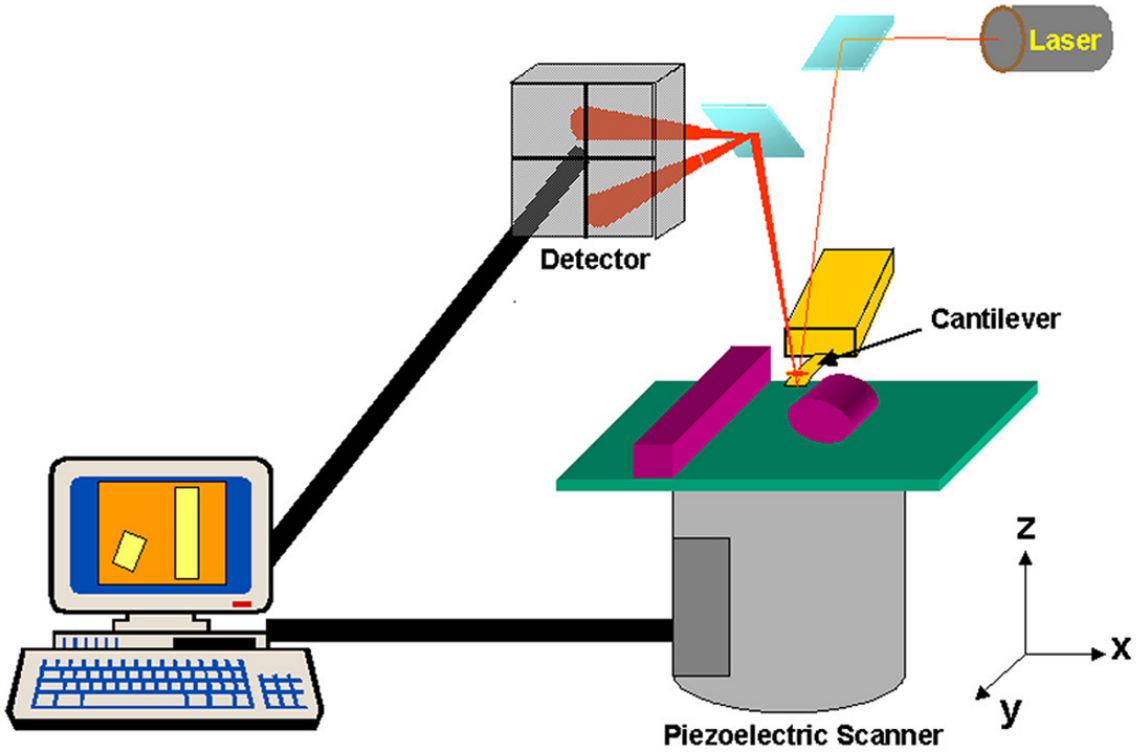

Figure 2.1. General experimental setup of an atomic force microscope. The essential components are displayed: cantilever, scanner, detector, and computer.

fabricated with a radius of curvature of >30 nm. This limited the lateral resolution to a few nanometers. Sharper tips are manufactured through different proprietary processes. Current AFM tips can have a radius of curvature of <2 nm. As the tips are scanned across the surface, they can become worn, reducing resolution. In general, sharper tips lack the mechanical stability of the larger tips and blunt faster.

Cantilevers can be modified to enhance their sensitivity and selectivity to measure different interfacial interactions between the tip and the substrate. Improvement to sensitivity is achieved by depositing a thin coating of metal on the backside of the cantilever. This significantly increases the reflectivity of the cantilever and improves the signal to noise ratio for optical detection methods. Cantilevers can be chemically modified by various methods, e.g. derivatization of a silicon cantilever using silanization or deposition of a self-assembled monolayer on a gold-coated cantilever. By altering the chemical species on the tip, different surface interactions can be preferentially selected. For example, antibody/antigen recognition can be favored by coating the tip with an antibody and scanning over the surface of a cell. Cantilever tips can also be modified with single molecules[73, 74] or objects.[75, 76] The limit of modification is constrained only by the investigator's creativity.

2.2.2 Piezoelectric Scanner

Piezoelectric materials are deformed by an applied potential. The amount of deformation is directly related to the applied potential. Piezo scanners have a fast response time and are capable of operating at kHz frequencies. The range of motion is determined by the type and dimensions of the scanner and the voltage range. Displacement of a tenth of an angstrom is possible. The disadvantage of piezoelectric scanners is that the response is only linear over a small voltage range. Adjustment for this non-linearity in response can be performed in two ways. The scanner may be calibrated at different scan ranges with samples with known, well-defined dimensions.

Alternatively, a feedback circuit can be used to adjust the voltage applied to achieve the desired deformation. Since the piezo response drifts with temperature and time, it must be calibrated regularly. The controlled and calibrated response of piezoelectric materials makes them ideal scanners for AFM.

2.2.3 Detectors

Several methods have been used to detect cantilever motion. The first published detector employed a scanning tunneling microscope (STM).[6] By measuring changes in tunneling current, the motion of the end of the cantilever was deduced. The limitation of this method is that it required separate instrumentation to detect, measure and interpret the tunneling current. Another method involves patterning electrodes on the cantilever chip and conductive pathways up and down the length of the cantilever.[77-79] This effectively makes the cantilever a strain gauge: changes in the cantilevers deflection cause changes in resistance of the conductive pathway. By deflecting the cantilever over a known distance on a hard surface, the change in resistance can be directly related to the displacement of the cantilever. The optical lever method reflects a laser off the end of the cantilever.[80, 81] The reflected laser is directed to a position sensitive detector (PSD), typically a photodiode array.

Movement of the cantilever causes the laser spot to move on the PSD, which causes a change in voltage. The detector sensitivity can be determined by deflecting a cantilever a known distance on a hard surface. A derivative of the optical detection method is using interferometry.[82] Reflected laser light causes constructive or deconstructive interference that changes the measured intensity of the laser spot. The most common method for commercial AFMs is the optical lever detection method. The deflection of the cantilever is measured by a change in voltage over a split photodiode array. Initially, the photodiode array had only two sectors. A two segment PSD is capable of measuring vertical deflection only. Any torsional movement is construed as

vertical deflection. A PSD with four segments is capable of separating the vertical and horizontal movement of the cantilever. This allows for the measurement of cantilever torsion. Figure 2.2 demonstrates how a deflection signal is acquired using a four-segment PSD.

2.2.4 Computer

Depending upon the manufacturer, the computer can be one or multiple pieces of equipment. For the sake of discussion, it is treated as one entity. The computer handles all signal acquisition and processing. The resolution of acquired data is a direct result of bit resolution of the analog to digital converter (ADC), digital to analog converter (DAC), and the sampling rate. Since the signals sent to and from the AFM are measured in volts, the computer uses the calibration parameters to convert the signals into more useful units such as height, force or amplitude. The computer provides a user interface for controlling the AFM scan parameters and recording the data.

2.3 Imaging Modes

There are several imaging modes in AFM. To Binnig et al.'s credit, all of them were proposed in the first AFM paper.[6] In contact mode imaging, the tip is in contact with the surface and applies a force as it is rastered. In noncontact mode imaging, the cantilever is oscillated near its resonance frequency at small amplitudes, <10 nm. The tip is not in contact with the surface, but is held tens of angstroms above the surface. The long-range surface forces affect the amplitude of the oscillating cantilever. Intermittent contact mode, or Tapping Mode™, imaging is similar to noncontact mode. The cantilever is oscillated near its resonance frequency, but with a much larger amplitude, >50 nm. The reduction in amplitude occurs as the cantilever comes into momentary contact with the surface. A diagram relating the surface forces to distance away from the surface is shown in Figure 2.3. The force regime for each imaging mode is also depicted.

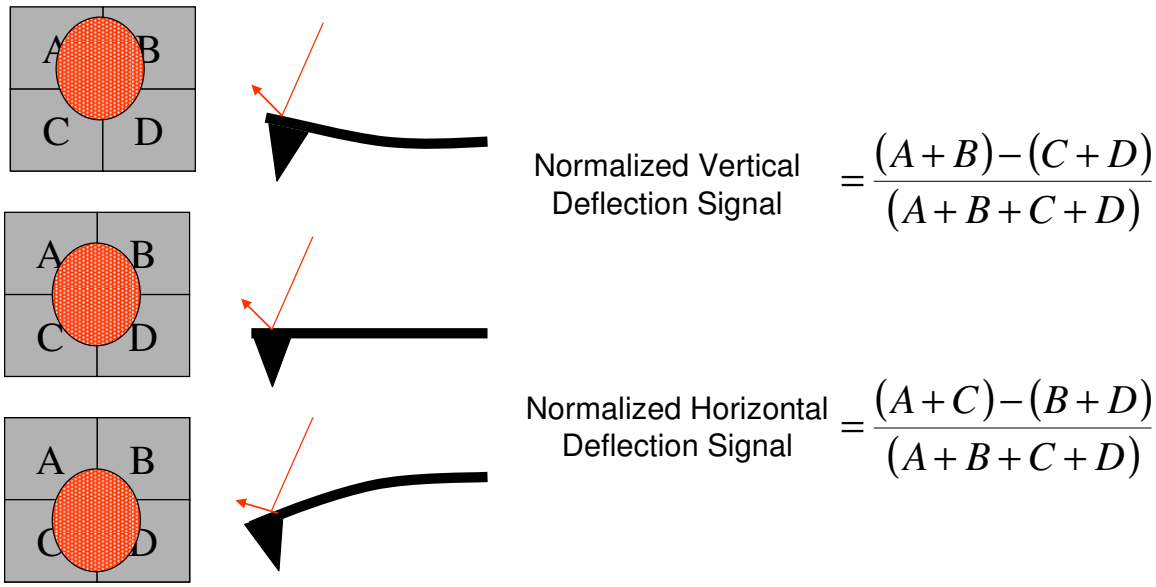

Figure 2.2. Diagram demonstrating the measurement of the deflection signal for a four-segment photosensitive detector. The location of the reflected laser light on the PSD changes as the cantilever deflects. This causes a change in voltage. The relationship of the intensity of light on each segment (A-D) for each the vertical and horizontal deflection is also shown. The output signal is normalized to the total measured intensity of the laser light.

2.3.1 Contact Mode Imaging

Two modes of contact imaging exist: constant deflection and constant height. In the latter, the applied load varies with substrate topography. Additionally, there is no feedback loop to keep the cantilever in contact with the surface. Instead, it is up to the user to place the cantilever at the correct position in space. It is possible for the cantilever to release from the surface if the surface topography goes below the position of the cantilever, preventing any true measurement of topography. Constant deflection is preferred because imaging is done under constant applied load using a feed back loop. This ensures that the cantilever is always in contact with the surface. For these reasons, the following discussion will focus on constant deflection.

Contact mode imaging implies that the AFM probe is in intimate contact with the surface. The typical method of detection is by constant deflection, i.e. constant force. As the cantilever is rastered, the feedback loop adjusts the scanner extension so a constant force is applied to the surface. The voltage applied to the scanner to maintain the applied force is recorded for every (x, y) location. The sample topography can be reconstructed by applying the calibration parameters to convert the scanner voltages into distance. The largest drawback to contact mode imaging is the force applied to the sample. Soft samples can appear flattened or crushed from the applied load. Similarly, dragging the probe tip across the surface can alter the topography by creating grooves along the path of the AFM probe or by moving material. Tips must be replaced often as they wear down from being dragged across the surface.

A direct application of contact mode is torsional mode, or friction mode. Both vertical and horizontal forces act on the cantilever as the cantilever is dragged across the surface. Since a fixed load is applied to the surface, changes in the horizontal force can be directly related to change in friction. The cantilever undergoes torsion in response the changes in horizontal force. This mode has been used to map phase separation in thin

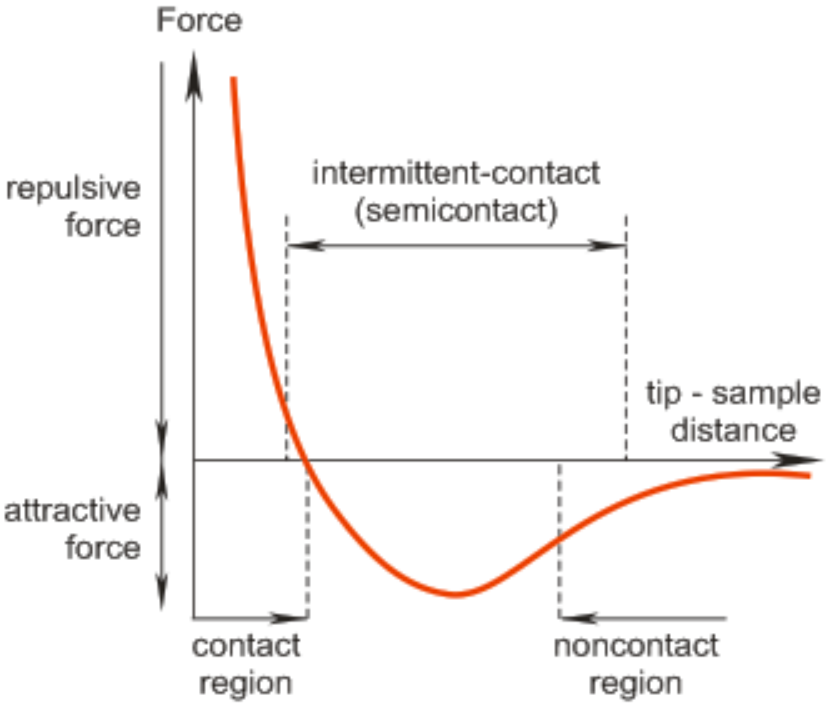

Figure 2.3. Force versus tip-sample distance as it pertains to different AFM imaging modes. Contact mode operates in contact with the surface, resulting in large forces. Noncontact mode operates off the surface measuring long-range force between the tip and sample. Intermittent contact mode operates between the other two. (Figure used with permission from NT-MDT.)

films at the nanometer level.[83-86] Previous spectroscopic methods were only able to resolve a few hundred nanometers. This mode is for imaging purposes only. It can identify regions of different friction, but it cannot identify the chemical species that give rise to the changes in friction.

Force modulation mode is another derivative technique of contact mode. This mode can be used to measure changes in compliance of the surface as the cantilever is dragged across it.[87] The cantilever is oscillated at a frequency other than its natural frequency, typically in the range of 5-20 kHz. The frequency must be greater than the scan rate. This ensures that a sufficient number of oscillation occur so the system is at steady state for each data point. Stiff material resists the oscillation of the cantilever causing the amplitude of the oscillations to increase. Soft materials deform with the oscillation causing the amplitude to decrease. As with friction mode, force modulation is an imaging technique only. It differentiates between soft and hard surfaces, but it cannot identify the chemical species that comprise different regions.

2.3.2 Noncontact Mode Imaging

In noncontact, or dynamic force, mode imaging, the cantilever is held a few nanometers off the surface.[88] The cantilever is driven near its resonance frequency to maintain a small oscillation amplitude, <10 nm. The topography of the sample is mapped similar to contact mode imaging, but the focus of the feedback loop is not the deflection of the cantilever. Instead, the feedback loop is set to maintain a fixed amplitude. Long-range forces extending from the surface cause shifts in the oscillation ampltidue. Noncontact mode is ideal for imaging soft samples because the probe does not apply a force that could deform, disturb or destroy. As the probe tip is not in contact with the surface, it does not wear with repeated use.

2.3.3 Intermittent Contact Mode Imaging

Intermittent contact mode, or Tapping Mode™, imaging also oscillates the cantilever at a frequency near the resonance frequency. The amplitude of oscillation is much greater than noncontact mode. This enables a greater sensitivity to changes in oscillation amplitude. The large oscillation causes the AFM probe to contact the surface. The contact occurs at the downswing of the cantilever so very little force is applied to the surface. Additionally, the tip only applies a vertical force to the surface, avoiding lateral perturbation of the surface. Intermittent contact mode imaging has been used to image soft materials without deforming them.[89-96] The soft interactions with the surface and high dimensional resolution has made intermittent contact the primary imaging mode for the AFM.

Phase imaging is a direct development of intermittent contact mode. The measured oscillation amplitude always has a phase lag from the frequency driving the cantilever oscillation. As the sample interacts with the surface, the phase lag changes. As the compliance and adhesive force of the surface changes, the phase shifts. This technique has been used to image inside cell membranes,[89, 97, 98] and locate defects or phase separations in polymer films.[99-105] An example of a phase image of a cell is shown in Figure 2.4. The resolution of phase imaging and its ability to map different surface interactions makes it an invaluable method for imaging with an AFM. Although phase imaging is sensitive to changes in force of adhesion and compliance of the surface, it cannot distinguish between the two. Additionally, a shift in the phase lag occurs at step edges. As such, the shift in phase from adhesion or compliance cannot be separated from changes in topography on a rough surface.

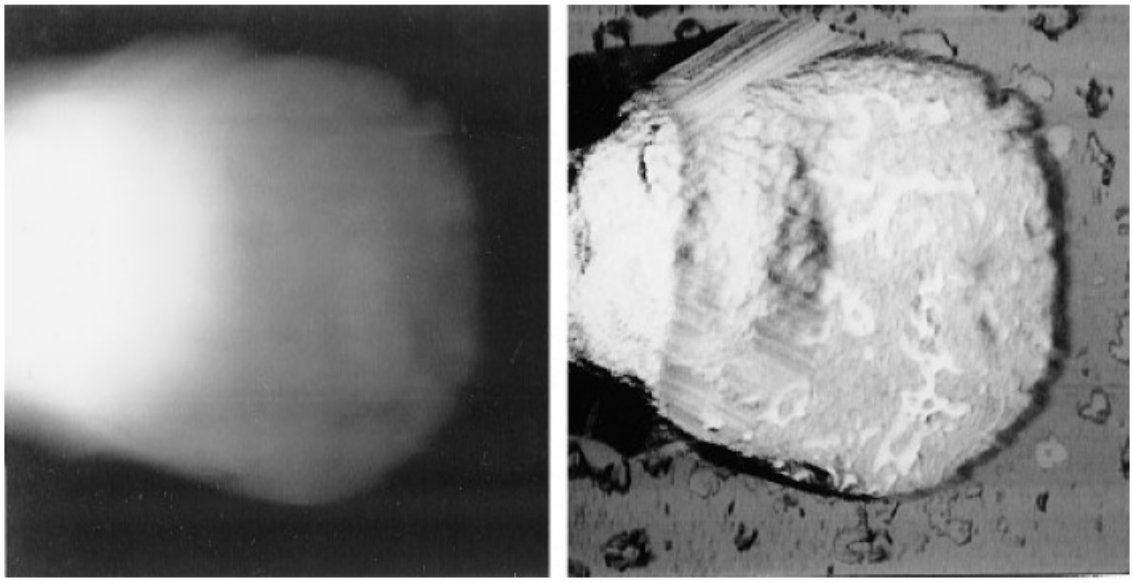

Figure 2.4. Height and phase images of a human sperm nucleus. The images were acquired simultaneously. The height image (left) shows the characteristic shape of the nucleus. Residual nuclear material inside the nuclear membrane can be seen in the phase image (right). (Reprinted from [98], Copyright 1997, with permission from Elsevier.)

2.4 Force Spectroscopy

2.4.1 Static Force Spectroscopy

The original intent of the AFM to measure very small forces[6] has not been neglected, and several improvements to the AFM have been made to measure different types of forces. Static force spectroscopy is the primary technique for using the AFM to measure forces by acquiring force curves. A force curve presents the deflection of the cantilever as a function of distance from the surface. If the spring constant of the cantilever is well known, then its displacement can be directly related to force. The force curve can be used to measure the collective surface forces acting on the probe.[17, 106-109]

Static force spectroscopy is limited to the measurement of the cantilever deflection as the scanner extends and retracts. Simple force curves are depicted in Figure 2.5. The forces observable by static force spectroscopy include, but are certainly not limited to, surface compliance, capillary force, electrostatic interactions between the tip and the substrate, adhesion, and force-induced elongation and unfolding of molecule(s) found in the contact region. The ability to measure so many different types of forces is both the strength and weakness of static force spectroscopy. The strength lies in its applicability to many scientific fields. The weakness results in being unable to deconvolute the effects from all of the forces acting on the AFM probe. Several areas of research are aimed at improving the understanding the results obtained during force spectroscopic data.

Chemical Force Spectroscopy (CFS) is a static force spectroscopic technique that can obtain chemical specific information and quantify the force of adhesion between two chemical species.[35, 110-115] In this technique, the cantilever, the surface, or both are derivatized with a specific chemical species. The force required to pull the two species apart is recorded. The force measurement is typically repeated hundreds of times at

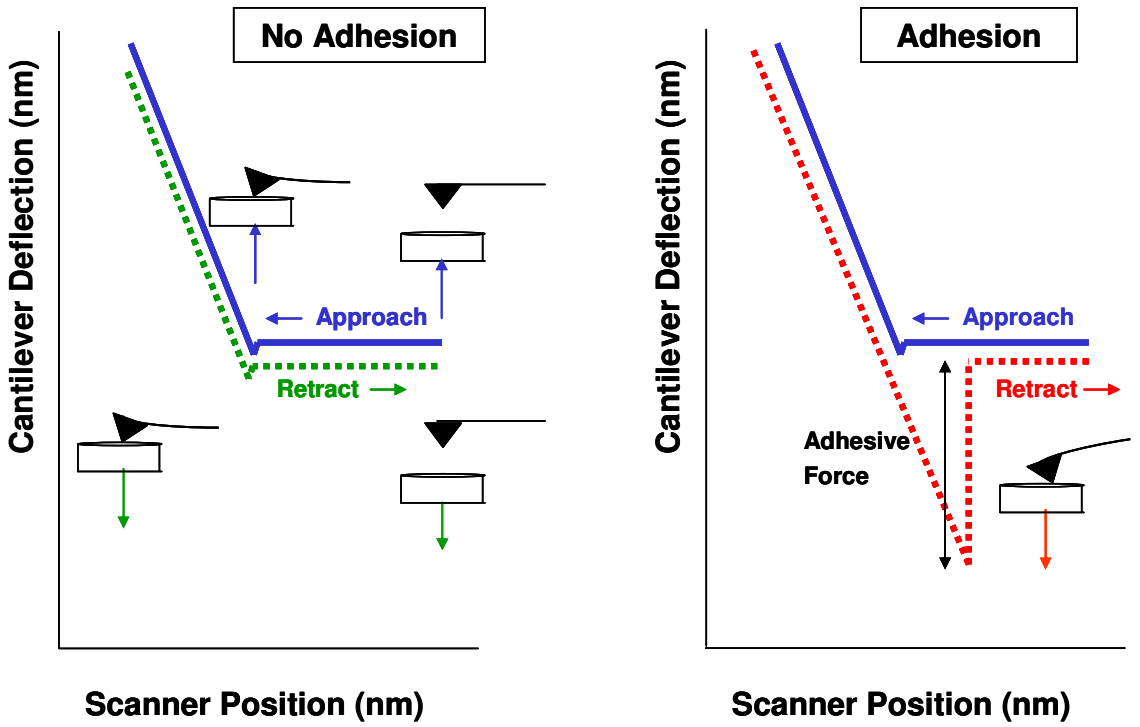

Figure 2.5. Examples of force curves. During approach, the probe is free above the surface. There is a small jump to contact followed by repulsion of the probe as the scanner extends upward. During scanner retraction, the cantilever bends down with the scanner. In the left force curve, the cantilever lets go of the surface at the point where the probe contacted the surface because there is no adhesive interaction. The right force curve shows the effect of strong adhesive interaction. The probe is bent downward until the restoring force of the cantilever is strong enough to pull it off the surface.

different locations on the surface. The adhesion force is determined by the product of the cantilever spring constant and the magnitude of downward cantilever deflection at the moment of release of the tip from the surface. When adhesion forces are plotted as a histogram, a Gaussian shape usually emerges. Based on the distribution, authors often conclude that their measurements are statistically significant, and the average force of the sample is taken to be the actual value.

Acquiring a large number of force curves is necessary to produce a sample that can be considered representative. One problem that can arise during these experiments is changes in morphology of the surface. This can produce a non-Gaussian distribution, making it difficult to draw conclusions on the force of adhesion. Poggi et al. observed a bimodal distribution when performing CFS on carbon nanotube paper. They mapped the adhesion force to the (x, y) coordinates using force volume imaging. Force volume imaging is an AFM mode that acquires force curves and topography while scanning the surface laterally. They correlated the magnitude of adhesion forces with contact area. A portion of their results is shown in Figure 2.6.

As the measured forces become more complex, e.g. tension, capillary forces and intermolecular bonding, static force spectroscopy fails to differentiate between the forces and can only measure the total work required to pull the AFM probe off the surface. More information is needed to be able to interpret the force curve.

2.4.2 Dynamic Force Spectroscopy

Dynamic force spectroscopy (DFS) is a force spectroscopic technique that has grown out of the dynamic imaging modes, i.e. intermittent contact and noncontact.[88] In this spectroscopic technique, the cantilever is oscillated near its resonance frequency by an external source. The deflection of the cantilever and the oscillation amplitude are acquired simultaneously as a function of scanner position. An example of a force curve and oscillation amplitude plot is shown in Figure 2.7. The phase lag can also be acquired

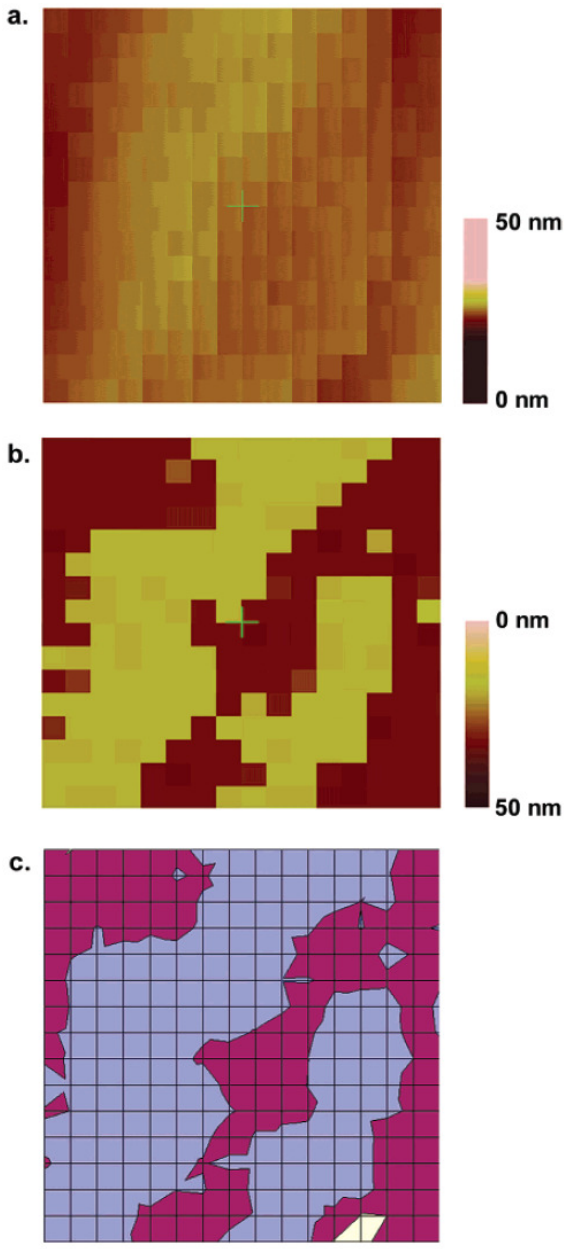

Figure 2.6. Topography, force, and adhesion results from a force volume image acquired on carbon nanotube paper. (a) Topographical image of carbon nanotubes. The image is highly pixelated because of the data storage limitations of the software. (b) Force volume image acquired simultaneously with the topographical image. (c) A map of the adhesion measured from the force curve. The colors in the adhesion map are blue, 0 to 4 nN; purple, 4-8 nN; and yellow, 8-12 nN. Comparison with the topographical images shows that the smaller forces, blue, occur on top of a nanotube whereas the higher forces, yellow, occur between nanotubes. (Reprinted with permission from [113]. Copyright 2005 American Chemical Society.)

simultaneously if a lock-in amplifier is used to monitor the frequency of oscillation. The extra information from oscillation amplitude and phase can be used to help interpret the force curve.[116, 117]

Changes in phase and oscillation amplitude occur as energy is dissipated from the oscillation of the cantilever. There have been different approaches to quantify the energy dissipation. Cleveland et al. related energy dissipation to changes in amplitude and phase from an energy balance perspective.[118] They reported that the average rate of energy dissipation from tip-sample interactions, P_{ts}, is given by

$$P_{ts} = \frac{1}{2}\frac{kA^2\omega_0}{Q_{cant}}\left[\left(\frac{A_0}{A}\right)\sin\varphi - 1\right] \qquad \text{Equation 2.1}$$

where k is the spring constant of the cantilever, A is the measured oscillation amplitude, ω_0 is the natural resonance frequency of the cantilever, Q_{cant} is the quality factor of the cantilever, A_0 is the driven oscillation amplitude, and φ is the measured phase lag. Only A and φ are measured quantities. The other parameters are properties that can be derived from cantilever motion in air.[119, 120] A similar analytical description was published by Tamayo and Garcia.[121] Other solutions have also been derived.[88, 122-129] The greatest limitation of these solutions is that they only describe the dissipation of energy. DFS is able to distinguish attractive and repulsive interactions, but it is up to the investigator to design experiments to distinguish the sources of energy loss.

There have been numerous publications using DFS that includes single molecule force spectroscopy,[42, 43, 66, 130-135] friction,[69, 136, 137] and adhesion.[131, 138-141] Many of these experiments involve mechanical systems, such the unfolding and stretching of polymers[73, 135, 142, 143] or the elastic deformation of objects. [137, 144, 145] DFS is a high visibility force spectroscopic technique that has been used to study numerous systems.

The general assumption of DFS is that as the tip approaches the surface the long-range forces cause the oscillation amplitude to dampen and the frequency slightly decreases from the small increase in effective mass. This description only applies to the

region where long-range forces occur. For reference, this area is highlighted by green boxes in Figure 2.7. It should be noted that other forces of interest occur outside the region modeled by DFS theories.

DFS has been regularly used to measure both the elasticity of polymer molecules at the air-substrate or liquid-substrate interface and the force required to detach the polymer from the surface.[40, 73, 130, 135, 139] Relating features in the cantilever deflection versus the tip-surface separation results requires knowledge about the points of contact to the polymer and a precise estimate of the number of molecules undergoing elongation. Interpretation of this data is often based on a set of assumptions. These include the assumption that all of the components in the probe molecules (i.e., the molecule and linking moieties that provide points of contact to the tip and the opposing surface) behave ideally and that repeated pulls on the probe molecules do not change this behavior. In practice, however, polymer relaxation following force-induced elongation results in significantly different conformations. This often results in non-orthogonal pulling geometries and changes in the way the molecule interacts with the surface. There has been no indication in literature to the awareness of these assumptions.

2.4.3 Peeling Force Spectroscopy

Peeling force spectroscopy is an emerging technique. It is different from previous spectroscopic techniques because of how it measures the intermolecular forces. Previous results of force spectroscopy have used Hertz, JKR or DMT theories of adhesion to model and then quantify the results.[14, 17, 108, 146, 147] Although the mathematical solution to each of these theories is slightly different, the basic assumption is the same: complete rupture from the surface must occur for the adhered object to be released. The object is either adhered or not. Peeling theory has a different basic assumption: adhesive force is in direct relation to the new area created by the release. This means that part of the object can still be attached to the surface. A macroscopic example would be a piece of scotch

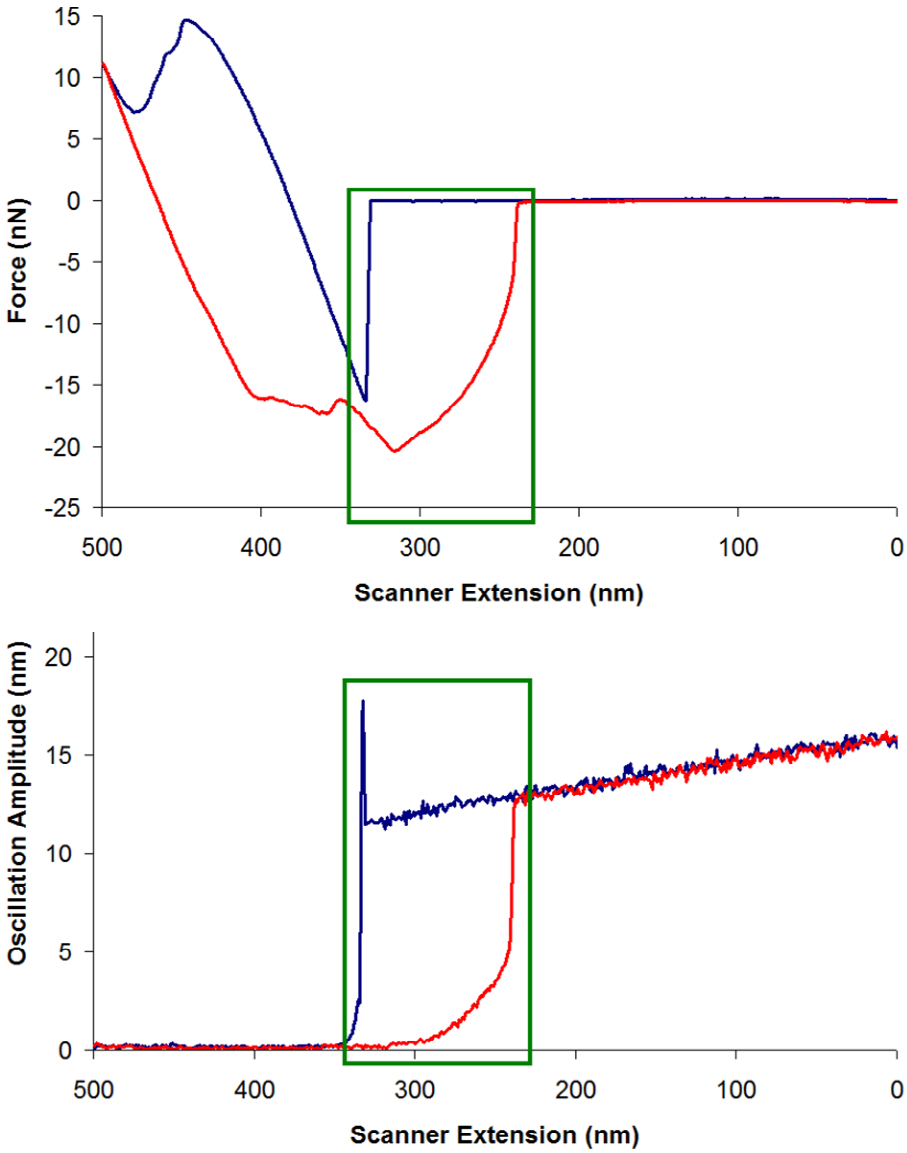

Figure 2.7. Example plots of a force curve and oscillation amplitude on a compliant fiber. This force curve was acquired on a fiber with a low elastic modulus. This example shows the complexity of a force curve that is convoluted with the fiber's compliance and adhesion. The green box highlights the area where theories of DFS can be applied.

tape adhered to a surface. Under the rupture theories, the models predict the force required pull the entire piece of tape off at once. Peeling theory models the force required to free an area of the tape.

Peeling theory dates back over five decades, and has been used extensively to measure the adhesive interactions of a variety of macro-scaled systems.[14, 148-159] These tests find wide applications because they are relatively simple to perform and the results are reliable. The appeal of this theory lies in its straightforward models. Figure 2.8 shows the most basic model of the peel test: a thin strip is pulled from a substrate at an angle. In this model, peeling of the strip is assumed to be the only source of energy dissipation from the applied load. By applying a load to the extended strip, work is done in the form of fracturing the adhesive energy from the intermolecular forces. The adhesive fracture energy, G_{adh}, can then be described as

$$G_{adh} = \frac{F \cdot d(1 - \cos\theta)}{S_A} \qquad \text{Equation 3.1}$$

where F is the applied load to the peeling arm, d is the distance between the initial and final point of contact, θ is the peeling angle and S_A is the new surface area generated by the peeling event. The normalized adhesive fracture energy is a direct result of the intermolecular bond energies between the strip and the substrate. It is evident from this equation why peeling is such an attractive technique to measure the intermolecular bond energies.

As elegant as this model is, it can be too simple for all peeling tests. The basic assumption that the energy from the applied load is only dissipated through the act of peeling is often not applicable. In the case of a realistic system, there is dissipated energy, U_{dis}, from the extension of the peeling arm. In terms of single molecules, the dissipated energy is the unraveling of the peeling arm to full extension. Essentially this is the axial elastic modulus of the single molecule. Another outcome of this unraveling is that it stores strain energy, U_{str}, in the peeling arm of the molecule. These energies must

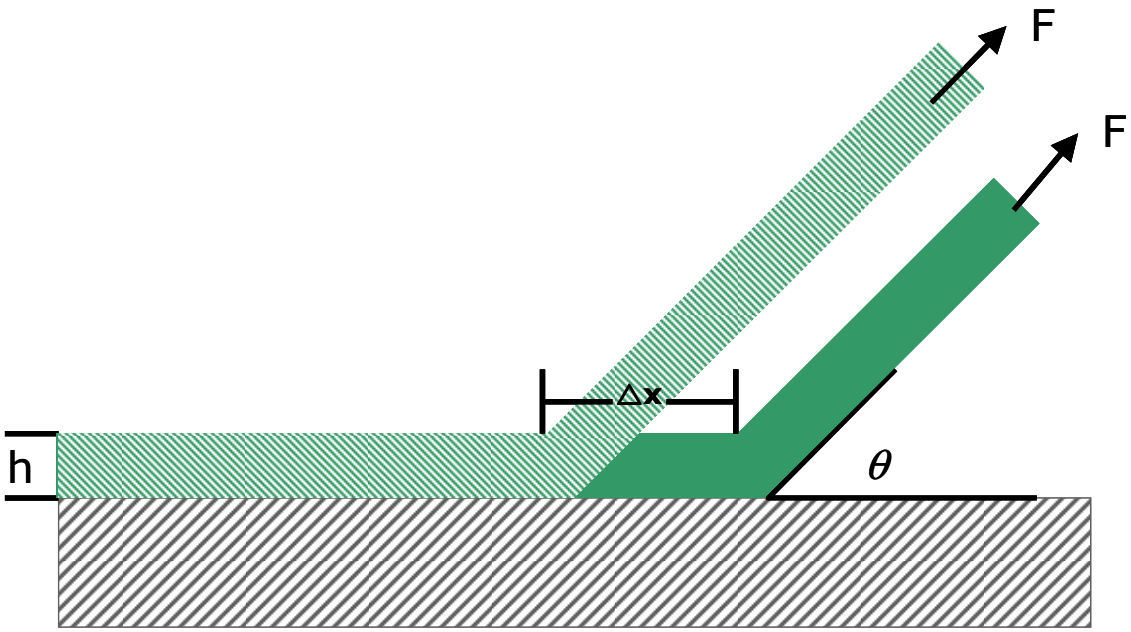

Figure 2.8. Schematic of a simple peel test. A force, F, is applied to the peel arm at angle θ. As the strip is peeled from the substrate, a new surface area is created. The work to create that new surface area is equivalent to the adhesion fracture energy. That energy is directly related to the intermolecular bond energy.

be subtracted from the external energy, i.e. the applied load, such that the adhesive fracture energy is redefined as

$$G_{adh} = \frac{F \cdot d(1-\cos\theta) - \Delta U_{dis} - \Delta U_{str}}{S_A}. \qquad \text{Equation 3.2}$$

If the single molecule undergoes linear elastic unraveling/extension, which is reasonable for slow load rates and applied loads that anticipate the elastic modulus of the peeling arm, then Equation 3.2 can take the form of

$$G_{adh} = \frac{F \cdot d}{S_A}\left(1-\cos\theta+\frac{\varepsilon}{2}\right) \qquad \text{Equation 3.3}$$

where ε is the strain in the peeling arm, which can defined as

$$\varepsilon = \frac{F}{A_{cr} \cdot E} \qquad \text{Equation 3.4}$$

where A_{cr} is the cross-sectional area of the peeling arm and E is the elastic modulus of the peeling arm. Another source of energy dissipation takes the form of plastic deformation at the bending point. To account for this energy, the yield stress of the peeling arm must be well known and either the local angle at the peeling front must be known or the radius of curvature at the peeling front must be known. In macro-scale experiments, this is much easier to do, but on the single-molecular scale, this can be exceedingly difficult. However, since these investigations include single molecules, the only possible plastic deformation would require permanent changes in the bond lengths, angles, and/or geometries. Clearly, this type of molecular change is outside the practical realm for the proposed experiments, so it is reasonable to ignore the factors from plastic deformation at the bending front. This leaves Equation 3.3 as the model for peeling single molecules from a surface.

Peeling theory first entered force spectroscopy in 2005 through molecular dynamics simulations.[160] Shi et al. modeled the forces and energies needed to peel short strands of single stranded DNA off a surface. The theory included in their work is a

direct application of the general theory of peeling discussed above. Others attempted to model peeling carbon nanotubes from graphite. Coffin et al. derived an area dependent solution to the Lennard-Jones potential for two graphite surfaces.[161] Sasaki's research team also used the Lennard-Jones potential, but included molecular mechanics.[162, 163] Their theoretical results were able to distinguish the peeling force for nanotubes of different chirality.

The first peeling experiments soon followed. Manohar et al. peeled DNA from graphite.[164] Their work, however, is rife with assumptions that do not match their experimental design. For example, they assume only a single molecule is bound near the apex of the AFM tip. The entire cantilever is covered with gold, so multiple DNA molecules could bind at the apex of the tip. They also assume a constant peeling angle of 90°, for which there is no well-defined basis. The list of assumptions continues, but even so, theirs is the first peeling experiments of DNA to be performed. Others have performed peeling force spectroscopy on carbon nanotubes.[71, 165, 166]

It should also be noted that previous investigators have misinterpreted peeling as friction.[69] Their experimental design exactly follows the peeling model depicted in Figure 2.8, yet they claim to measure friction. This distinction is noted by some of the original authors, [167] but with no attempts to modify their results. Reinterpretation of their results using peeling theory rather than friction may lead to more meaningful conclusions. Under proper application, peeling force spectroscopy is a new technique that may be capable at determining the strength of intermolecular forces.

Force spectroscopy is still a growing field of interest. Most of the literature favors the ability of DFS to deconvolute the forces acting on the cantilever. Peeling force spectroscopy shows promise as a technique to measure the interfacial energy. A consensus, however, has not been reached.

2.4.4 Calibration of Cantilever Spring Constant

The most important aspect of force spectroscopy is the measurement of the forces. The spring constant of the cantilever must be well known to accurately convert from deflection to force. There have been many different methods to determine the spring constant of cantilevers. Cleveland et al. suggest measuring the resonance frequency of the cantilever before and after a known mass is added to the end of the cantilever.[168] The change in resonance frequency is directly related to the spring constant of the cantilever. This method is very accurate, but required exact positioning of micrometer scale objects at the end of the cantilever. Hutter and Bechhoefer also used cantilever resonance to determine the spring constant of a cantilever.[120] They applied the equipartition theorem to the thermal vibrations of the cantilever. Statistical mechanics states that the simple harmonic motion of the cantilever must be equal to the thermal energy. To convert the thermal resonance frequency of the cantilever into SI units, the position sensitive detector must be calibrated. This requires that the AFM probe must be brought into contact with a hard surface. Butt and Jaschke offered an important correction to the application of the equipartition theorem by correcting for the angle at which the cantilever is mounted in most AFMs.[169] Sader et al. provided a method of solving for the spring constant from the geometry of the cantilever, its resonance frequency, and quality factor.[119, 170] This method takes viscous damping into account, which allows for the spring constant to be determined in fluid. Their solution for the geometry of the cantilever was based on a perfect rectangle. Very few cantilevers are perfect rectangles. Poggi et al. suggested a correction to Sader's method for cantilevers with trapezoidal cross-sections.[171] Sader's method is the preferred method for cantilever manufacturers. Gibson et al. and Torii et al. published similar methods using a reference cantilever.[172, 173] Their methods rely on accurately determining the spring constant of one cantilever. The calibrated cantilever can serve as a reference for a secondary cantilever. The two cantilevers are brought into contact with each other and a force curve is acquired. A force curve is also acquired

when the cantilever with the unknown spring constant is brought into contact with a hard surface. The ratio of the slopes from the two force curves is directly related to the ratio of the two spring constants. The difficulty in this method centers on positioning two cantilevers on top of each other. To maintain certainty of the measurements, the two spring constants must be within an order of magnitude. This often means that several calibrated cantilevers are needed. Other methods focus on finite elemental analysis computations.[174] These require precise measurements of the dimensions of the cantilever and generally assume homogeneous density and elastic modulus throughout the cantilever. An excellent review of the strengths and weakness of all the methods described herein is provided by Burnham and coworkers.[175]

CHAPTER 3

CARBON NANOTUBES

3.1 History of Carbon Nanotubes

Carbon nanotubes were an accidental discovery first published in 1991 by Iijima.[176] He discovered carbon nanotubes as a byproduct of the arc-discharge method he was using to synthesize fullerenes. Instead of being spherical like fullerenes, carbon nanotubes (CNT) are hollow cylinders of graphitic carbon. The structure of CNTs is similar to a sheet of graphene that has been rolled up. Later discoveries showed that there are two main types of carbon nanotubes: single walled carbon nanotubes and multi-walled carbon nanotubes. Single walled carbon nanotubes are a single carbon atom thick and can range from 1.5-20 nm in diameter. Multi-walled carbon nanotubes are several single walled tubes wrapped around each other. The concentric tubes of a multi-walled carbon nanotube (MWNT) are not bonded to each other. Each interior tube is free to rotate, much like layers of graphite slip past one another.

The carbons atoms of CNTs are sp^2 hybridized with 120° between each bond. The carbon atoms are arranged in hexagons, as depicted in Figure 3.1. Carbon nanotubes are differentiated by the direction in which the graphene sheet is rolled into a tube. The wrapping vector, or chirality, of the CNT is defined by the number of carbon atoms in each basal vector a_1 and a_2, first used by White.[177] The chiral vector can be used to predict properties of the carbon nanotube.

The physical properties of the CNT are controlled by the chirality of the nanotube.[21] The in-plane rigidity is based on the strength of the sigma bonds from the sp^2 hybridization. All carbon nanotubes are expected to display similar mechanical strength in the axial direction since the inner walls of MWNTs are not bound to one another. The

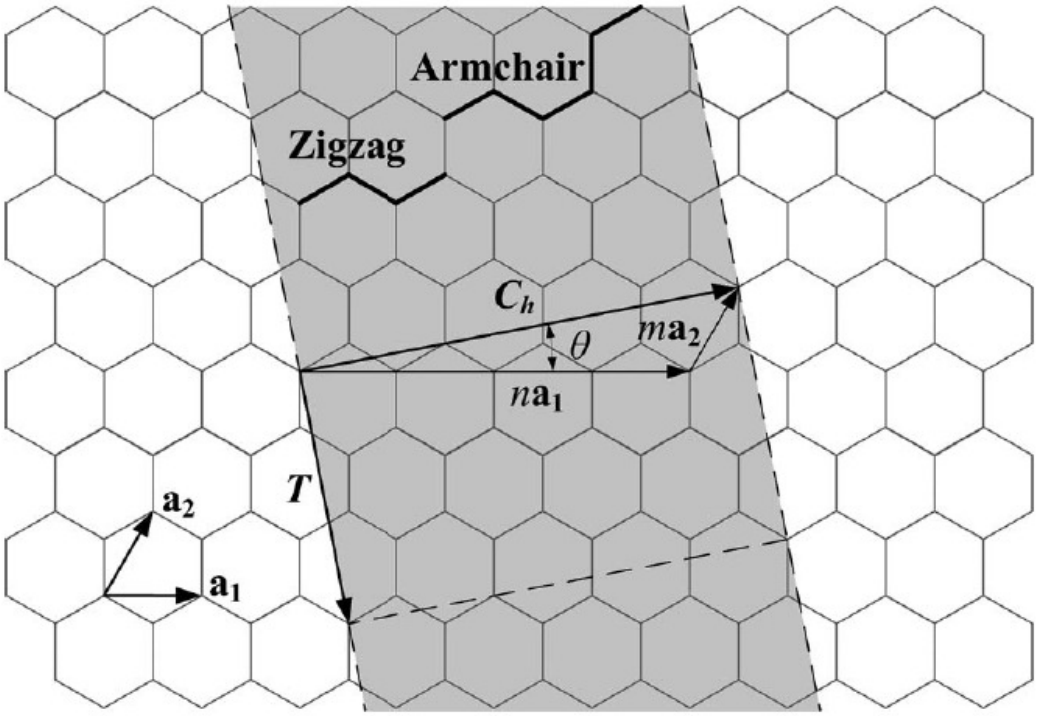

Figure 3.1. Illustration of how a carbon nanotube can be generated by wrapping a graphene sheet. The chirality of the nanotube is determined by the wrapping vector, C_h, which is usually defined the coordinate pair (n, m). In this schematic, the outlined nanotube would have a chiral vector of (4, 1). ((Reprinted with permission from [178]. Copyright 2008, American Institute of Physics.)

electrical conductivity and bending modulus are controlled by the delocalized pi bonds. The pi bonds can be aligned during wrapping to permit a high electron conductivity, similar to the conductive pathway in graphite and graphene. Mintmire and coworkers predicted in 1992 that single walled nanotubes with an armchair configuration, where $n = m$, would be excellent conductors, with conductances in the comparable to metals.[179] The wall bending depends on both the chirality and the number of walls. MWNTs have been shown to have a much higher stiffness than single walled carbon nanotubes because the concentric tubes reinforce one another.[180]

The timely predictions of Mintmire et al. along with Iijima's discovery of carbon nanotubes led to an explosion of research in carbon nanotubes as a means to provide nanometer scaled conductive paths. One of the outcomes of the increased interest in carbon nanotubes is the measurement of their mechanical strength and stiffness. It has been shown through both experiment and modeling that carbon nanotubes have an elastic modulus >500 GPa, exceeding that of any known material.[181, 182] For comparison, steel has an elastic modulus of 200 GPa and concrete has an elastic modulus of 30 GPa. The high strength, stiffness, and electrical conductivity of CNTs warrant the amount of research to characterize and then use them.

3.2 Carbon Nanotube Synthesis

There are two main categories of methods to synthesize carbon nanotubes. Plasma condensation methods involve using a high-energy source to generate a plasma at the surface of a carbon containing substrate. As the plasma cools, the carbon condenses into amorphous carbon, fullerenes and carbon nanotubes. The second category is classified as chemical vapor deposition (CVD). A catalyst is placed on an inert substrate in an atmosphere that contains a gaseous source of carbon. The system is heated to several hundred degrees, which causes the carbon source to decompose into elemental carbon at the catalyst. The catalyst mediates the formation of the carbon nanotubes.

Catalyst size, amount, and composition influence the defect density, number of walls, and diameter of the CNT grown in CVD methods. High-resolution transmission electron microscope (TEM) images of CNTs grown by different methods are shown in Figure 3.2.

The arc-discharge method is classified as plasma condensation. This method was used when Iijima first discovered carbon nanotubes in 1991.[176] The method was later refined by Ebbesen and Ajayan a year later.[183] Pure graphite electrodes serve as the carbon source in this method. A voltage is applied across the two graphite electrodes. As the carbon electrodes are brought closer together, an arc of plasma forms between the two electrodes. The current passing through the electrodes is typically 100 A. To prevent oxidation of the carbon source during arc discharge, an inert gas, e.g. He or Ar, is used at a reduced pressure. This method is the earliest reported in literature and is easy to perform. It can also be scaled up for industrial production.[24, 183-185] The disadvantage is that growth is rather uncontrolled. Both single and multi-walled carbon nanotubes are produced. Carbon nanotubes are not the only product, and they must be separated and purified from the other carbonaceous material. The yield of CNTs is low, 30%, and the purification methods can even result in damage to the CNTs.[21, 185-187]

Laser ablation is another prominent plasma condensation method. This method was first used by Smalley et al. in 1995 to synthesize MWNT by focusing a laser on a pure graphite target.[188] The laser generates a localized plasma at the surface of the graphite target. The same group later discovered that adding a small amount of metal catalyst alters the growth mechanism, yielding single-walled nanotubes.[189] The laser power, temperature of the reaction vessel, and composition of the target affect the purity and size of the nanotubes.[190-194] In contrast to the arc-discharge method, the parameters of laser ablation can be tuned to synthesize the desired carbon nanotube structures. This method does suffer from high cost in both the instrumentation and materials. Additionally, the carbon nanotubes must still be separated from the other soot generated during the condensation of the plasma. A 70% percent yield is attainable because the

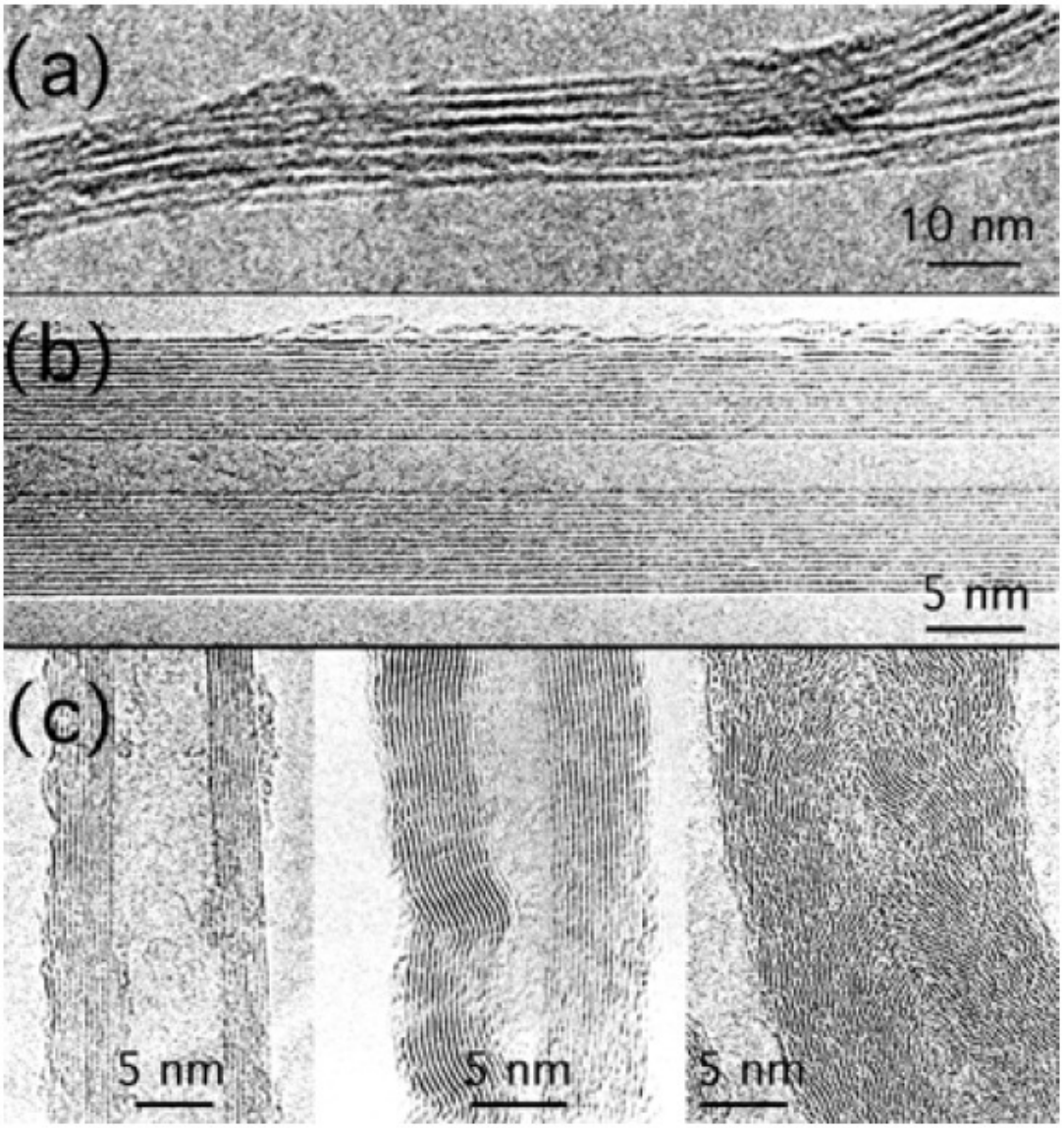

Figure 3.2. TEM images of carbon nanotubes. (a) Single-walled nanotube ropes are bundled together grown by laser ablation. Each nanotube is approximately 1.4 nm in diameter. (b) The center of a hollow MWNT is incased by several concentric walls. This MWNT was produced using the arc-discharge method. (c) CVD grown MWNTs have varying degrees of order. The size, composition and amount of catalyst can control the defect density of the MWNT. (With kind permission from Springer Science+Business Media: [195])

separation and purification process is much less rigorous than for the arc-discharge method.[185-187, 196]

The other category for nanotube synthesis contains the numerous CVD methods. CVD was first used in 1993 by José-Yacamán and coworkers to produce MWNTs with a helical twist in 1993 by decomposing acetylene on an iron catalyst.[197, 198] Pressure and composition of the gases, size and composition of the catalyst, use of a plasma, and temperature of the reaction vessel allow for precise control of the growth of the CNTs.[199-210] The yield of CNTs is very high but requires purification of the catalyst.[186, 196, 199, 206-208, 211-213] The CVD methods are easily scaled to production level.[184, 185, 208, 213-216]

3.3 Applications of Carbon Nanotubes

3.3.1 Composite Materials

The use of carbon nanotubes as the reinforcement material in composites dates back to the prediction of their high strength.[18-23, 217-220] The hope is that lightweight, but very strong composites will be produced from the use of CNTs as the reinforcing material inside polymer matrix. Although early predictions indicated that nanotube composites would revolutionize materials science and application, only minor improvements have been made. There are three main impediments preventing realization of high strength composites incorporating CNTs: 1) self-aggregation of CNTs; 2) poor alignment of nanotubes within the polymer matrix; 3) poor adhesion at the nanotube/polymer interface.[20, 22-26, 161, 219, 221-233] When nanotubes are dispersed in a polymer matrix, they form aggregates. Aggregates of nanotubes do not act as reinforcement throughout the entire composite, resulting in weak sections. Even when the nanotubes are aligned, studies have shown that they can slip within the polymer matrix because of poor adhesion between the nanotube and polymer matrix. If the nanotubes are able to slide inside the

polymer, their ability to reinforce is severely impeded. Before nanotube composites become commercially viable, these problems must be solved.

3.3.2 AFM Probes

The aspect ratio and diameter of carbon nanotubes make them ideal probes for atomic force microscopy.[234-236] Their high aspect ratio allows them to image inside trenches and pores.[237] Their diameters, as small as 1.2 nm, result in unparalleled lateral resolution,[238-242] with some claiming atomic resolution.[64, 243] Their high strength allows them to be used over many experiments without being damaged by wear.[244] For comparison, conventional AFM probes have a radius of curvature from 2–10 nm, but become blunted with extended use. CNT probes can also be used for chemical force microscopy on both chemical and biological surfaces.[34, 48, 67, 238, 245-249] Using CNTs as probes does cause image artifacts as the sidewall of the CNT interacts with the sides of trenches or holes.[240, 241, 250-253]

The preferred method for manufacturing CNT modified AFM probes is performed by growing a nanotube on the end of an AFM.[254-257] The method of synthesis is performed by CVD, with the catalyst deposited only at the apex of the probe tip. The previously described benefits of CVD synthesis remain true for nanotubes grown on probe tips. CVD synthesis has already been scaled to produce entire wafers of CNT modified AFM probes.[75] Another method for manufacturing CNT modified AFM probes involves welding the nanotube to the AFM tip. This method has the advantage that the user can design the location and angle of the nanotube on the AFM tip.[258, 259]

3.3.3 Nanoelectromechanical Devices

The high thermal and electrical conductivity of CNTs makes them suitable for incorporation in nanoscale electronics devices.[260, 261] Recent activity has focused on their use as transistors.[262-267] Carbon nanotubes have also been included into electrochemical

capacitors.[268] Fabrication of graphite electrodes with carbon nanotubes extending from the surface significantly improves the total surface area electrode and the total charge density that can be stored in the capacitor. Nanotubes have also been shown to serve as memory storage,[269] with one group claiming stability for billions of years.[270] Other applications include nanotube actuators which could be used as artificial muscles.[271-275] With the extent and magnitude of research invested in carbon nanotubes, one can expect to see their use in future electronic devices.

3.4 Physical Properties of Carbon Nanotubes

Before any commercial application can be realized, the physical properties of carbon nanotubes must be well understood. There has been a host of research investigating the electrical, mechanical, and tribological properties of carbon nanotubes. Included herein is a small sample of the research aimed at measuring the physical properties of carbon nanotubes with the goal of incorporating them into useful applications.

3.4.1 Investigations of CNT Conductivity

An exciting property of carbon nanotubes were their predicted high conductivity.[179] Research has focused on measuring the conductivity when the nanotube is relaxed and bent.[228, 276-284] Ebbesen et al. studied the conductivity of individual nanotubes by depositing tungsten on top of each CNT, and then measuring the resistance using the four-point probe technique.[285] De Heer's research has shown that CNTs are quantum conductors.[286-289] The experiments were performed by dipping individual carbon nanotubes into mercury and applying a voltage. Their results show that the conductance is not dependent on the length. Tombler et al. have shown that the conductance does depend on the stress applied to the nanotube.[290] By deforming a nanotube with an AFM tip, they were able to change the conductance of a CNT.

Collectively, these studies demonstrate the useful electrical properties of CNTs. The calculated current density has been measured to range from 10^7 to 10^{11} A/cm^2 depending on the geometry of the CNT.[276, 285, 291] The reported current densities are at least an order of magnitude greater than copper. With their small diameters, long lengths and high conductivity, CNTs are poised to become the wiring for future nanoscale electronic devices.

3.4.2 Investigations of CNT Elastic Modulus

Soon after their discovery, their were several attempts to predict the strength of CNTs by molecular modeling.[292-297] The theoretical calculations unanimously predicted that nanotubes have the highest strength of any known material with an elastic modulus exceeding 1 TPa and a shear modulus greater than 50 GPa.

The first experiments aimed at measuring the elastic modulus of CNTs were performed by vibrational analysis. It was noted by Treacy et al. that nanotubes vibrated during imaging by TEM.[297, 298] By adjusting the temperature of the chamber inside the TEM, the spring constant of each nanotube could be calculated by applying the equipartition theorem. Euler beam theory was then used to estimate the elastic modulus for each CNT based on the length, inner and out diameters, and spring constant. The elastic modulus for single-walled carbon nanotubes was calculated to be 1.3 (±0.5) TPa, and 1.8 (±1.4) TPa for MWNTs. Poncharal et al. also used vibrational analysis to calculate the elastic modulus of CNTs.[299] Rather than changing the temperature, they applied an electrostatic field to cause the CNTs to vibrate at their resonance frequencies. The elastic modulus was shown to vary depending on the diameter of the MWNT, with a range of 0.1-1.0 TPa.

Mechanical displacement by applying a load to individual nanotubes has also been used to calculate the elastic modulus. Salvetat et al. estimated the elastic modulus of CNTs by measuring their displacement after applying a load with an AFM probe.[300, 301]

They accomplished this by laying CNTs on a porous membrane, and pushing on individual CNTs with an AFM probe, as illustrated in Figure 3.3. The AFM probe was used to apply a load to the center of the CNT, causing it to deflect. The force and amount of deflection was measured by AFM force spectroscopy.

Ruoff and his research team have used a more elegant method to estimate the elastic modulus of both carbon nanotubes and nanocoils.[302-304] They attached individual nanotube/coils between two AFM probes, as seen in Figure 3.4. Using a micromanipulator, they moved AFM probes apart. The cantilevers deflected based on the displacement during separation. This applied a force that put the nanotube/coil into tension, which caused the nanotube to extend. The product of the cantilevers' displacements with their spring constants is the force applied to the system. That force causes the extension of the nanotube/coil, which is directly related to the spring constant of the nanotube/coil. Using the length, number of walls, and tube diameter, the elastic modulus of the individual nanotubes was calculated to be in the range of 11-63 GPa for MWNTs, and shear modulus of 2.3 (± 0.6) GPa for the carbon nanocoils. Their results for MWNTs are significantly lower than other published values. They attribute this to the nanotubes being covered with amorphous carbon left over from the method of synthesis, arc-discharge. It is also possible their method of attaching the nanotubes to the AFM tips, electron beam induced deposition, weakened the CNTs by creating defects at or near the point of attachment to the cantilever. This may also explain why their yield strength, 5.3%, is much lower than 16% measured previously.[293, 305] Although this method is elegant in the direct measurement of the elastic modulus under tension, it requires highly specialized instrumentation that operates inside the vacuum chamber of an SEM.

Recently, the behavior of carbon nanocoils has been shown to correlate with their structure.[306] Using multi-parameter force spectroscopy, Barber was able to differentiate the mechanical response of nanocoils that were tubes and fibers. By changing the contact

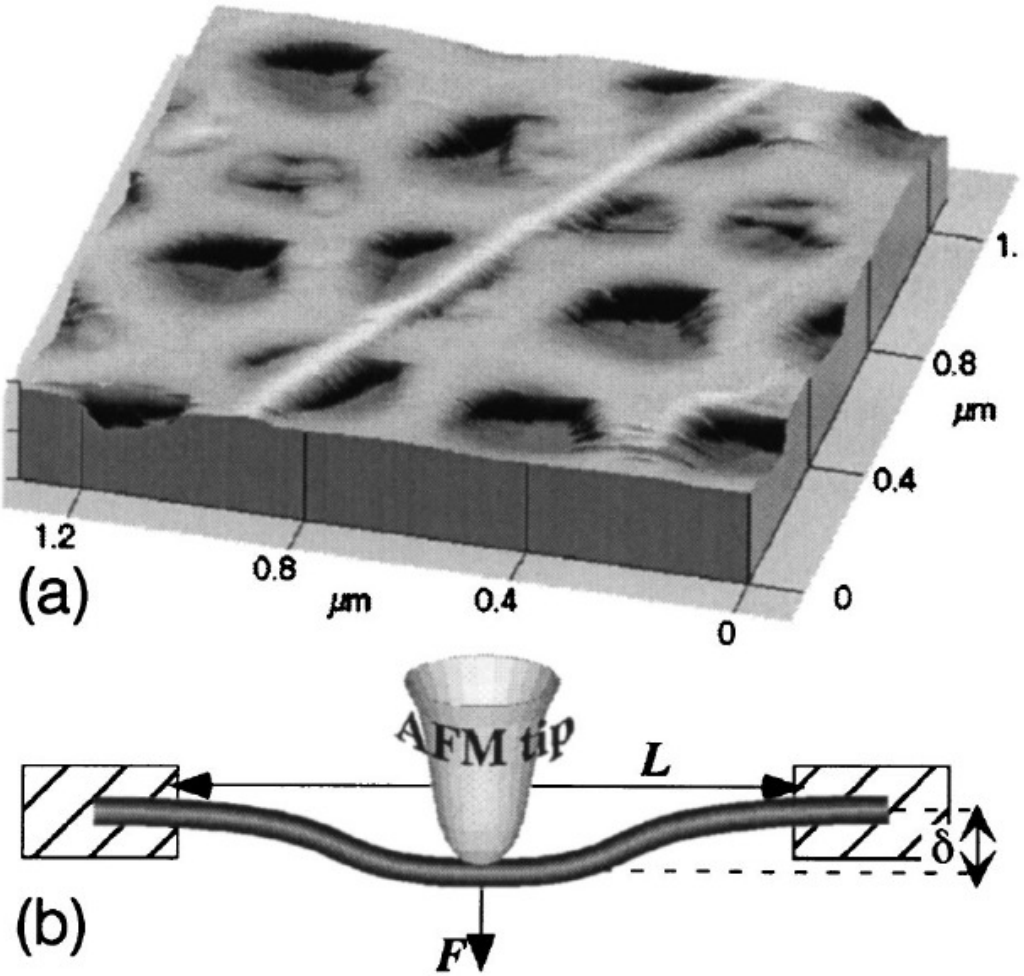

Figure 3.3. Image and schematic of an experiment to measure the deflection of a carbon nanotube and calculate the elastic modulus. (a) AFM image of a single-walled carbon nanotube bundle laying across pores of an alumina membrane. (b) Illustration of Euler beam theory applied to calculate the elastic modulus of the nanotube from the deflection of the nanotube, δ, at any point along the length of the nanotube, L. (Reprinted figure with permission from [300]. Copyright 1999 by the American Physical Society.)

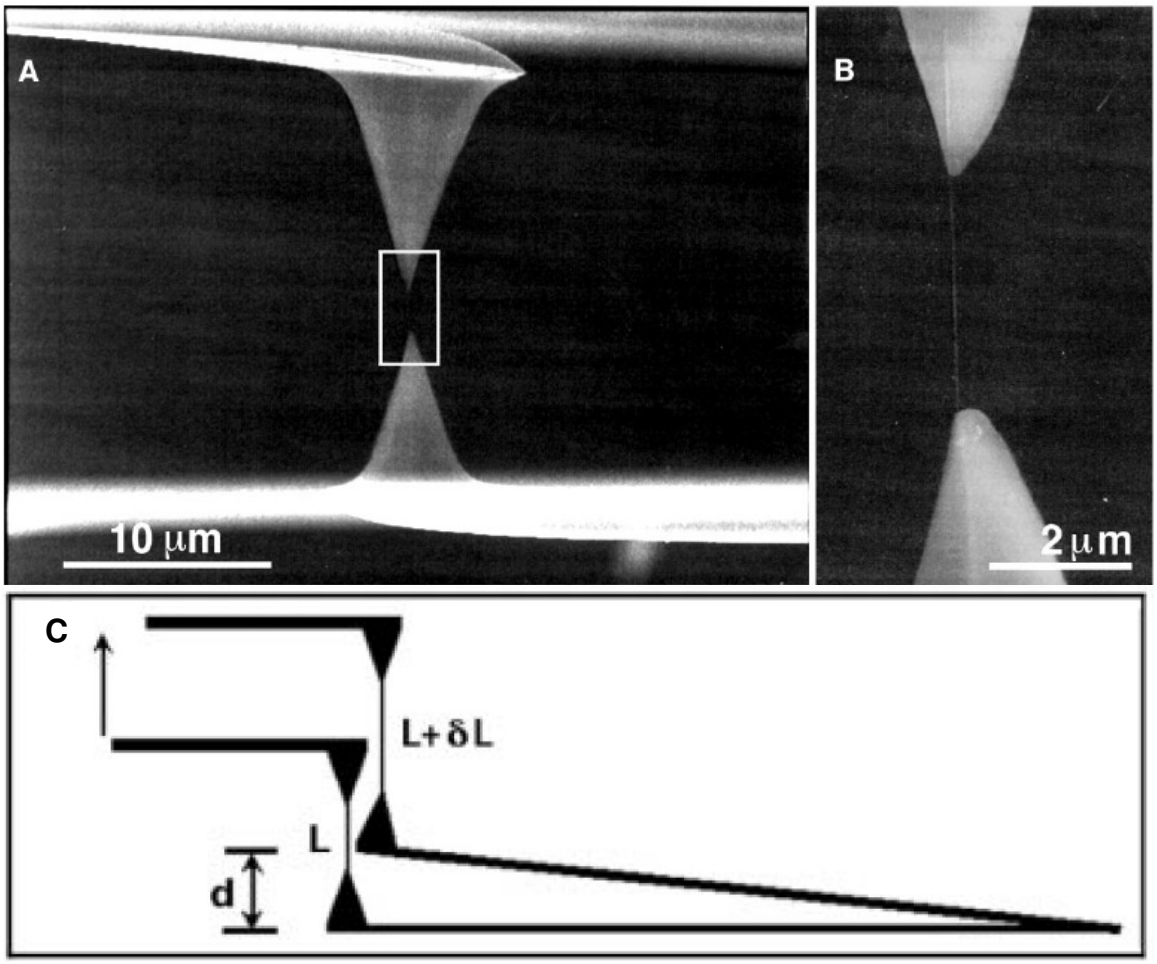

Figure 3.4. Image and schematic of the experimental method to measure the elastic modulus of carbon nanotubes in tension. (A) SEM image of two AFM probes with a CNT attached between them. (B) Magnified SEM image of the area highlighted in (A). The CNT can be seen spanning the gap between the two AFM probes. (C) Illustration of the measurable displacement, *d*, of the less stiff cantilever and the displacement of the nanotube, δL. (From [303], www.sciencemag.org. Reprinted with permission from AAAS.)

angle of the nanocoil with the substrate, he was able to distinguish between buckling and slip-stick events. Finally, he estimated the elastic and shear moduli of the carbon nanocoils by applying macro-scale spring models.

All of the above experimental methods rely on applying a force to displace the CNT, measuring the induced deflection, and then applying Euler beam theory to solve for the elastic modulus. Through both experiment and theory, the elastic modulus of CNTs has been shown to depend on the number of walls and diameter.[180-182, 226, 302, 303, 307-314] Both theory and experiment regularly reach the comparable values for the elastic modulus of nanotubes with similar dimensions.[181, 182] The experimental evidence has shown that CNTs have the largest elastic modulus of any known material.

3.4.3 Investigations of CNT Adhesion

A direct application of the high strength of carbon nanotubes is to use them as reinforcement in composite materials. To produce composites, the interface between CNTs and the surrounding matrix must be well understood. The fundamental question of adhesion is what work must be done to separate two materials. Traditionally, this has been performed by measuring the force required to pull two materials apart. Poggi et al. set out to answer this question directly using chemical force spectroscopy.[113, 315] A chemically modified AFM probe was repeatedly brought into contact with nanotube paper. Their results show that the contact area is directly related for the force of adhesion, as predicted by JKR theory.[146] Friddle et al. later repeated the same experiments as Poggi et al., but with fewer chemical functionalities and used ab initio calculations to interpret the forces.[114] Their conclusions show the same trend of the strength of adhesion for the terminal functional group as Poggi et al.: $-NH_2 > -COOH > -C{=}C > -OH > -CF_3 \approx -SH > -CH_3$. Both of these experiments attempt to determine the rupture force between a single molecule and a nanotube. Neither succeeds directly, but both are able to estimate the force of adhesion by assuming the number of molecules per

unit area. Both research teams leave the calculations at rupture force, and do not relate the force to work or energy.

A different approach to measuring adhesion is through friction. The theory behind these measurements is that a nanotube inside a polymer matrix cannot rupture, but it is possible for it to slide within the matrix. A better understanding of the tribology of the nanotube/polymer interface could help produce composites that reduce nanotube slippage.[316] Falvo et al. were the first to investigate the frictional force of nanotubes on surfaces.[305] They used an AFM probe to translate and bend CNTs on a mica surface, but no direct measurements of friction were made. Ishikawa's research group has measured the frictional force of carbon nanotubes.[67, 317] They have performed their experiments both with the nanotube on the surface and by dragging a nanotube attached to an AFM probe across a surface. Very few experiments have directly measured the friction of a nanotube in contact with a chemically modified surface. Instead the primary focus has been using CNT probes in frictional force microscopy, where changes in friction can be used to distinguish different chemical interactions occurring between the probe tip and the surface.[34, 236, 238, 245, 247, 249, 250, 318] Bhushan et al. have measured the force of friction between an CNT modified AFM probe and individual CNTs.[137, 144] They performed their experiment by sliding a CNT modified AFM probe along a CNT suspended across a trench. A schematic of their experimental setup is shown in Figure 3.5. Using dynamic force spectroscopy to determine the tribological properties of the two CNTs, they estimated the following forces acting on the nanotubes: intershell adhesion of 6.0 nN, static force of friction of 1.3 nN, static coefficient of friction of 0.2, and kinetic coefficient of friction of 0.003. Even with the abundant use of CNTs as AFM probes, there remains no direct measurement of the frictional force or coefficient of friction on chemically modified surfaces.

As a direct experiment to measure the strength of CNTs in a polymer matrix, Cooper et al. measured the force required to pull a nanotube out of a polymer matrix.[319]

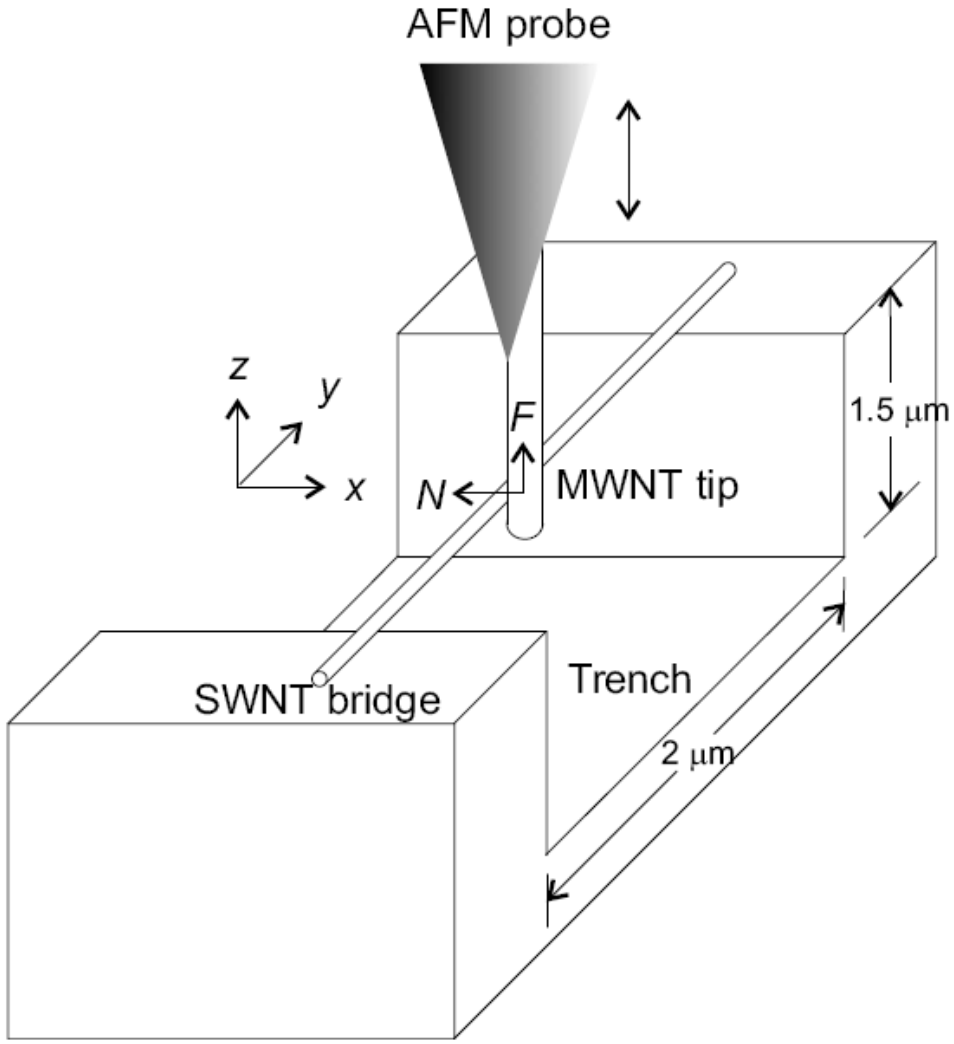

Figure 3.5. Schematic of the experimental setup used to measure friction between individual nanotubes. The AFM probe is cycled in the z direction while it applies a force, *N*, to the CNT bridge. The frictional force, *F*, is measured by the vertical deflection of the AFM probe. (Reprinted figure with permission from [137]. Copyright 2008 by the American Physical Society.)

By acquiring force curves while pulling on the nanotube, they calculated the shear strength of the nanotube/polymer interface. Their results showed no correlation between the shear strength and the length of the nanotube embedded in the polymer matrix. Other studies have focused on the failure of the composite material and the bulk properties.[225, 226, 230] Theses experimental methods are useful for testing and predicting failure of nanotube composites, but have not shown any results that can be used to predict which chemistries adhere to CNTs.

Recently, peeling theory of adhesion has been applied to carbon nanotubes. A theoretical approach to solving peeling for carbon nanotubes was first introduced by Sasaki et al.[162, 163] They generated simulated force curves for peeling CNTs off graphite. They followed up their theoretical calculations with experiment and were able to visualize peeling a CNT off of graphite inside an SEM using a custom built detector.[165] SEM images captured during their experiments are shown in Figure 3.6. They used their theory to calculate the energy of adhesion to be 78 keV. Considering van der Waals binding energy to be 10 kcal/mol, this would represent breaking approximately 1.8×10^5 intermolecular bonds. Strus et al. performed the similar experiments on both graphite and polymer surfaces.[71, 166] They calculated an interfacial energy of 15 eV between the nanotube and a graphite surface, which could be approximately 35 intermolecular bonds. Strus and coworkers claim that the large discrepancy between the two results exists because each research group used a different model to interpret their results. It is more likely that the number of interactions is different. A solution to this disagreement is needed. The fundamental question of adhesion between carbon nanotubes and chemically modified surfaces remains unanswered.

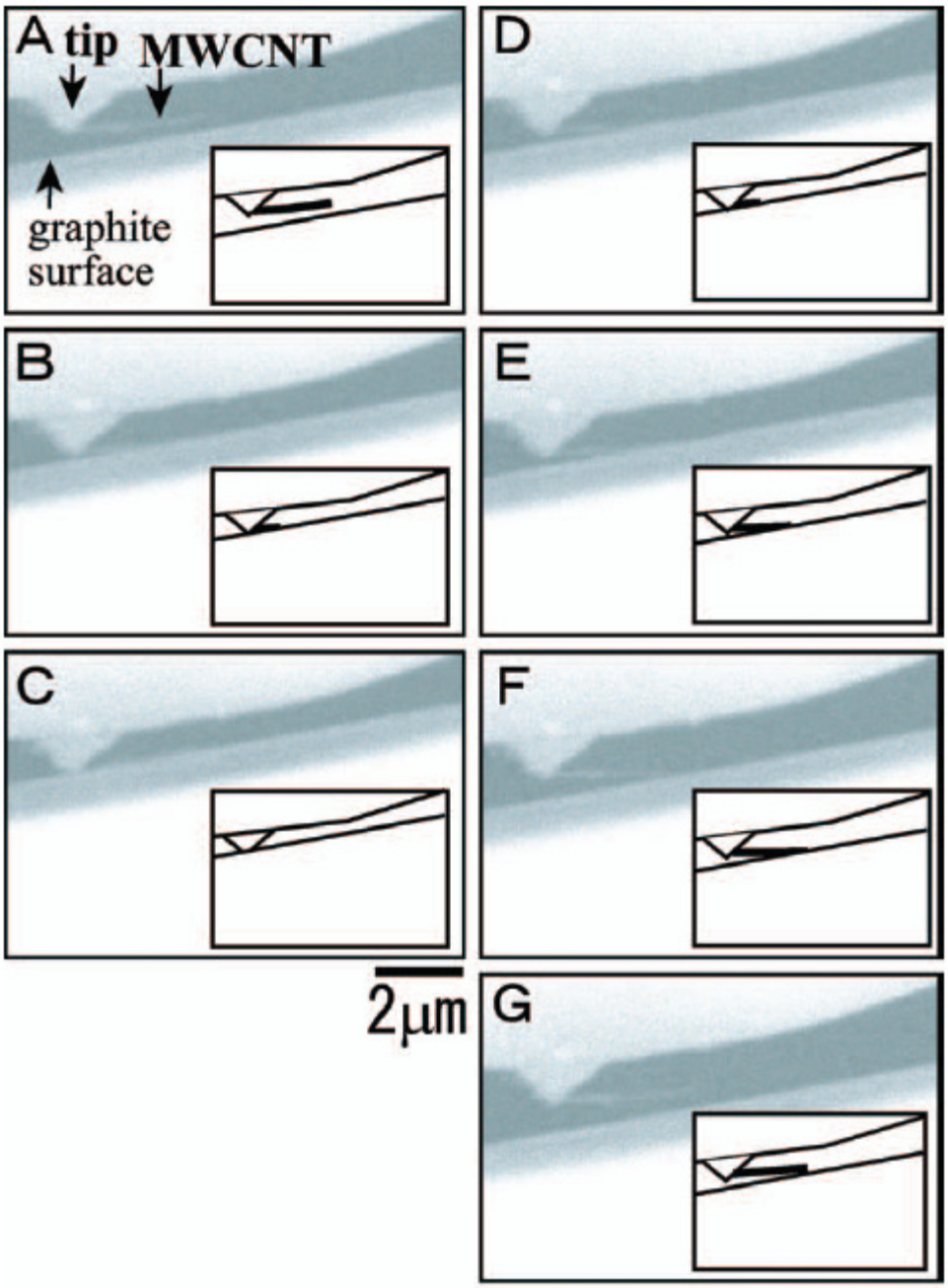

Figure 3.6. SEM images of a carbon nanotube as it is peeled off a graphite surface. (A) The probe is above the surface. (B) The CNT makes contact with the surface. (C) The silicon tip of the AFM probe makes contact. (D-F) The AFM probe is retracted from the surface, and the CNT slowly peels off from the graphite. (G) The nanotube is released from the surface. (Reprinted with permission from [165]. Copyright 2008, American Institute of Physics.)

CHAPTER 4

MULTI-PARAMETER FORCE SPECTROSCOPY

4.1 Overview of Multi-Parameter Force Spectroscopy

A commercial AFM in force spectroscopic mode is capable of providing data from the cantilever deflection and the amplitude of oscillation at the cantilever's resonance frequency. Multi-parameter force spectroscopy (MPFS) monitors several additional parameters: horizontal movement, thermal resonance frequency, and scanner movement. The AFM base was previously modified to gain access to these raw voltage signals that are not normally recorded on commercial AFMs.[28, 306] A block diagram of this setup is provided in Figure 4.1. The extra parameters provide the advantage of being able to monitor and/or pre-process signals from the AFM base that are not normally recorded on commercial AFMs. The extra data is crucial to being able to accurately interpret the mechanical response of the various systems in this study.

4.2 Parameters Acquired during MPFS

4.2.1 Conventional Parameters

The conventional data of cantilever deflection and oscillation amplitude are obtained in force spectroscopic mode using the commercial software. Recalling from Chapter 2, the vertical deflection of the cantilever is measured in volts from a position sensitive detector. Cantilever bending results from either attractive or repulsive forces from interaction of the probe tip with the surface. The oscillation amplitude data represents the RMS amplitude of cantilever vibration at its resonance frequency. External energy must be applied to the cantilever for this amplitude to be measureable. As the oscillating probe tip interacts with the surface, the amplitude of vibration is

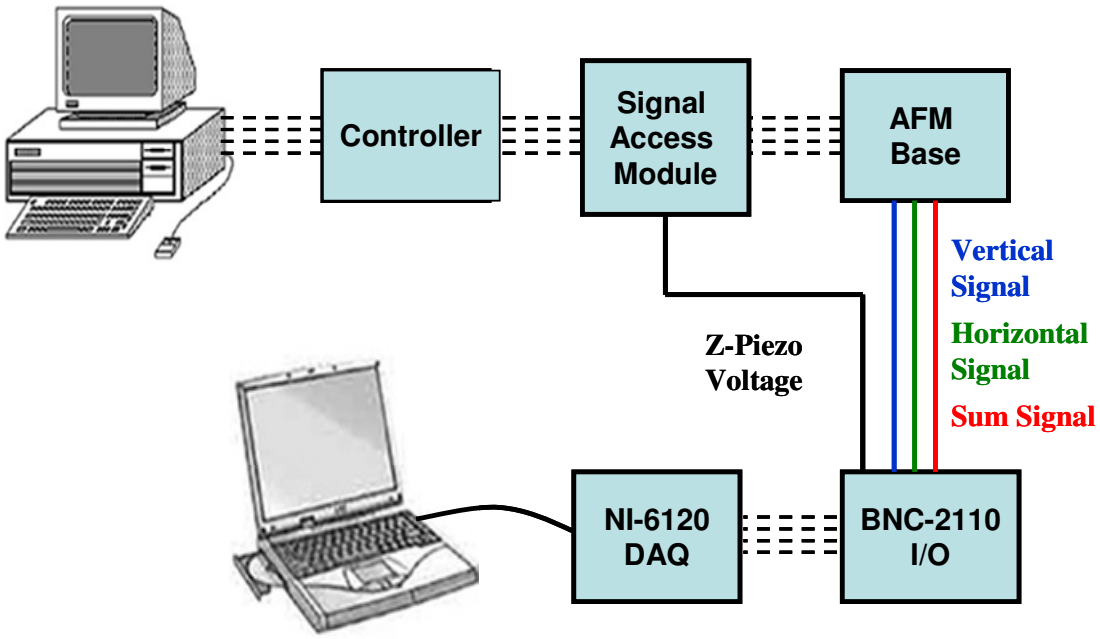

Figure 4.1. Schematic of the experimental setup for MPFS. The commercial components of the setup include the AFM base, the signal access module, the controller, and a computer. The commercially provided software is used to control and acquire conventional force spectroscopic data. The additional components, the I/O interface, the data acquisition card (DAQ), and a computer with custom software are used to acquire the extra parameters that define MPFS.

damped. Contact between two hard surfaces results in complete damping at the resonance frequency; contact with a compliant surface results in a partial decrease.

The cantilever deflection response can be convoluted with the mechanical response of the surface.[27, 68, 113, 145, 252, 293, 307, 315, 316, 320-330] Oscillation amplitude represents only the change in amplitude at the resonance frequency of the cantilever. The cause of the change can only be described as attractive or repulsive interactions with the surface.[145, 331-333] A more complete method needs to incorporate additional data that can help provide a better interpretative framework.

4.2.2 Horizontal Movement

Typically, only the vertical deflection is recorded during force spectroscopy experiments as it provides the most sensitivity to forces exerted between the tip and the substrate. This is appropriate when a cantilever with a perfectly centered, hard tip contacting a hard, flat, planar surface. In this ideal case, the cantilever would not undergo any torsional movement. However, most systems investigated by force spectroscopy are far from ideal. Recording the horizontal deflection data provides additional information about the movement of the cantilever.

The horizontal deflection signal is acquired by the data acquisition card. Custom software records the data as voltage versus time, similar to a conventional oscilloscope output. Any horizontal deflection of the cantilever is recorded as a shift in voltage, similar to the way a change in vertical displacement of the cantilever results in a change in the voltage signal from the position sensitive detector. Incorporating the horizontal deflection data to MPFS gives additional credence to any interpretation. The cantilever response can be interpreted within the three dimensions it actually moves.

4.2.3 Thermal Resonance

The thermal resonance provides the most information concerning changes in the mechanical system. As the cantilever interacts with the surface, several changes to the resonance frequency can occur. The amplitude can be damped,[88, 127, 133] but the system can also change resonance frequency. Being able to monitor these changes is an essential step toward correctly interpreting results from a complex mechanical system.

In addition to the unprocessed vertical deflection acquired through the NanoScope software, a raw vertical deflection signal of the undriven cantilever is also acquired from the base of the AFM. The time variant voltage signal for the vertical deflection undergoes a discrete Fourier transform (DFT). A Blackmann-Harris window is applied to the voltage signal prior to DFT to prevent spectral leakage. Spectral leakage occurs if a frequency is not evenly divisible by the time domain. A Blackmann-Harris window is used because it has a high dynamic range. After the DFT, the amplitude-frequency results are ensemble averaged to improve the signal to noise ratio. The ensemble averaged data is displayed as a power spectral density plot (PSD). Each PSD is time stamped as it is acquired. The PDSs are then displayed in waterfall (WF) format correlated with time. Figure 4.2 demonstrates the pre-processing method for the data from thermal resonance. The waterfall plot is used to monitor changes in resonance frequency and amplitude over time.

4.2.4 Scanner Movement

Because the horizontal deflection and the thermal resonance are acquired separately from the NanoScope software, a signal that represents the scanner movement is acquired from a signal access module. The actual voltage applied to the z-piezo can range from ±220 V, which is typically far above the voltage range of most signal analyzers. The signal acquired from the signal access module has a reduced range, ±12

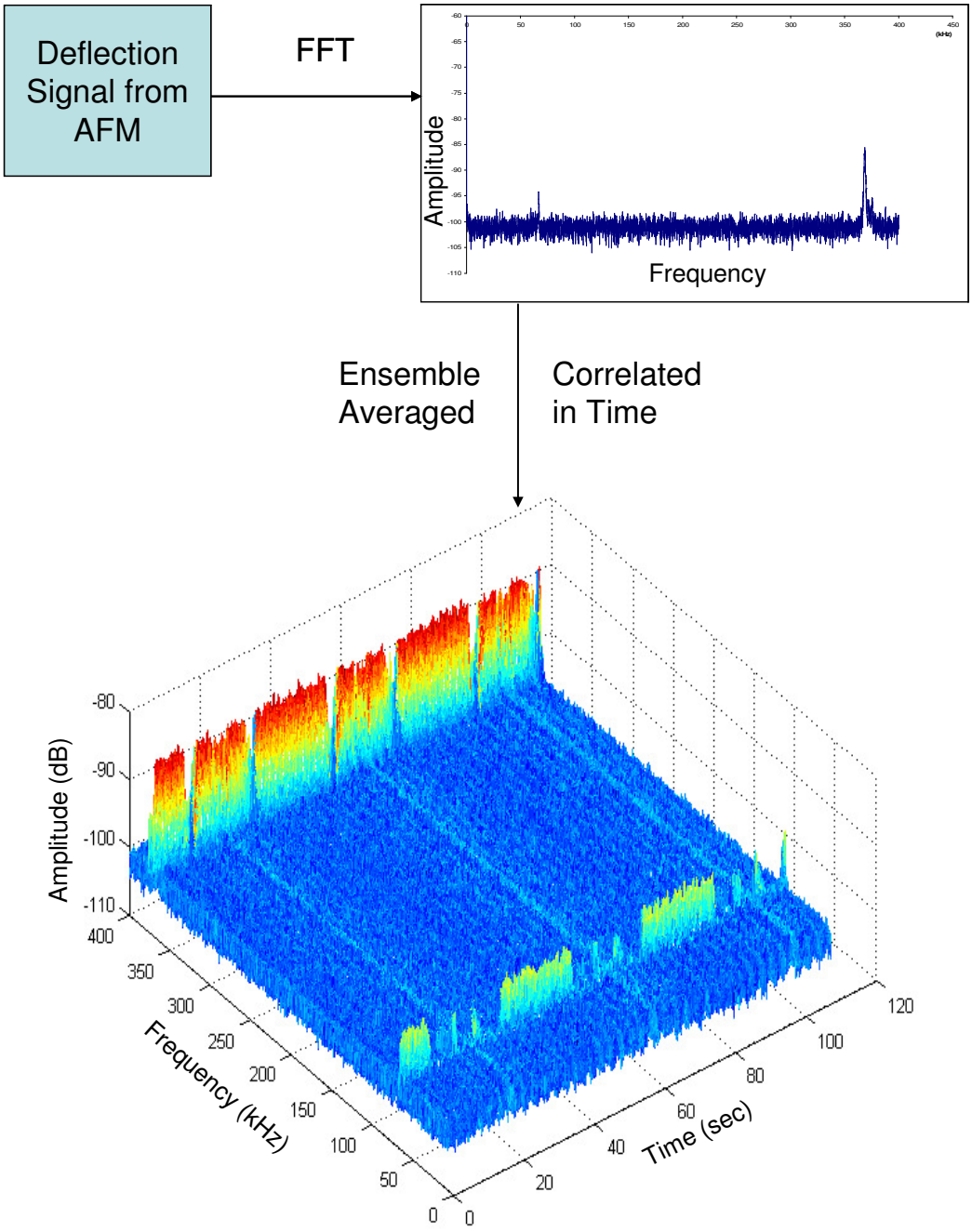

Figure 4.2. Process for acquisition and conversion of thermal resonance frequency data. The time variant vertical deflection signal is sampled and undergoes a DFT into the frequency domain. Amplitude-frequency data are ensemble averaged and time encoded. The power spectral density plots are then displayed with respect to time in a three dimensional waterfall format. Amplitude, the z-axis, is color encoded to help distinguish features. In this particular case, resonance peaks can be seen to alter in time. Changes in resonance frequency can be correlated with scanner motion.

V, which is compatible with signal analyzers. The scanner movement is correlated in time so the horizontal movement and the thermal resonance can be directly related scanner displacement. Comparison among vertical deflection, oscillation amplitude, horizontal deflection and thermal resonance can be accomplished because the scanner movement is recorded for both data sets.

4.3 Modeling Cantilever Motion

Appropriate models must be used to interpret the data. A cantilever is often modeled as a spring with a mass. As the cantilever interacts with the surface, different models of springs can be applied to interpret the results.

4.3.1 Modeling Cantilever Deflection

Deflection at the end of the cantilever, z, is directly related to the force applied at the end of the cantilever, F, given by Hooke's law:

$$F = -kz \qquad \text{Equation 4.1}$$

where k is the spring constant of the cantilever. Figure 4.3 compares cantilever deflection to a spring. An AFM cantilever is shown as it is compressed by an extending surface. The extension of the surface causes the end of the cantilever to deflect upwards the same distance the scanner is extended. The reverse is true for retraction as long as the cantilever remains in contact with the surface. The change in deflection of the cantilever is measured by reflecting a laser beam off the end of the cantilever and onto a position sensitive detector.

The single spring model is an accurate description when AFM cantilever makes contact with a hard surface. The only response to the applied force is the deflection of the cantilever. If, however, another compliant object is between the cantilever and the surface, then that compliant object can compress. Figure 4.4 demonstrates the effect of the addition of a compliant object to the system. Extension of the surface, z_{surf}, results in

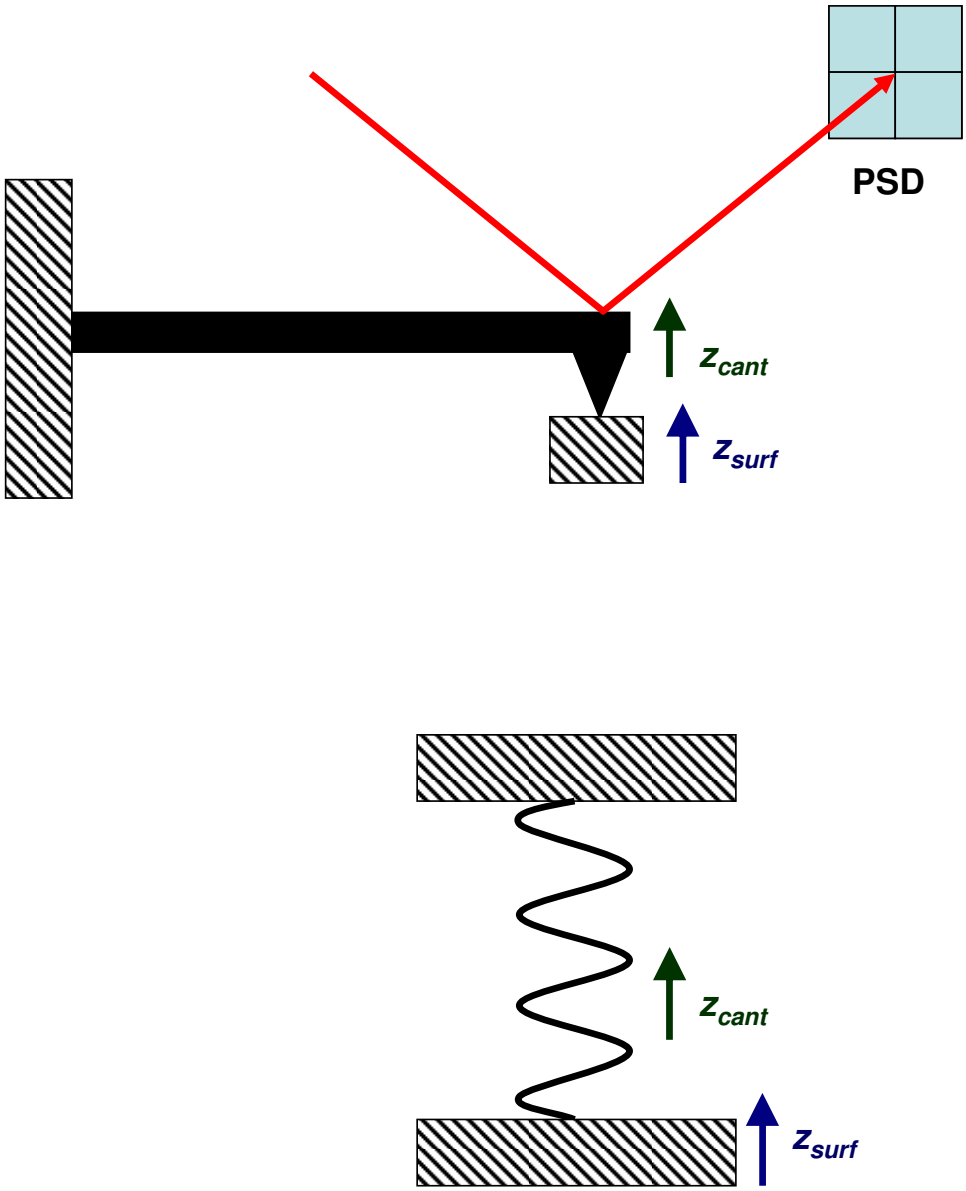

Figure 4.3. Diagram demonstrating the equivalence of cantilever deflection to deflection of a spring. The movement of the surface, z_{surf}, displaces the cantilever, z_{cant}. An equivalent description is that movement of a surface displaces a spring. For an AFM cantilever, the deflection at the end of the cantilever is measured by reflecting a laser beam off the end of the cantilever and onto a position sensitive detector. The deflection at the end of the cantilever can be described as the deflection of the mass attached to the spring.

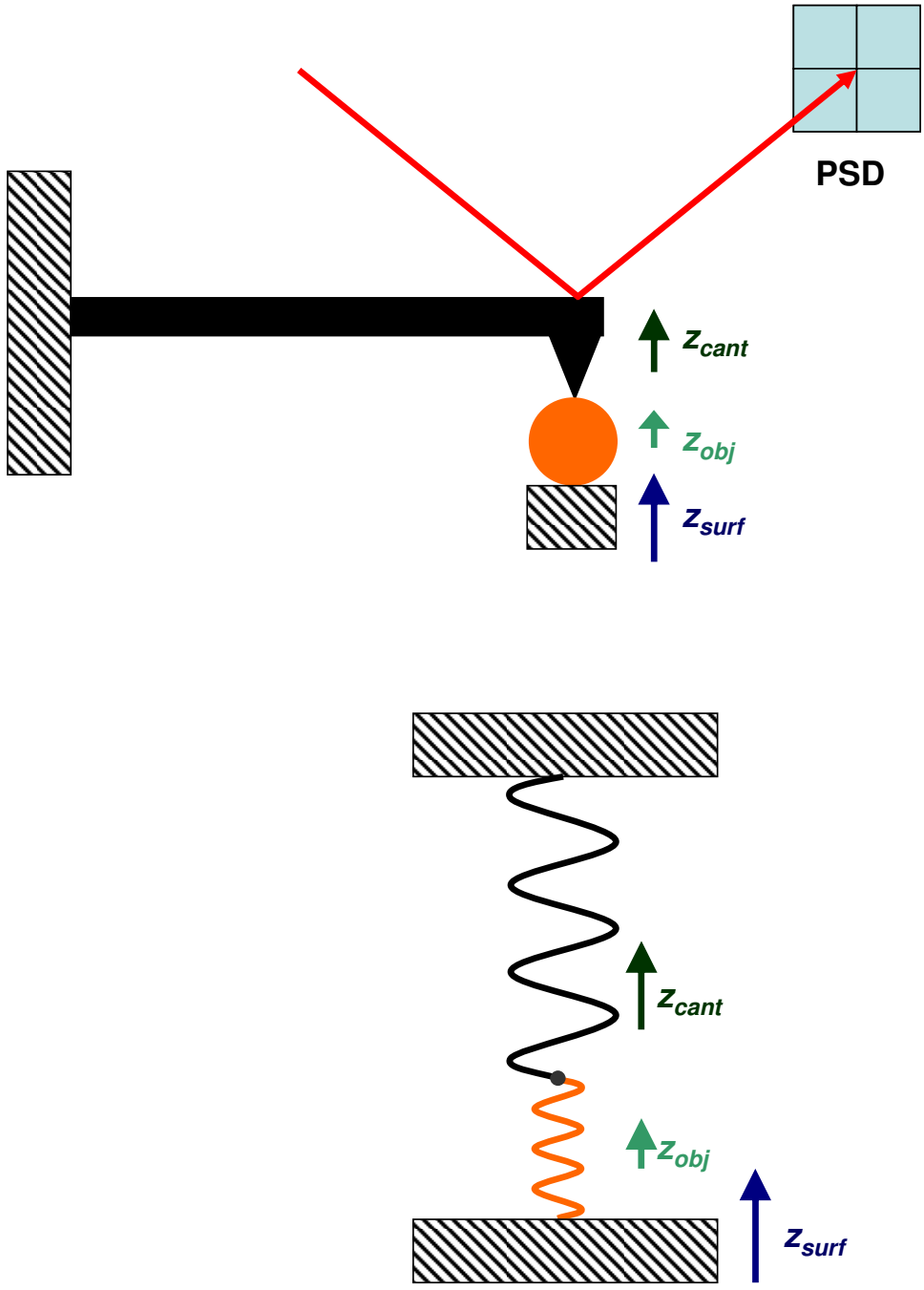

Figure 4.4. Diagram demonstrating the equivalence of cantilever deflection to deflection of springs in series when a compliant object is placed between the cantilever and the surface. A displacement of the surface, zsurf, causes the cantilever and the compliant object to displace. The displacement of the cantilever, z_{cant}, is not equal to the displacement of the object, z_{obj}. For an AFM cantilever, the deflection at the end of the cantilever is measured by reflecting a laser beam off the end of the cantilever and onto a position sensitive detector. The deflection at the end of the cantilever can be described as the deflection of node connecting the two springs.

a force being applied to both springs. The applied force causes the object to compress and the cantilever to deflect; only the deflection of the cantilever, z_{cant}, is measurable. The addition of the compliant object requires another spring to be added to the model. The amount of compression for the object is related its spring constant. The total displacement of the surface is equal to the sum of the displacement of the compliant object and the cantilever. The spring constant of the system is given by

$$\frac{1}{k_{sys}} = \frac{1}{k_{cant}} + \frac{1}{k_{obj}}. \qquad \text{Equation 4.2}$$

The system is modeled as springs in series because the force distributed between each of the springs is the same, and the displacement of each spring is determined by its spring constant.

Often, only the spring constant of the cantilever is known. The spring constant of the object must be calculated. This can be accomplished by first calculating the spring constant of the system. On a hard surface, the slope of the deflection distance-curve is directly related to the spring constant of the cantilever. On a compliant surface, the slope is directly related to the spring constant of the system.[310, 325, 334-336] The ratio of the two slopes can be used to calculate the spring constant of the system as described by

$$k_{sys} = \frac{s_{hard} k_{cant}}{s_{sys}}, \qquad \text{Equation 4.3}$$

where s_{hard} and s_{sys} are the slopes of the deflection-distance curve on a hard and compliant surface, respectively. This relationship holds true for the linear region of the slope. Rearranging Equation 4.2, the spring constant of the compliant object can be calculated using

$$k_{obj} = \frac{k_{sys} k_{cant}}{k_{cant} - k_{sys}}. \qquad \text{Equation 4.4}$$

Using the model of springs in series, the spring constant of the system and the compliant object can be calculated from the response of the deflection distance curve and the spring constant of the cantilever.

4.3.2 Modeling Cantilever Resonance in Free Space

The oscillation of the first mode of vibration of a cantilever in free space is described as a spring with a mass. The mass at the end of the spring undergoes periodic vibration, which is that of a simple harmonic oscillator (SHO). The vibration at the end of the cantilever is equivalent to the oscillation of the mass at the end of the spring. Any modification of the AFM probe can be ignored in this description as long as it does not add significant mass. For higher modes of vibration, it is more appropriate to model the cantilever motion using beam theory.[337-340] Figure 4.5 displays the first three modes of vibration for a beam in free space. The model applied to the cantilever vibrating in free space uses boundary conditions of a clamped-free beam. In the case of an AFM cantilever, the clamped end is attached to the chip, and the free end is vibrating in space. The higher modes of the cantilever have reduced amplitudes and higher frequencies of vibration. Nonetheless, they can still be acquired using MPFS. It should be noted that the model of SHO can be used to describe each mode of vibration individually.

Cantilever vibration arises from thermal energy. This relationship is defined by the equipartition theorem:

$$k_B T = k\left\langle A^2 \right\rangle; \qquad \text{Equation 4.5}$$

where k_B is Boltzmann's constant, T is temperature, k is the spring constant of the spring/cantilever, and $<A^2>$ is the mean-square amplitude of the oscillation. Equation 4.5 models an ideal oscillator. Butt and Jaschke point out that when an optical lever detection system is used for an AFM cantilever, the mean-square amplitude that is measured is not the absolute mean-square amplitude.[340] The measured amplitude of

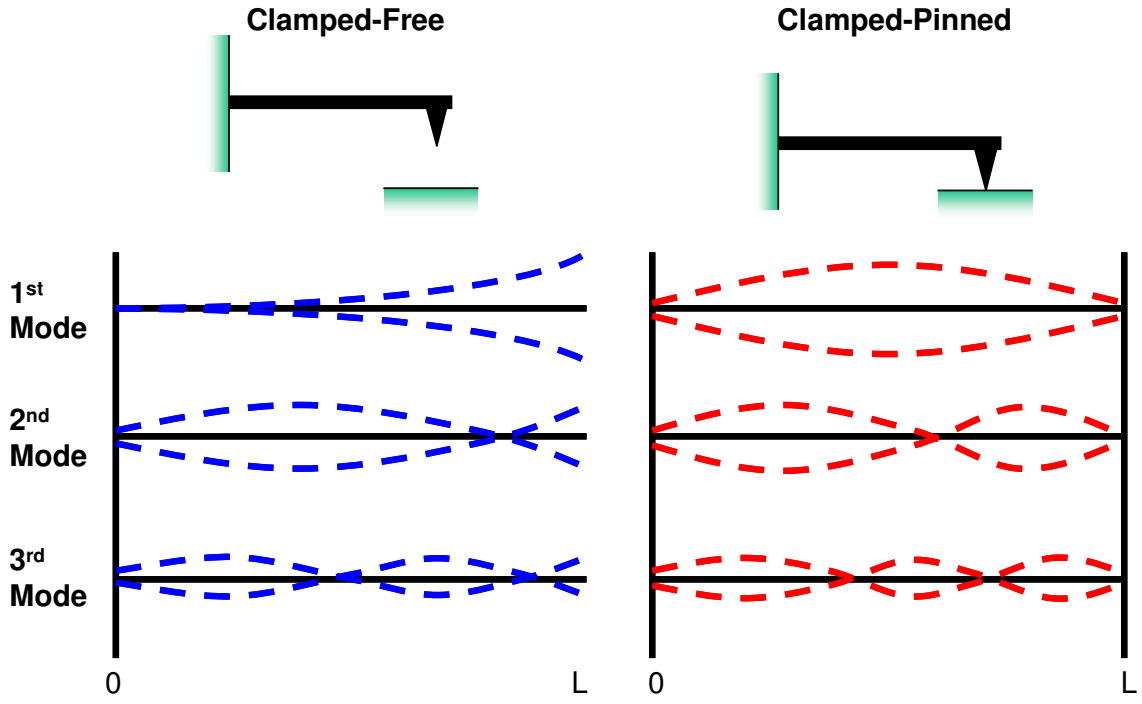

Figure 4.5. Shape of the first three vibrational modes of a cantilever as predicted by beam theory. The left figure describes the motion of a cantilever in free space. The right figure describes the motion of a cantilever adhered to a surface. The shape, frequency and amplitude of the cantilever vibration change when it makes contact with the surface.

vibration is affected by the inclination of the cantilever. They offer a correction to Equation 4.5 to account for the optical lever detection method:

$$k_B T = \frac{3}{4} k \left\langle A^2 \right\rangle . \qquad \text{Equation 4.6}$$

The corrected form of the equipartition theorem is a better description of what is measured in the thermal spectrum using the optical lever detection method.

The frequency of oscillation of the cantilever is described by the time variant solution for Hooke's Law:

$$f_0 = \frac{1}{2\pi} \sqrt{\frac{k}{m_{eff}}} , \qquad \text{Equation 4.7}$$

where f_0 is the resonance frequency, k is the spring constant, and m_{eff} is the effective mass of the cantilever. Both the resonance frequency and the amplitude of the simple harmonic motion rely on the spring constant of the cantilever.

Hutter and Bechhoefer developed a method of calculating the spring constant of a cantilever based on the assumptions of the equipartition theorem for a SHO.[120] The amplitude at any frequency, $A(f)$, of a SHO, can be fit to a Lorentzian function:

$$A(f) = A_{DC} f_0^2 \left[\left(f_0^2 - f^2 \right)^2 + \frac{f_0^2 f^2}{\gamma^2} \right]^{-\frac{1}{2}} , \qquad \text{Equation 4.8}$$

where A_{DC} is the base amplitude, and γ is the amplitude scaling factor. It should be noted that γ is not the beam quality factor, Q, as has been previously reported.[28, 306, 341] For a Lorentzian function, γ relates the maximum amplitude of the resonance peak to the base amplitude. The beam quality factor is defined as the full width at half height at the resonance frequency and represents the rate of energy dissipation for a SHO. Because of the geometry of a SHO resonance peak, there is a direct relationship between γ and Q: γ is greater than Q by a factor of the square root of three. The previously reported values of Q are actually γ. The authors, therefore, overestimated Q by the square root of three.

Equation 4.8 can be fit to the thermal resonance data recorded by MPFS. The results of the fit are integrated numerically to provide the mean-square amplitude. The mean-square amplitude can be used in Equation 4.6 to calculate the spring constant of the cantilever.

Rarely, however, does Equation 4.8 adequately model the system measured in MPFS. Often, white noise and the 1/*f* noise from the position sensitive detector are also incorporated in the data. The noise terms are added into Equation 4.8 to generate

$$A(f) = C_0 + \frac{C_1}{f^{C_2}} + A_{DC} f_0^2 \left[\left(f_0^2 - f^2 \right)^2 + \frac{f_0^2 f^2}{\gamma^2} \right]^{-\frac{1}{2}}, \qquad \text{Equation 4.9}$$

where C_0 is the white noise amplitude, C_1 is the amplitude effect for the 1/*f* noise, and C_2 is the damping constant for the 1/*f* noise. With the addition of the noise parameters from the position sensitive detector, a better fit to the data is possible.

A previous investigator fit Equation 4.9 to the data directly only over a *reduced* bandwidth, with all six variables (C_0, C_1, C_2, A_{DC}, f_0, and γ) fit *simultaneously*.[306] The noise variables are, by definition, independent of the SHO. Fitting Equation 4.9 to the thermal spectrum *sequentially* is a more accurate method. The white noise, C_0, can be fit by finding the average amplitude of a narrow bandwidth far from the influence of the 1/*f* noise, any SHO contributions, and any systematic noise. With the white noise set at a fixed value, the first two terms of Equation 4.9 are then fit to a bandwidth that is dominated by the 1/*f* noise. Once the noise parameters are fixed, Equation 4.9 can be fit to a reduced bandwidth centered at the resonance peak.

Both the method previously reported, i.e. simultaneous, and the method described herein, i.e. sequential, are used to fit Equation 4.9 to a thermal spectrum using least-squares regression. A comparison of the fit for each method is shown in Figure 4.6. Upon initial comparison, it appears that the simultaneous method (Figure 4.6A) fits the

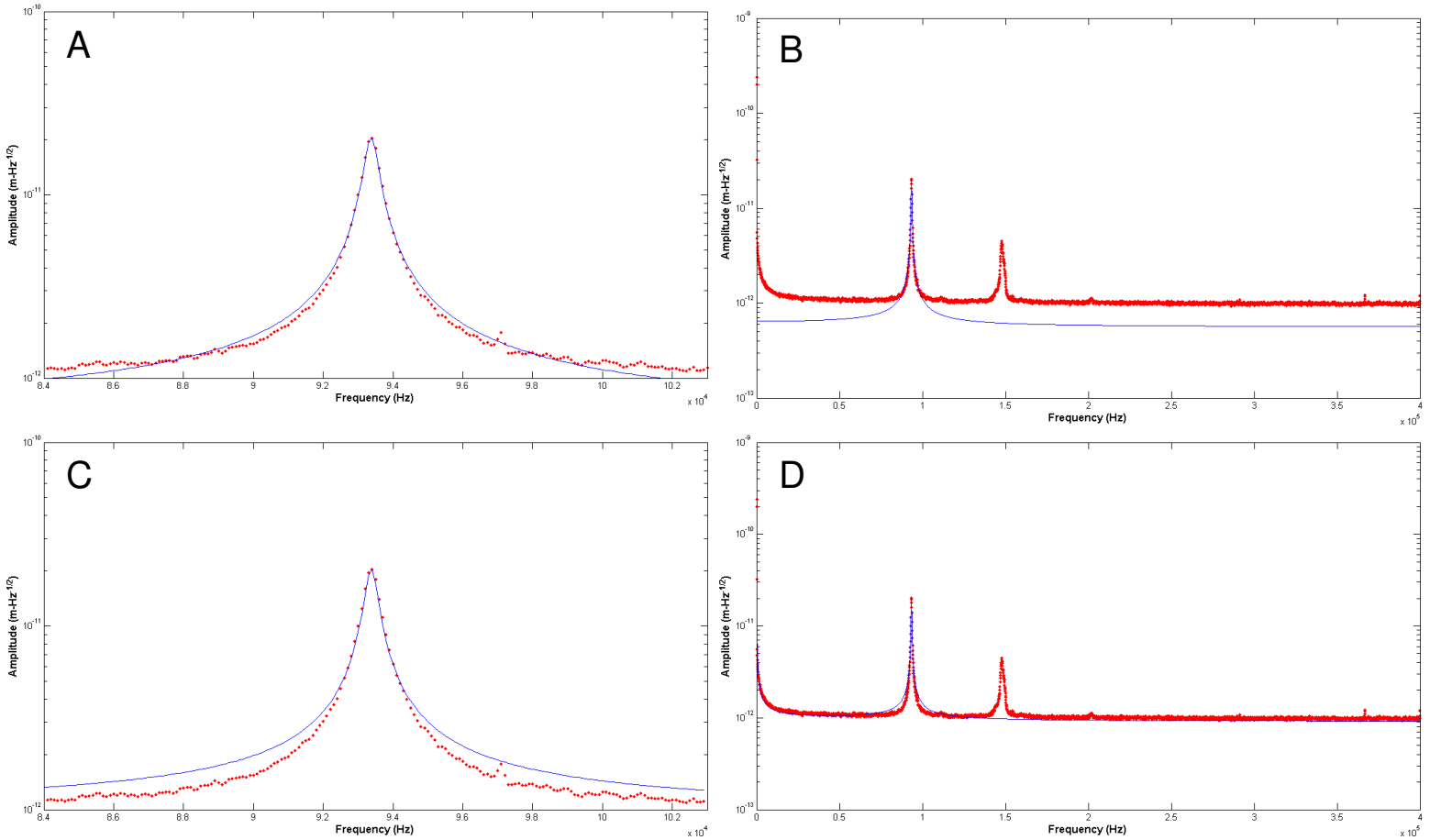

Figure 4.6. Comparison of the fits of simultaneous and sequential methods to the same PSD data. In each plot, the red points are the data from the thermal spectrum, and the blue line is the fit. A and B are the reduced and full spectrum, respectively, with the data fit to Equation 4.9 simultaneously. C and D are the reduced and full spectrum, with the data fit to Equation 4.9 sequentially. Both methods are fit over a reduced range: 84-103 kHz. As a note, the additional peak at ~150 kHz is from a higher mode of vibration that is not fit by either method.

Table 4.1. Comparison of the results from fitting the simultaneous and sequential methods to several cantilevers. The cantilevers included in this comparison have a wide range of spring constants. The fitting parameters follow a similar trend for both methods, excluding the 1/*f* parameters C_1 and C_2. In general, there is good agreement between the two methods, k^* and $k^§$, on soft cantilevers. The simultaneous method fails to return reasonable values for stiff cantilevers. For comparison with the sequential method, A_{DC}, f_0, and γ parameters from the simultaneous method were integrated numerically using the SHO term only, generating $k^†$. Excluding the noise improves the agreement between the two methods, $k^†$ and $k^§$. It should be noted that both f_0 and k do not fall within the range provided by the manufacturer for several of the cantilevers. The manufacturer uses a different method to calculate the spring constant.[119]

	Fit from Simultaneous Method								**Fit from Sequential Method**							**Manufacturer Specifications**	
Probe ID	**C_0 (pm)**	**C_1 (nm •Hz)**	**C_2**	**A_{DC} (fm)**	**γ**	**f_0 (kHz)**	**k^* (N/m)**	**$k^†$ (N/m)**	**C_0 (pm)**	**C_1 (nm• Hz)**	**C_2**	**A_{DC} (fm)**	**γ**	**f_0 (kHz)**	**$k^§$ (N/ m)**	**f_0 (kHz)**	**k (N/m)**
CSC12-E	7.9	0	0	1450	64	12.0	.13	0.21	9.4	14.1	1	1360	65	12.0	0.20	7-14	0.01-0.08
CSC12-F	4.3	0	0	1054	86	16.3	0.17	0.22	5.9	12.3	1	994	84	16.3	0.23	14-28	0.02-0.2
NSC12-E	5.5	0	0	664	93	21.8	0.22	0.39	6.7	9.1	1	616	93	21.8	0.36	17-24	0.1-0.4
CSC12-D	2.8	0	0	612	109	22.4	.29	0.38	4.9	8.3	1	581	102	22.4	0.40	9.5-19	0.01-0.1
CSC12-A	1.3	0	0	243	197	65.9	0.39	0.45	2.5	5.5	1	218	207	65.9	0.48	65-150	0.25-2.5
NSC12-F	3.2	0	0	412	117	29.3	0.41	0.59	4.3	10.3	1	368	124	29.3	0.60	33-49	0.35-1.2
CSC12-C	1.3	0	0	241	167	48.1	.63	0.74	2.4	4.2	1	216	173	48.1	0.79	50-105	0.15-1.5
NSC12-D	5.6	0	0	189	170	43.1	0.49	1.3	6.5	7.5	1	165	179	43.1	1.1	23-34	0.2-0.7
CSC12-B	0.55	0	0	81	254	93.4	1.9	2.2	0.98	2.4	1	73	266	93.4	2.3	95-230	0.45-5.0
NSC12-C	2.4	0	0	21	469	141.5	1.9	12	2.5	4.1	1	19	462	141.5	8.8	120-190	3.5-8.5
NSC12-A	1.6	0	0	11	729	195.1	3.7	20	1.7	3.7	1	11	707	195.1	15	165-240	3.5-12.5
NSC12-B	2.1	0	0	4	1064	278.6	2.0	73	2.1	2.3	1	4	1023	278.6	33	240-405	6.5-27.5

*Numerical integration of *A(f)* includes SHO and noise terms from the simultaneous method. †Numerical integration of *A(f)* includes SHO term only using parameters from the simultaneous method. §Numerical integration of *A(f)* includes SHO term only using parameters from the sequential method.

data better in the reduced range than the sequential method (Figure 4.6C). However, the comparison of the fit to the full thermal spectrum shows the importance of using the correct fitting routine. The simultaneous method does not fit the full thermal spectrum. The sequential method provides a much better fit over the entire range of the thermal spectrum. The discrepancy lies in that the simultaneous method can arbitrarily adjust the noise components and the SHO components in the reduced range to create a better fit. The sequential method takes the noise from the full range, and then uses the noise components while fitting to a SHO in the reduced range. As can be clearly seen from the results, noise components should be fixed before fitting the reduced data range.

Both methods are applied to cantilevers with a large range of spring constants. A term-by-term comparison of the two fitting methods is displayed in Table 4.1. The simultaneous method fails to fit any 1/*f* contribution for all of the cantilevers, i.e. it sets those parameters equal to zero. This is discouraging since several of the less stiff cantilevers have resonance peaks in the 1/*f* region. The simultaneous method consistently returns spring constants that are lower than those fit by the sequential method.

Interestingly, the simultaneous method includes the noise components in the numerical integration,[306] even though the mean-square amplitude should only include the contributions from the SHO.[120] Including the noise terms in the numerical integration results in a larger mean-square amplitude, which yields a lower calculated spring constant. The calculated values from the simultaneous method for the stiff cantilevers, NSC12-A, B, and C, are grossly below the range provided by the manufacturer. The sequential method performs the numerical integration only on the SHO term of Equation 4.9, as dictated by the equipartition theorem.

For comparison, only the SHO terms from the simultaneous method were integrated numerically. These calculated spring constants match those from the sequential method, except for the stiffer cantilevers. In this case, the spring constants are significantly larger than those calculated using the sequential method. The simultaneous

method fails to calculate reasonable values for the spring constant of stiff cantilevers. By fitting all six variables simultaneously, multiple optima exist. The simultaneous method can calculate values that are a better fit mathematically, but an incorrect fit according to the model.

The critical issue in choosing a fitting routine is that the model is accurate. Integrating noise components is not a correct application of the equipartition theorem. In contrast, the sequential fitting routine, Appendix A.3, is self-consistent within the bounds of the equipartition theorem. By fitting the each term of Equation 4.9 sequentially, the problem of multiple optima is drastically reduced. The sequential method is the better method for fitting the equipartition theorem to the thermal resonance data.

4.3.3 Modeling Thermal Resonance in Contact

Beam theory is used to describe the motion of the cantilever when it contacts a hard surface.[337-340] The boundary conditions of the model used to describe the cantilever change when the cantilever makes contact with the surface. It is no longer appropriate to describe the cantilever as clamped-free. The clamped-pinned boundary condition is a more accurate description. Figure 4.5 displays the motion of a beam pinned to a surface. The shape, frequency, and amplitude of cantilever vibration change when it makes contact with the surface. Note that for an optical lever detection method, a small amplitude for the first mode of vibration can be observed because the laser spot covers an area at the end of the cantilever. This makes it possible to detect the oscillation of the cantilever. The measured amplitude is small because of the location of the laser spot in relation to the maximum displacement of cantilever motion. A larger amplitude would be measured if the laser spot were centered on the cantilever. When the laser spot is at the end of the cantilever, the measured amplitude is near or below the noise floor, especially for stiff cantilevers.

If a compliant object is placed between the cantilever and the surface, the end of the cantilever is free to vibrate. This system can be described with springs in parallel. The arrangement of the cantilever/object system and the spring model is shown in Figure 4.7. As with the previous descriptions, the vibration at the end of the cantilever is measured from the laser light reflecting off the cantilever and onto a position sensitive detector. This is equivalent to the oscillation of the effective mass in the spring model. Springs in parallel can be drawn two ways. The left diagram looks similar to that of the cantilever system. The diagram on the right is the same system, but drawn in a way to illustrate the parallel nature of the springs. The movement of the end of the cantilever is modeled by the movement that of the mass between the two springs. For springs in parallel, the relationship of the spring constant of the system is given by:

$$k_{sys} = k_{cant} + k_{obj} . \qquad \text{Equation 4.10}$$

The vibration of the two spring system does not necessarily occur at the resonance frequency of the cantilever. The resonance frequency is dependent on the spring constant of the system. The resonance frequency of the system can be calculated by inserting Equation 4.10 into Equation 4.7, which yields,

$$f_0 = \frac{1}{2\pi}\sqrt{\frac{k_{cant} + k_{obj}}{m_{eff}}} . \qquad \text{Equation 4.11}$$

The model describes the motion of the mass between the two springs, which is equivalent to the vibration at the end of the cantilever. For springs in parallel, the amount of force compressing the two springs does not affect the resonance of the system.

For all four different scenarios, the only observable is the movement of the cantilever. Cantilever motion can be described by four different spring models. In the case of cantilever deflection, this is modeled as the deflection of a spring. The deflection of the cantilever can be convoluted by the compression of a compliant object. By adding a spring in series to the deflection model, the contribution of the compliant object can

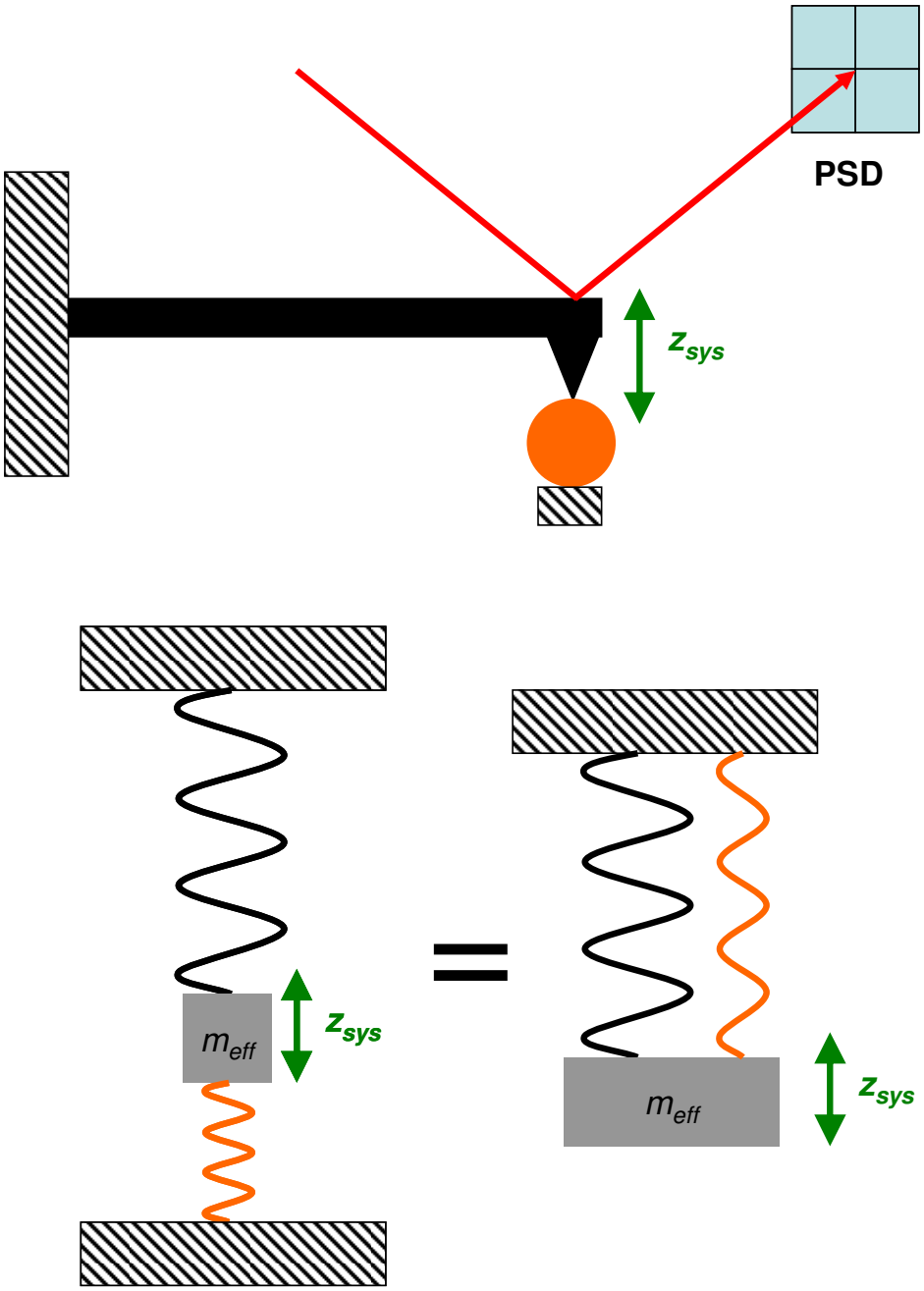

Figure 4.7. Diagram demonstrating the equivalence of cantilever resonance to resonance of springs in parallel when a compliant object is placed between the cantilever and the surface. The frequency of the system, z_{sys}, is only dependent on the two spring constants, as Equation 4.11 suggests. As a reminder, the deflection at the end of the cantilever is measured by reflecting a laser beam off the end of the cantilever and onto a position sensitive detector. The resonance measured at the end of the cantilever can be described as the resonance of the mass between the two springs.

easily be deconvoluted. For cantilever resonance in free space, the cantilever vibration is modeled as the simple harmonic motion of a mass hanging from a spring. For cantilever resonance in contact with a compliant object, a model of springs in parallel describes the motion of a mass between two springs. Each of the different scenarios is encountered in MPFS, and the application of the correct model is essential for accurate interpretation.

4.4 Improving Multi-Parameter Force Spectroscopy

Because the thermal resonance acquired during MPFS originates from small changes in voltage, electronic noise both from within the MPFS setup and from external sources often acts as interference peaks. To improve the quality of the thermal resonance data, the source of the noise needs to be isolated and then corrected.

4.4.1 Random Noise

As expected with any small, transient voltage signal, the random noise inherent to the electronics results in a poor signal-to-noise ratio after a single DFT. The signal-to-noise ratio can be improved by ensemble averaging individual PSDs. The effect of averaging can be seen in Figure 4.8. Increasing the number of PSDs averaged together improves the signal-to-noise ratio. For example, the noise peak at 300 kHz can only be distinguished above the noise after 64 averages. The drawback to using a large number of averages is time. During a MPFS experiment, the z scanner is moving. By having a large number of averages making up a single PSD, the scanner displacement per PSD increases. Any sudden changes in the resonance frequency or amplitude of the system could be averaged out. If the number of averages is left too low, changes in the resonance frequency or amplitude could be obscured by the random noise. A balance between the signal-to-noise ratio and the ability to discriminate changes in time must be made.

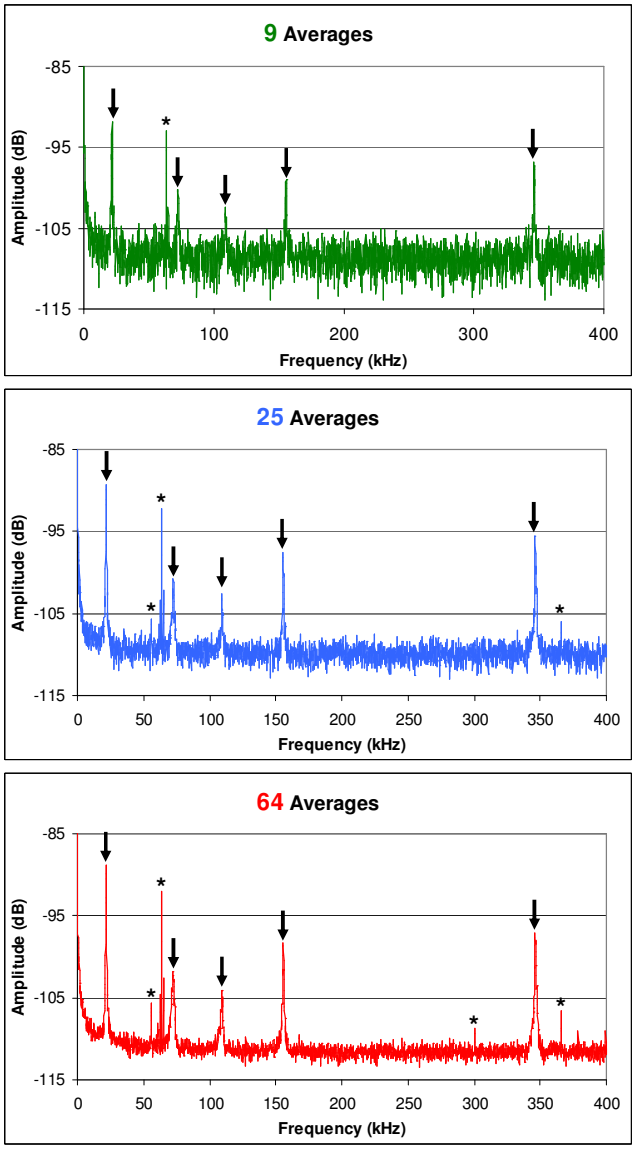

Figure 4.8. Comparison of the effect of averaging on the random noise for a power spectral density plot. The signal-to-noise ratio improves with increasing number of averages in each PSD. A noise peak at 300 kHz can only be differentiated after 64 averages. Averaging, however, does not alleviate systematic noise. Peaks at 55, 63, 300, and 370 kHz are all peaks from systematic noise, denoted with *. The peaks at 20, 70, 110, 160, and 345 kHz result from oscillatory motion of the cantilever, indicated with arrows.

4.4.2 External Systematic Noise

Averaging improves the signal to noise ratio for random noise. Another source of noise is systematic. A large source of the systematic noise in MPFS comes from displays that use a cathode ray tube (CRT) to produce the image. CRT monitors produce electromagnetic fields that are coupled to the signal carrying wires. When any CRT monitor is on, several sharp noise peaks appear in the PSD. Previously protocol dictated that the monitors were to be turned off before MPFS data is acquired. This left the user unable to observe and control the AFM because the monitors are off. Several solutions exist for this problem. Faraday cages are placed around essential monitors to help alleviate the noise from the CRT. Some monitors can be relocated away from any signal carrying wires. All other monitors are turned off during data acquisition. This significantly reduces the noise peaks recorded in the PSD.

4.4.3 Internal Systematic Noise

Even after reducing random noise and removing external noise, a strong noise peak at 63 kHz remains, as seen Figure 4.8. This peak's location and intensity often interferes with MPFS data. Several cantilevers used herein have resonance frequencies in the 50-80 kHz range. This peak and the other smaller noise peaks, denoted with (*) in Figure 4.8, exist at a fixed amplitude and frequency for all cantilevers and even when no cantilever is present. This suggests that the noise is internal to electronics of the MPFS system. A thorough investigation of the MPFS instrumentation was needed to locate the source of the noise.

Each component of the MPFS experimental setup was removed in sequence to isolate the source of the electronic noise peaks. The noise peaks exist even when no power is provided to the AFM base. Without power to the AFM, there is no signal generated for MPFS to acquire. This suggests that the noise is not generated by the

MPFS electronics. It is possible the noise is from an RF source that is coupled in the signal wires. Most of the signal wires are shielded to prevent coupling of RF noise. Shielding was added to all signal wires, but the noise peaks remained. The only remaining reasonable explanation for persistent noise peaks is a ground loop.

A ground loop exists when there is a potential difference between two grounds. This potential difference causes a current to run through the ground connections. Since ground is often used as the reference voltage for signal analysis, any current in the ground will create noise in the signal. Figure 4.9 is a block diagram of the MPFS setup highlighting the connections to ground. The only connections to ground occur through the safety grounds of the power cords. The connection to ground is transmitted through the signal wires. Every component counterclockwise from the red dashed line in Figure 4.9 was removed from the experimental setup to verify the existence of the ground loop. The instrumentation to the left of the red dashed line must be powered and grounded to record any frequency data. Each component was added in sequentially and connected to ground. The connection to ground was made from the shielding for wires and from the case for all other components. Any time a ground connection was made, the noise returned. For verification, the safety ground to all the components of the setup was removed while the system was powered, and the noise peaks disappeared. Unfortunately, removing the connection safety ground is not an acceptable solution. Safety grounds are needed to prevent the voltages from building up on the instrumentation. If voltage is allowed to build up, the discharge of that voltage could damage the instrumentation and/or the user.

Any connection to ground (e.g. grounding through power cords, manually grounding the case, or connecting the cable ground line to building ground) resulted in the same noise peaks with the same amplitude. Since the amplitude of the noise was fixed, a preamplifier was added in-line between the vertical deflection signal and the DAQ with the intention of amplifying the amplitude of the signal over the noise.

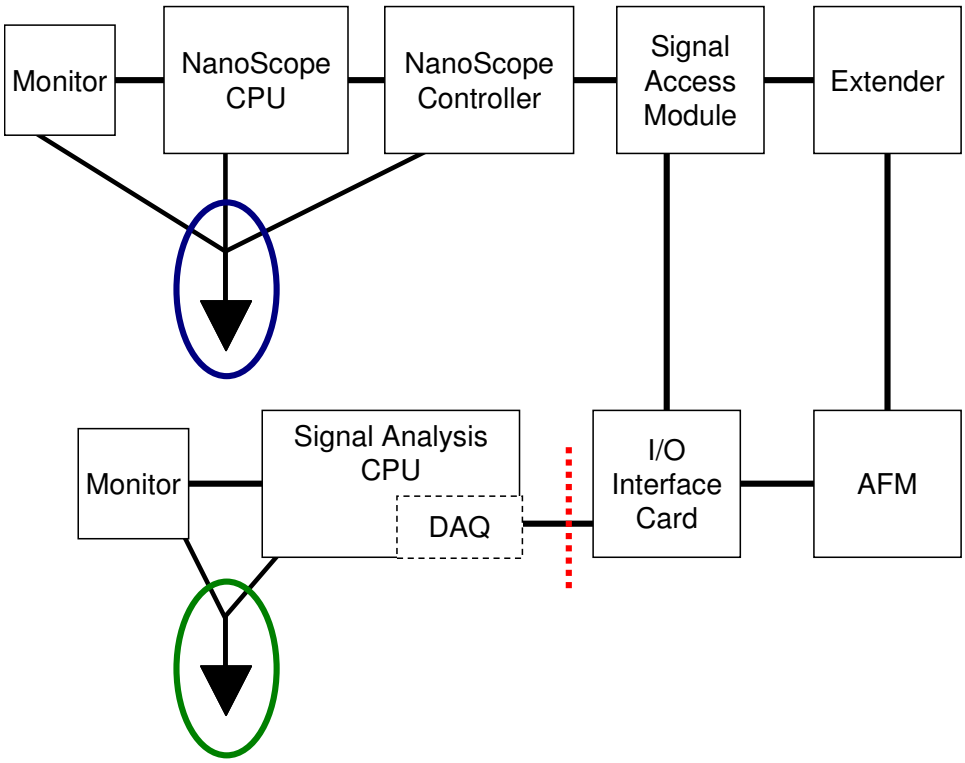

Figure 4.9. Schematic of the MPFS experimental setup highlighting the connections to ground. The ground connection circled in green is made through the power cords for the monitor and Signal Analysis CPU. The ground connection circled in blue is made by through the power cord for the monitor, NanoScope CPU and NanoScope controller. Both of these connections to ground are safety grounds and are required during MPFS experiments. The ground loop is carried circles around the instrumentation through the shielded wires and case grounds. Removing all connections to ground counterclockwise of the red dashed line removed the noise peaks.

The effect of the preamp gain on to the noise signal is shown in Figure 4.10. The first thing to note is the increase in the number of noise peaks from the raw (red) to the preamp with a gain of one (blue). The addition of preamplifier altered the noise frequencies and amplitudes. These extra noise peaks were verified to be ground loop noise using the same procedure discussed above. Even though the ground loop noise changed, the peak at 63 kHz remains, and there are several additional large noise peaks above 100 kHz. The gain on the preamp was increased to amplify the signal above the noise peaks. As Figure 4.10 shows, increasing the gain on the preamp causes the noise floor to raise above the noise peaks. The noise still exists, but it is below the amplified noise floor.

Amplification does not alter the shape or location of the resonance peaks, as seen in Figure 4.10. It does increase the measured base amplitude and amplitude of the noise floor. Recalling from the SHO model, Equations 4.6 and 4.9, changing the measured amplitude significantly affects the calculated spring constant. Each term in Equation 4.9 contains an amplitude coefficient. Since the gain is amplifying all signals, its effect on each amplitude coefficient can be factored out of Equation 4.9. The next step in the fitting routine is the numerical integration of Equation 4.9. The square of the gain can be factored out of this step. To correct for the amplification of the preamp, the mean-square amplitude of the measured PSD is divided by the square of the gain. This can be done by inserting a correction factor into Equation 4.6:

$$k_B T = \frac{3}{4}\frac{k\langle A^2\rangle}{G^2}. \qquad \text{Equation 4.12}$$

where G is the gain setting from the preamp. By adding this correction factor, the spring constant of the cantilever can be calculated for any gain setting.

In summary, a methodical investigation of the sources of noise resulted in the reduction of noise in the PSD plots acquired during MPFS. It has been shown that altering the signals from the AFM affects the calculated results. Any changes to the raw

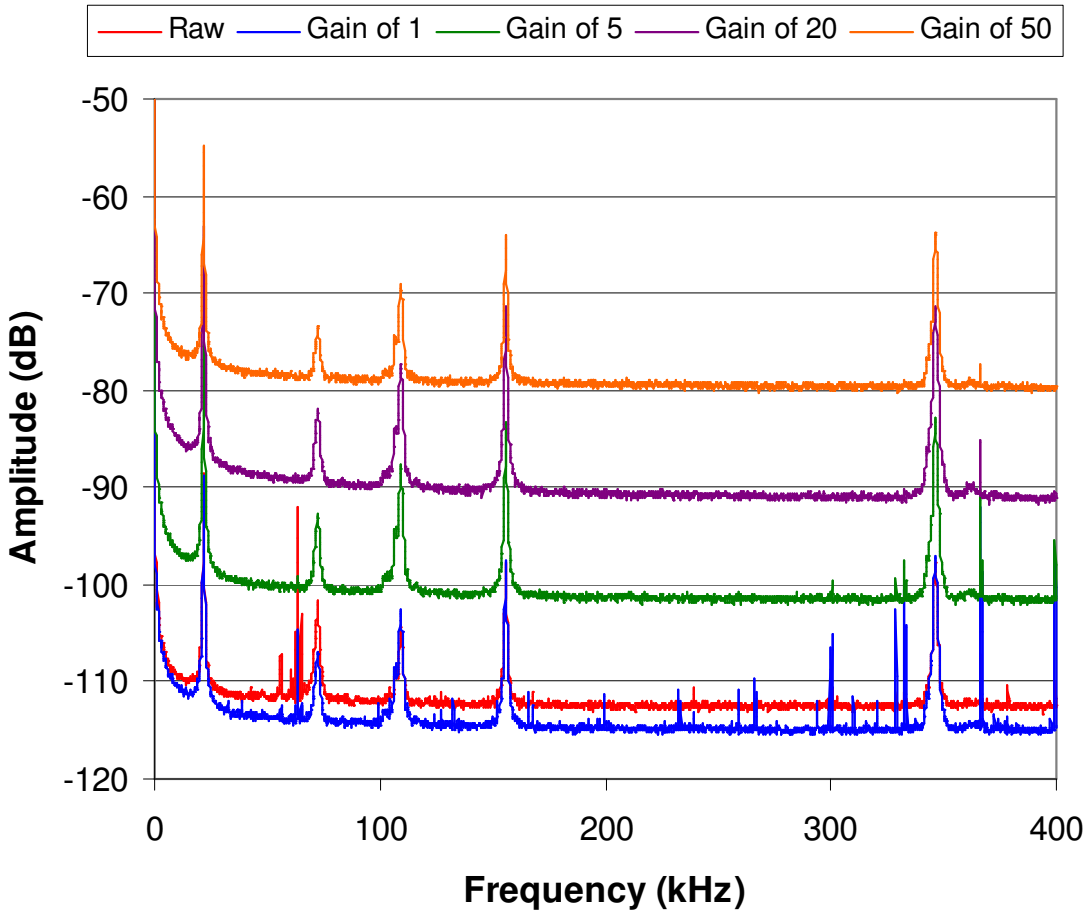

Figure 4.10. Plot showing the effect of amplifying the signal from the position sensitive detector. The red line is the raw voltage signal, without the preamp in-line. The blue line is after the addition of the preamp, but with the gain set to one, i.e. no amplification. The other plots are with increasing gain. With the gain set at 5 (green line), most of the noise that appears with a gain of 1 is below the amplified noise floor. At a gain of 50, only the most intense noise peak, 365 kHz, remains above the noise floor. The noise peaks are removed from the PSDs by amplifying the vertical deflection signal from the base of the AFM.

signals must be carefully thought out. These changes must be accounted for in any post processing or calculations.

4.5 Experimental Methods

Multi-parameter force spectroscopy was performed using the following methods. These methods were established to acquire data that could be compared among experiments and to be compatible with pre-existing and custom programs for data extraction and analysis.

4.5.1 AFM Settings

The atomic force microscope used in this study was a Multimode AFM with a NanoScope IIIa controller with an extender electronics package (Veeco Metrology, Santa Barbara, CA). The AFM was also equipped with a signal access module. The NanoScope software (version 5.31r1) was used to control the AFM during MPFS experiments. The software allows the user to define and control the scan range, scan rate, scan offset, drive amplitude, and drive frequency. The NanoScope software is used to acquire the vertical deflection of the cantilever and the oscillation amplitude of cantilever at its natural resonance frequency.

Several precautions were taken to prevent damage to AFM probes during engagement. Image acquisition was commenced in Tapping Mode™ without the probe in contact with the surface. The x-y scan range was set to zero so that if the AFM tip did make contact, it would not be dragged across the surface. With the AFM probe above the surface, the z scanner was extended in small increments (~10 nm) while monitoring the vertical deflection and oscillation amplitude.

As soon as the first event occurred in the oscillation amplitude plot, MPFS experiments were carried out at several increasing steps of the z-scanner. Vertical deflection and oscillation amplitude were acquired through the force spectroscopic mode

of the software with 1024 pixels per trace per data set. Data was acquired with the external drive voltage both on and off at each increment of the z scanner. Figure 4.11 shows the response recorded by the NanoScope software for both the driven and the undriven case. When the external drive voltage is off, the oscillation amplitude falls to the baseline. The data was extracted using custom software that is provided in Appendix A.1.

4.5.2 Dynamic Signal Analyzer Settings

The vertical deflection, horizontal deflection and scanner movement were routed through a BNC-2110 I/O interface card and acquired on a PCI-6120 DAQ (National Instruments, Austin, TX). The vertical deflection signal was amplified using a SR560 Low-Noise Preamplifier (Stanford Research Systems, Sunnyvale, CA) that was placed in-line between the AFM base and the I/O interface. The preamp was set for DC coupling and no high/low pass filters were applied. The maximum input for the preamp was 3 Vpp and the maximum output of the preamp was 10 Vpp. To prevent the preamp from overloading during experiments the gain was set to 10 and the input voltages were kept below 1.0 Vpp. The gain was reduced if the amplitude of the input signal exceeded 1.0 Vpp.

The signals from the DAQ card were acquired using custom software written in LabVIEW™ (National Instruments, Austin, TX) by Jeff Boyles (Georgia Institute of Technology, 2006). The software graphical user interface is depicted in Figure 4.12. It operates like a three channel dynamic signal analyzer (DSA). The horizontal deflection voltage and scanner movement are displayed in voltage versus time. The acquisition rate was set to 5 Hz for each, which was at least two orders of magnitude greater than the scan rate. The raw vertical deflection signal was sampled at 800 kHz. Each sampling was processed through a Blackmann-Harris window. After windowing, the time-variant signal went through a DFT into frequency space to generate a PSD. The resolution of the

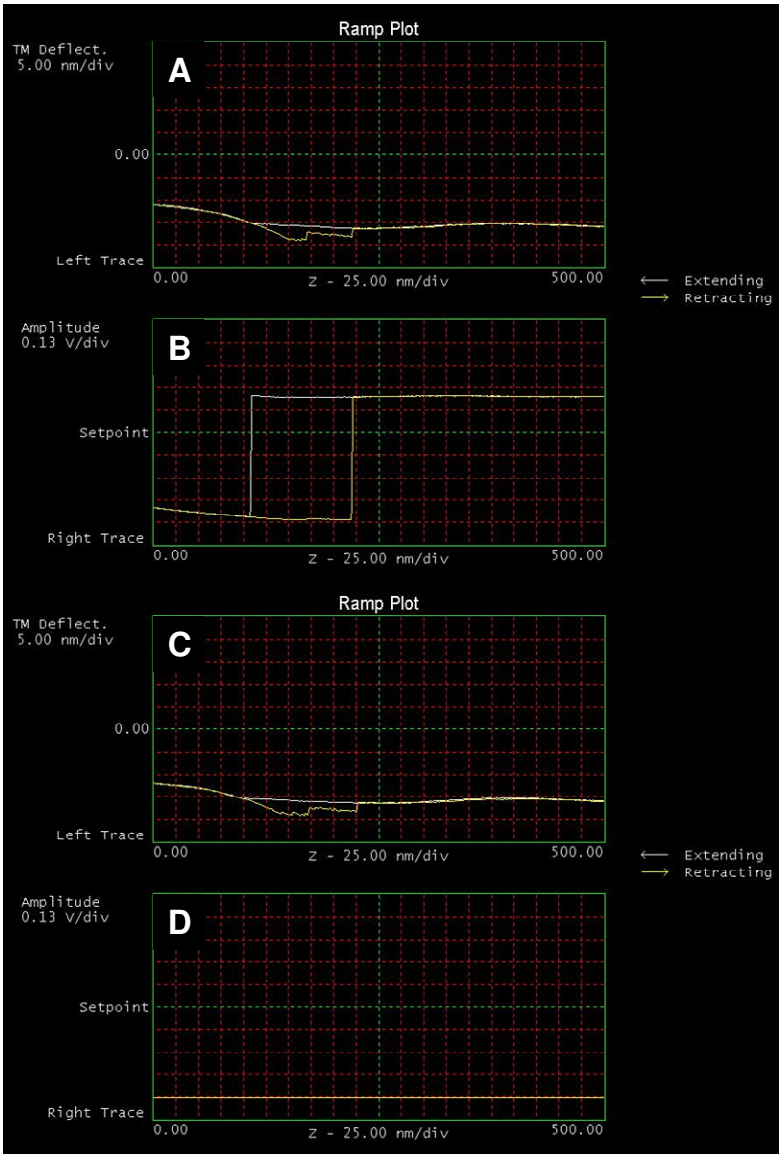

Figure 4.11. Force spectroscopy data acquired using the NanoScope software. Vertical deflection (A and C) and oscillation amplitude (B and D) are captured at the same z-scanner offset, scan range, and scan rate. In A and B, the external drive voltage is turned on, whereas in C and D the external drive voltage is set to zero. There is no discernable change between the two vertical deflection-distance curves (A and C). External drive voltage must be off to acquire the other parameters in MPFS.

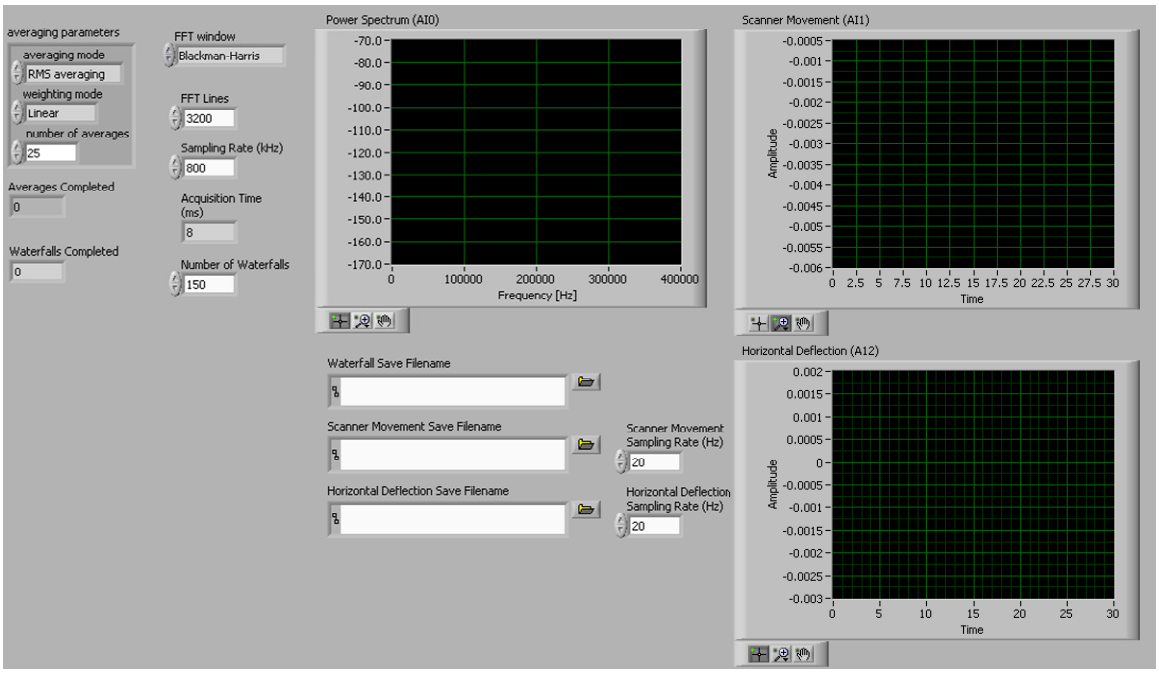

Figure 4.12. Graphical user interface used to control the acquisition of MPFS data. The software interface allowed several parameters to be adjusted during the acquisition of MPFS data. The data is displayed in real-time in each of the plot windows during MPFS experiments.

DFT is determined by the number of DFT lines. There was a tradeoff between acquisition time and DFT resolution. Typically, 4000 DFT lines were used over the 800 kHz sampling rate, which resulted in a resolution of 100 Hz and an acquisition time of 10 ms per PSD. Several PSDs were then ensemble averaged to reduce the random noise. The typical number of averages for MPFS was set between 15 and 25, depending on the rate of the z-scanner. The number of waterfalls, i.e. averaged PSDs, determined the duration of the acquisition of the entire data set, and was set high enough to capture two full cycles of the z-scanner.

4.5.3 Calibration of Spring Constant

Before and after each experiment, PSDs were acquired similar to that for MPFS, with a few key alterations. The cantilever was withdrawn far way (>100 μm) from the surface and the z-scanner was halted, preventing any short or long range forces from damping the cantilever's thermal vibration. The number of averages per PSD was set to 625. The high number of averages ensured that the random noise was significantly reduced, enabling improved estimates of the noise floor. Equations 4.9 and 4.12 were fit to the data using custom code written in MATLAB version 7.4 (The MathWorks, Natick, MA). The source code for this program can be found in Appendix A.3.

The amplitude of the cantilever vibration is measured in volts from the position sensitive detector. In order to be able to relate the voltage to the displacement of the cantilever, the detector needs to be calibrated. This is traditionally done by bringing an unmodified cantilever into contact with a hard surface. The slope of the deflection-distance curve (in V/nm), often called the deflection sensitivity, is the detector calibration for that cantilever. With a modified AFM probe, this is not possible if the modification is compliant, e.g. nanotube. The slope of the deflection-distance curve will always be convoluted with the relationship between the compliance of the object and the compliance of the cantilever per Equation 4.2. The deflection sensitivity must be

acquired away from the compliant modification. Since most modifications occur at the tip of the AFM probe, either the front edge of the cantilever or the area immediately behind the tip can be used to obtain the deflection sensitivity.

To avoid possibly damaging or removing the modification on the tip of the AFM probe, the area immediately behind the AFM tip is used to acquire the deflection sensitivity. A schematic of this method is shown in Figure 4.13. A modified AFM probe is brought into contact with another cantilever, perpendicular to each other. To differentiate between the two cantilevers during further discussion, the cantilever whose deflection sensitivity is being measure is referred to as the cantilever, and the cantilever that is acting as the substrate is referred to as the crossbeam. The crossbeam is mounted sideways on a shim so the side crossbeam makes contact with the cantilever. The cantilever is brought into contact with the crossbeam near the attachment point of crossbeam to its chip. This reduces any sway or torsion that occurs at the end of the crossbeam and any physical interference from the tip on the crossbeam. The crossbeams are 2 μm thick, which allows for fine placement directly behind the tip of the cantilever. The crossbeam method has been verified by measuring the deflection sensitivity of unmodified AFM probes by bringing them into contact with both a hard surface and a crossbeam. The same deflection sensitivity was obtained for both methods.

4.6 Materials

AFM cantilevers were modified with CNTs in two ways. Cantilevers with small walled nanotubes (SWNT) attached to the probe tip were purchased from NanoDevices (now Veeco Metrology, Santa Barbara, CA). These SWNT modified tips were fabricated using a chemical vapor deposition method similar to that previously described.[75] Attachment of the SWNT to the tip is assured by patterned deposition of the catalyst onto the tip and direct growth of the nanotube onto the catalyst. The nanotubes were purchased to be shapes that were not useful for AFM imaging. These included long

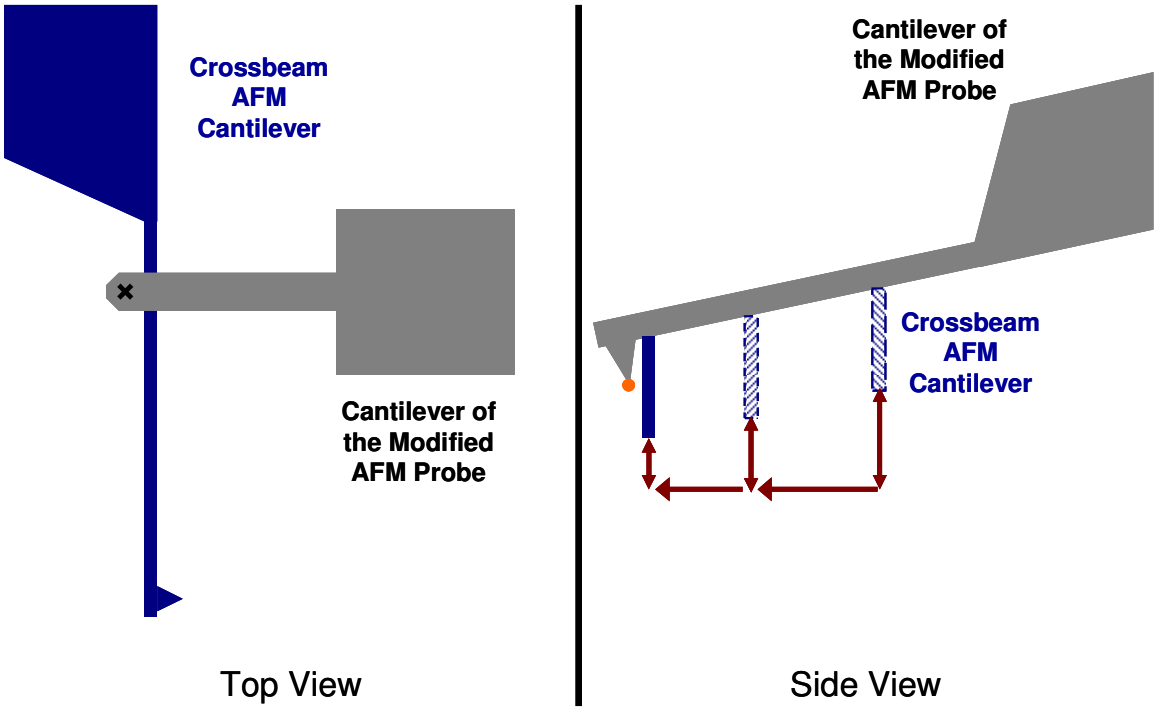

Figure 4.13. Schematic of the crossbeam method for obtaining the deflection sensitivity for modified AFM probes. The top view shows the approximate location of contact between the modified AFM probe and the crossbeam cantilever. The "x" designates the position of the modified AFM tip, which is into the plane of the paper. The contact is made closer to the base of the crossbeam to reduce any sway or torsion effects from the crossbeam. The side view depicts the stepwise approach of the crossbeam. The crossbeam would be brought into contact far away from the modified AFM tip. The crossbeam was repeatedly moved into contact while slowly decreasing the distance between the AFM tip and the crossbeam. The compliant object attached to the tip of the AFM probe is depicted as an orange circle.

(length ≥2 um) straight SWNTs, kinked SWNTs, and looped SWNTs.

Coiled carbon nanotubes (CCNT) were synthesized by a CVD method by C.V. Nguyen and R.M. Stevens at NASA Ames Research Center (ARC) using a proprietary catalyst. The coiled carbon nanotubes were attached to NSC18 cantilevers (MikroMasch USA, San Jose, CA) by arc welding the nanotubes onto nickel coated AFM tips.[27, 250, 306] This method grants user control of the orientation of the CCNT with respect to the AFM tip.

Prior to and following the AFM studies described herein, each SWNT modified tip was examined with a LEO 1550 scanning electron microscope (Carl Zeiss, Thornwood, New York) or a Nova NanoLab 200 dual ion/electron beam microscope (FEI Corp., Hillsboro, OR). The accelerating voltages were kept below 10 kV to reduce nanotube vibration and possible damage incurred from exposure to the electron beam. The ion beam on the Nova was left off to prevent any beam-induced damage. Examples of several of the types of SWNTs used in this investigation are included in Figure 4.14. After MPFS experiments were concluded, the nanotube modified AFM tips were imaged in a JEOL100CX-2 transmission electron microscope (TEM) using a custom built holder.[306] The AFM chip is too large for a traditional TEM grid; the cantilevers would have to be broken from the chip to acquire TEM images. The custom holder allows the intact AFM chip to be brought into the TEM for imaging.

Several surfaces were used throughout this study. Silicon chips were diced from <100> silicon wafers into 1 cm x 1 cm squares. The chips were cleaned with a hot piranha (7:3 H_2SO_4:H_2O_2) solution, rinsed in filtered absolute ethanol, dried under a stream of N_2, and stored in a desiccator until use. Highly oriented pyrolytic graphite (HOPG) of SP-1 grade (SPI Supplies, West Chester, PA) was freshly cleaved immediately before each experiment using the tape method. Template stripped gold

(TSG) was used as the substrate for self-assembled monolayers (SAM).[342, 343] TSG was created by depositing ~500 nm of gold onto freshly cleaved mica sheet using any physical vapor deposition technique, e.g. thermal evaporation, electron beam evaporation, or sputtering. Circles 7/16" in diameter were punched from the gold/mica sheet and fixed onto silicon chips using epoxy 377 (Epoxy Technology, Chelmsford, MA) with the mica side facing up. The mica was released from the gold by soaking the substrate in THF for several seconds. The TSG was quickly rinsed off using filtered absolute ethanol and then immersed in a 2 mM thiol solution of filtered absolute ethanol for self-assembly for 2 hours. This method of generating self-assembled monolayers of thiols on gold is well documented.[344, 345] The thiols used in this study were 1-undecanethiol, 11-hydroxy-undecanethiol, 11-mercapto-undecanoic acid and 11-amino-undecanethiol. The first three were used as received from Sigma-Aldrich (St. Louis, MO); the last was used as received from Dojindo Chemicals (Rockville, MD). These thiols were chosen for increasing polarity of the end group. Surfaces of each thiol were periodically imaged using AFM to verify that the monolayer was intact. The RMS roughness of the films measured to be 0.5 (± 0.2) nm.

Trenches were etched into silicon to serve as substrates for mechanical testing. The trench pattern was designed by this author, but the following steps were performed in the MiRC Cleanroom facilities by Jabulani Barber (Georgia Institute of Technology, 2009). A four inch silicon <100> wafer was RCA cleaned: 1) organic contaminants are removed by soaking in an aqueous solution of 5:1:1 H_2O:H_2O_2:NH_4OH; 2) The thin silicon dioxide layer is removed by soaking in a dilute 20:1 H_2O:HF solution; 3) ionic and heavy metal contaminants are removed using an aqueous solution of 6:1:1 H_2O:H_2O_2:HCl. A thermal oxide ~550 nm thick was grown on a clean <100> silicon wafer using dry/wet/dry thermal oxidation for 5/45/5 minutes, respectively. The wafer was then patterned using photolithography. The wafer was coated with an adhesion promoting layer of 1,1,1,3,3,3-hexamethyldisilazane (MicroSi, Phoenix, AZ) which was

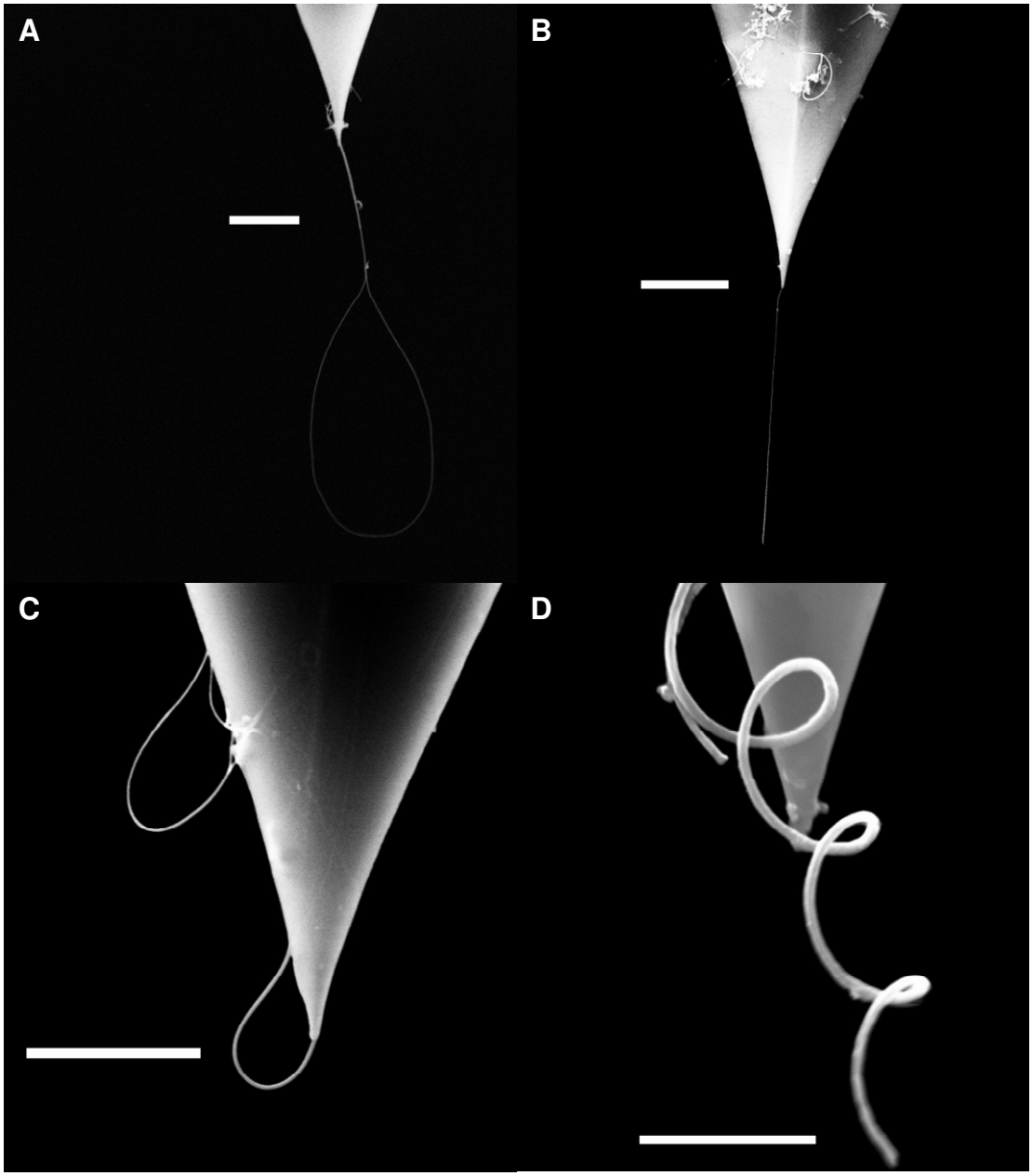

Figure 4.14. SEM Images of different carbon nanotube modified AFM probes used in this investigation. Operating voltage was set to 10 kV or less to reduce electron beam induced damage of the carbon nanotubes. The perspective for each of these images is looking at the front of the AFM probe down the length of the cantilever. The scale bar in each image represents 1.0 µm. A-C are SWNTs grown from a catalyst on the AFM tip. D is a CCNT that was arc welded onto a nickel coated AFM probe.

rapidly spun off after coating. Shipley Microposit® S1813 photoresist (MicroChem Corp., Newton, MA) was deposited on the wafer by spin-coating at 4000 rpm for 30 seconds. The photoresist was soft-baked at 115 °C for 60 seconds. The pattern was exposed into the photoresist using a MA-6 mask aligner (Karl-Suss, Palo Alto, CA). The exposed photoresist was developed using Microposit® 351 developer (MicroChem Corp., Newton, MA) with a 1:5 dilution in water. After development, the remaining photoresist was hard baked at 115 °C for 20 minutes. Portions of thermally grown oxide layer were now exposed from the photolithography. The wafers with the remaining photoresist were transported to this author for further processing. The thermally grown oxide layer that was exposed during photolithography was etched using buffered oxide etch, 1:5:5 $HF:NH_4HF:H_2O$ for 2.5 minutes. This exposed bare silicon, which was etched with 35% aqueous solution of KOH at 80 °C for 7 minutes. KOH etches silicon anisotropically, which results in angled sidewalls of the trenches but reduces over etching. The KOH also removes all the photoresist. The thermally grown oxide layer prevents the KOH from etching any undesired locations. Figure 4.15 shows an optical and SEM image of the trenches. Each 1 cm x 1 cm square contained 70 trenches that had integer widths ranging from 4 µm to 10 µm with each width having 10 trenches.

Each of the above surfaces was mounted to a steel shim using double-sided tape. The steel shims were held in place by a magnet in the piezo scanner. Steel shims of three different angles, 0°, 5°, and 10° were used to tilt the surface with respect to the 12° inclination of the cantilever in the cantilever holder.

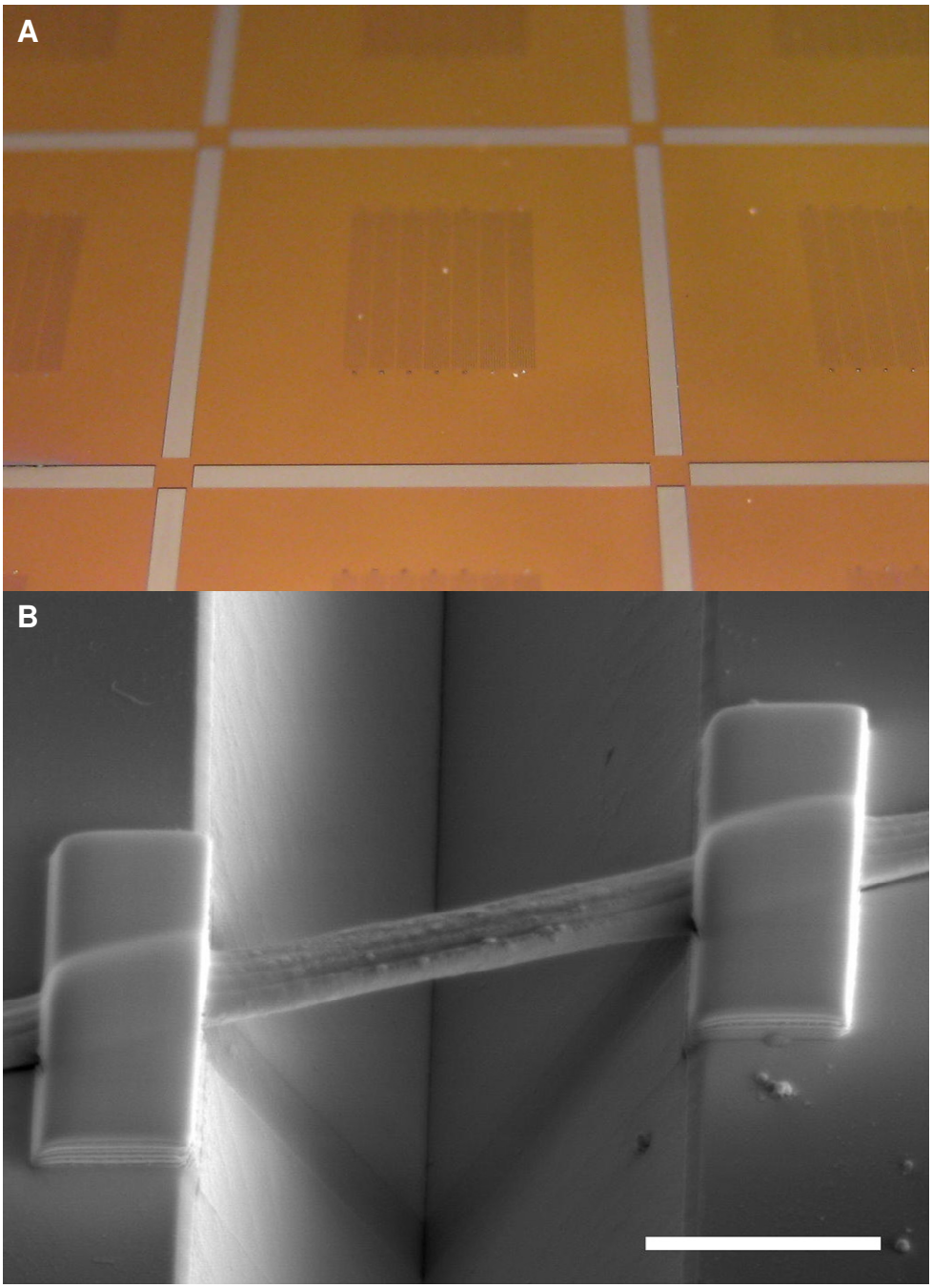

Figure 4.15. Optical and SEM images of trenches etched into silicon wafers. The optical image (A) shows the layout of the silicon chips after etching but prior to dicing. Each trench width is in groups of ten, which are separated from each other and have markings to indicate their width. The color in the image comes from the thickness of the oxide layer. The large rectangles are guide lines for dicing. A SEM image (B) of one trench shows the angled sidewalls created by the anisotropic etch of silicon by KOH. The substrate has been tilted 52°, and the scale bar represents 5 µm. A polymer fiber spans the trench and has been patterned with platinum using ion beam induced deposition.

CHAPTER 5

MPFS OF LONG CARBON NANOTUBES

This chapter contains an investigation of the adhesive and mechanical response of small walled carbon nanotubes (SWNT) during both compression and tension. The SWNTs were repeatedly brought into and out of contact with the substrate by extending and retracting the scanner in the z-direction while monitoring cantilever deflection and thermally driven resonance. The results from compression and tension data can be examined in three different ways. An elastica model was applied to the results to draw conclusions about nanotube buckling, elastic modulus, and the static coefficient of friction. For clarity, each of these results is discussed individually.

5.1 Buckling of Carbon Nanotubes

An example of the SWNTs included in this investigation is provided in Figure 5.1. The nanotubes were long (>2 μm) and straight. Approach of the substrate to the probe was performed in intermittent contact mode. The point of contact is established with a drop in oscillation amplitude as illustrated in Figure 5.2A. The oscillation amplitude of the externally driven cantilever only shows a partial decrease at initial contact, but it quickly returns to the preset drive amplitude. This suggests that any damping forces at contact are quickly removed. Upon retract the amplitude completely drops for a brief distance while the scanner retracts. Figure 5.2B shows a typical force curve acquired with a SWNT tip with reversal of the direction of the scanner movement 60 nm after contact of the probe with the surface. The force curve was acquired at the same scan parameters as Figure 5.2A but with the drive amplitude of the oscillation set to zero. Note that the sinusoidal pattern in this curve is a result of the optical interference from the laser reflecting from both the cantilever and the substrate surface. Also note that

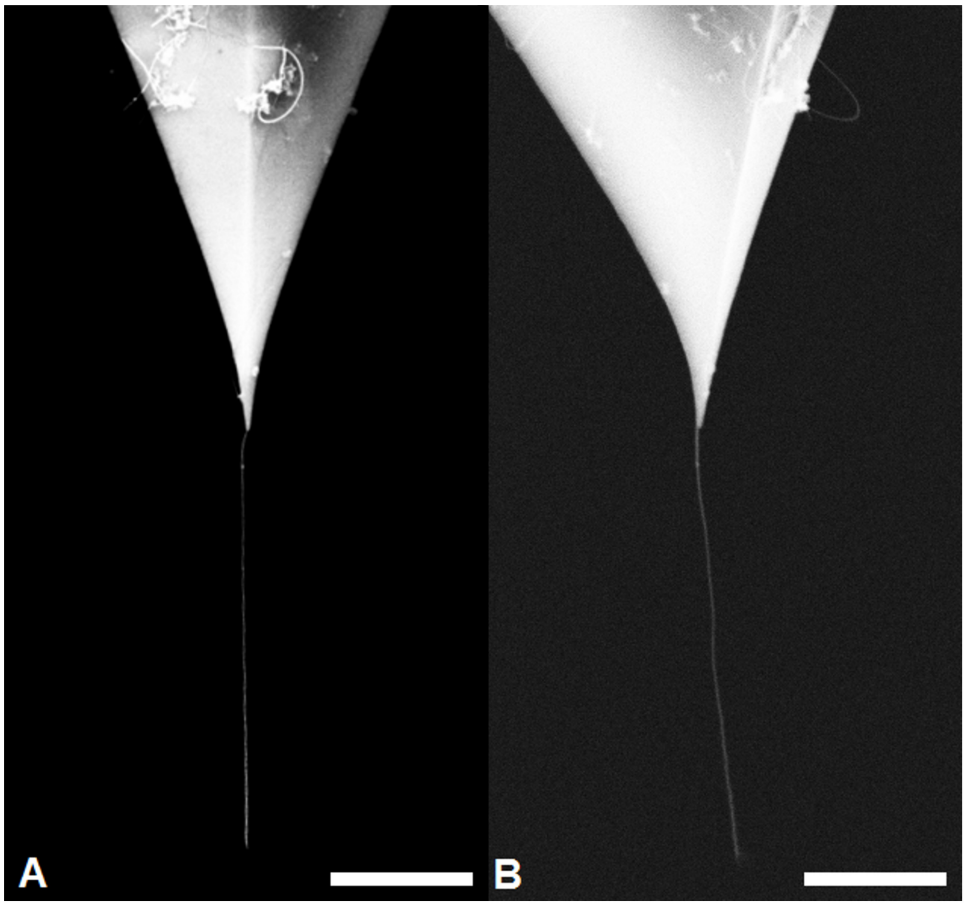

Figure 5.1. SEM images looking at the front (A) and the side (B) of a carbon nanotube modified AFM tip. This carbon nanotube is a good representation of the carbon nanotubes used in this investigation. From the side view, the nanotube is pointing towards the front of the cantilever. The scale bar in each image represents 1 um.

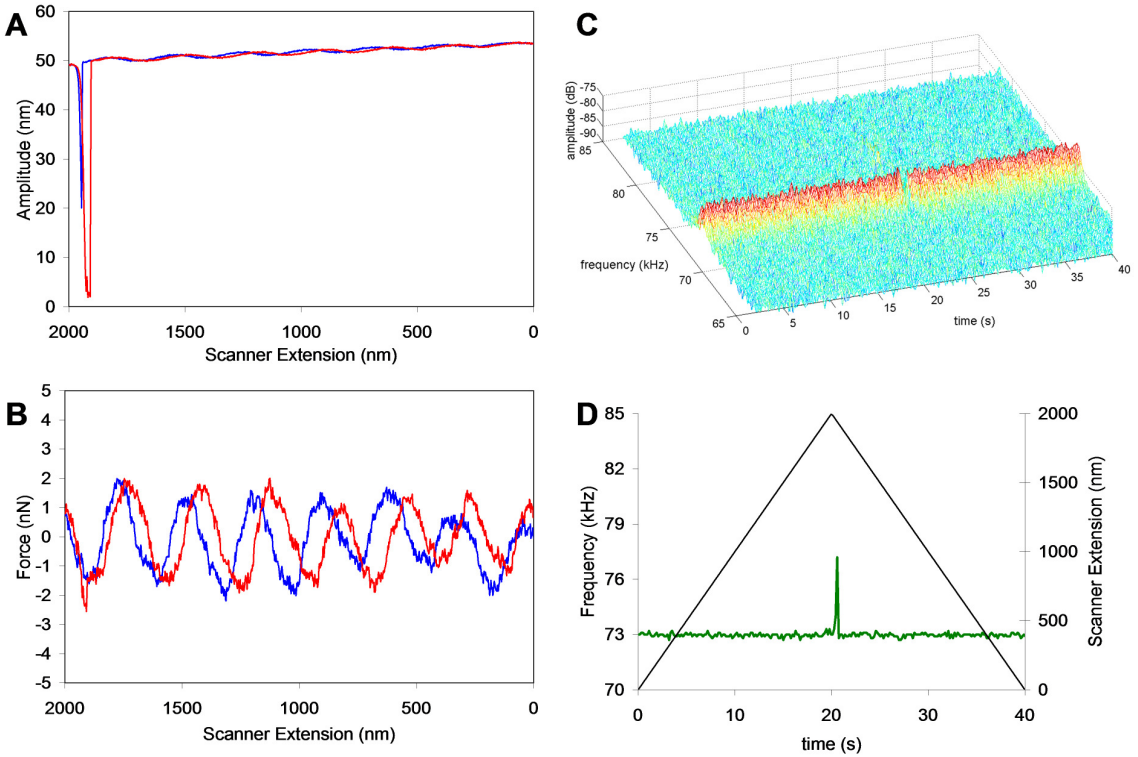

Figure 5.2. A representative MPFS data set for a carbon nanotube modified AFM tip under short (<60 nm) compression on an alkanethiol modified template stripped gold surface. Oscillation amplitude (A) of the externally driven nanotube modified AFM cantilever shows partial decrease in amplitude on approach (blue) and a complete drop on scanner retraction (red). The force curve (B) for the undriven cantilever at the same scan settings in (A) shows no deflection on approach and small adhesion on scanner retraction. The sinusoidal shape is characteristic of optical interference from the spillover of the laser onto a highly reflective surface. The measured frequency response results in a three dimensional waterfall plot (C). Time and frequency are the in-plane axes, with the amplitude of thermal resonance on the z-axis. The amplitude is color encoded to help visualize changes. Because of the complexity of the three dimensional plot, the waterfall data is passed through a peak-picking routine and displayed in two dimensions (D). This allows correlation of changes in frequency (green) with the scanner displacement (black). This method to display the waterfall data will be used throughout the rest of the chapter.

there is no measurable deflection of the cantilever during approach and that only a small downward deflection occurs on scanner retract. The zero or little deflection is attributed to the high spring constant of the cantilevers (2-3 N/m) relative to the spring constant of the SWNT.

The thermal resonance of the cantilever-SWNT system was acquired continuously during force curve acquisition. Figure 5.2C is waterfall plot for the force curve data presented in Figure 5.2B. Time and frequency are the in-plane axes, with the amplitude of thermal resonance on the z-axis. The amplitude is color encoded to help visualize changes. To reduce complexity, the data is presented in an alternative format. The plot presented in Figure 5.2D depicts the frequency of maximum amplitude for cantilever resonance as a function of time. Superimposed onto this data is the movement of the scanner over the identical time period to enable correlation of changes in frequency with scanner extension. Note that there is no shift in the thermal resonance frequency during approach. A shift of 4 kHz is measured upon retract and indicates that during retraction, the nanotube is put into tension.

When the nanotube came into contact with the substrate, the momentary decrease in the oscillation amplitude plot along with no measured shift in the thermal resonance frequency suggest that the nanotube mechanically failed, i.e. it buckled. Our interpretation that the nanotube undergoes buckling is in agreement with the similar observations made by Jiang et al.[145] Using a scanning electron microscope, they clearly saw that compression of multi walled carbon nanotubes resulted in buckling at short compression distances.

The critical buckling load for the nanotubes used herein was calculated to verify the assumption of buckling. Applying a clamped-pinned model from the Euler equation to this system, such that the nanotube is clamped at the AFM tip and pinned by the adhesive interactions at the surface, yields the critical buckling load, F_{crit}, defined by

$$F_{crit} = \frac{EI\beta^2}{(L_{SWNT})^2}$$ Equation 5.1

where E is the elastic modulus of the SWNT, I is the area moment of inertia, β is a constant determined by the boundary conditions, and L_{SWNT} is the effective length of the SWNT. For a clamped-pinned column, β = 4.4934. Using the median values for a SWNT,[181, 182] with an outer diameter of 1.3 nm, an inner diameter of 0.62 nm, an elastic modulus of 1.0 TPa, and a representative length from the samples of 3.0 um, the critical buckling load is calculated to be 0.6 pN. Considering the spring constants of the cantilevers used this experiment, the critical buckling load is reached in the first nanometer of compression. This would strongly suggest that the nanotubes buckle upon initial contact with the surface.

5.2 Tensile Loading of Carbon Nanotubes

When the scanner retracts away from the nanotube tip, the nanotube-cantilever system is put into tension and shifts to a singular frequency. The shift in frequency when the nanotube is put into tension can be modeled as two springs in parallel: the nanotube along its long axis is one spring, the AFM cantilever the other spring, with the mass of the AFM tip separating the two springs. The change in resonance frequency, Δf, for such a system is directly proportional to the ratio of the two spring constants. For springs in parallel, the change in resonance frequency is given by

$$\frac{\Delta f}{f_0} = \sqrt{1 + \frac{k_{SWNT}}{k_{CANT}}} - 1$$ Equation 5.2

where f_0 is the thermal resonance frequency of the system in free space, k_{SWNT} and k_{CANT} are the spring constants of the SWNT and cantilever, respectively. In free space, f_0 is dominated by the AFM cantilever spring constant and cantilever's effective mass. This equation assumes that there is no change in the effective mass of the system. This is reasonable since the mass of the SWNT is negligible compared to the mass of the

cantilever and tip. The spring constant of the SWNT can be used to determine its elastic modulus, E, such that

$$E = \frac{k_{SWNT}\, S}{L_{SWNT}}, \qquad \text{Equation 5.3}$$

where S is the cross-sectional area and L_{SWNT} is the length of the nanotube.

Figure 5.3 shows the frequency response of the system as the SWNT probe is slightly compressed onto three different surfaces. Under the low compression regime displayed in this figure, no frequency shift is measured during scanner extension. During scanner retraction, the nanotube-cantilever system is put into tension and shifts to a singular frequency. Note that the frequency shift is similar for all of the surfaces even though each surface is known to have different adhesive interactions with SWNTs.[114, 315] For springs in parallel, the resonance frequency is independent of system loading. As Equation 5.2 points out, the shift in frequency is dependent only upon the constants of the two springs. Since the results do not show a correlation between adhesion and the frequency shift, this model is appropriate.

To compute the elastic modulus of the SWNT using Equations 5.2 and 5.3, an accurate measure of tube dimensions is required. Measurement of the length of these long SWNTs was made with a scanning electron microscope. Measurement of the diameter is best performed with a transmission electron microscope (TEM). Attempts to acquire the latter met with two undesirable outcomes. Attempts to acquire TEM images prior to mechanical loading experiments resulted in pyrolysis of the tube presumably due to charging effects and poor grounding of the probe while being imaged at high voltages. Pyrolysed nanotubes were no longer suitable for mechanical testing. Acquisition of TEM images was delayed until after mechanical loading studies. During this phase of the investigation, the all of the nanotube modified AFM tips were separated from the AFM tip as evidenced in Figure 5.4. The repeated mechanical stresses imposed on the CNTs during experiments, including compression of 30% of the length of the nanotube, caused

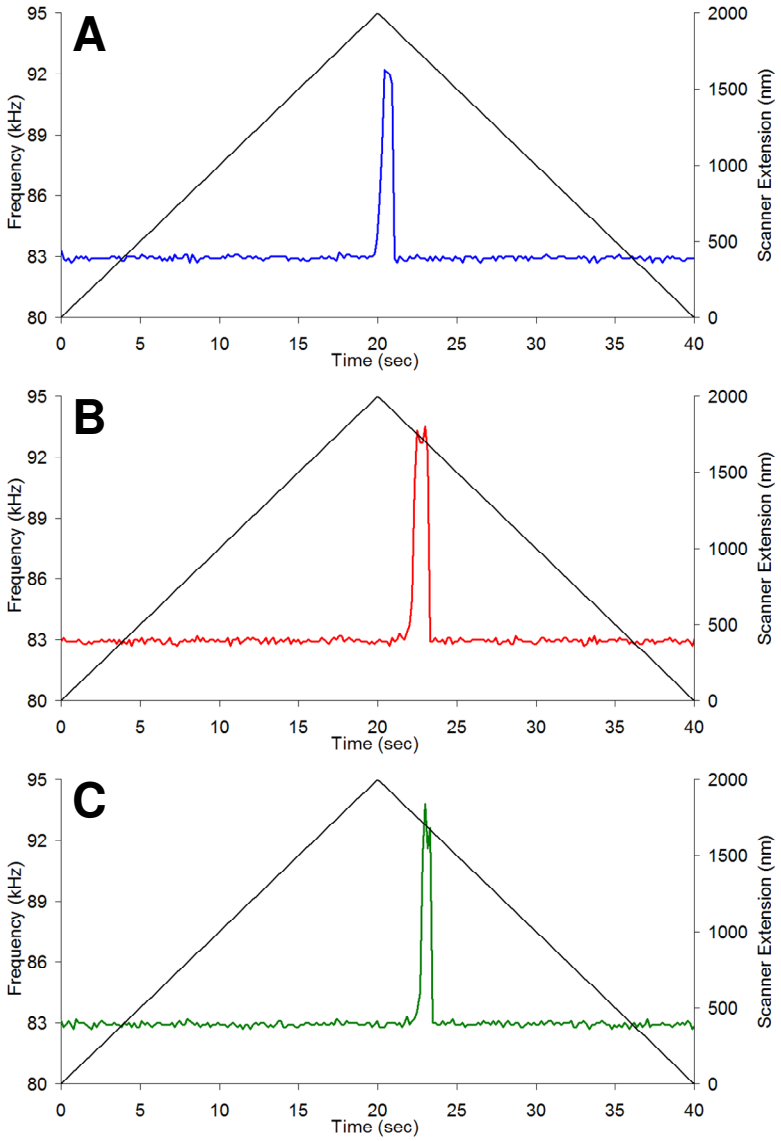

Figure 5.3. Waterfall data for three different self-assembled monolayers on template stripped gold: (A) methyl alkyl thiol, (B) hydroxyl alkyl thiol, (C) amino alkyl thiol. Despite the different chemical functionalities of each surface, the thermal resonance frequency of the nanotube and cantilever system has the same shift in frequency, 10 kHz, when put into tension.

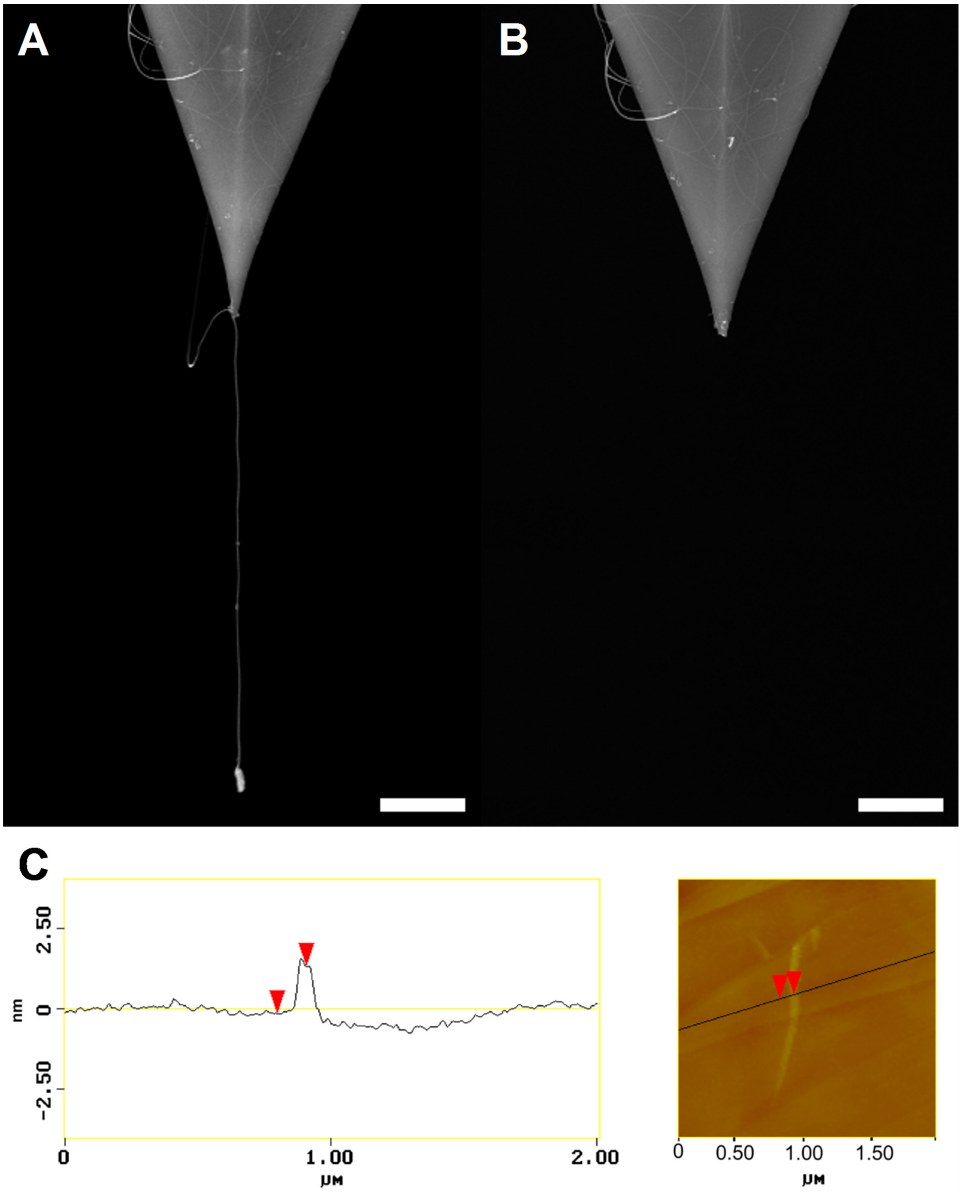

Figure 5.4. Images demonstrating the mechanical failure caused by repeated compression. SEM images of the same carbon nanotube modified AFM tip before (A) and after (B) the carbon nanotube broke off. The scale bar represents 1.0 µm. Sectional analysis of an AFM image (C) of one of the nanotubes that was found after fracture reveals the height of the nanotube on the surface to be 1.4 nm. The AFM image was acquired in intermittent contact mode using the same tip from which the nanotube broke off.

the nanotubes to break at the nanotube/catalyst junction. Some of the broken nanotubes were able to be located on the surface while imaging with the AFM tip to which they were formerly attached, as shown in Figure 5.4C. This author was unable to locate any of the broken SWNTs on the surface, but SWNTs from the same batch were located by Mark Poggi (Georgia Institute of Technology, 2004).[28] Since the SWNTs are from the same batch, it is reasonable to assume that they have similar dimensions. Tube diameters were determined from measured heights.

The cross sectional area needed in Equation 3 was computed in the following way. An average diameter of 1.4 ± 0.1 nm was found from AFM images of broken nanotube tips. The manufacturer of the SWNT probes claimed that they were assumed to be single-walled; the measured diameter is consistent with this claim. Nanotube lengths were determined from SEM images and ranged from 2.0 to 5.7 μm. Using these values, the elastic modulus of the small-walled carbon nanotube is found to be 1.6 ± 1 TPa. This is in good agreement with previous literature values for the elastic modulus of SWNT.[181, 182] The uncertainty in our reported result is due to the precision of frequency measurements and the relative magnitudes of k_{SWNT} and k_{CANT}. In our system, k_{CANT} is an order of magnitude greater than k_{SWNT}; the uncertainty of the calculated modulus decreases exponentially as the ratio of the spring constants approaches unity.[172]

5.3 Friction Analysis of Carbon Nanotubes

The SWNT tips were also subjected to larger compression displacements. Thermal resonance data for a nanotube brought into and out of contact with amino-terminated alkanethiol modified gold surface is presented in Figure 5.5 as the extent of compression is increased. In each graph, the dashed line indicates the initial contact determined from the oscillation amplitude. The frequency response changes in magnitude and duration with increasing compression. Figure 5.5A is similar to the previous pattern of contact with immediate buckling during extension, followed by

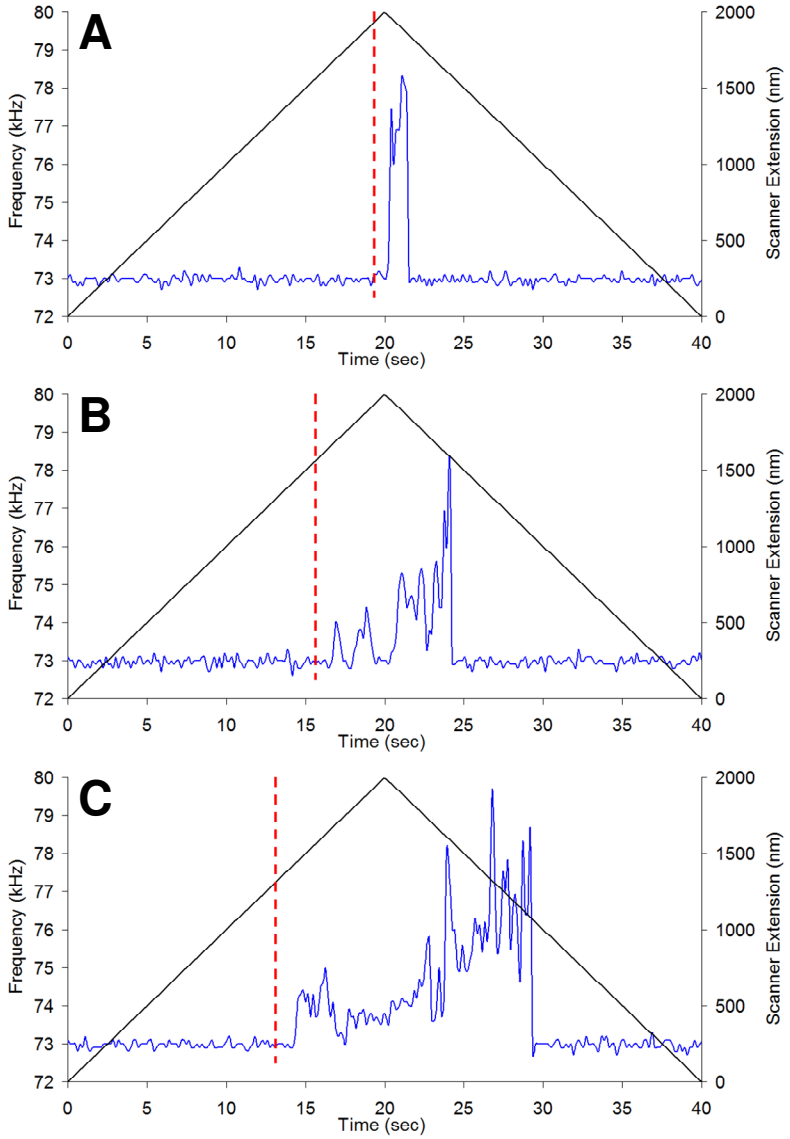

Figure 5.5. Waterfall data for a SWNT compressed for three different distances on an 11-amino-undecanethiol monolayer: (A) 50 nm, (B) 300 nm, and (C) 710 nm. The dashed line indicates the contact point calculated from the oscillation amplitude when the system was externally driven with the same scan settings. At each increasing compression step, the oscillation amplitude is acquired by externally driving the system and performing cycle. The external drive signal is then turned off, and the thermal resonance frequency data is acquired without changing any of the scan settings. This allows correlation to the point of contact with the MPFS waterfall data.

tension during retract. In Figure 5.5B, after initial contact and buckling, the frequency rises and falls with scanner extension. Sudden shifts to higher frequency indicate that the nanotube is pinned on the surface and provides resistance to cantilever oscillation. Sudden shifts to lower frequency indicate that the nanotube buckles and slips on the surface, removing this resistance. During scanner retraction, larger shifts in frequency are observed; upward shifts in frequency result from increased tension in the system. Downward shifts in frequency indicate sudden decreases in tension that result from slip or release events. In Figure 5.5B, the nanotube undergoes two distinct slip-stick-buckle events during approach. During retract, several stick-tension-slip events are observed. The retract portion of the force curve displays a saw tooth pattern that is indicative of slip-stick motion. As the compression on the nanotube is further increased, additional slip-stick-buckle and stick-tension-slip events are observed (Figure 5.5C). Note that the magnitude of frequency shifts in Figure 5.5C are greater than that found in Figures 5.5A and B. This increase in magnitude reflects increased tension on the nanotube that results from increased slippage. The effective length of the spring is inversely proportional to the amount of slippage.

The slip-stick phenomenon depends upon the chemistry at the SWNT-substrate interface. Figure 5.6 shows the thermal resonance frequency response for a single SWNT probe brought in and out of contact with three different chemically-modified gold substrates. Figure 5.6A depicts the interaction of the SWNT with a methyl-terminated alkanethiol. Minimal shifts in frequency are observed during compression and tension indicating that the nanotube slides freely along the surface. Figure 5.6B depicts the interaction of the SWNT with a hydroxyl-terminated alkanethiol. A measurable frequency shift is observed; increased affinity of the nanotube with the hydroxyl-terminated surface is indicated by the increased tension seen during scanner retraction. Figure 5.6C depicts the interaction of the SWNT with an amino-terminated alkanethiol. The frequency response for this surface has been discussed above for Figure 5.5. Taken

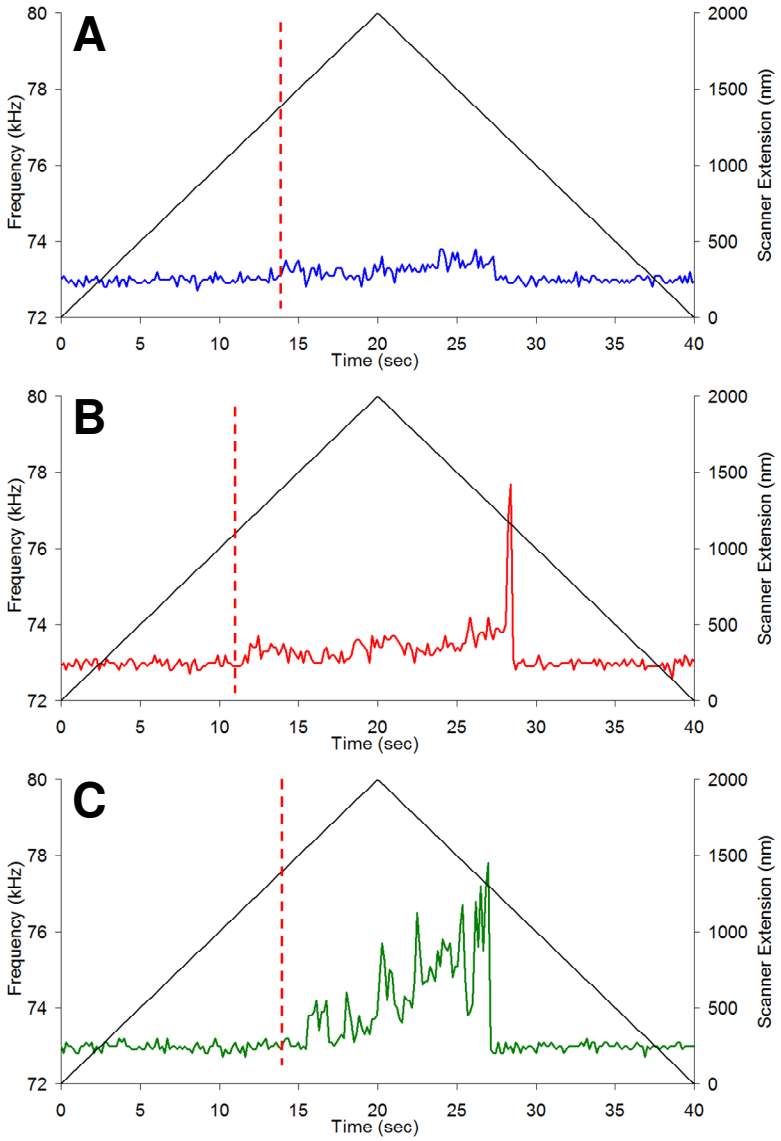

Figure 5.6. Waterfall data of a large compression for three different self-assembled monolayers on template stripped gold: (A) methyl alkyl thiol, (B) hydroxyl alkyl thiol, (C) amino alkyl thiol. The dashed line indicates the contact point estimated from the oscillation amplitude when the system was externally driven. At larger compression, the different chemical functionalities result in different responses. The larger frequency shift during scanner retraction follows that the force of adhesion is $CH_3 < OH < NH_2$.

collectively, the data presented in Figures 5.5 and 5.6 suggests that the number and extent of slip events is indicative of the strength of adhesion between the nanotube and the surface, i.e. $-CH_3 < -OH < -NH_2$. This trend is consistent with previously published adhesion measurements.[113, 114, 315] There is currently no consensus as to what gives rise to the strength of adhesion. Polarity, hydrophilicity and electronic interactions have been suggested.

The results in Figures 5.3 and 5.6 may, at first glance, appear to be in conflict. At minimal compression, the SWNT buckles but does not slip. In the absence of slip, the surface chemistry has no effect on the frequency response of the system. In the presence of slip, nanotube-substrate chemistry mediates the extent and duration of the observed frequency shifts. Differences in the chemistry of the interface can be distinguished after compression-induced buckling and slip. Thus, there is no conflict between the data presented in the two figures.

Interestingly, after the buckling event (the system is now defined as post-buckled), the force required to overcome the adhesion at the pinned end of the nanotube and enter the slip-stick domain is, by definition, the frictional force. A prediction can be made about the shape of the buckled nanotube as it undergoes further compression by applying an elastica model of a post-buckled column. The ordinary differential equations (ODE) from elastica theory for a post-buckled column are given by

$$\begin{aligned} \frac{dz}{ds} &= \cos\theta \\ \frac{dx}{ds} &= \sin\theta \\ \frac{d\theta}{ds} &= m \\ \frac{dm}{ds} &= p_H \cos\theta - p_V \sin\theta \end{aligned} \quad , \qquad \text{Equation 5.4}$$

where z and x are the coordinate system used for calculation, s is the arc length along the nanotube, θ is the angle the nanotube makes with respect to the surface, m is the bending

moment and p_H and p_V are the horizontal and vertical loads in the nanocoil. For simplicity of modeling, the terms in Equation 5.4 are dimensionless. Conversion to real values can be accomplished by

$$\begin{aligned} Z &= zl \\ X &= xl \\ M &= \frac{ml}{EI}, \\ P &= \frac{pl^2}{EI} \end{aligned} \qquad \text{Equation 5.5}$$

where l is the length of the nanotube and EI is the bending rigidity of the nanotube. Figure 5.7 shows the general solution of this boundary value problem immediately after the first buckling event, $L(z) = 0.99$, and is overlaid with the parameters contained within the ODE. The boundary conditions were set to model a clamped-pinned column,

$$\begin{Bmatrix} z_c = 0 \\ x_c = 0 \\ \theta_c = 0 \end{Bmatrix}, \begin{Bmatrix} z_p = L = 1 \\ x_p = 0 \\ M_p = 0 \end{Bmatrix}, \qquad \text{Equation 5.6}$$

where the first set of boundary conditions describe the clamped end of the column, i.e. at the AFM tip. The second set describes the pinned end of the column, i.e. adhered to the surface.

Through the solutions of the boundary value problem, the horizontal and vertical forces at the pinned endpoint can be calculated at different compression steps. The distance from the unbuckled length of the nanotube, l, is given by dimensionless $L(z)$. The horizontal force, P_H, is equivalent in magnitude to the force of static friction, F_f, and the vertical load, P_V, is equivalent to the magnitude of the normal force, F_N, exerted by the buckled nanotube. The coefficient of friction, μ, can be found using

$$F_f = \mu F_N . \qquad \text{Equation 5.7}$$

For each compression step, the minimum coefficient of friction required to keep the tube pinned can be calculated using Equation 5.7. As compression increases, the minimum

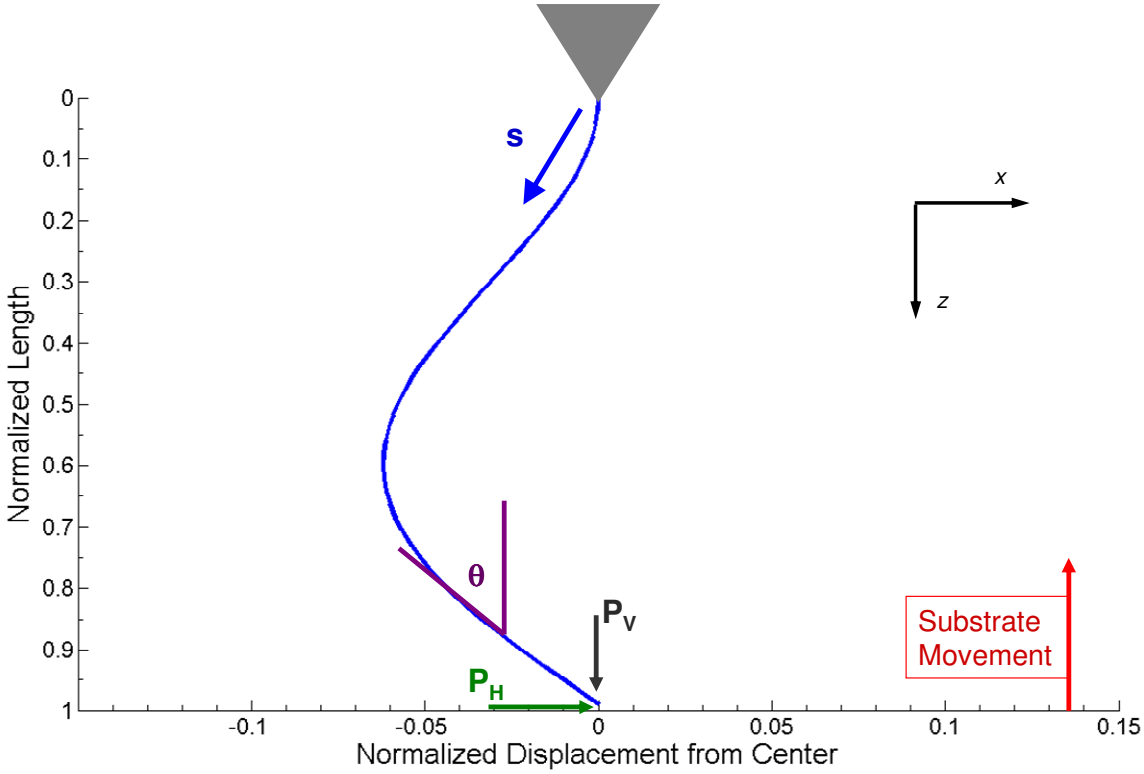

Figure 5.7. Theoretical parameters for the elastica model of a post-buckled column. The AFM tip is included for reference to the clamped end of the nanotube. The vertical and horizontal forces are indicated. The magnitude of these forces is used to calculate the minimum force of friction to keep the nanotube from slipping out of its pinned condition. The shape of the post-buckled column depicted is for the compression step $L(z) = 0.99$.

coefficient of static friction must increase if the nanotube is to remain pinned to the surface. This effect is depicted graphically in Figure 5.8. Applying this model to the displacement of the scanner necessary to transition from the post-buckled state and into the slip-stick domain allows for the calculation of the minimum coefficient of friction for three surfaces of self-assembled monolayers on template stripped gold: 0.02 ±0.02, 0.06 ±0.02, and 0.08 ±0.02 for 11-methyl-, 11-hydroxyl-, and 11-amino-undecanethiol, respectively. These results are within the ranges seen by others who worked on friction of Si_xN_y AFM tips and self-assembled monolayers[346] and different carbon materials.[67, 144, 347] For comparison, the coefficient of friction between hydrogenated amorphous carbon, a lubricant in hard disks, and silicon was measured to be 0.33.[347]

5.4 Conclusions

The advantages MPFS offers to studying mechanical and adhesive interactions at the nanoscale have been demonstrated. By monitoring the shift in the thermal resonance frequency, MPFS enables the calculation of the spring constant and elastic modulus of carbon nanotubes under ambient conditions. This approach described herein is not limited to SWNTs; it is directly applicable to a wide variety of nano-objects. Additionally, an elastica model of the post-buckled state of the nanotube has been developed. By monitoring the location of the frequency shift in thermal resonance, the static coefficient of friction has been calculated from experiments performed on three different chemically modified surfaces. The results presented herein are the first static friction results for carbon nanotubes on self-assembled monolayers.

In a broader context, this work cautions that high aspect ratio nanotube probes buckle under minimal compressive loads. Nanotube buckling leads to imaging artifacts.[253] Imaging in intermittent contact mode does not, necessarily, prevent this artifact. As demonstrated in Figure 5.2A, a buckled nanotube does not necessarily reduce cantilever oscillation. Proper imaging protocol requires acquisition of an oscillation

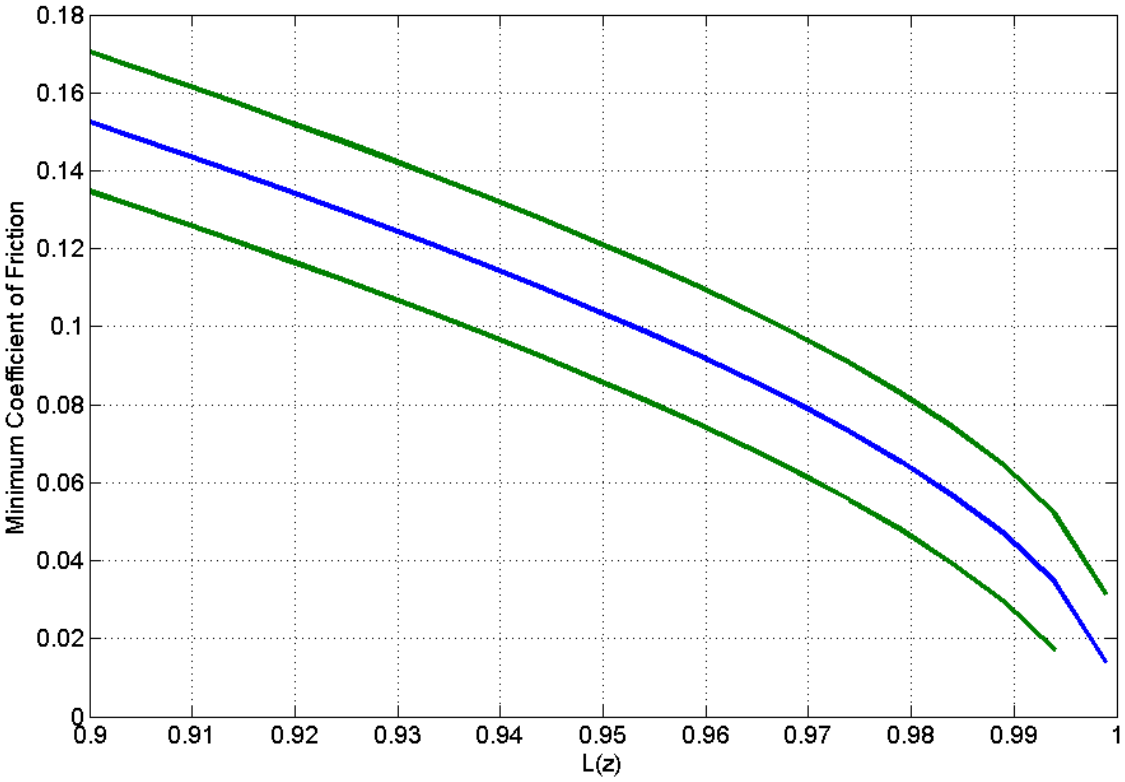

Figure 5.8. Plot of minimum coefficient of friction as a function of nanotube compression. The plot is extracted from the elastica model at each compression step, L(z). The blue line models a nanotube contacting the surface at 90°. The green lines account for an error of ±1°.

amplitude plot and setting the set point value to the first reduction of the oscillation amplitude. The spring constant of the cantilever must also be carefully chosen. Equation 1 predicts the force at which a SWNT buckles. The following equation is suggested for choosing a cantilever with spring constant k_{CANT} so that it will not cause a nanotube with an aspect ratio, A_R, and outer diameter, d, to buckle after contact and 10 nm of axial compression:

$$k_{CANT} < \frac{Ed^2}{A_R^2}\left(9.3\times10^7\ m^{-1}\right). \qquad \text{Equation 5.8}$$

This equation treats the nanotube as a column whose inner diameter is half of its outer diameter because that approximates the relationship for SWNTs. The constant at the end of the equation is for conversion product of all other constants and conversion factors to SI units. During intermittent contact mode imaging, it is possible that the nanotube can experience compressive loads up to 10 nm. Without careful consideration of the spring constant of the AFM cantilever relative to the critical buckling load, high aspect ratio carbon nanotube AFM probes will buckle during imaging, even in intermittent contact mode.

CHAPTER 6

MPFS OF CARBON NANOCOIL AT LARGE CONTACT ANGLES

Coiled carbon nanotubes are a unique vehicle to study adhesion and mechanical properties using multi-parameter force spectroscopy. They behave like springs, and their coils provide distinct regions where contact can occur. Previous work has focused on their compression mechanics and correlation of physical properties to their structure.[306] In this investigation, a coiled carbon nanotube, henceforth nanocoil, was studied to interrogate its mechanical and adhesive properties.

A nanocoil was attached to an AFM cantilever using previously described techniques.[250] Three substrates were used in this study: silicon chips diced from a polished <100> silicon wafer, silicon chips with trenches etched into them, and highly oriented pyrolytic graphite (HOPG). A complete description of the materials used herein can be found in Chapter 4.

6.1 Results of Compression and Tension

An SEM image of the nanocoil used in this investigation is shown in Figure 6.1. The grey boundary, added to the image after it was acquired, provides a visualization of the contact angle the nanocoil makes with the surfaces used herein. Each surface was tilted to alter the angle the nanocoil makes contact. By changing the angle, the distance between contact and release of each coil was altered. Additionally, changing the angle has been shown to affect the mechanical behavior of the nanocoil as it is compressed.[306]

6.1.1 Contact Angle of Fifty-nine Degrees

The force spectroscopic responses for the nanocoil on both silicon and HOPG are shown in Figure 6.2. The contact angle for each substrate was 59° (±1°) as measured from the normal to the surface. The nanocoil was brought into contact with each

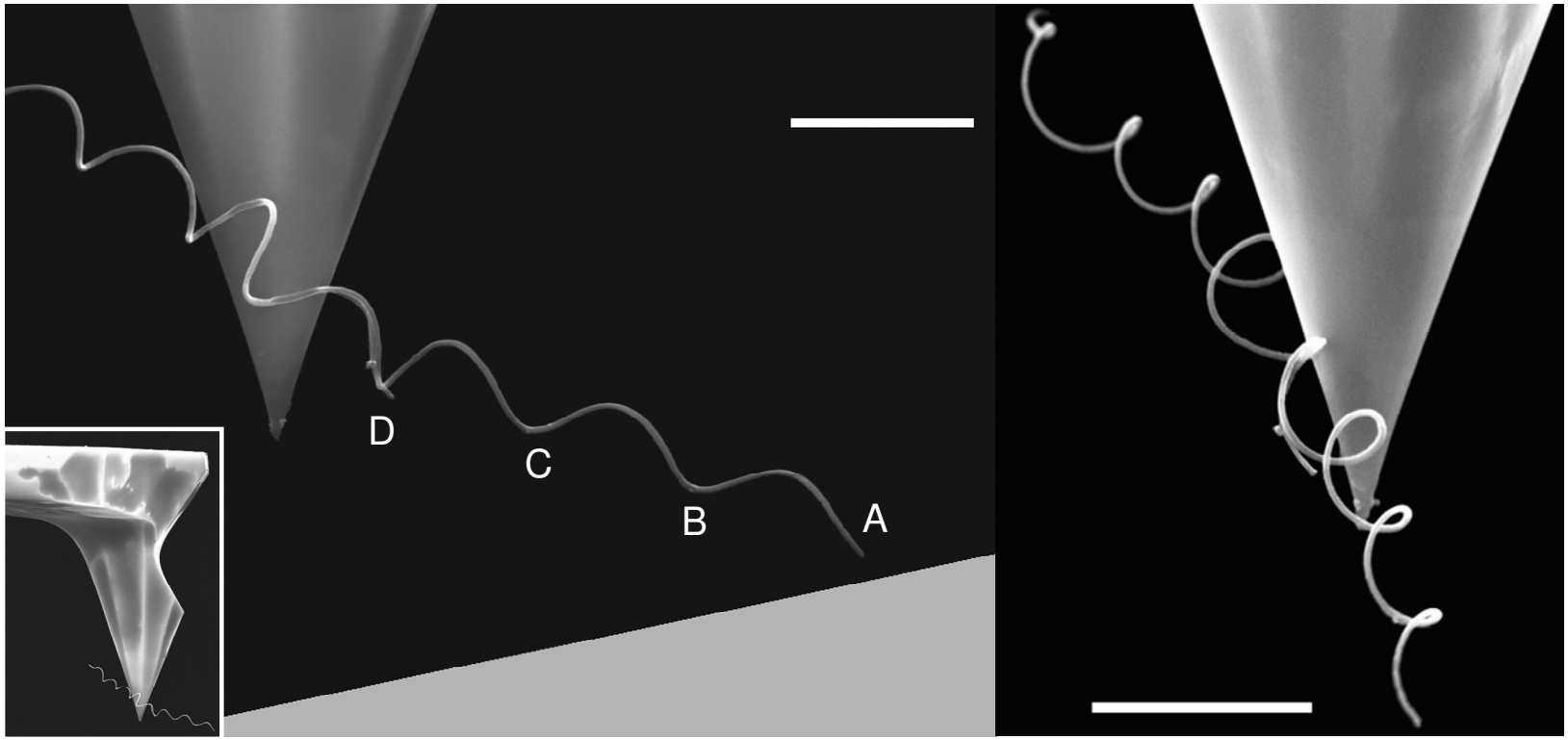

Figure 6.1. SEM images of a carbon nanocoil attached to an AFM probe. The left image is from the taken from the side, and the coils are labeled for discussion throughout this chapter. The gray boundary at the bottom was added to the image to illustrate the contact angle with respect to the surface. This angle includes the angle of inclination inherent to the cantilever holder used in the investigation. The nanocoil extends towards the front of the AFM cantilever (see inset). The right image is taken looking at the front of the cantilever and shows the helicity of the nanocoil. The scale bar in both images represents 2.0 μm.

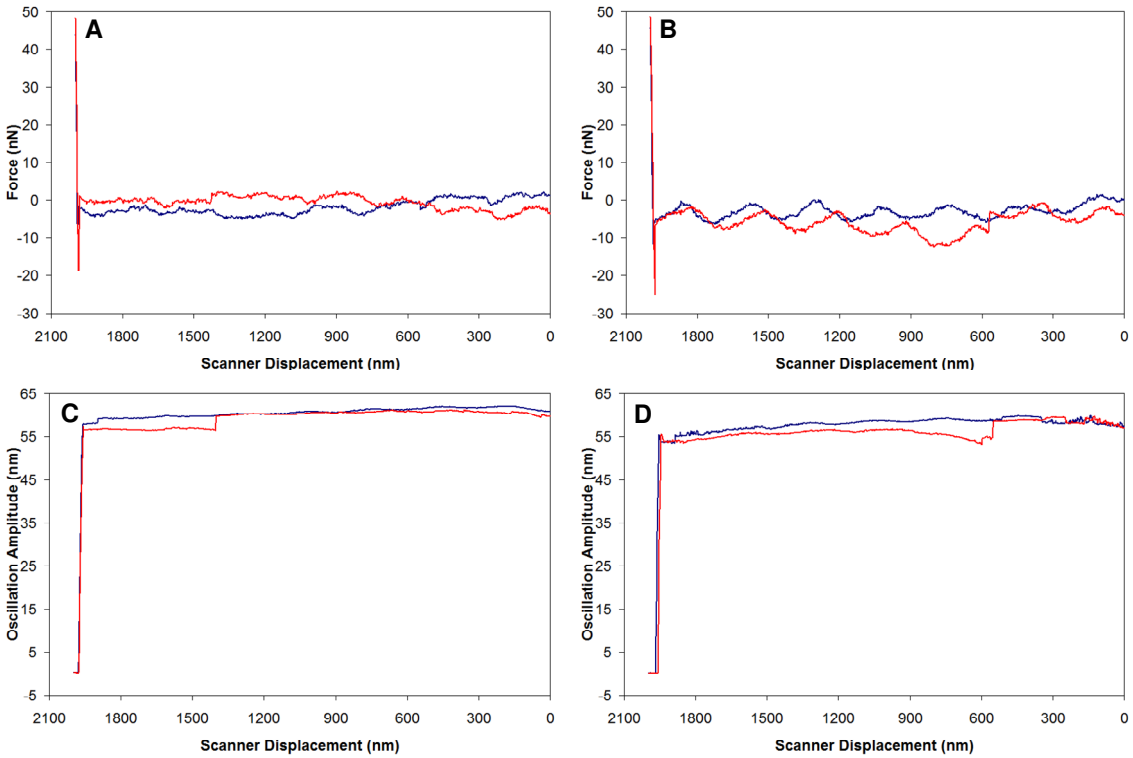

Figure 6.2. Force spectroscopy response of a nanocoil on silicon and HOPG. Force curves (A and B) and oscillation amplitude (C and D) of the same nanocoil at a contact angle of 59°, where blue is the trace for the approach and red is for the retract (this color scheme will be used throughout this chapter). A and C are data from contact with a silicon surface, whereas B and D are on HOPG. The sharp, linear increase in force to the left of each graph is the AFM tip touching the surface. This is accompanied by the oscillation amplitude falling zero. Approximately 50 nm before the AFM tip makes contact there is a small drop in oscillation amplitude. On retract from the silicon surface the oscillation amplitude of the nanocoil-cantilever system remains diminished for 550 nm after the tip is released from the surface, which is accompanied by 2.6 nN of adhesion in the force curve. On retract from the HOPG surface, amplitude of the system remains diminished for 1390 nm after the tip is released from the surface, which is accompanied by 5.0 nN of adhesion in the force curve.

substrate in small steps of the z-scanner and stepper motor while monitoring the deflection and oscillation amplitude. During the approach, no change in either the force curve or the oscillation amplitude was discernable until the contact point displayed in Figure 6.2. A sharp, linear increase in force to the left of each graph is accompanied by oscillation amplitude falling to zero. Approximately 50 nm before the AFM tip makes contact there is a small drop in oscillation amplitude. The thermal resonance frequency showed no shift from its free space value until contact was established. Upon contact, the amplitude of the thermal resonance frequency fell below the noise floor (data not shown). This is characteristic of the primary mode of vibration changing frequency and amplitude when placed in contact with a hard surface.[340] Based on the evidence from the force curve, the oscillation amplitude and the frequency response, the contact event is the AFM tip hitting the surface. This would suggest that at this large of a contact angle, the nanocoil readily gives way to the force from the undeflected cantilever.

During retract, the oscillation amplitude does not immediately return to its free-space amplitude. On retract from the silicon surface the oscillation amplitude of the nanocoil-cantilever system remains diminished for 550 nm after the tip is released from the surface, which is accompanied by 2.6 nN of adhesion in the force curve. On retract from the HOPG surface, the oscillation amplitude of the system remains diminished for 1390 nm after the tip is released from the surface, which is accompanied by 5.0 nN of adhesion in the force curve. The force of adhesion is measured from the minimum of the downward deflection to the next data point. This method to measure force was chosen because the interference pattern prevented an accurate measurement of the nominal deflection value. The reduced oscillation amplitude can only be caused by a portion of the nanocoil remaining in contact with the surface. This is interesting considering there was no evidence of nanocoil contact during scanner extension in any of the frequency data sets for a contact angle of 59°.

6.1.2 Contact Angle of Forty-nine Degrees

Each substrate was tilted 10° by attaching it to an angled shim to interrogate more of the nanocoil-substrate interactions. This resulted in a contact angle of 49° (±1°). In this configuration, the contact of the end of the nanocoil with the substrate can be discerned in the oscillation amplitude, as shown in Figure 6.3. The drop in oscillation amplitude from contact is small and short, suggesting that the nanocoil slips or buckles. During approach, there is no measureable deflection on the cantilever, as evidenced in the inset of Figure 6.3. Upon retract, an adhesion event does occur between the end of the nanocoil and the substrate. The adhesion force was 3.4 nN on silicon and 6.6 nN on HOPG. Even though contact is made during approach, the oscillation amplitude returns to its free space value and there is no measured upward deflection of the cantilever.

Further compression steps using the z-scanner resulted in no new events until the upper limit of the scanner was reached (an additional 1.5 µm from the contact point seen in Figure 6.3). Then the stepper motor was used to bring the raise the substrate. The substrate was raised approximately 2 µm before the next event was recorded. After traveling approximately 3.5 µm from the contact event in Figure 6.3 using both the z scanner and the stepper motor, distinct compression and adhesion events were measured in the force, amplitude and frequency responses; these are depicted in Figure 6.4. The bottom trace is the first measured events while using the stepper motor to raise the substrate. The z scanner was extended 115 nm to generate the middle trace each plot. The scanner was again extended 40 nm more (155 nm from bottom trace) to generate the top trace in each plot. Several of the events are highly reproducible, suggesting that the events result from the geometry of the nanocoil.

The scan cycle with the largest compression (top trace) from Figure 6.4 was repeated at a slower scan rate of 50 nm/s to improve the temporal resolution in the frequency plot, seen in Figure 6.5. The force curve and thermal oscillation amplitude are displayed as a function of time for correlation with the frequency response. The scanner

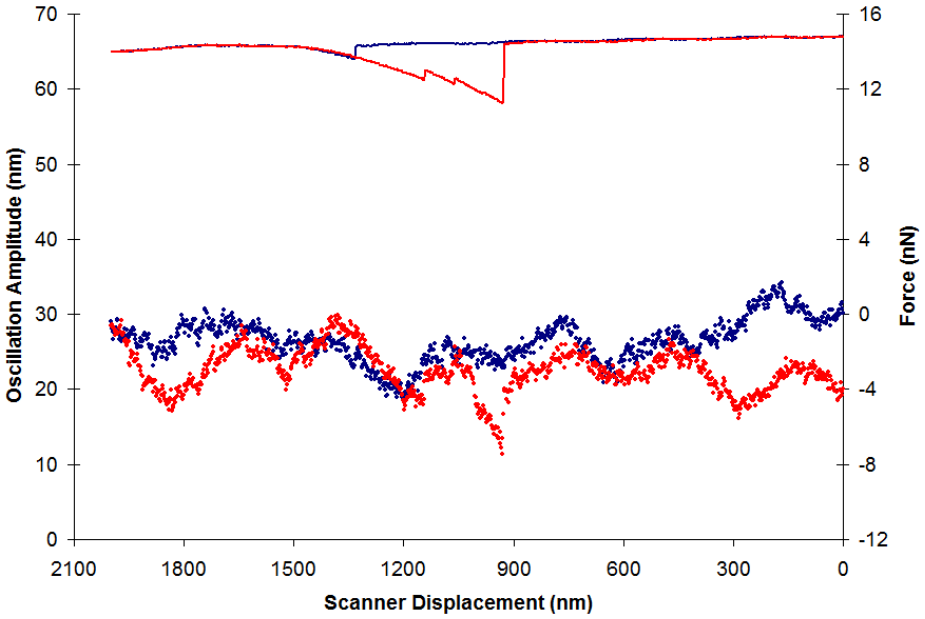

Figure 6.3. Force spectroscopy response of a nanocoil on a silicon surface that was tilted ten degrees. A drop in the oscillation amplitude, red and blue lines, occurs well before the AFM tip makes contact. The force curve, red and blue dots, shows that the cantilever does not deflect during scanner extension and has a small downward deflection that occurs during scanner retraction. A similar response was recorded on HOPG (data not shown). The adhesion force on silicon and HOPG were 3.4 nN and 6.6 nN, respectively. Even though contact is made during approach, the oscillation amplitude returns to its free space value and there is no measured upward deflection of the cantilever.

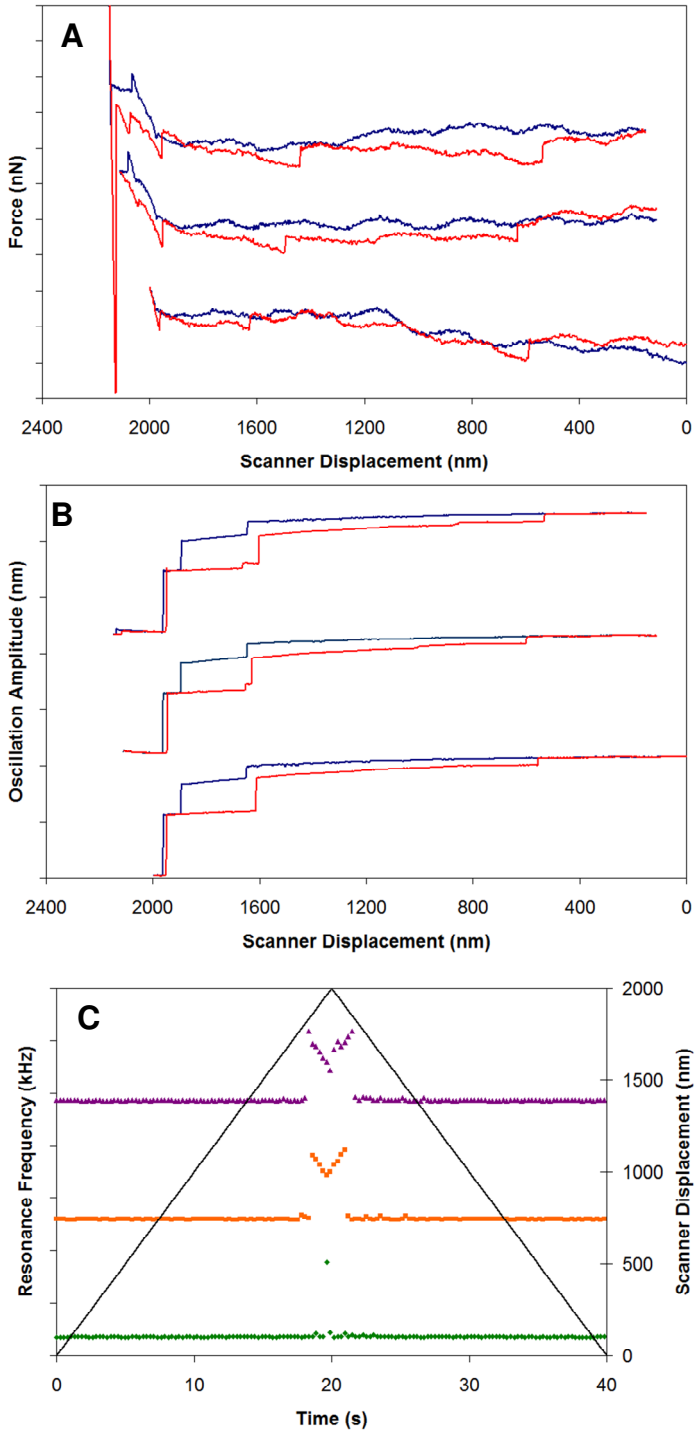

Figure 6.4. MPFS results for the nanocoil on a tilted HOPG surface at three different compression steps. In the force curve (A), oscillation amplitude (B), and resonance frequency (C), the middle plot is 115 nm more compression than the bottom plot, and the top is an additional 40 nm more compression than the middle plot. Many of the features are reproducible for each compression step.

changes direction at the 40 s mark, depicted as a color change in the force curve and thermal oscillation amplitude plots. The thermal oscillation amplitude is obtained from the waterfall data at the resonance frequency of the undriven cantilever, 81.4 kHz. This is exactly how the oscillation amplitude in Figure 6.4B is obtained, except the cantilever is externally excited at its resonance frequency. The thermal oscillation amplitude has a poor signal to noise ratio because the noise floor is not a fixed value. The signal to noise ratio could be improved by increasing the number of averages for each data point, but the tradeoff would be temporal resolution. Even with the poor signal to noise ratio, the same events that are recorded in the externally driven oscillation amplitude, Figure 6.4B, are observed in the thermal oscillation amplitude, Figure 6.5B.

The compression and adhesion events can be interpreted by comparing the force, thermal oscillation amplitude, and the frequency of the cantilever-nanocoil system. The events of interest are numbered in Figure 6.5. At point 1, the resonance frequency becomes noisy, the cantilever begins to deflect slightly, and the thermal oscillation amplitude decreases. This would suggest that one of the upper coils (B or C in Figure 6.1) makes contact but either slips or buckles. Starting at point 2, the thermal resonance frequency increases by 5.5 kHz, the deflection of the cantilever increases non-linearly, and the oscillation amplitude falls. It is incorrect to call the drop in oscillation amplitude at point 2 damping because the resonance frequency of the system changes. The thermal resonance frequency decreases during compression from point 2 to 3 then starts to level off. This leads to the conclusion that the nanocoil is buckling; a similar conclusion has been drawn from previous work on nanocoils.[306] At point 3, the cantilever deflection drops suddenly and levels off. Additionally, the resonance frequency shows a marked drop back towards the free-space frequency, but there is no change in the thermal oscillation amplitude. This would strongly suggest that the force at the end of the buckled nanocoil overcame the surface adhesion, causing the nanocoil to slip from the surface and undergo slip stick motion, as discussed in Chapter 5. At point 4, a sharp

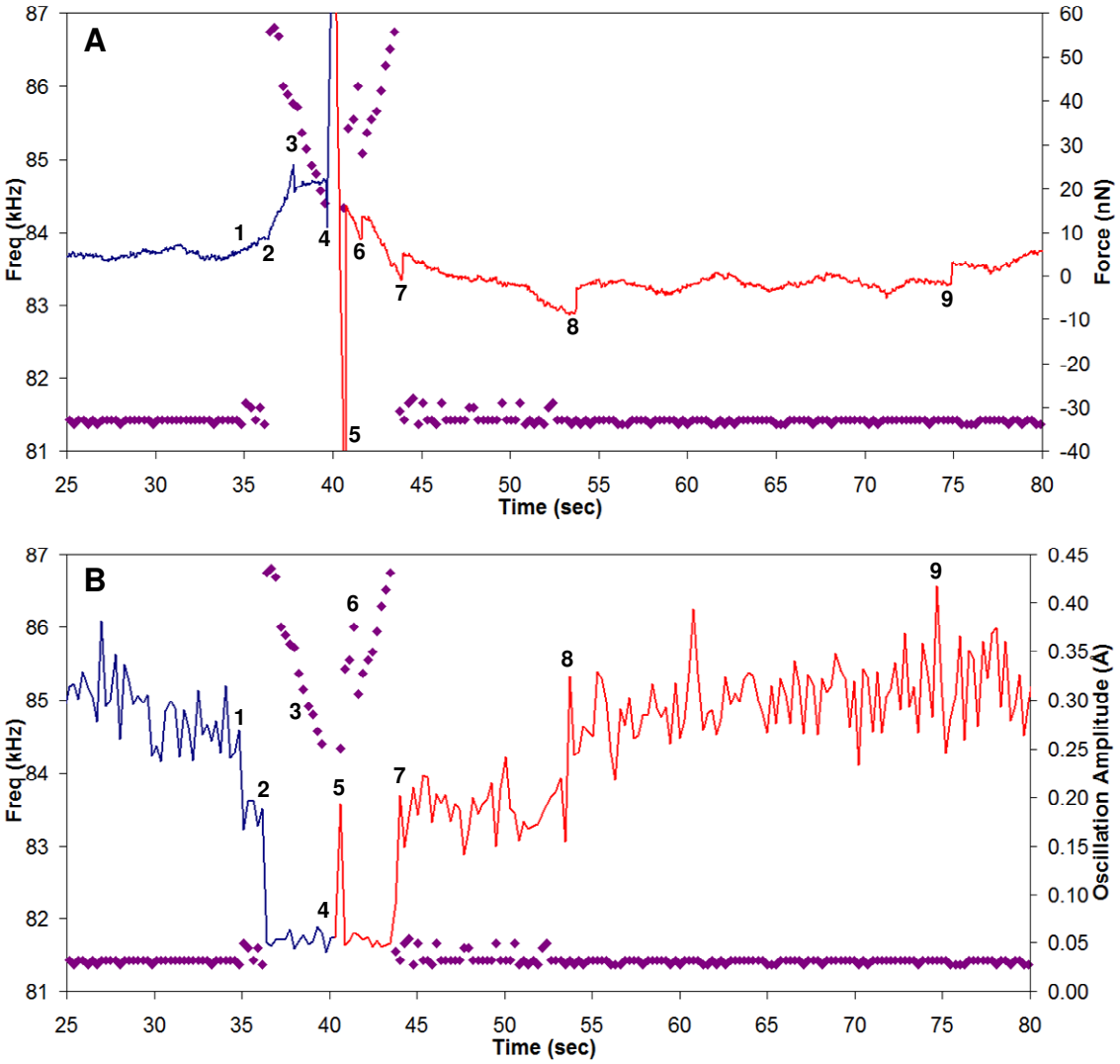

Figure 6.5. MPFS results of the nanocoil on HOPG at a reduced scan rate of 50 nm/s. A complete scan cycle is performed in 80 seconds at this scan rate. Only a partial cycle of the scan range is shown so that the features are easily distinguished. The frequency response (purple) is overlaid with the force curve, A, and the thermal oscillation amplitude, B. The thermal oscillation amplitude is the amplitude of the waterfall data at the resonance frequency, 81.4 kHz.

increase in deflection occurs, which is usually attributed to the AFM tip making contact. The frequency response, however, does not fall below the noise floor as it did on the previous untilted surfaces. Instead, the frequency jumps to 384 kHz and undergoes a symmetric U-shape that is indicative of buckling, shown in Figure 6.6. This suggests that the nanocoil is between the AFM tip and the surface, allowing the end of the cantilever to vibrate.[348] The slope of the force curve in Figure 6.5 is reduced from that on untilted substrates, Figure 6.2. This change in slope has been used by other authors for calibration of cantilever spring constants[172, 173, 175] or for investigating the mechanical properties of fibers.[325, 334-336]

Upon retract, there is a large adhesion force from the compressed spring as it is removed from the surface, point 5. The thermal oscillation amplitude increases momentarily from the energy of the release event. A second adhesion event occurs at point 6. This adhesion is most likely from the point to which the nanocoil slid during the slip-stick motion between points 3 and 4. It should be noted that there is no change in the oscillation amplitude at point 6. The increase in resonance frequency suggests that the nanocoil is put into tension. The conclusion that point 3 is slip-stick motion is corroborated in that the location and magnitude of the adhesion at point 6 varies with correlation to the distance the nanocoil slid. Comparing the location of this adhesion event for the top and middle trace of Figure 6.4A illustrates this idea. Point 7 aligns with the original buckling of the nanocoil at point 3. This adhesion event is highly reproducible regardless of compression, and results in a partial relaxation of the oscillation amplitude and resonance frequency. It is therefore most likely attributed to the nanocoil geometry. From point 7 to 8, there is a slight decrease in the deflection of the cantilever. This would suggest that the nanocoil is pulling on the cantilever until its rupture from the surface at point 8. The frequency response from point 7 to 8 mimics the response from points 1 to 2. At the rupture of point 8, the oscillation amplitude steps towards its nominal value and the cantilever deflection and resonance frequency return to

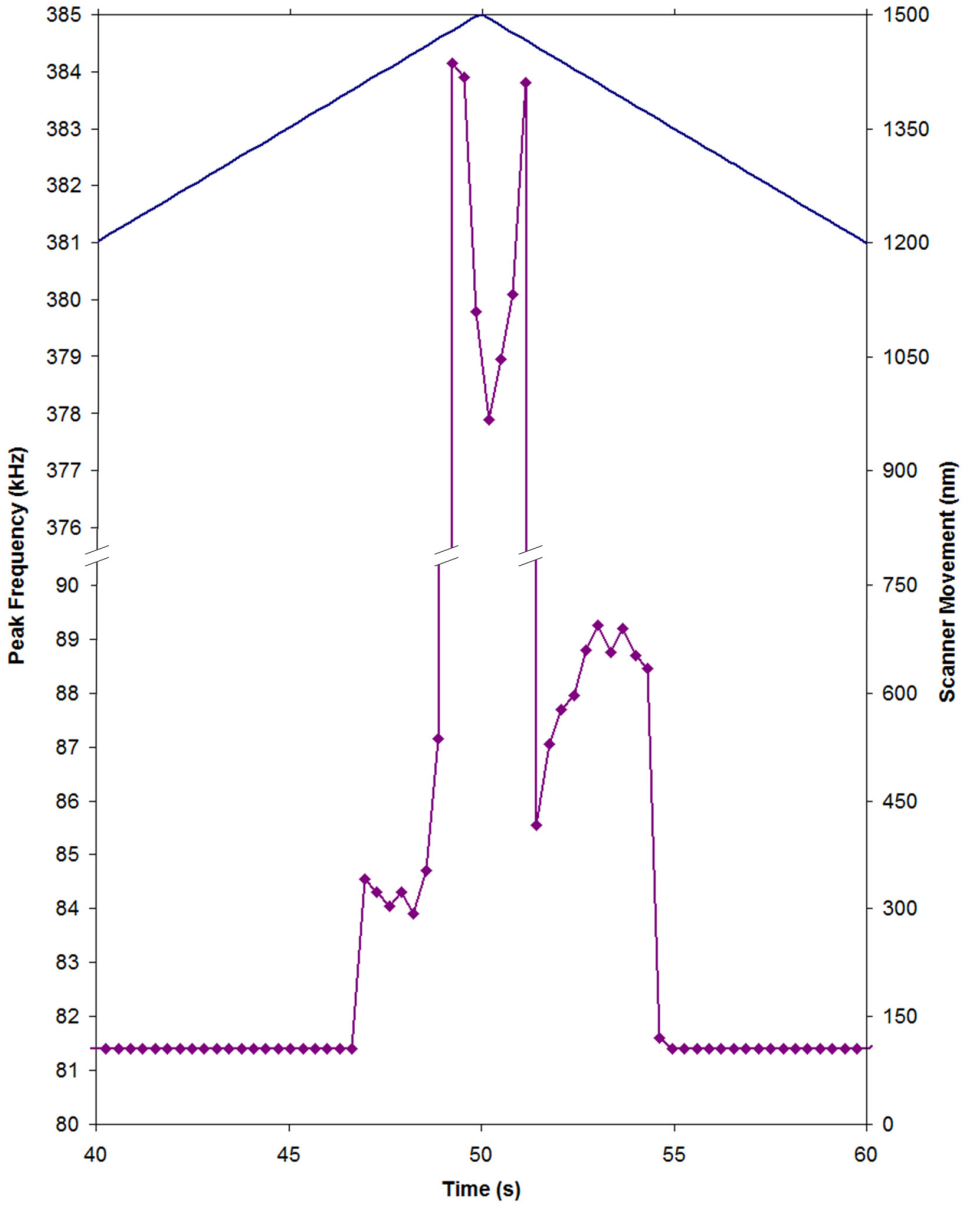

Figure 6.6. Thermal resonance frequency response of the nanocoil-cantilever system at a contact angle of 49° on HOPG. The thermal resonance frequency (purple, left axis) shifts upwards twice on scanner extension (blue, right axis). The first shift occurs during the non-linear compression of the nanocoil, as seen at point 2 in Figure 6.5, and the second shift to 384 kHz occurs at point 4 in Figure 6.5. Only a portion of the data is displayed so features in the thermal resonance frequency response can be distinguished. The scan rate was 30 nm/s over a scan range of 1500 nm.

their free space values. This suggests that the rupture event at point 8 is related to the nanocoil geometry. At point 9, there is another rupture event. For both release events at points 8 and 9, there is no shift in the thermal resonance frequency, which suggests that the nanocoil-cantilever system is free to vibrate up and down at its thermal resonance frequency because the nanocoil buckles or bends easily. This is supported by the thermal oscillation amplitude. The reader is reminded that the end of the nanocoil is still in contact even after further retraction of the scanner from point 9. The final release of the nanocoil cannot be captured in the same window because of the scan range limitations of the z scanner.

6.1.3 Contact Angle of Four Degrees

The nanocoil was brought into contact with the sidewalls of trenches etched into silicon. The x-y controls of the piezo scanner were used to control placement of the nanocoil within the trench. The results are shown in Figure 6.7. When the nanocoil was positioned against the sidewall of the trench but without the AFM making contact, A, there is no response in the force curve. The oscillation amplitude decreases linearly with scanner extension leading up to contact with the surface. Once contact is made, B, the oscillation amplitude drops to zero. The AFM probe was translated to the other sidewall of the trench so that the nanocoil was facing into the trench but not able to make contact with a sidewall, C. In this case, there is no decrease in the oscillation amplitude until the AFM tip makes contact. The force curves, green and orange for approach and retract respectively, are unremarkable and do not contain any compression or adhesion events besides tip contact. For both B and C, the contact event was verified to be the AFM tip from the frequency response, which showed the resonance frequency falling below the noise floor.

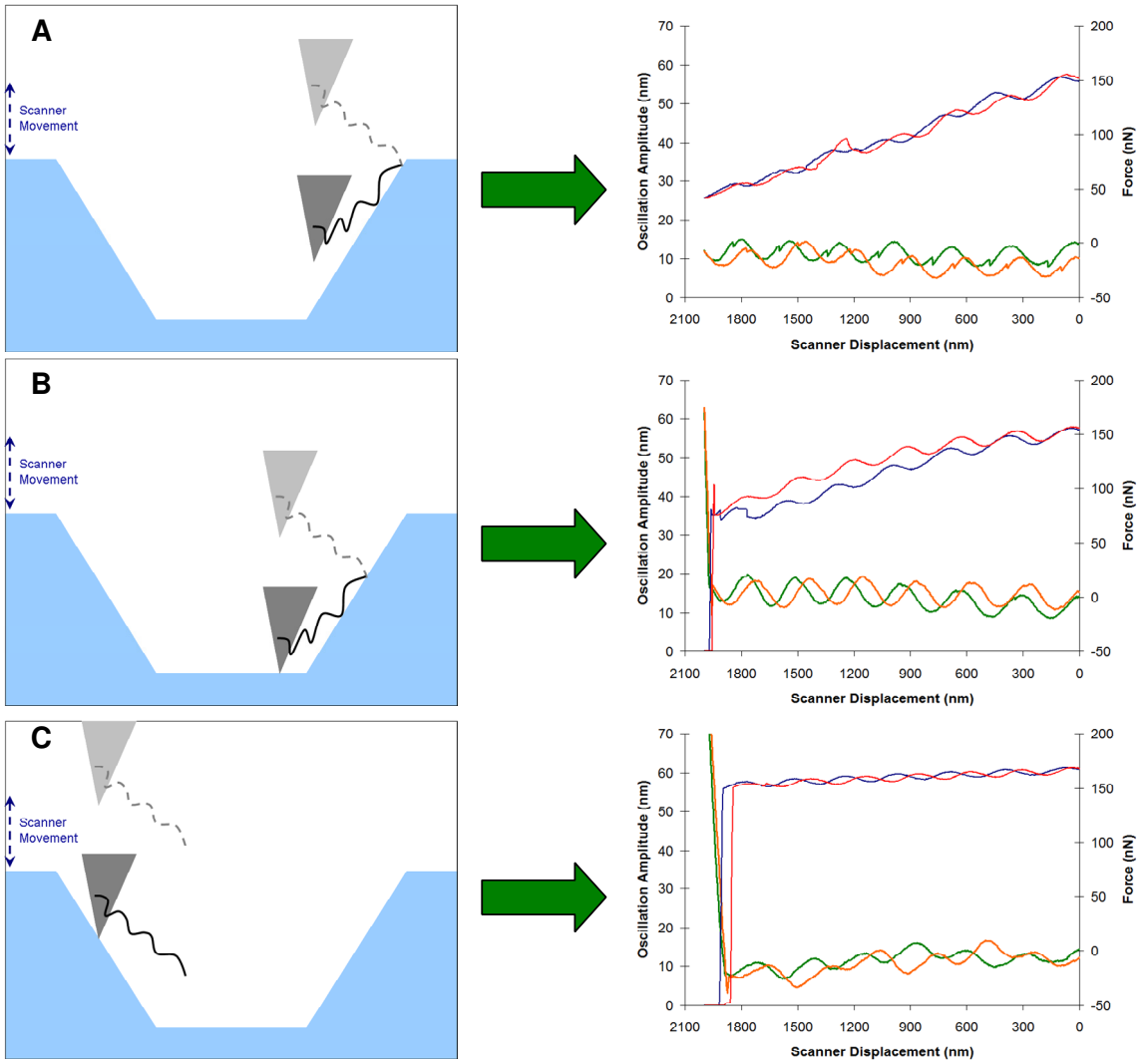

Figure 6.7. Illustrations of scanner cycles between nanocoil-cantilever system and a silicon trench with the corresponding results. The x-y piezo controls were used to position the nanocoil inside the trench. The substrate was positioned so: A) only the nanocoil made contact; B) the nanocoil and the AFM tip made contact; C) only the AFM tip made contact. The oscillation amplitude for each scan is in blue and red for the approach and retract respectively. Force curves were acquired simultaneously; green is approach and orange is retract. The sinusoidal shape in each of the curves is from laser light spilling over the cantilever and reflecting off the sidewall of the trench, resulting in an interference pattern. The shape of the interference pattern changes with the location of the AFM probe over the trench.

6.2 Discussion of Nanocoil Response

6.2.1 Determining a Model for Interpretation

There are two different interpretative models to apply to the results: quasi-static and dynamic. The quasi-static model primarily relies on the contact geometries of the nanocoil for interpretation. This model recognizes that there is some motion of the cantilever and nanocoil but assumes that this oscillation is sufficiently small enough that the nanocoil and cantilever do not significantly deviate from their static geometries. In this model, the nanocoil is assumed to impose a force to restore itself to its static geometry, depicted in Figure 6.1.

The dynamic approach considers that the cantilever and the nanocoil are oscillating. The source of this oscillation can be either from thermal energy or from external energy provided by driving a piezo at the cantilever's resonance frequency. Since the cantilever oscillation is much faster than the scanner movement, and the nanocoil is presumed to vibrate at a high frequency as well, then the nanocoil would mostly likely contact the surface at the bottom of its down swing, as depicted in Figure 6.8. This model allows the nanocoil to contact the surface before the static geometry permits. From contact, there are two possibilities: the nanocoil buckles or it slips along the surface.

If the nanocoil buckled after initial contact, then the thermal resonance frequency should have shifted, the force curve should have undergone non-linear compression, and there should have been a decrease in oscillation amplitude. This is the response seen for nanocoil at smaller contact angles.[306] This response is only seen a couple of hundred nanometers before the tip makes contact, as seen at point 2 in Figure 6.5. At the contact angles used in this investigation, the data strongly suggests that the nanocoil does not buckle upon initial contact. The second possibility from the dynamic model, the end of

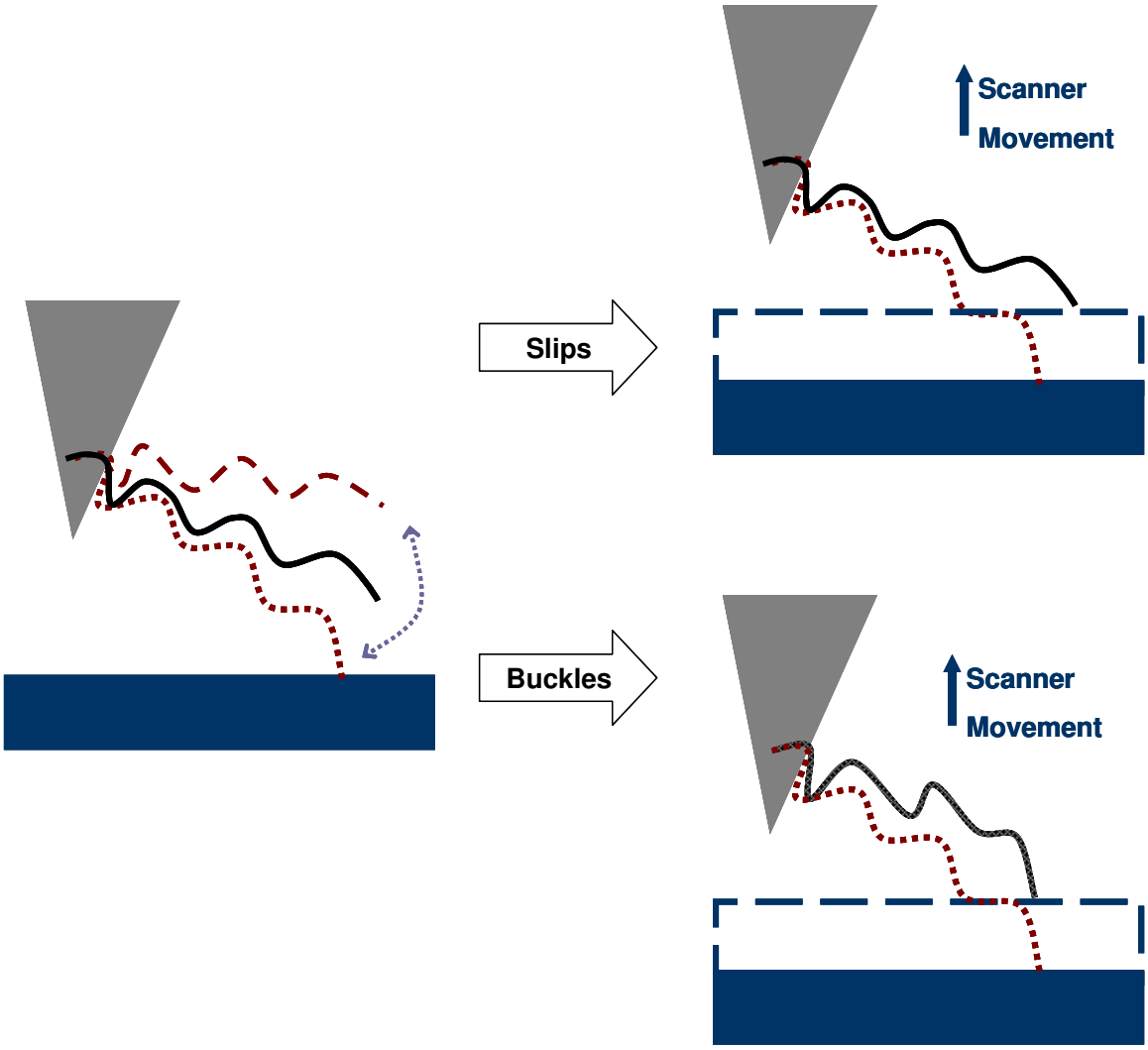

Figure 6.8. Illustration of the two conformations an oscillating nanocoil can make with a surface. Vibration of the nanocoil causes it to contact the surface before its static position (red dotted line). The nanocoil can either buckle or slip along the surface during scanner extension, blue dashed line. If the nanocoil sticks on the down swing and then buckles, hatched black line, it exerts a force on the AFM tip that would cause damping and/or deflection. If the nanocoil slips from its initial contact point, then no response would be measured by MPFS, and the nanocoil returns to its static configuration, solid black line.

the nanocoil slipping on the surface, suggests that the nanocoil returns to its static geometry, and can then be interpreted using the quasi-static model.

The strong similarity between driven and undriven data sets suggests that the amplitude of vibration does not affect the results. Several drive amplitudes were applied to the piezo holding the cantilever to test this hypothesis, seen in Figure 6.9. The amount of energy put into the system by driving the cantilever does affect the ability to resolve events in the oscillation amplitude, Figure 6.9A. During scanner retraction, at the large drive amplitude there are several small steps that occur between 1900 and 1250 nm. As the drive amplitude is reduced, these features become difficult to resolve. Considering the difficulty in resolving the features, changes in the drive amplitude have no effect on the location of any event in either the force curve or the oscillation amplitude. This makes a strong case for the quasi-static model. The same scanner cycle in Figure 6.9A was repeated with the drive amplitude off. The thermal oscillation amplitude plot is shown in Figure 6.9B. The same region between 1900 and 1250 nm exists, as it did in when the cantilever was driven. Based on this evidence, the decreases in oscillation amplitude seen in Figure 6.9A are *not* caused by damping, but from an increase in stiffness of the system. It is fair to conclude that the oscillation amplitude has no effect on the location of the compression and adhesion events, and the dynamic model does not describe the system. Further discussion uses the quasi-static model for interpretation.

6.2.2 Contact Angle of Fifty-nine Degrees

The compression results from contact angle of 59° are inconclusive. There is a 3% decrease in the oscillation amplitude 50 nm before the tip makes contact with either surface, but the distance does not correlate to structure. The distance between AFM tip contact and each labeled coil in Figure 1 are A) 2.30 µm; B) 1.46 µm; C) 540 nm; D) never. These distances are calculated from the contact angle and the geometry of the nanocoil measured from SEM images. During compression, the static geometry dictates

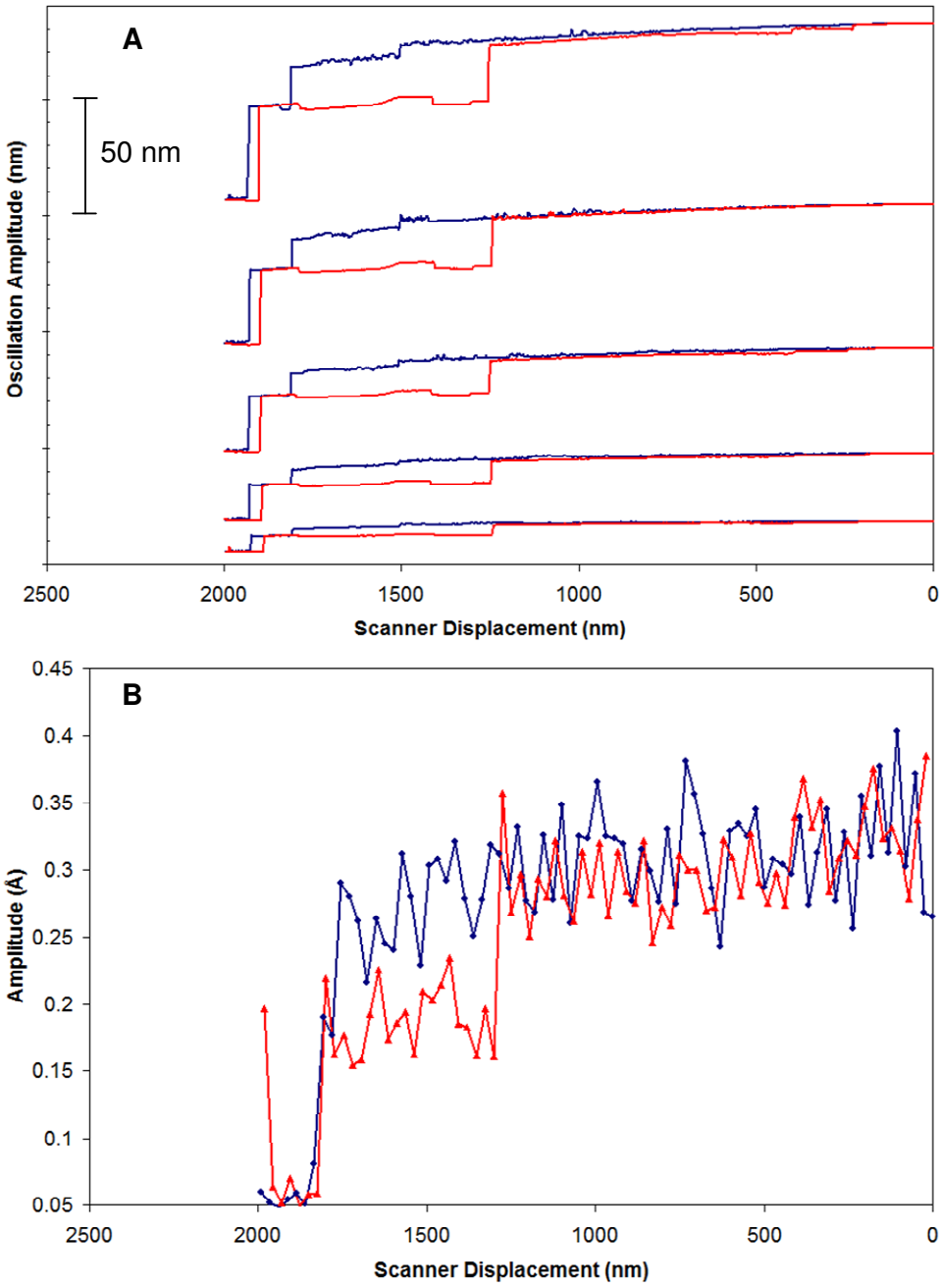

Figure 6.9. Effect of input energy on oscillation amplitude of the nanocoil-cantilever system at a contact angle of 49° on HOPG. The driven oscillation amplitude plots, A, show similar events regardless of drive amplitude. The plots are artificially offset on the y-axis for comparison purposes. An oscillation amplitude plot generated from the waterfall data, B, shows the same shape and location of events. The thermal oscillation amplitude plot suffers from a poor signal to noise ratio, but some features are discernable.

that the end of the nanocoil will make contact before any of the features. The difficulty with applying this model to scanner extension is that after the end of the nanocoil contacts the surface, the nanocoil is then forced to bend upwards, changing the geometry. The results suggest that at a contact angle of 59°, coils A-C either slip along the surface or the nanocoil bends with the surface.

The quasi-static model is more applicable to scanner retraction because the nanocoil will impose a force to restore itself to its static geometry. During scanner retraction at a contact angle of 59°, an adhesion event takes place 550 nm after the tip releases from the silicon surface and 1390 nm after the tip releases from the HOPG surface, as seen in Figure 6.2. The release point from the silicon surface agrees well with the distance required for coil C to return to its static position. The distance between tip release and the second adhesion event on HOPG suggests that coil C is adhered to the surface much past its static geometry. The adhesion force on HOPG, 5.0 nN, is almost twice that of on silicon, 2.6 nN. The larger adhesion force allows the nanocoil to bend and extend until the restoring force of both the cantilever and the nanocoil cause coil C to release from the surface. No release event is recorded for coil B on either surface. The oscillation amplitude does display small reduction at the turn around point of the scanner (Figures 6.2C and 6.2D). On the HOPG surface, this small decrease in oscillation amplitude is accompanied with an increase in noise. Based on geometry, coil B would begin to be put into tension at 1.46 μm after the tip releases, which is shortly before the oscillation is slightly reduced. The small, noisy reduction in oscillation amplitude is caused by the adhesive interaction between coil B and the substrate. There was no evidence of coil A releasing from the surface as the limit of the scan range prevented the scanner retracting far enough to see this event.

6.2.3 Contact Angle of Forty-nine Degrees

The contact geometry for a contact angle of 49° indicates that the coils should contact the surface at the following distances: A) 3.50 µm; B) 2.45 µm; C) 1.15 µm; D) 150 nm. The distance between the contact event shown in Figure 6.3 and the sharp compression at point 4 in Figure 6.5 is approximately 3.5 µm, which agrees well with the geometry of coil A. The compression event at point 2 in Figure 6.5 corresponds to the coil D contacting the surface. This event occurs 165 nm before the sharp increase at point 4, which is close to the value predicted by the static geometry of the nanocoil. . The discrepancy exists because the cantilever was deflecting upwards from points 2 to 4. No events are recorded for coils B or C. Their contact mostly likely occurs while the nanocoil is bending up with scanner extension.

As previously mentioned, the slope of the force curve in Figure 6.5 is reduced from the slope of the AFM making contact. Using Equations 4.2 and 4.3, the spring constant of the nanocoil is calculated to be 80 N/m with an uncertainty of 30%. The large uncertainty can be attributed to the poor match of spring constants.[172] The spring constant is calculated to be 100 N/m using the frequency shift method discussed in Chapter 5.2. The uncertainty for this method is also large, 35% because of the resolution in frequency and the poor match of spring constants. Since the calculated spring constant is for the buckled portion of the nanocoil, it cannot be used to calculate the elastic modulus of the coil. The reasonable agreement between the two methods for calculating the spring constant suggests that they can be used together to better estimate the spring constants of compliant materials between the AFM tip and a hard surface.

When the scan direction is reversed, a large adhesion event occurs when the buckled portion of coil D is released from the surface. The adhesion event at point 6 correlates to the release of coil D from the surface, and aligns well with the static geometry. The adhesion event at point 8 marks that the nanocoil is releasing from the surface, but it does not correlate to a return to static geometry. This release event occurs

because the nanocoil had slipped up the substrate as it approached. As the scanner retracts, the nanocoil is adhered to the surface at a different position than its static geometry would normally allow. This release event allows the nanocoil to relax from that position. Point 8 does correlate to the static geometry of coil C. This distance from the nanocoil buckling at point 5 to point 9 is 1.61 μm. This adhesion event occurs without any change in oscillation amplitude of frequency shift, supporting the claim that coils B and C contact the surface without perturbing the thermal resonance of the cantilever. Scan range limitations prevented seeing any more events.

6.2.4 Contact Angle of Four Degrees

The results from the compression of the nanocoil in the silicon trench are unremarkable concerning nanocoil geometry. Neither the oscillation amplitude nor the force curve display any adhesion events other than the AFM tip. The thermal resonance frequency data is also uneventful in that there is no change in resonance frequency until the AFM tip makes contact, at which point the resonance frequency drops below the noise floor. This is perplexing considering that the contact angle is 4° from the surface normal. A previous investigator has used angled shims to adjust the contact angle near perpendicular.[306] A careful examination of the direction of the applied force, however, shows that tilting the substrate does not move the force to coincide with the contact angle. There are two angles in which the force acting on the cantilever can occur: the contact angle and the compression angle. The compression angle is the angle at which the force is applied to the nanocoil, as is measured by the tilt of the surface normal from away from the z scan direction. At a contact angle of 0° and a compression angle of 0°, the nanocoil is compressed. This is equivalent to compressing a nanocoil perpendicular to the surface. For a contact angle of 50° and a compression angle of 0°, the nanocoil can compress, bend and/or slip along the surface. This scenario is equivalent to what is seen in section 6.1.2 on both HOPG and silicon. For a contact angle of 0° and a compression angle of

50°, the nanocoil can compress or more likely bend as the scanner extends. The results from the silicon trenches are best described by this scenario. Even though the contact angle is near perpendicular, the force applied to the nanocoil is not along the axis of the nanocoil. The cantilever and the scanner movement are responsible for the forces imposed upon the nanocoil, which cause it to bend rather than compress. Tilting the substrate does have an affect on the an effect on the slip-stick behavior of the nanocoil[306] but it does not mean the force applied to the nanocoil is along axis of the nanocoil.

6.3 Conclusions

Based on the evidence, the quasi-static model is the appropriate model to apply to the data. Results from each substrate and contact angle are dominated by the geometry of the nanocoil. It is clear that the drive amplitude has no affect on the location of any adhesion or compression events. This is interesting considering the fact that this is a dynamic system; even when the system is undriven, it has a measureable thermal resonance frequency. The ability of the quasi-static model to explain most of the adhesion events leads to the conclusion that the forces generated by the oscillating cantilever and nanocoil are small compared to the force of adhesion.

The direction of the applied force does not change upon tilting the surface. Instead, the tilt angle changes the magnitude of the force acting along the axis of the nanocoil and perpendicular to the nanocoil. This can influence whether the nanocoil bends like a cantilever, slips along the surface, or compresses. Only a sufficient force along the axis of the nanocoil is capable of compressing the nanocoil like a spring, which can best be achieved by having the contact angle and compression angle parallel to the movement of the z-scanner. In this investigation, the applied force causes the nanocoil to bend and slip, which makes the nanocoil behave like a cantilever during scanner extension.

The complexity of the system prevents an accurate measurement of the adhesion and mechanical forces. There are several forces acting in the system at each adhesion event that cannot be differentiated: the restoring force of the cantilever, the restoring force of the bent nanocoil, the restoring force of the compressed nanocoil, the friction force between the nanocoil and the surface, and the adhesive force between the each of the coils and the substrate. Gross assumptions concerning the contact area and off-axis spring constant of the nanocoil would have to be made before any attempt to could be made to calculate the force of adhesion. Although coiled carbon nanotubes offer a unique mix of mechanics and adhesion, deconvolution of these properties from there results presented herein is not possible. The high spring constant of the cantilever used in this study, 5 N/m, prevented the deconvolution of the forces because the frequency of cantilever vibration is the only observable in MPFS.

The results do raise questions about using oscillation amplitude for interpretation. In several instances, both the externally driven and thermal oscillation amplitudes do not show compression or adhesion events that do occur in the force curve and frequency response, e.g. points 3 and 6 in Figure 6.5. In both of these examples, the frequency of the system has shifted away from the frequency at which the oscillation amplitude is measured. It is also incorrect to use the term damping when the oscillation amplitude decreases if there is a positive shift in resonance frequency of the system, e.g. point 2 in Figure 6.5. The oscillation amplitude is not damped because the resonance frequency of the system has increased. This shift naturally results in the amplitude at the measured frequency to be reduced. By only monitoring the oscillation amplitude at a fixed frequency, information necessary to correct interpretation of changes in the mechanical system is not recorded. Damping and a change in resonance frequency are both observed as a decrease in the oscillation amplitude when measured at a fixed frequency. It is, therefore, unwise to use oscillation amplitude as a means to interpret changes in mechanical systems that could cause a change in the resonance frequency of the system.

A similar conclusion can be made about phase. The shift in phase is recorded by monitoring the phase lag of the cantilever oscillation compared to the signal sent the piezo that externally drives the cantilever. Like oscillation amplitude, phase is measured at a fixed frequency: the natural resonance frequency of the cantilever in free space. If there is a significant change in resonance frequency, i.e. >100 Hz, in the system, the phase lag becomes meaningless. It is grossly inaccurate to measure the phase lag between two different frequencies. Change in resonance frequency of the system significantly reduces the usefulness of oscillation amplitude and phase data for correct interpretation.

Several authors have used oscillation amplitude and phase to interpret protein[134, 136, 349, 350] and polymer[135, 142, 351] unfolding. Damping and changes in resonance frequency cannot be deconvoluted from the oscillation amplitude. Likewise, phase lag and changes in resonance frequency cannot be deconvoluted. If there is any significant change in resonance frequency of the system, then the results cannot be properly interpreted. Based on the evidence presented herein, it is questionable for any research team to draw conclusions of mechanical systems using only oscillation amplitude and phase without also measuring changes in frequency.

CHAPTER 7

MPFS OF CARBON NANOLOOPS

This chapter contains an investigation of the adhesive and mechanical response of three small walled carbon nanoloops during both compression and tension on five different surfaces. After the mechanical failure of the attachment point for long, straight carbon nanotubes, see Chapter 5, the extent of compression is purposely kept small. SEM images of the nanoloops are presented in Figure 7.1. The nanoloops were repeatedly brought into and out of contact with the substrates by extending and retracting the scanner in the z-direction while monitoring cantilever deflection and thermally driven resonance. The results for each nanoloop are presented separately. A qualitative discussion of the results follows. An elastica model developed for macro-scale loops is proposed to quantify the results. The results show characteristic differences between the force to bend the nanoloops and the force of adhesion for rupture and peeling.

7.1 MPFS Results for Nanoloops

7.1.1 MPFS of Loop-1

Loop-1 is a carbon nanotube loop (CNL) with a radius of curvature of 137 nm and an outer diameter of 14 nm. The radius of curvature was measured from SEM images and the diameter from TEM images. The curvature of this loop is parallel to the direction of the cantilever whose spring constant was calculated to be 8 N/m. SEM images of Loop-1 are provided in Figure 7.1A.

Loop-1 was brought into contact with five different surfaces to measure the mechanical and adhesive interactions. Loop-1 was brought into contact at six different extents of compression (25, 40, 65, 95, 120, and 150 nm) onto a methyl-terminated

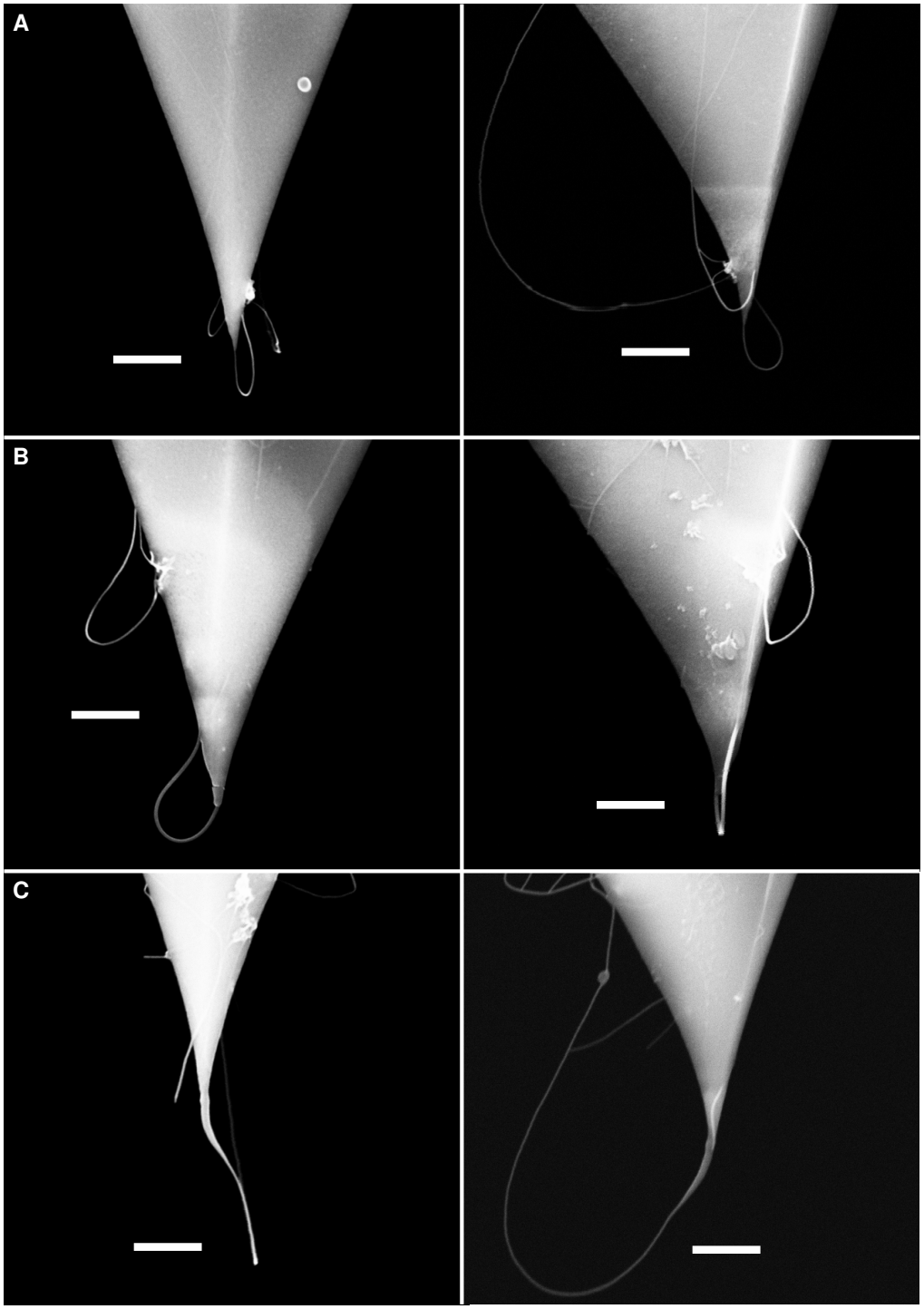

Figure 7.1. SEM images of a carbon three different carbon nanoloops. In each set, the left image is looking at the front of the tip, down the length of the cantilever. The right image is looking at the side of the tip, with the front facing to the right. (A) Loop-1 is oriented parallel to the direction of the cantilever beam. (B) Loop-2 is oriented perpendicular to the direction of the cantilever beam. (C) Loop-3 is oriented parallel to the direction of the cantilever beam. The scale bar in each image represents 500 nm.

alkanethiol monolayer. The results for the largest extent of compression are shown in Figure 7.2. The large interference pattern in the force curve is unavoidable because the template stripped gold is highly reflective. This makes it difficult to discern any changes in cantilever deflection. Upon contact with the surface at point 1, the abrupt change to a linear trace indicates the onset of cantilever deflection. This accompanied with an increase in the resonance frequency. As the scanner extends, the resonance frequency decreases. At point 2, the resonance frequency begins to increase and then levels off. The force curve becomes curvilinear again, typical of that observed prior to the loop coming into contact with the surface. This behavior suggests that Loop-1 is slipping on the surface. At point 3, the scanner begins to retract. From point 3 to 4, the cantilever deflection mirrors the deflection from point 2 to 3. The frequency, however, increases. At point 5, a small adhesion event in the force curve is accompanied with an increase in frequency. The final pull off force is measured to be 4.7 (± 2.1) nN. The frequency shift at the release event is measured to be 3.7 (± 0.5) kHz.

MPFS of Loop-1 was also performed on a hydroxyl-terminated alkane thiol monolayer at six different extents of compression: 5, 15, 30, 55, 70, and 95 nm. The results for the largest extent of compression are shown in Figure 7.3. At point 1, a small jump to contact is accompanied with an increase in resonance frequency. After this abrupt increase, the resonance frequency continues to rise slowly as the scanner extends. At point 2, the scanner changes direction. The frequency continues to increase as the scanner retracts until the release event at point 3. This trend is indicative of increased tension on the system up until the point of rupture of the loop from the surface. The force at the release event is measured to be 7.9 (± 2.7) nN and the frequency shift at the release event is 4.5 (± 0.4) kHz.

Loop-1 was brought into and out of contact with an amino-terminated alkane thiol monolayer at six different extents of compression: 5, 20, 35, 50, 65, and 80 nm. The results for the largest extent of compression are shown in Figure 7.4. A jump to contact

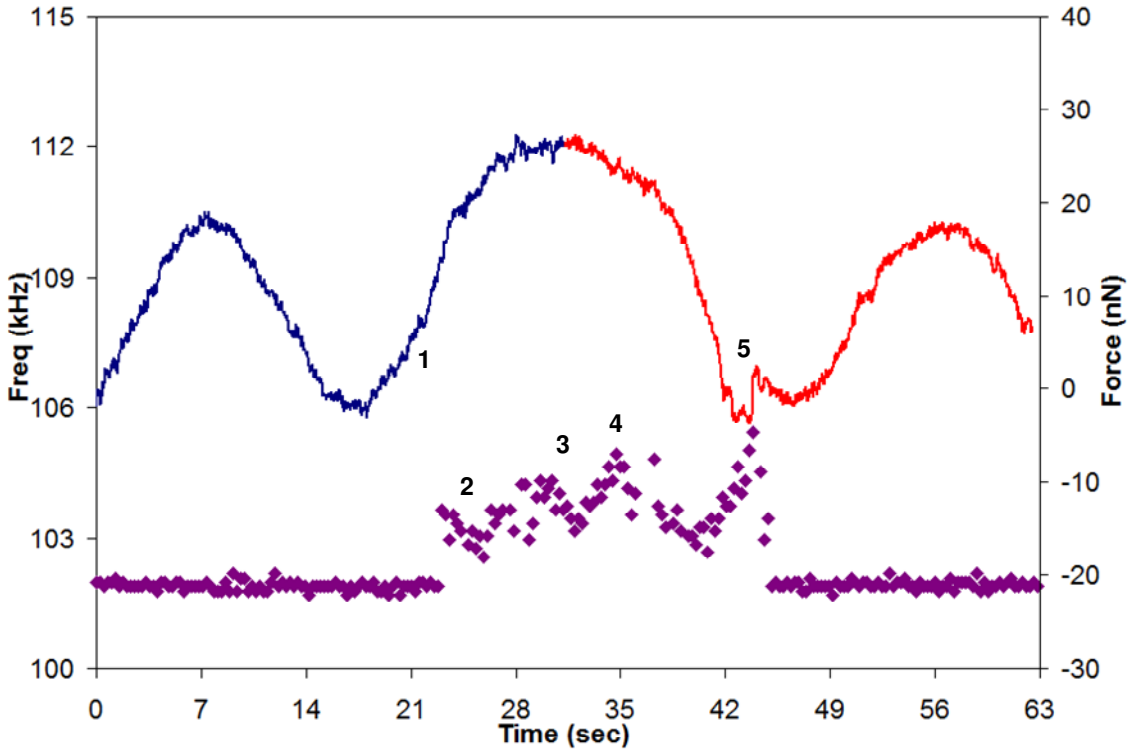

Figure 7.2. MPFS results of Loop-1 on a methyl-terminated alkanethiol monolayer. The blue trace is the force curve for scanner extension and the red trace is during scanner retraction. The purple data points are the thermal resonance frequency of maximum amplitude. This color scheme will be used throughout the rest of this chapter. The response in the force curve is overwhelmed by an interference pattern. Light reflected from the surface causes the interference pattern.

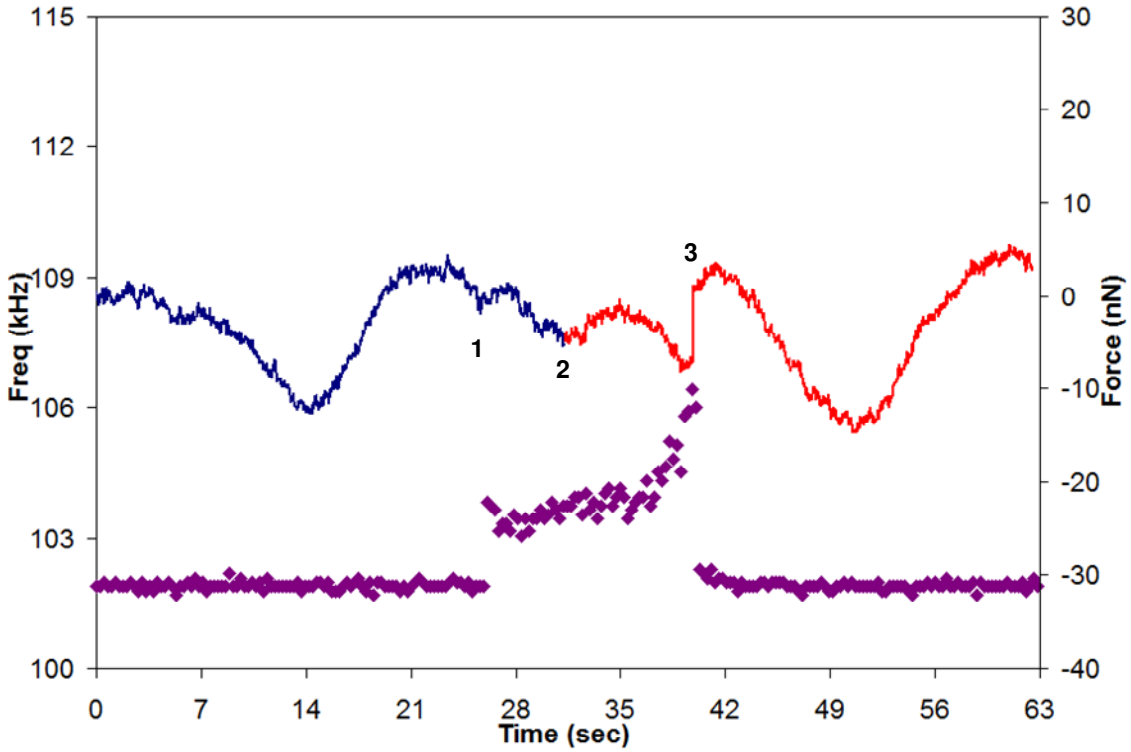

Figure 7.3. MPFS results of Loop-1 on a hydroxyl-terminated alkanethiol monolayer. Light reflecting from the surface causes the interference pattern, which makes interpretation from the force curve difficult.

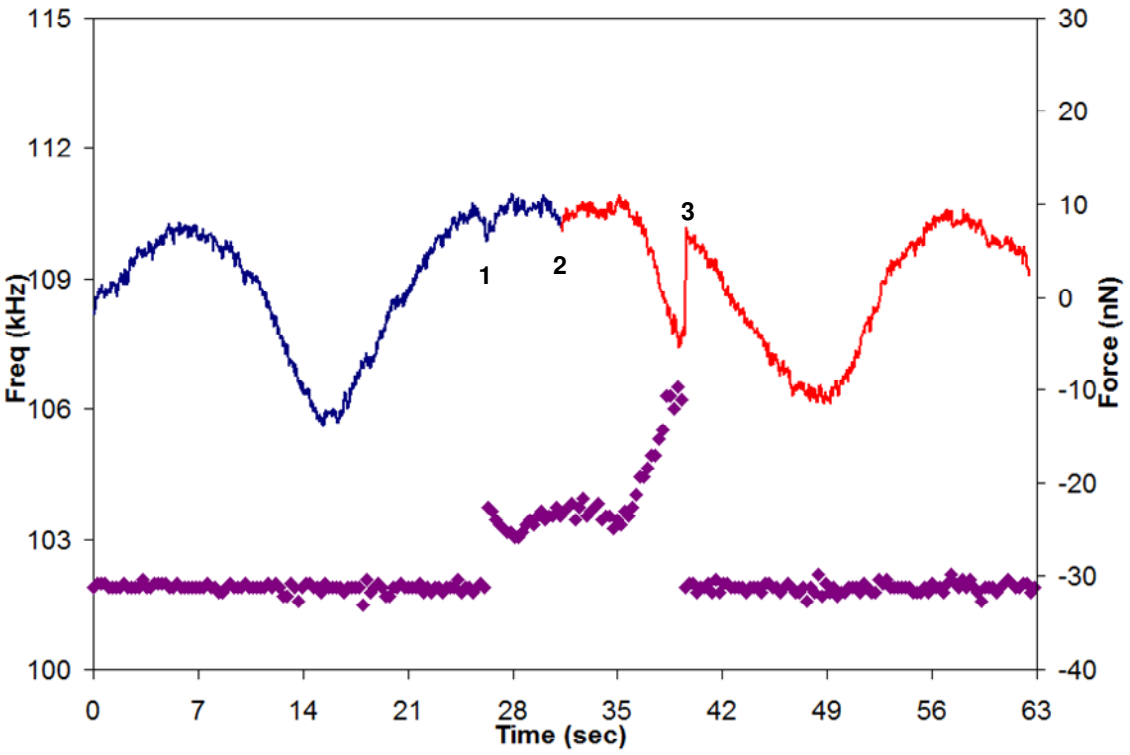

Figure 7.4. MPFS results of Loop-1 on an amino-terminated alkanethiol monolayer. A larger adhesion event is observed. The force curve response is masked by a large interference pattern.

occurs at point 1. The frequency increases when the loop contacts the surface. As the scanner extends, the deflection and frequency level off. At point 2, the scanner changes directions. A release event is observed at point 3. The force of adhesion is calculated to be 10.7 (± 3.7) nN and frequency shift is 4.8 (± 1.0) kHz.

Loop-1 was brought into and out of contact with a silicon surface at six different extents of compression: 10, 25, 40, 60, 70, and 85 nm. The results for the largest extent of compression are shown in Figure 7.5. Unlike contact with the previously described surfaces, no jump to contact is observed, but the frequency shift establishes the point of contact at point 1. A jump to contact may be hidden by the interference pattern. A similar shape of the frequency pattern seen on the previous surfaces is observed here. As the scanner extends, the deflection and frequency level off. At point 2, the scanner changes directions. A release event is observed at point 3 and the frequency increases as the system is put into tension. The force of adhesion is calculated to be 10.6 (± 3.2) nN, and frequency shift is 3.8 (± 0.6) kHz.

MPFS of Loop-1 was also performed on HOPG at six different extents of compression: 15, 30, 50, 60, 75, and 95 nm. The results for the largest extent of compression are shown in Figure 7.6. Any jump to contact at point 1 is obscured by the interference pattern. The increase in thermal resonance frequency is used to establish the point of contact. The resonance frequency dips and slowly rises as the scanner extends. This suggests that the nanoloop buckles and then stiffens as the scanner is extended. At point 2, the scanner changes direction. This results in a decrease of resonance frequency, which is interpreted as a reduction in the stiffness of the system. During scanner retraction, the frequency increases up to the release event at point 3. The force at the release event is measured to be 21.0 (± 3.0) nN and the frequency shift at the release event is 6.7 (± 0.7) kHz. The waterfall plot is included in Figure 7.6B to demonstrate that the frequency of maximum amplitude in 7.6A matches the shape of the thermal resonance frequency of the system.

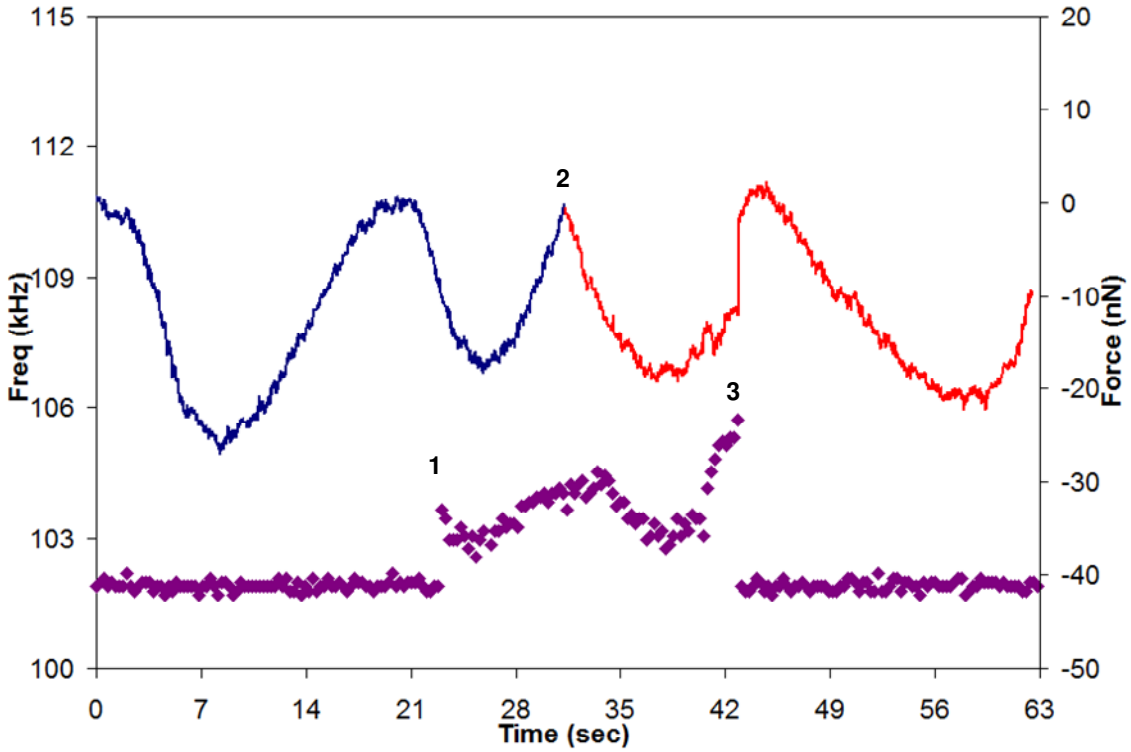

Figure 7.5. MPFS results of Loop-1 on a silicon surface. A larger adhesion event is observed. The force curve response is masked by a large interference pattern.

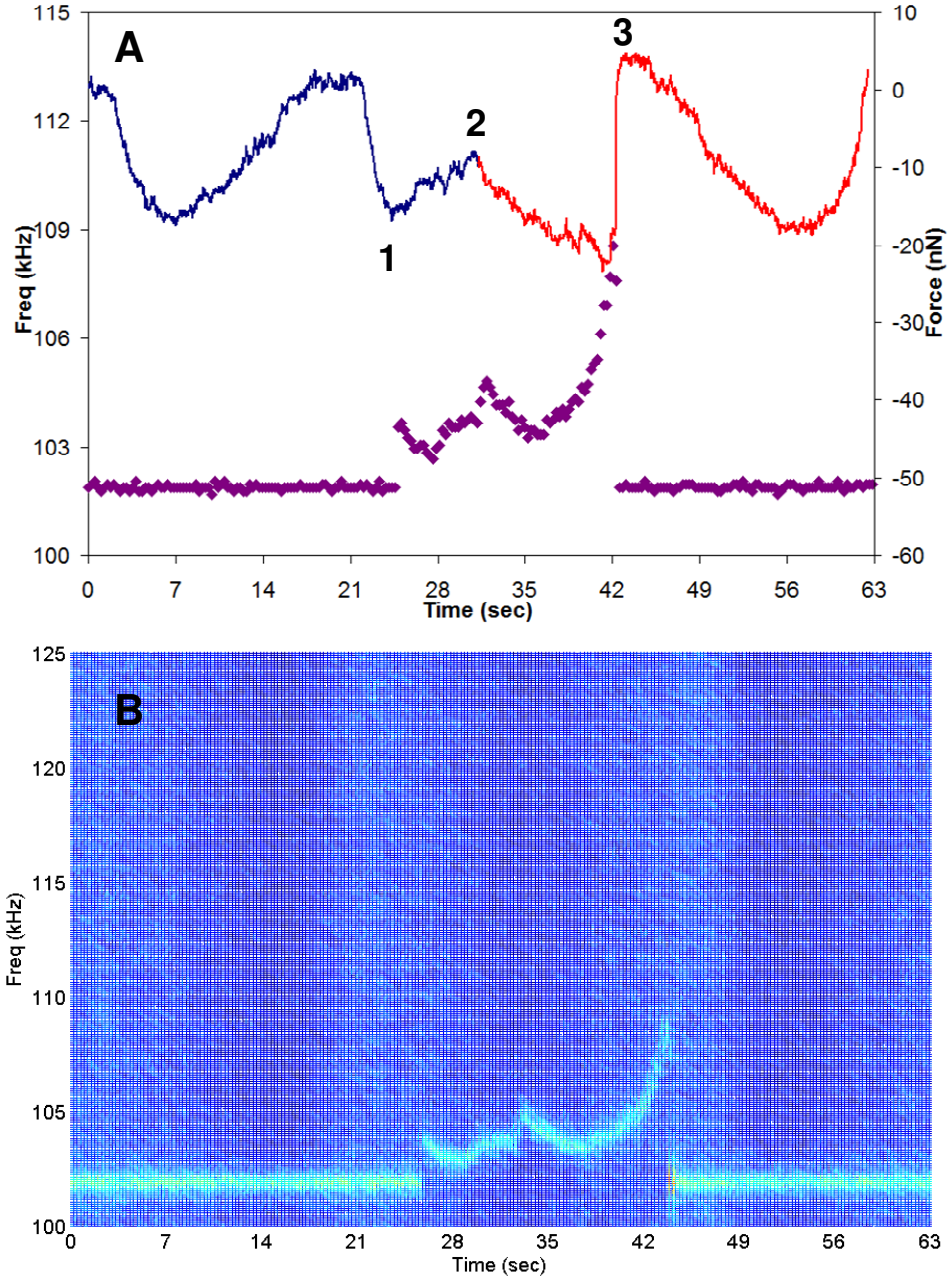

Figure 7.6. MPFS results of Loop-1 on HOPG. (A) A response similar to other surfaces is observed for both the force curve and the thermal resonance frequency plot. (B) Waterfall plot prior to the peak picking routine. Note the agreement between the color-encoded amplitude in the waterfall plot in B and the frequency trace in A.

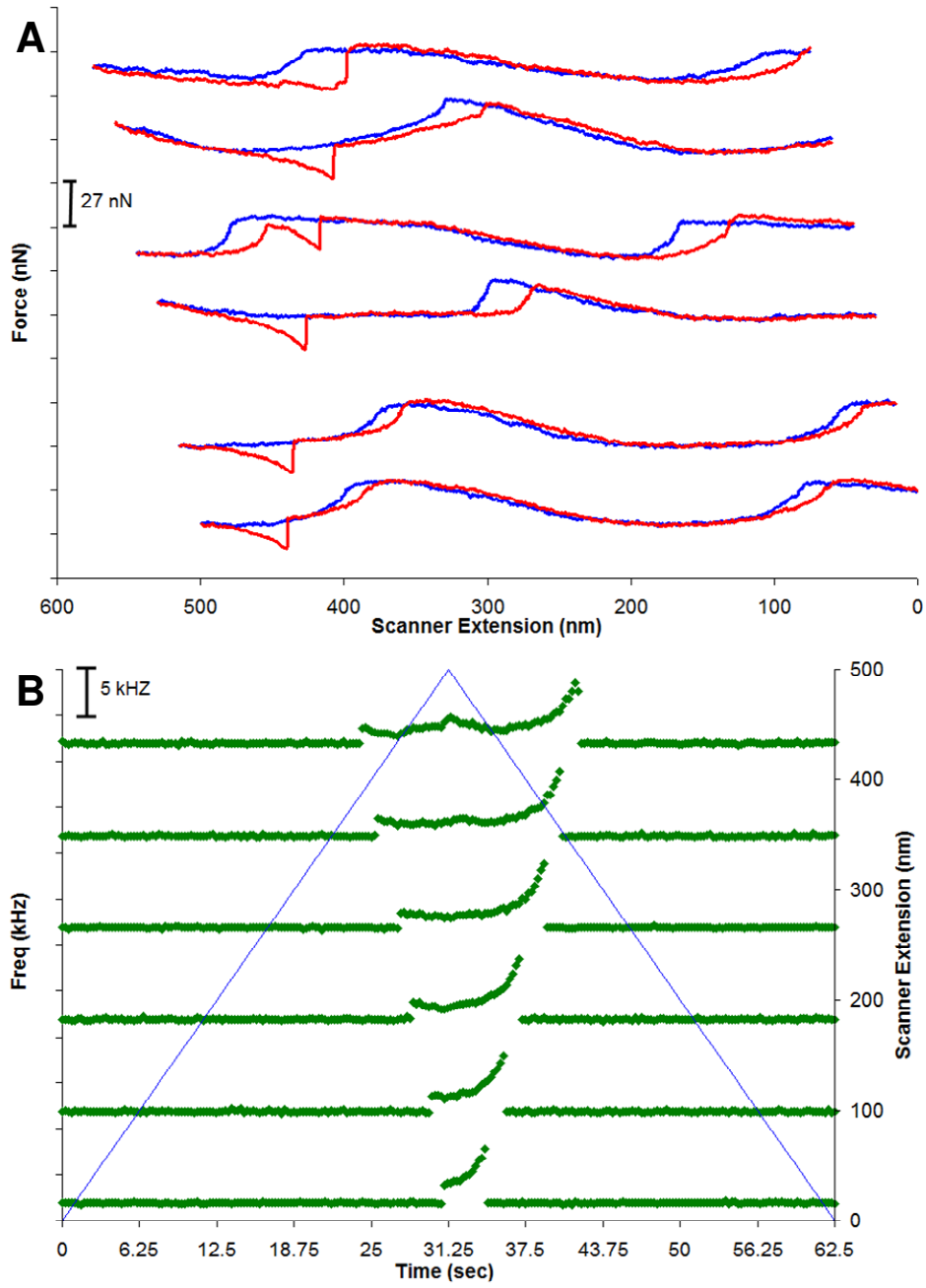

Figure 7.7. Force curves and thermal resonance frequency for Loop-1 at increasing extents of compression on HOPG. The force curves, A, are reproducible regardless of the extent of compression. The force curves are aligned to the jump to contact. The interference pattern makes any interpretation other than the release event difficult. The thermal resonance frequency, B, show the same shape regardless of the extent of compression. The thermal resonance frequency plots are aligned to scanner extension. The traces in each plot are artificially offset for to aid comparison. Starting from the bottom trace in each plot, the extent of compression is 15, 30, 50, 60, 75, and 95 nm.

The effect of the extent of compression on HOPG is shown in Figure 7.7. The force curves are reproducible regardless of the extent of compression. The sharp change in each of the force curves is from the reflectivity of the HOPG surface. In contrast to the force curves, resonance frequency curves change markedly with the extent of compression, suggesting that these changes in the resonance of the system are directly related to the compression of the nanoloop. The extent of compression is directly related to the distance in which the nanotube is relaxing during scanner retraction. The relaxation of the nanotube is evidenced by the decrease in resonance frequency after the scanner changes directions. The release event recorded in both the force curves and the frequency plots is reproducible, and is therefore not related to scanner extension. Similar responses were observed on all the other surfaces investigated with Loop-1. Only the compression events and subsequent relaxation events correlated to scanner movement. For each substrate, the force of adhesion and shift in resonance frequency are independent of scanner extension.

7.1.2 MPFS of Loop-2

Loop-2 is a carbon nanotube loop with a radius of curvature of 198 nm and an outer diameter of 28 nm. The curvature of this loop is perpendicular to the direction of the cantilever. The spring constant of the cantilever was calculated to be 3 N/m. SEM images of Loop-2 are provided in Figure 7.1B. Loop-2 was brought into contact with five different surfaces to measure the mechanical and adhesive interactions.

Loop-2 was brought into contact at six different extents of compression on a methyl-terminated alkanethiol monolayer: 10, 25, 35, 50, 65, and 80 nm. The results for the largest extent of compression are shown in Figure 7.8. A jump to contact occurs at point 1 in the force curve (Figure 7.8.A). The frequency shifts at contact and then falls off while the cantilever is deflected upwards while the scanner continues to extend (Figure 7.8.B). This suggests that the nanoloop is buckling. A similar conclusion has

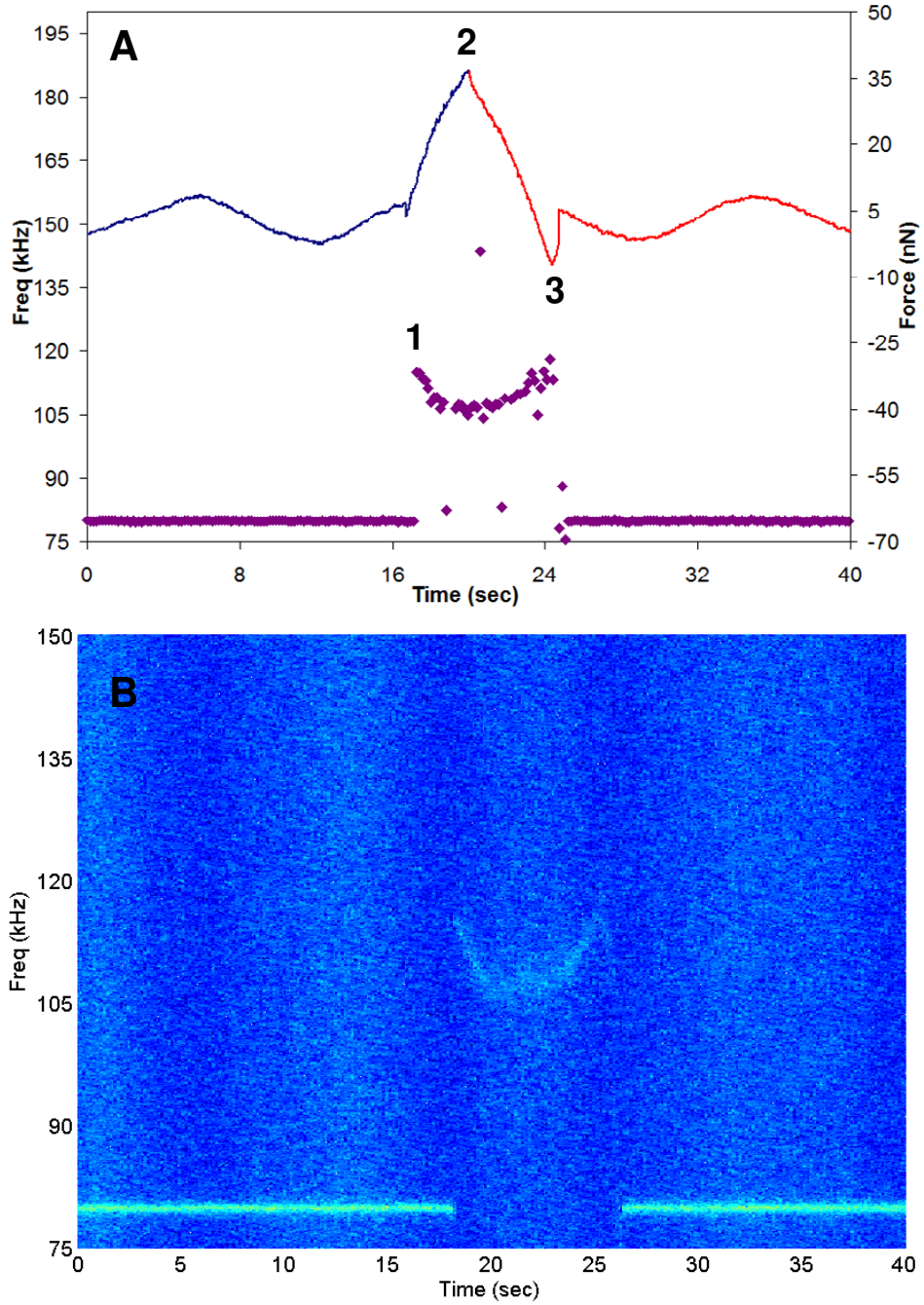

Figure 7.8. MPFS results of Loop-2 on a methyl-terminated alkanethiol monolayer. (A) The response in the force curve is similar to that of a typical force curve. There is a slight curvature in the force of the cantilever as the scanner extends past the point of contact. The frequency response is a symmetric "U" shape, which is indicative of the nanoloop buckling and unbuckling from scanner extension and retraction. (B) Waterfall plot of the same frequency response in (A) is provided because the amplitude of the frequency response is approaching the noise floor. This plot helps the reader better view the shape of the thermal resonance frequency response.

been drawn for carbon nanocoils.[27, 306] At point 2, the scanner begins to retract. The cantilever relaxes from its deflected state until it is put into tension at point 3. The state of tension is determined by the increasing resonance frequency of the system leading up to point 3. The force of the release event is measured to be 12.0 (± 2.9) nN. The frequency shift at the release event is measured to be 37.9 (± 2.1) kHz.

An interference pattern from the reflected light still exists in the force curve, but cantilever motion is easily distinguished. This can be attributed to the fact that the cantilever to which Loop-2 is attached has a lower spring constant than the cantilever to which Loop-1 is attached. In the frequency response, the white noise floor often has peaks larger than the thermal resonance frequency of the system. The white noise floor also is affected by the interference pattern from the reflected light. As in this case, the optical interference increases the amplitude of the white noise floor. The peak picking routine is not capable of discerning between the two. For clarity, the waterfall plot is provided in Figure 7.8B. The thermal resonance frequency shifts are more easily discerned in the waterfall plot.

MPFS of Loop-2 was performed on a hydroxyl-terminated alkane thiol monolayer at six different extents of compression: 20, 45, 70, 95, 120, and 145 nm. The results for the largest extent of compression are shown in Figure 7.9. At point 1, there is a small jump to contact that is accompanied with an increase in resonance frequency. On this particular surface, the amplitude of the thermal resonance frequency of the system is at the noise floor. A symmetric "U" shape can be discerned in the waterfall plot provided in Figure 7.9B. At point 2, the scanner changes direction. The slope of the force curve during scanner retraction is non-linear, indicating that the nanoloop transitions from unbuckling to tension. The frequency increases until the release event at point 3. The force at the release event is measured to be 17.2 (± 4.1) nN and the frequency shift at the release event is 40.0 (± 2.1) kHz.

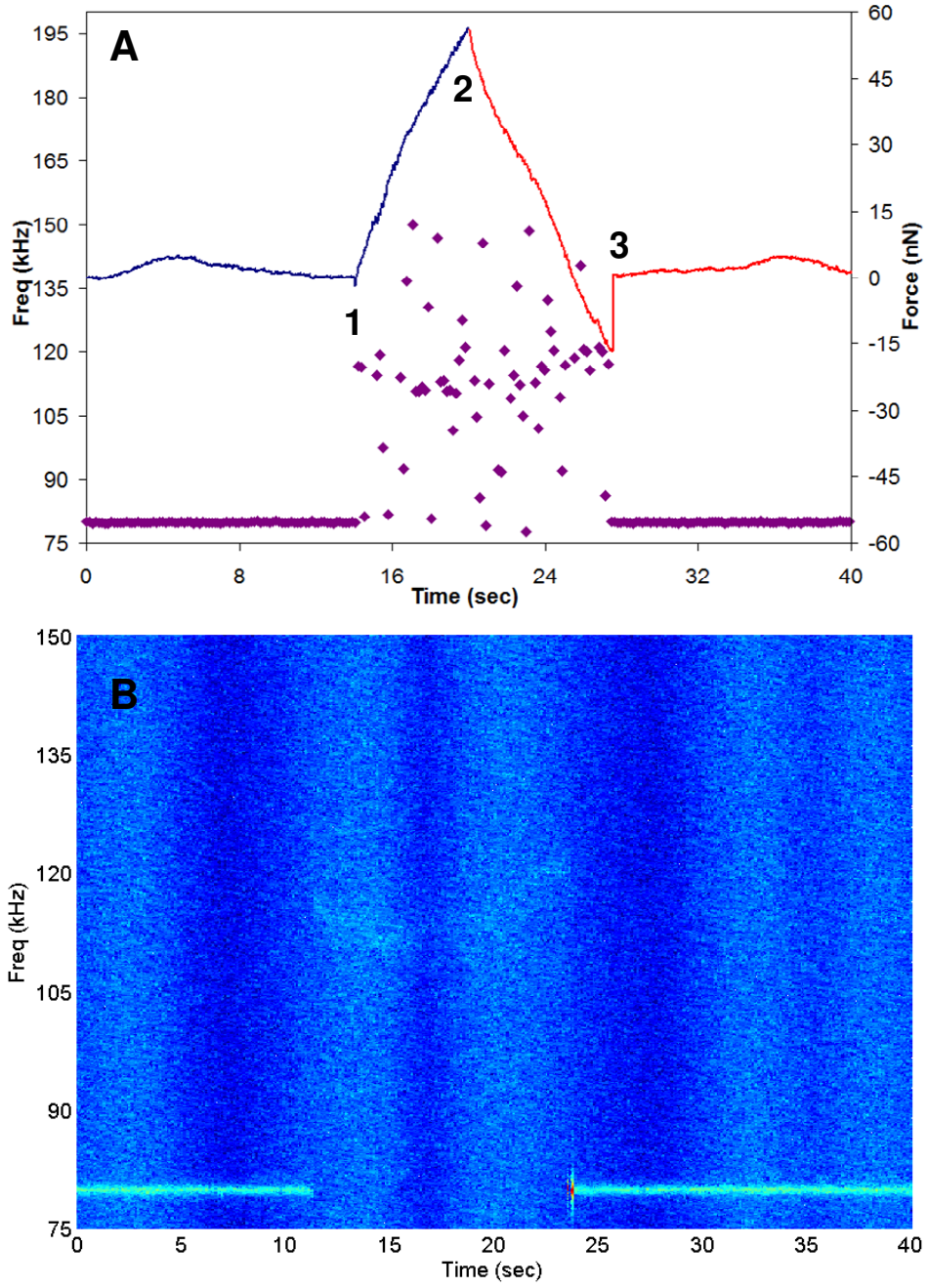

Figure 7.9. MPFS results of Loop-2 on a hydroxyl-terminated alkanethiol monolayer. (A) The response in the force curve is similar to that of a typical force curve. There is a slight curvature in the force of the cantilever as the scanner extends and retracts between the point of contact, 1, and the release event, 3. The frequency response is difficult to discern above the noise floor. (B) Waterfall plot of the same frequency response in A is provided but the amplitude of the thermal resonance frequency is near the noise floor. This plot is provided to help the reader better view the shape of the thermal resonance frequency response.

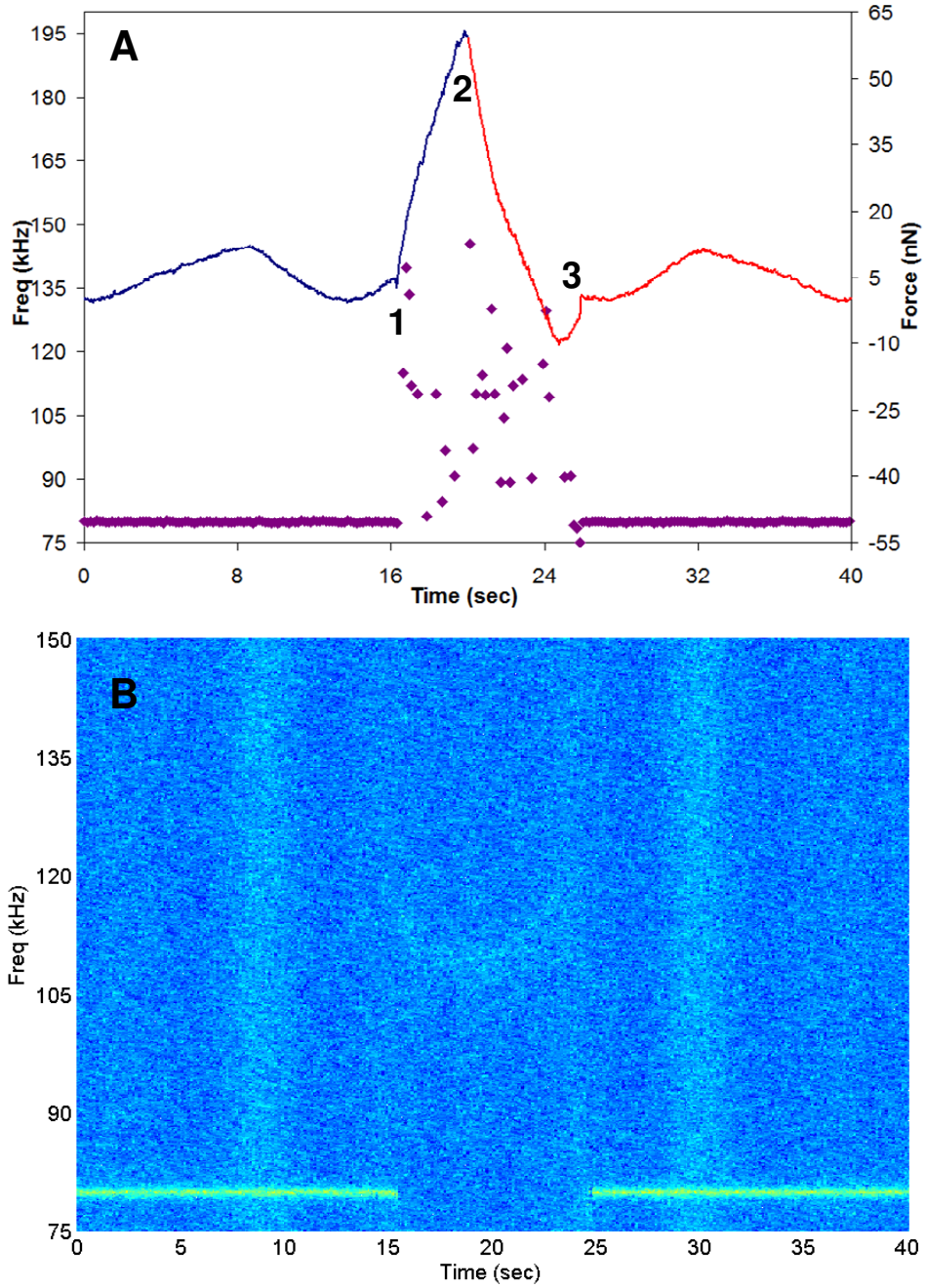

Figure 7.10. MPFS results of Loop-2 on an amino-terminated alkanethiol monolayer. (A) The response in the force curve is similar to that of a typical force curve. The release event at point 3 is not sharp which indicates that the nanoloop is slowly released from the surface. The frequency response is difficult to discern above the noise floor. (B) Waterfall plot of the same frequency response in (A) is provided but the amplitude of the thermal resonance frequency is at the noise floor. Any shape that is observed in the waterfall plot is not meaningful because the signal to noise ratio is approximately 2.

Loop-2 was brought into and out of contact with an amino-terminated alkane thiol monolayer at six different extents of compression: 15, 30, 40, 55, 75, and 90 nm. The results for the largest extent of compression are shown in Figure 7.10. A small jump to contact occurs at point 1. At the point of contact, the frequency increases. As the scanner extends, the deflection of the cantilever increases. The ratio of noise floor and the amplitude of the thermal resonance frequency prevent any interpretation. A keen eye may be able to discern a "U" shape in the waterfall plot, but the signal to noise ratio is approximately 2. This prevents any concrete discussion of the results for the thermal resonance frequency. At point 2, the scanner changes directions and the cantilever begins to relax. At point 3, a release event is observed. Note that the shape of the release event is not sharp as it is for Loop-2 on previous substrates. This suggests that Loop-2 is gradually released from the amino-terminated monolayer. The force of the cantilever's largest downward deflection to it free space is measured to be 10.8 (± 3.9) nN. A frequency shift at the release event cannot be determined because of the proximity of amplitude of the thermal resonance frequency to the white noise floor.

Loop-2 was brought into and out of contact with a silicon surface at six different extents of compression: 15, 40, 60, 75, 100, and 115 nm. The results for the largest extent of compression are shown in Figure 7.11. As before, the peaks from the noise floor overwhelm the peak-picked thermal resonance frequency. The shape of the thermal resonance frequency is better discerned in the waterfall plot in Figure 7.11B. A jump to contact is observed at point 1, and the frequency increases. As the scanner extends, the cantilever continues to deflect. At point 2, the scanner changes directions. At point 3, there is a discrete change in the slope of the force curve during scanner retraction. This change is observed to occur at the same point for each extent of compression. The frequency levels off from point 3 to 4, which also occurs regardless of the extent of compression. A release event occurs at point 4 and the frequency increases as the system

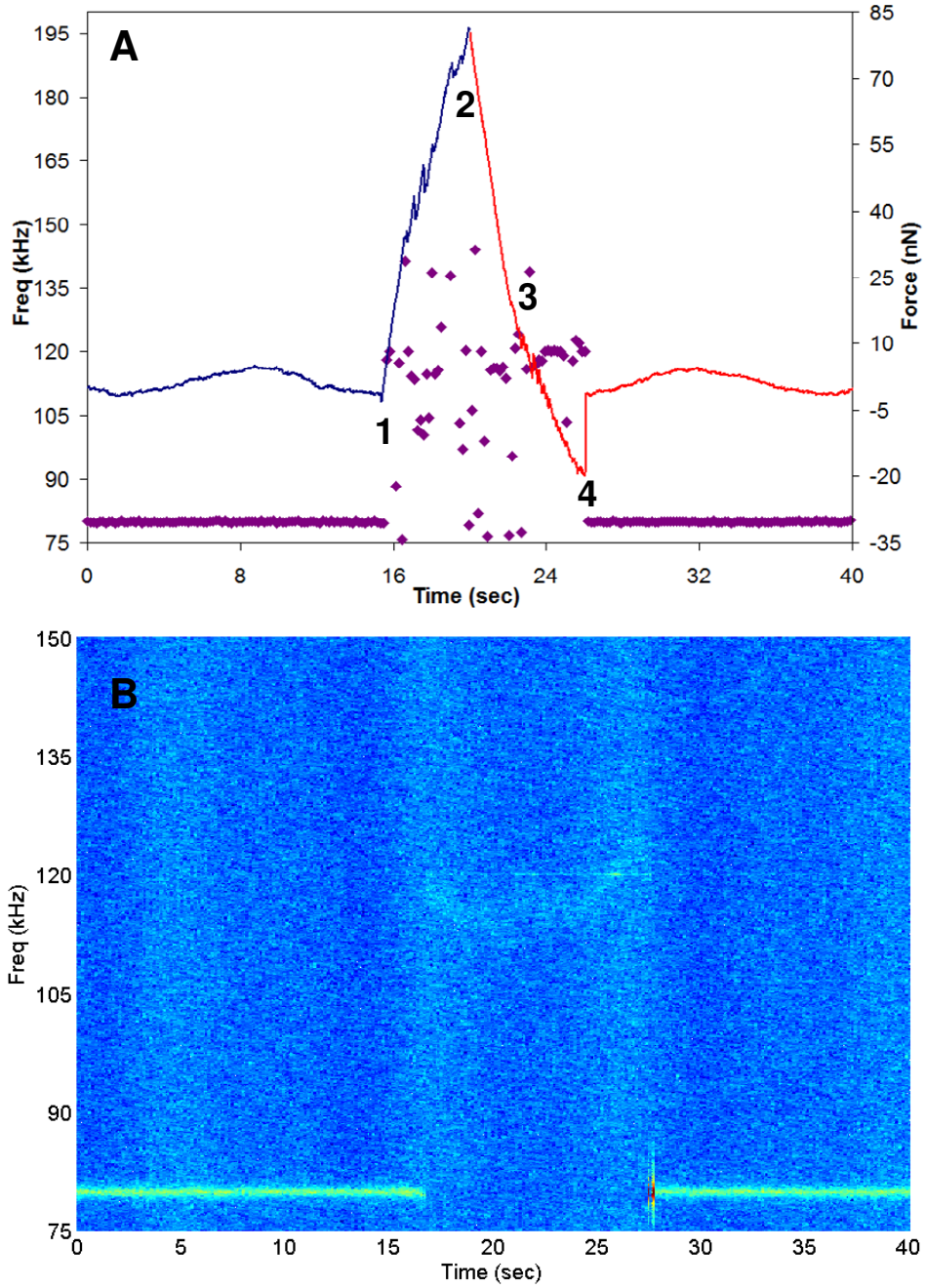

Figure 7.11. MPFS results of Loop-2 on a silicon surface. (A) The force curve displays non-linearity after the nanoloop makes contact during both scanner extension and retraction. The frequency response levels off at point 3. This is accompanied with a discrete change in the force curve, which indicates that the system reaches a steady state in its vibration, even though the force in the system increases. (B) Waterfall plot of the same frequency response in (A) is provided to aid the reader in seeing the shape of the thermal resonance frequency response.

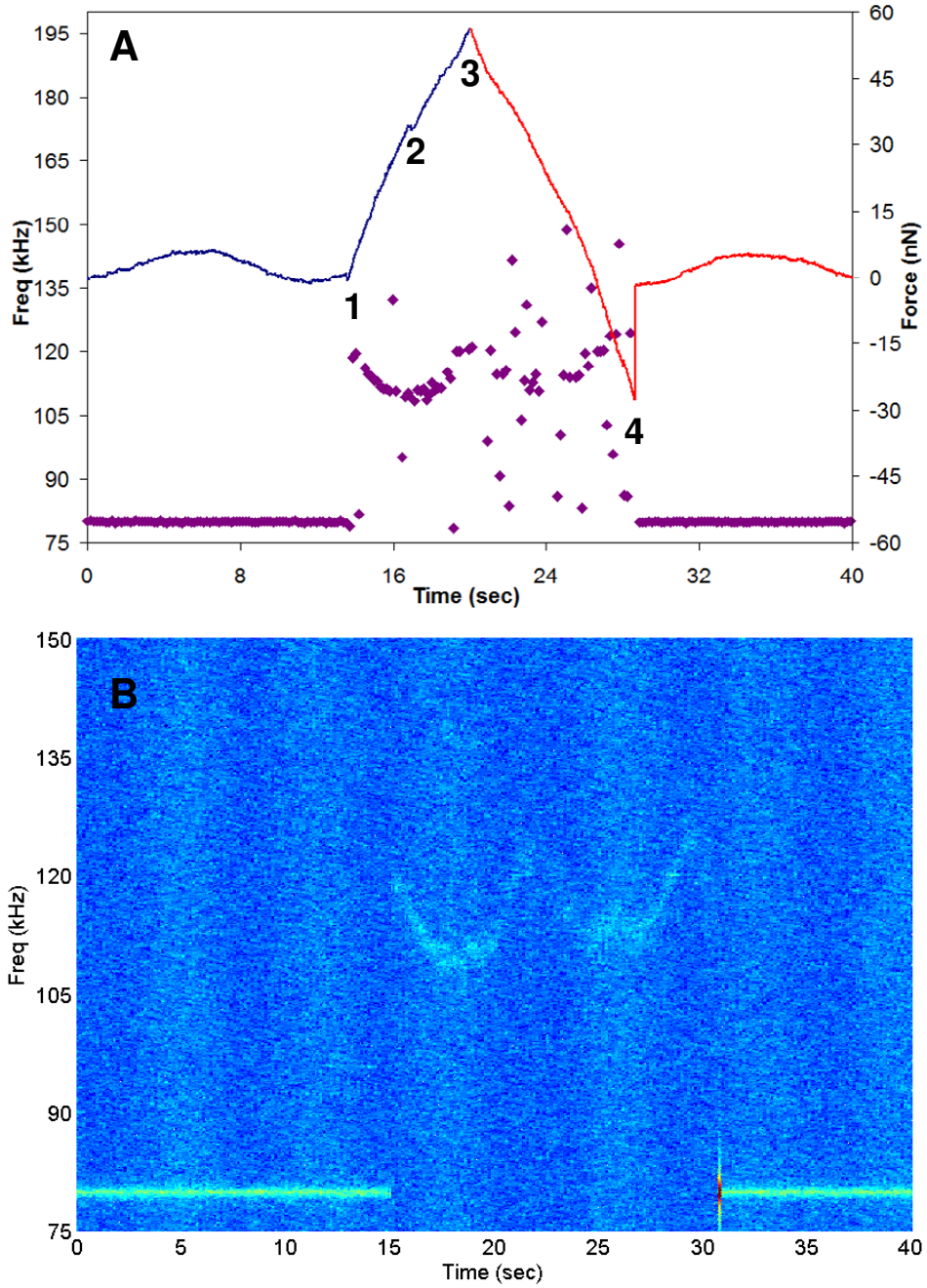

Figure 7.12. MPFS results of Loop-2 on HOPG. (A) The force curve displays non-linearity after the nanoloop makes contact during both scanner extension and retraction. The event at point two causes a change in the slope of the force curve, and the resonance frequency increases during continued scanner extension. (B) Waterfall plot of the same frequency response in (A) is provided to aid the reader in seeing the shape of the thermal resonance frequency response.

is put into tension. The force is measured to be 17.8 (± 4.2) nN, and frequency shift is 40.0 (± 0.6) kHz.

MPFS of Loop-2 was also performed on HOPG at six different extents of compression: 25, 60, 85, 110, 135, and 160 nm. The results for the largest extent of compression are shown in Figure 7.12. At point 1, the system jumps to contact and the resonance frequency increases. During scanner extension, the cantilever deflects upward and the resonance frequency falls. At point 2, a discrete event results in a change of the slope of the force curve. Additionally, the frequency response shifts upward as the scanner continues to extend. This suggests that the event at point 2 causes the nanoloop to shift such that stiffness is added to the system as the scanner extends. At point 3, the scanner changes direction. During scanner retraction, the frequency response mirrors that observed during scanner extension leading up the release event at point 4. The force at the release event is measured to be 25.7 (± 6.1) nN and the frequency shift at the release event is 44.3 (± 2.1) kHz.

The effect of the extent of compression on HOPG is shown in Figure 7.13. The force curves are reproducible regardless of the extent of compression. During scanner extension, the thermal resonance frequency is a direct result of the extent of compression. As the extent of compression is increased, the shape of the frequency response transitions for a “U” shape to a “W” shape. The “U” shape indicates that the nanoloop undergoes symmetric buckling and unbuckling as the scanner extends and retracts. The W shape suggests that after the initial buckling period, stiffness is added to the system. The release event recorded in both the force curves and the frequency plots is not related to scanner extension. For each substrate, the force of adhesion and shift in resonance frequency are independent of scanner extension.

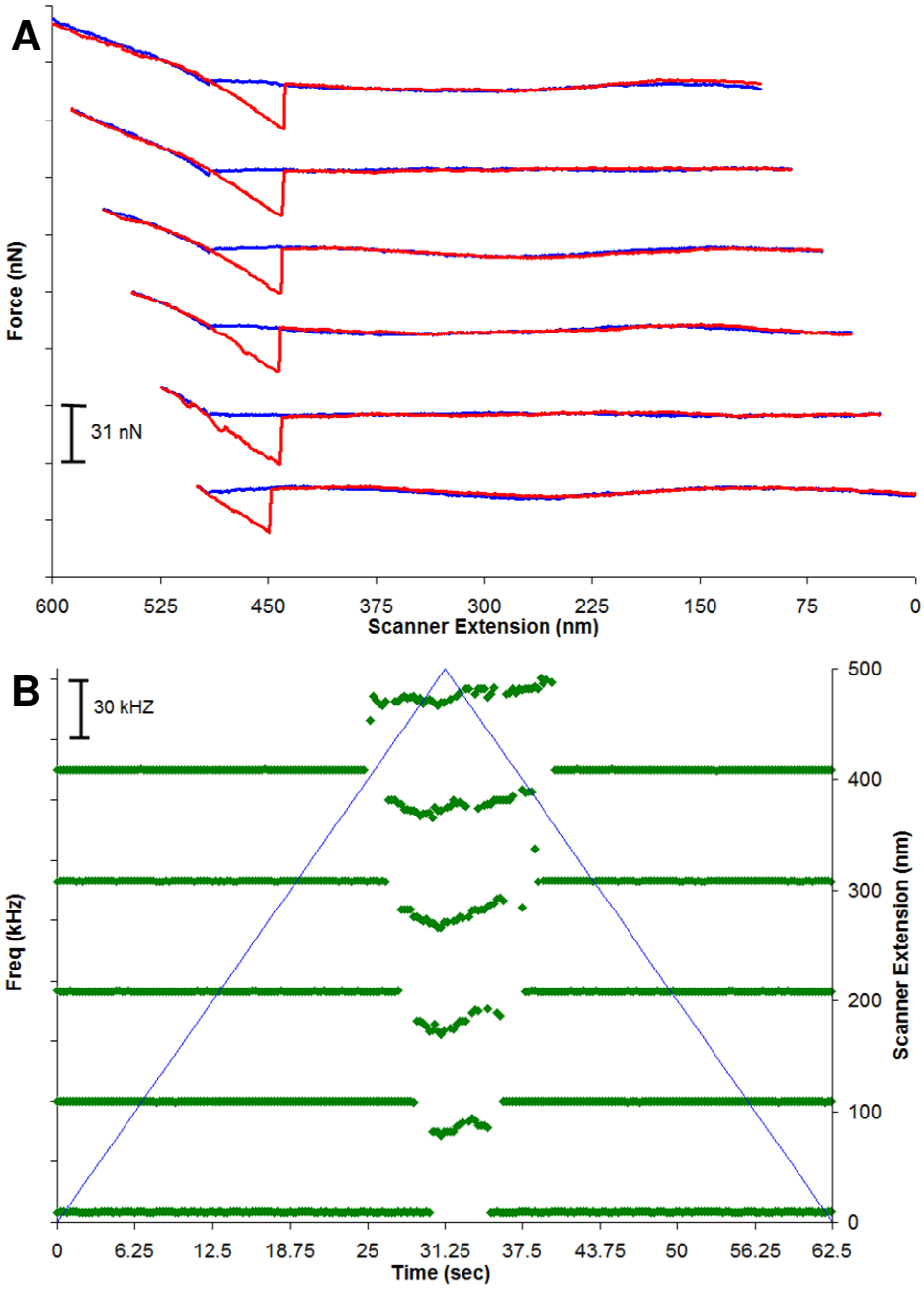

Figure 7.13. Force curves and thermal resonance frequency for Loop-2 at increasing extents of compression on HOPG. The force curves, A, are reproducible regardless of the extent of compression. The force curves are aligned to the jump to contact. The thermal resonance frequency, B, transitions from a "U" shape to a "W" shape as the extent of compression is increase. The thermal resonance frequency plots are aligned to scanner extension. The traces in each plot are artificially offset for to aid comparison. Starting from the bottom trace in each plot, the extent of compression is 25, 60, 85, 110, 135, and 160 nm.

7.1.3 MPFS of Loop-3

Loop-3 is a carbon nanotube loop with a radius of curvature of 525 nm and an outer diameter of 7 nm. The curvature of this loop is parallel to the direction of the cantilever. The spring constant of the cantilever was calculated to be 3 N/m. SEM images of Loop-3 are provided in Figure 7.1C. Loop-3 was brought into contact with five different surfaces to measure the mechanical and adhesive interactions. The waterfall plots are not included in the following results because the amplitude of the thermal resonance frequency remains above the noise floor.

Loop-3 was brought into contact at six different extents of compression on a methyl-terminated alkanethiol monolayer: 5, 15, 40, 50, 60, and 80 nm. The results for the largest extent of compression are shown in Figure 7.14. A jump to contact accompanied with an increase in thermal resonance frequency occurs at point 1. At point 2, the scanner begins to retract. On the way to point 3, the cantilever deflects downward while there is no discernable shift in thermal resonance frequency. After the small release event at point 3, the cantilever deflection remains constant while the frequency shifts upward, indicating the system is in tension. After the release event at point 4, the cantilever begins to deflect downward during scanner retraction. The frequency shifts upward until a small release event at point 5. Points 5, 6, 7 and 8 all display release events in the force curve and are accompanied with increases in resonance frequency leading up to the release event, followed by a drop after the release. The release events in the retract portion of the force curve are highly reproducible are not affected by extent of compression.

MPFS of Loop-3 was performed on a hydroxyl-terminated alkane thiol monolayer at six different extents of compression: 15, 20, 30, 35, 50, and 60 nm. The results for the largest extent of compression are shown in Figure 7.15. At point 1, a large jump to contact is accompanied with an increase in resonance frequency. At point 2, the

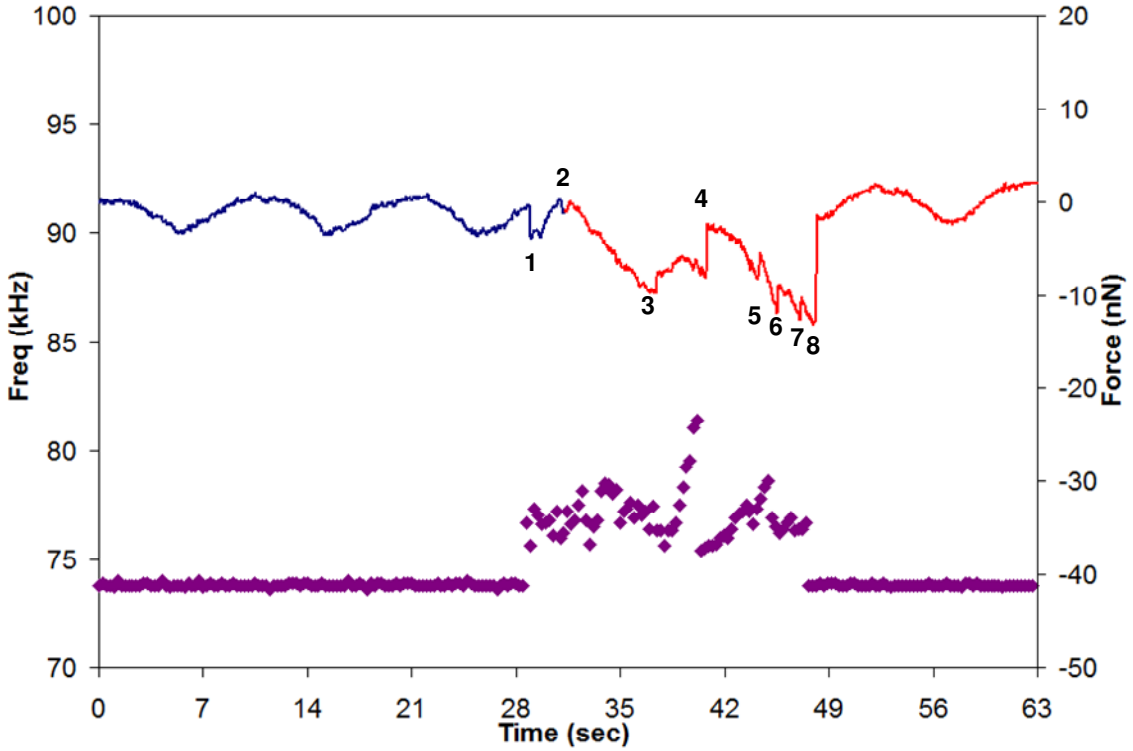

Figure 7.14. MPFS results of Loop-3 on a methyl-terminated alkanethiol monolayer. From point 1 to point 4, the frequency response has a "W" shape, indicating the nanoloop buckles and then resists compression during scanner extension whereas the nanoloop relaxes and is then put into tension during scanner retraction. Points 5-8 display a saw tooth pattern that indicates several release events. Each release event is accompanied with an increase in frequency leading up to the release, followed by a sharp drop in the frequency of the system after release.

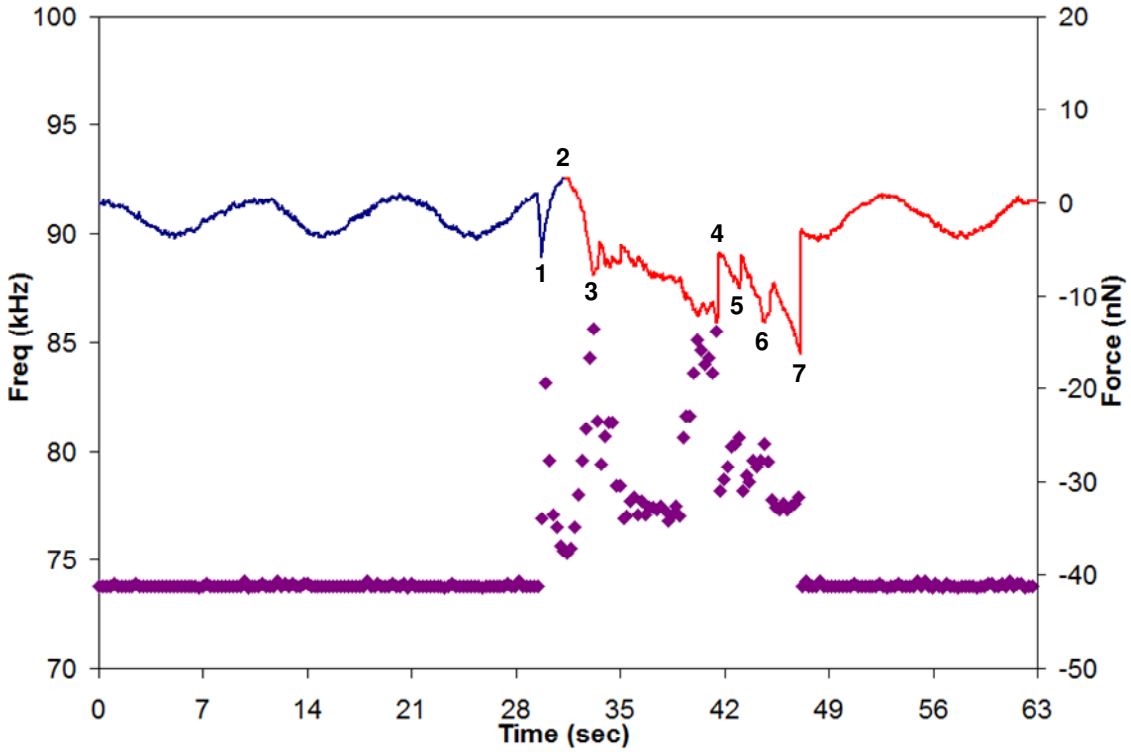

Figure 7.15. MPFS results of Loop-3 on a hydroxyl-terminated alkanethiol monolayer. From point 1 to point 3, the frequency response has a "U" shape, indicating the nanoloop buckles during compression and then unbuckles during scanner retraction. Points 4-7 display a saw tooth pattern that indicates several release events. Each release event is accompanied with an increase in frequency leading up to the release, followed by a sharp drop in the frequency of the system after release.

scanner changes direction. From point 1 to 3, both the force curve and frequency response show symmetry around point 2. The frequency response is a "U" shape, strongly suggesting that the nanotube undergoes reversible buckling. From point 3 to 4, the cantilever deflection decreases. The frequency first falls and then increases with the tension of the system until the release event at point 4. Points 5 through 7 each display release events in the force curve and are accompanied with increases in resonance frequency leading up to the release event, followed by a drop after the release. The release events in the retract portion of the force curve are highly reproducible are not affected by extent of compression.

Loop-3 was brought into and out of contact with an amino-terminated alkane thiol monolayer at six different extents of compression: 15, 30, 40, 55, 75, and 90 nm. The results for the largest extent of compression are shown in Figure 7.16. A small jump to contact occurs at point 1, and the thermal resonance frequency increases. At point 2, the scanner changes directions and the cantilever begins to deflect downward. This is accompanied with a sharp increase in the resonance frequency until point 3. At point 3, a small release event is observed. Note that the resonance frequency does not fall immediately after the release event as it previously has. Instead, the resonance frequency decreases with scanner retraction even though the cantilever continues to deflect downward. As the restoring force of the cantilever increases, the resonance frequency decreases. This result is opposite to normal adhesion events where increasing the restoring force causes an increase in the resonance frequency. At point 4, the nanoloop is released from the surface. These results suggest that tension is not building up in the system during scanner retraction even through the nanoloop is still adhered to the surface and the restoring force of the cantilever is increasing. The waterfall plot is included in Figure 7.16B to demonstrate that the frequency of maximum amplitude in 7.16A matches the shape of the thermal resonance frequency of the system.

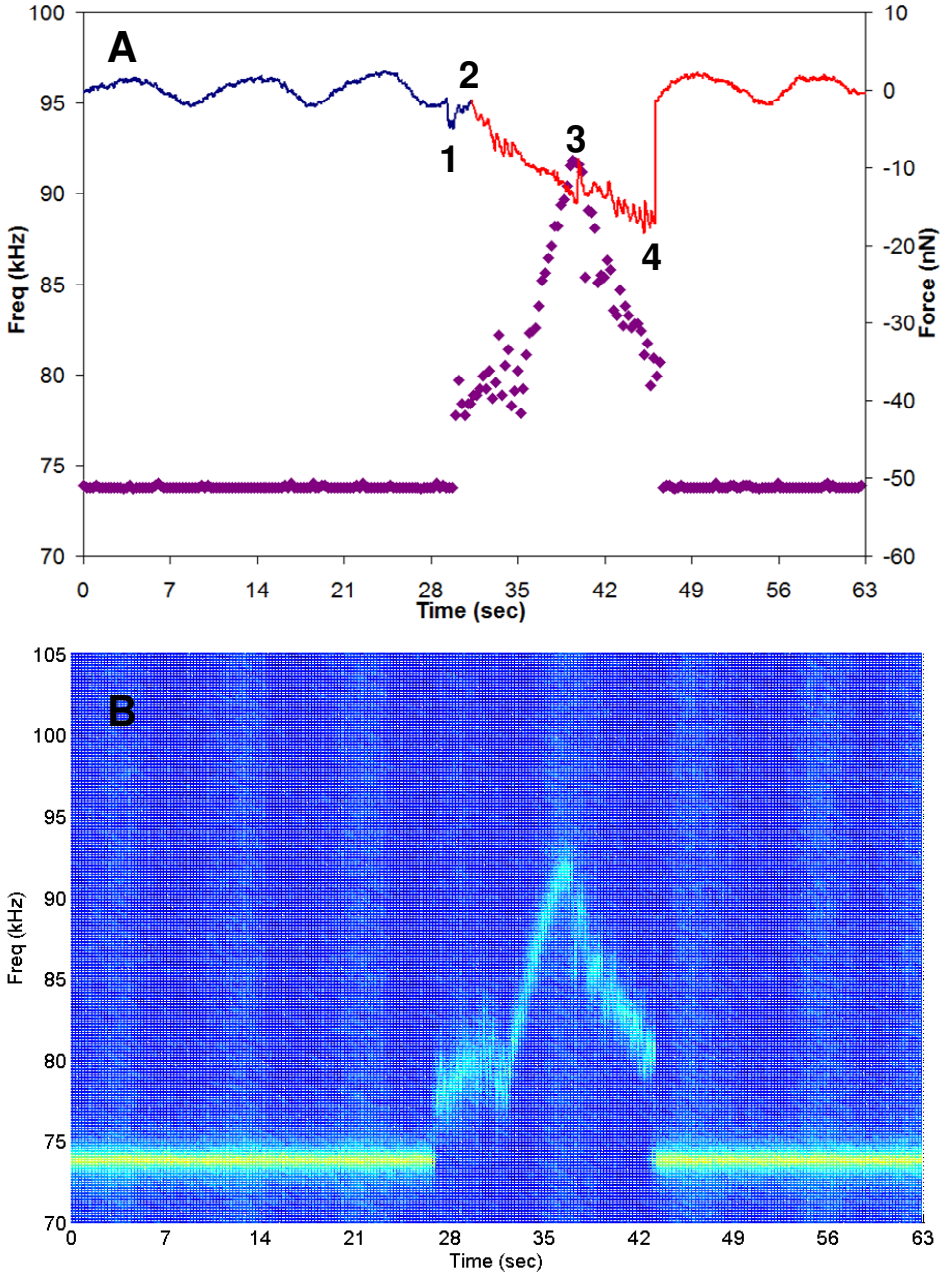

Figure 7.16. MPFS results of Loop-3 on an amino-terminated alkanethiol monolayer. The force curve and frequency response, A, is very asymmetric. Point 1 is the jump to contact. From point 2 to 3, the force curve and the frequency response indicate that the system is put into tension. The frequency does not immediately fall after the release event at point 3. Instead, the resonance frequency of the system gradually decreases as the restoring force of the cantilever increases. The nanoloop is released from the surface at point 4. The waterfall plot, B, is included to demonstrate that the frequency response in A follows the true frequency shift.

Loop-3 was brought into and out of contact with a silicon surface at six different extents of compression: 25, 50, 75, 110, 140, and 170 nm. The results for the largest extent of compression are shown in Figure 7.17. The jump to contact occurs at point 1 and the thermal resonance frequency of the system increases. During scanner extension, there are two small events at point 2 where the cantilever deflection suddenly decreases. The frequency response at each of these events also decreases. The cantilever then deflects linearly until the scanner changes direction at point 3. From point 3 to 4, both cantilever deflection and the frequency response of the system mirror that from point 2 to 3. Release event is observed at points 5 and 6. The frequency response shows an increase leading up to the release event, followed by a sharp decrease in frequency after the release event. After the release event at point 6, the cantilever deflects downward and the resonance frequency increases, apparently leading up to a release event. Instead, the cantilever deflection levels off at point 7, and it remains steady for 340 nm of scanner retraction. The frequency response decreases during this portion of scanner retraction. As with the amino-terminated alkane thiol monolayer, this suggests that tension in the system is decreasing even though the cantilever exerts a restoring force.

MPFS of Loop-3 was also performed on HOPG at six different extents of compression: 45, 70, 100, 125, 155, and 185 nm. The results for the largest extent of compression are shown in Figure 7.18. The nanoloop makes jumps into contact at point 1. The resonance frequency of the system increases. During scanner extension from point 1 to 2, the cantilever deflects upward while the resonance frequency decreases. At point 2, the cantilever deflection decreases slightly and the resonance frequency increases sharply. The scanner changes directions at point 3. During scanner retraction, the resonance frequency increases leading up to the release event at point 4. After the release event, the resonance frequency remains high for 50 nm of further retraction of the scanner until it drops sharply at point 5. No force response is observed during this change in thermal resonance frequency. During scanner extension from point 5 to 6, the

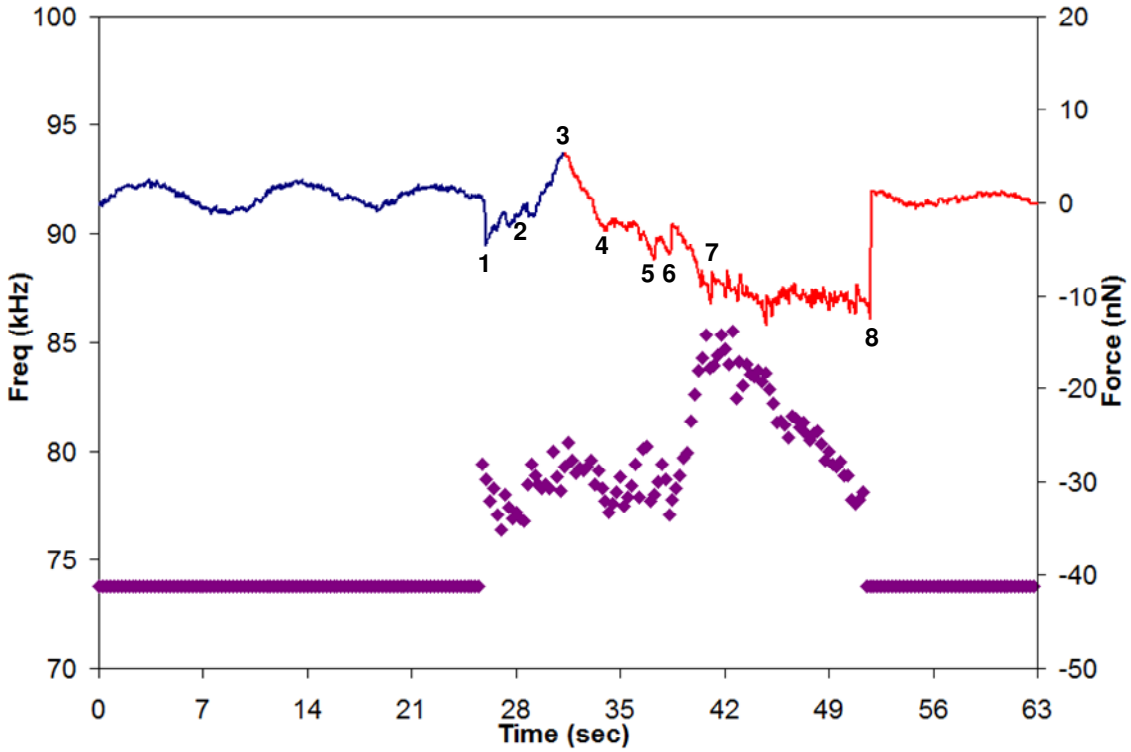

Figure 7.17. MPFS results of Loop-3 on a silicon surface. After the jump to contact at point 1, the response from point 2 to point 4 is symmetric around the change in direction of the scanner at point 3. Discrete release events are observed at points 5 and 6. At point 7, the system cantilever deflection levels off while the frequency of the system gradually decreases. The nanoloop is finally released from the surface at point 8.

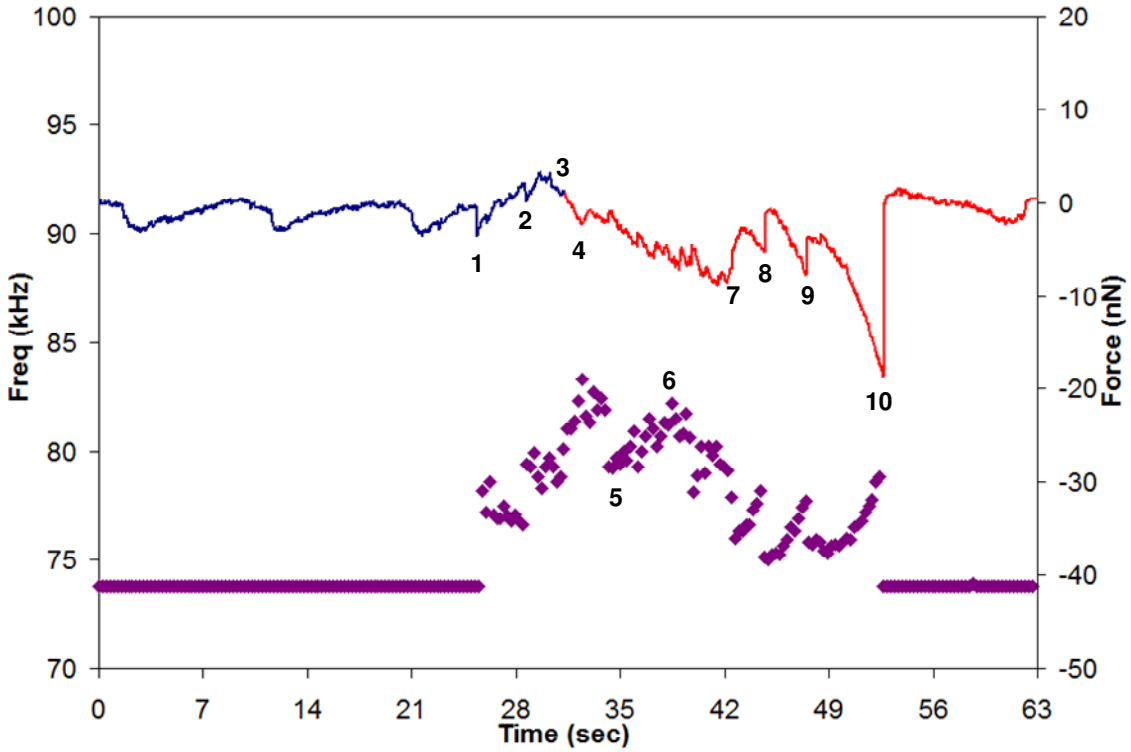

Figure 7.18. MPFS results of Loop-3 on HOPG. Of note is the decrease in resonance frequency from point 6 to 7 while the restoring force of the cantilever increases. In addition, discrete release events are observed at points 8, 9, and 10. The frequency response shows that each of the release events occur while the system is in tension.

cantilever deflects downward while the resonance frequency increases. At point 6, the shift in the resonance frequency changes directions, but again the cantilever deflection continues its previous trend. At point 7, a release event is observed in the force curve and there is a sharp decrease in the resonance frequency. Points 8 through 10 are discrete tension events that have the characteristic deflection of the cantilever and the increase in resonance frequency immediately followed by a sharp decrease. After point 10, the nanoloop is free from the surface.

The effect of the extent of compression on silicon is shown in Figure 7.19. The retract portion of the force curve is independent of the extent of compression. Similarly, the retract portion of the thermal resonance frequency response is highly reproducible. The extent of compression only affects the response during compression and immediately after the scanner changes directions. Figure 7.20 demonstrates the results for the extent of compression on HOPG. As with the silicon surface, the response during scanner retraction is reproducible. Each release event appears in the same place regardless of the extent of compression. This is interesting considering the difference in response between the two surfaces. Taken collectively, this suggests that the nanoloop adheres to the surface at the jump to contact and no new additional portion of the nanoloop adheres upon further compression.

7.2 Discussion of MPFS Results for Nanoloops

7.2.1 Discussion of Loop-1 and Loop-2

Quantifying the results from Loop-1 and Loop-2 proved challenging. The interference pattern generated by reflected laser light in the data sets for Loop-1 obscured any subtle features that could exist in the force curve. Additionally, the interference pattern reduces confidence in the measured force of adhesion. For Loop-2, the amplitude of the thermal resonance frequency is in or below the white noise floor. The white noise

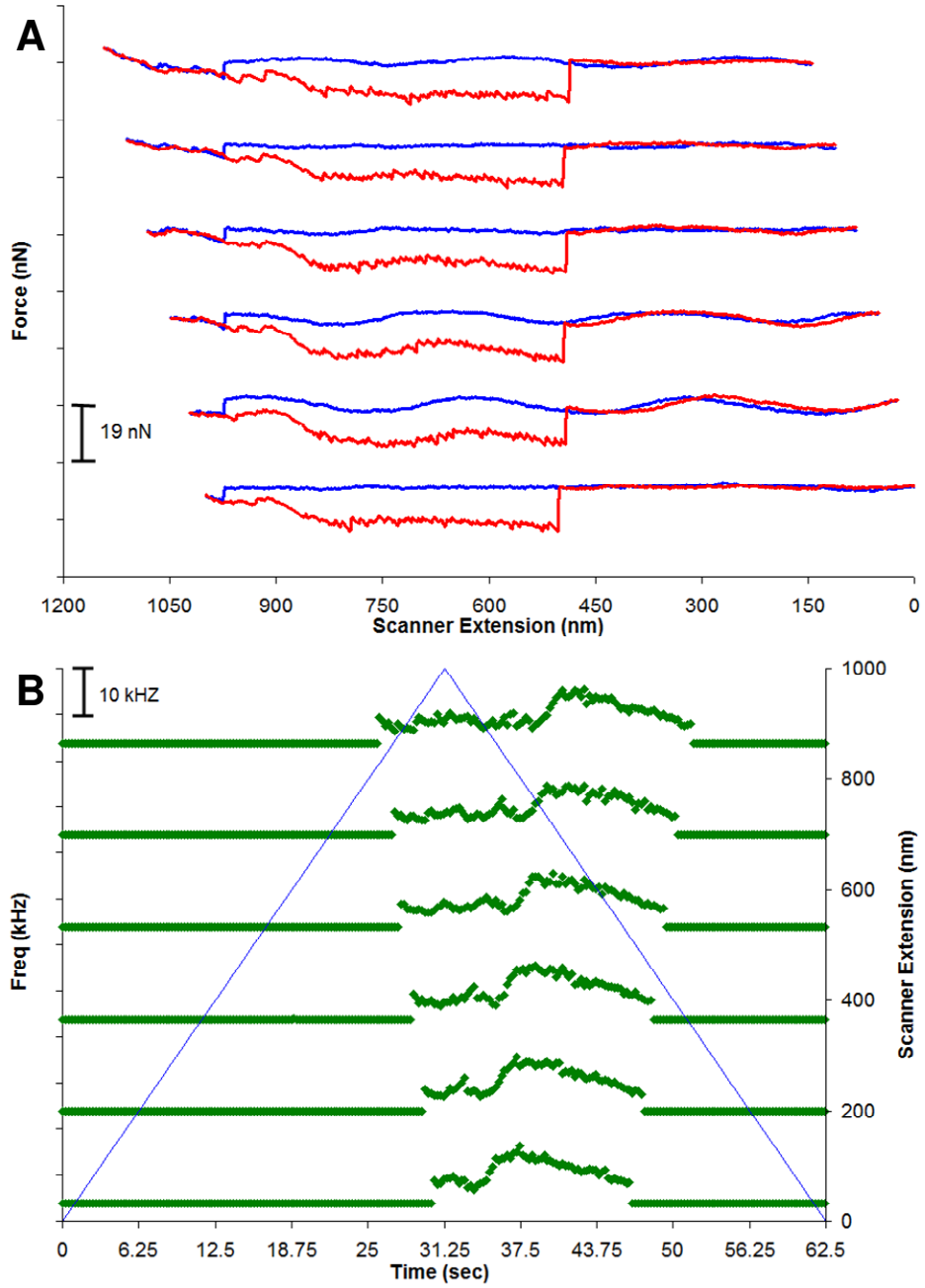

Figure 7.19. Force curves and thermal resonance frequency for Loop-3 at increasing extents of compression on a silicon surface. The force curves, A, are aligned to the jump to contact. The thermal resonance frequency, B, plots are aligned to scanner extension. The traces in each plot are artificially offset for to aid comparison. Note the highly reproducibility during scanner retraction for both the force curves and the thermal resonance frequency plots. Starting from the bottom trace in each plot, the extent of compression is 25, 50, 75, 110, 140, and 170 nm.

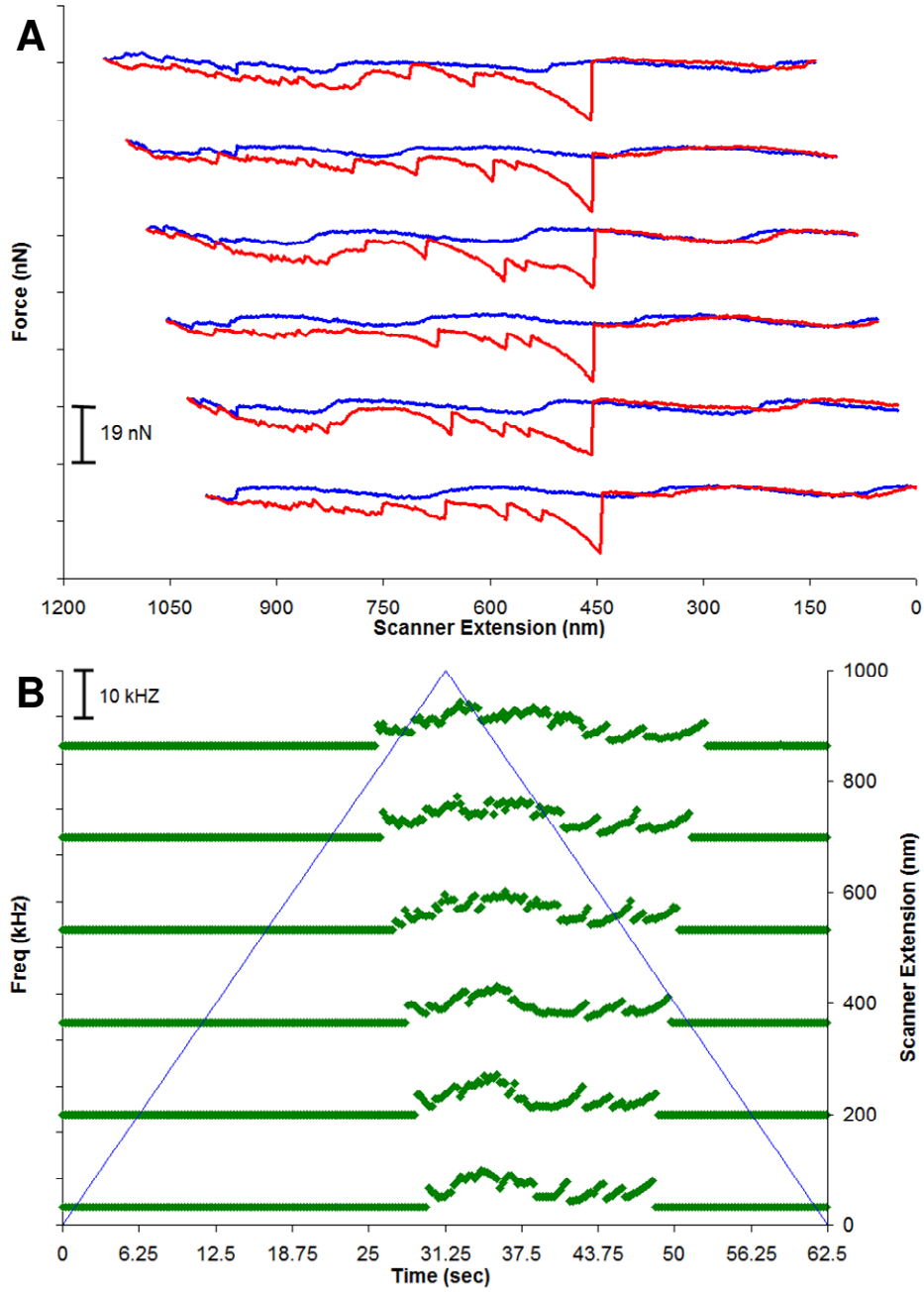

Figure 7.20. Force curves and thermal resonance frequency for Loop-3 at increasing extents of compression on HOPG. The force curves, A, are aligned to the jump to contact. The thermal resonance frequency, B, plots are aligned to scanner extension. The traces in each plot are artificially offset for to aid comparison. Note the highly reproducibility during scanner retraction for both the force curves and the thermal resonance frequency plots. Starting from the bottom trace in each plot, the extent of compression is 45, 70, 100, 125, 155, and 185 nm.

floor is also affected by the interference pattern caused by the reflected light. When viewed as amplitude with respect to time, the vertical bands visible in each waterfall plot have a sinusoidal shape that is similar to the interference pattern in the force curves. The forces can still be measured, but, as has been demonstrated throughout the work presented herein, the frequency response is critical to interpreting the mechanical response of the system. Thus, the results for Loop-1 and Loop-2 can be discussed qualitatively.

Comparison of the dimensions of the two nanoloops suggests that Loop-1 is less stiff that Loop-2. Although the radius of the curvature of the loop for Loop-2 is 30% larger, the diameter of the tube is 100% larger. The results confirm that conclusion in two ways. The cantilever deflection is very small for Loop-1, whereas the cantilever holding Loop-2 does deflect significantly. Using the frequency shift immediately before the final release event with Equation 5.2, the spring constant of Loop-1 is estimated to be approximately 1 N/m. The spring constant of Loop-2 is estimated to be approximately 4 N/m. The spring constants are only estimates because the exact state of the loop and the direction of the applied force are unknown.

Another comparison can be made about the adhesive force. For each loop, the shape of the force curves and frequency responses are qualitatively similar among all the substrates and are unaffected by the extent of compression. This strongly suggests that any adhesive interactions are determined by the geometry of the nanoloop at initial contact. The contact area is assumed to be the portion of the tube that is within 1 nm of the surface, which for undeformed loops is an ellipse. The radius of curvature for both nanoloops was measured from SEM images and the radius of the tube was measured from TEM images. Table 7.1 displays the estimated adhesion force per unit area for Loop-1 and Loop-2 on all five surfaces. The marginal agreement between the two loops suggests that the contact area may be a means at quantifying the work required to pull the nanoloops off each substrate. If the number of interactions per unit area is assumed to be

Table 7.1. Estimated force of adhesion per unit area for Loop-1 and Loop-2. The marginal agreement between the two loops suggests that a more accurate model that takes the force exerted by the nanoloop may be able to quantify the force of adhesion per unit area.

	Dimensions	
	Loop-1	**Loop-2**
Loop R_c (nm)	137	198
Tube r (nm)	7	14
Contact Area (m^2)	2.0×10^{-16}	3.3×10^{-16}

	F_{adh}/Area (N/m^2)	
$-CH_3$	2.4×10^{7}	3.7×10^{7}
-OH	3.9×10^{7}	5.3×10^{7}
$-NH_2$	5.4×10^{7}	3.2×10^{7} *
Si	5.3×10^{7}	5.3×10^{7}
HOPG	1.0×10^{8}	8.0×10^{7}

	Estimated Work of Adhesion (kcal/mol)	
$-CH_3$	0.69	1.0
-OH	1.1	1.5
$-NH_2$	1.5	0.91 *
Si	1.1	1.1
HOPG	0.15	0.11

*The release event for Loop-2 on the amino-terminated alkanethiol monolayer was gradual, not rupture like other data sets. It is possible that this event could be described as peeling.

limited by the number of thiols per unit area for the self-assembled monolayers (5×10^{18} molecules/m^2),[110, 352] the number of silicon <100> atoms per unit area (7×10^{18} atoms/m^2) and carbon atoms per unit area in HOPG (1×10^{20} atoms/m^2),[161] then the force to rupture each interaction can also be calculated. If rupture from the surface is assumed to require moving the atoms one nanometer apart, then the work of adhesion can be estimated. The estimated work of adhesion is included in Table 7.1. The work of adhesion is equivalent to the energy required to break the intermolecular bonds.

The number of assumption required to estimate the work done by adhesion is significant. The assumptions ignore any strain stored by the deformed nanoloops. Additionally, the contact area is calculated from the undeformed nanoloop. Nonetheless, the bond strength is the same order of magnitude as weak van der Waals interactions. A more accurate calculation of the bond strength would require a better model that includes the force stored in the nanoloop and is capable of calculating the actual contact area of the nanoloop.

7.2.2 Discussion of Loop-3

The results from Loop-3 are very interesting. The duration and length in contact for each surface during scanner retraction is highly reproducible regardless of scanner extension. This suggests that Loop-3 takes shape as soon as it contacts the surface. The tension events during scanner retraction for the methyl-, hydroxyl- and HOPG surfaces suggest that they are related to the geometry of the nanoloop. It is possible that these events arise out of defect sites. The noteworthy aspect of the MPFS results for Loop-3 are from the amino- and silicon surfaces. On these surfaces, the thermal resonance frequency shows that as the loop is pulled off the surface the tension in the system is decreasing. The only possible explanation is that the nanoloop is peeling off the surface. Upon initial contact, a large portion of the base of the nanoloop adheres to the surface. This is reasonable considering the length of contact during scanner retraction. As the

scanner retracts, the restoring force of the cantilever levels off. A constant force is needed to peel the nanoloop off the surface. This is consistent with peeling theory assuming the peeling angle does not change.

As the nanoloop peels, less of the nanoloop is in contact with the surface. From a resonance perspective, this is directly related to the reduction in stiffness of the system if one assumes that the nanoloop was in tension before peeling begins. Considering the results presented in Figures 7.16 and 7.17, the system is in tension immediately before the peeling starts. The peeling results in a slow release of this tension.

While the force and frequency results demonstrate that peeling is observed modeling the peeling, however, requires knowledge of the forces in the loop. Previous investigators have used elastica models to interpret loop flexure and force.[353-356] These models have been applied to adhesion of macro-scaled loops. The general assumptions about the interfacial forces made in these models are not applicable on the molecular scale. Instead, a force law that has a basis in intermolecular forces is needed.

Strus et al. used a discrete solution for the universal graphite potential from the Lennard-Jones potential.[71, 166] They obtained their force model from solutions provided by others.[161, 357] Interestingly, Strus et al. use the universal graphite potential to model surfaces that are not graphite.[166] A more generalized force law is needed. Following the derivation of Coffin et al. a generalized force per unit length as a function of separation distance, *F(d)*, can be determined by stopping short of their substitution of parameters strictly associated with the universal graphite potential,

$$F(d) = 8\pi\chi_1\chi_2\varepsilon\sigma\left[\left(\frac{\sigma}{d}\right)^5 - \left(\frac{\sigma}{d}\right)^{11}\right], \qquad \text{Equation 7.1}$$

where χ_1 and χ_2 are the number of interacting molecules or atoms per unit area, ε is the potential well depth and σ is the distance of zero potential. Both of the potential terms are dependent on the identity of the interacting species. To solve for the forces, ε and

σ must be known. For modeling purposes, the ratio of ε and σ may be parametrically determined. The results from the parametric study could be used to determine the transition from rupture to peeling and possibly quantify the force of adhesion. If nothing else, the elastica model will be able to deconvolute the force in the loop from the adhesive forces.

7.3 Conclusions

It should be noted that the oscillation amplitude of the externally driven cantilever was also acquired for all of the data sets presented herein. Considering the conclusions of Chapter 6, it has not been included in the discussion. To reiterate that point, the oscillation amplitude of the driven cantilever compared to the thermal resonance frequency is provided in Figure 7.21. The oscillation amplitude of Loop-2 on hydroxyl-terminated alkane thiol, Figure 7.21A, does not show any fine structure. Likewise, the oscillation amplitude of Loop-2 on HOPG, Figure 7.21B, does not show any fine structure that corresponds to any possible compression, buckling, slipping, tension, or release events over the full range of scanner movement. Recalling Figures 7.9 and 7.12, there is a noticeable difference in the observed frequency response on each surface even though the amplitude of the thermal resonance frequency is near the white noise floor. It is worth noting that the oscillation amplitude does indicate the point of contact and the point of release from the surface. Again, oscillation amplitude at a fixed, driven frequency cannot be used to interpret force spectroscopy of a system that changes resonance frequency as it is compressed or put into tension.

Both peeling and rupture of nanoloops has been observed. Based on early calculations, the force of adhesion is directly related to contact area for those loops that rupture. This would suggest that a JKR model could be applied to the data. The results from Loop-3 strongly suggest that peeling is a viable release mechanism. Figure 7.22 shows the expected difference between rupture and peeling as the loop is released from

the surface. After contact, the loop is put into tension. From this point, there are two pathways. The left pathway shows increasing tension in the system, but the contact area remains the same. The tension in the system overcomes the adhesive forces and the loop is released from the surface and returns to its regular conformation. The right pathway shows that as tension is placed in the system, the loop peels from the surface. The tension in the system is released both from peeling and by the loop returning to its regular conformation. As the surface continues to move away, the loop is peeled off the surface.

Comparison between peeling and rupture has been discussed with interpretation of the results awaiting a better model. As of this writing, the results from an elastica model and the force law presented in Equation 7.1 are forthcoming. They will soon be used to interpret the peeling and rupture phenomena observed herein.

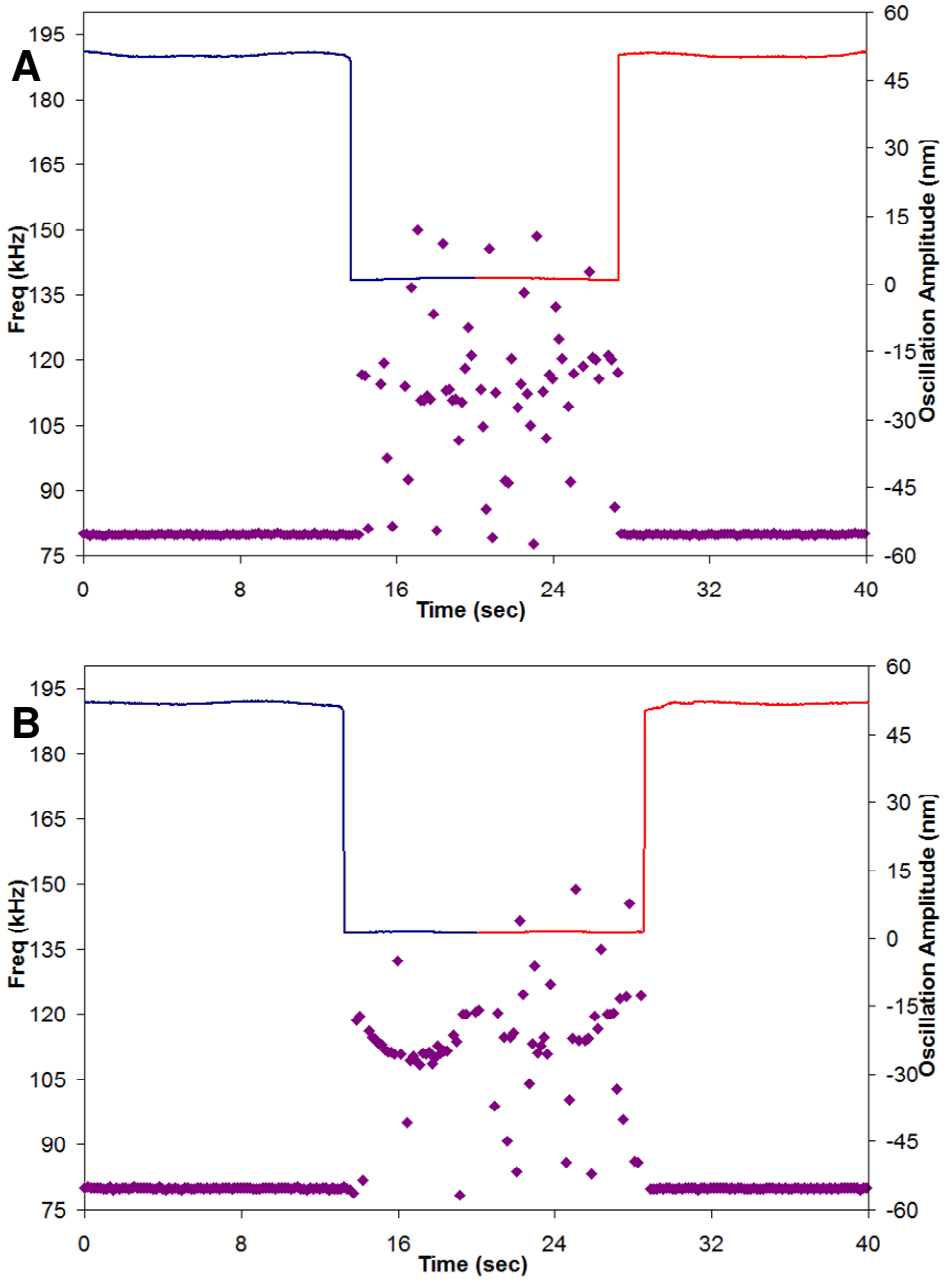

Figure 7.21. Plots of oscillation amplitude compared to thermal resonance frequency. The oscillation amplitude of Loop-2 on (A) hydroxyl-terminated alkanethiol surface and (B) HOPG. Note the high degree of similarity between the two oscillation amplitude plots even though the frequency response is very different.

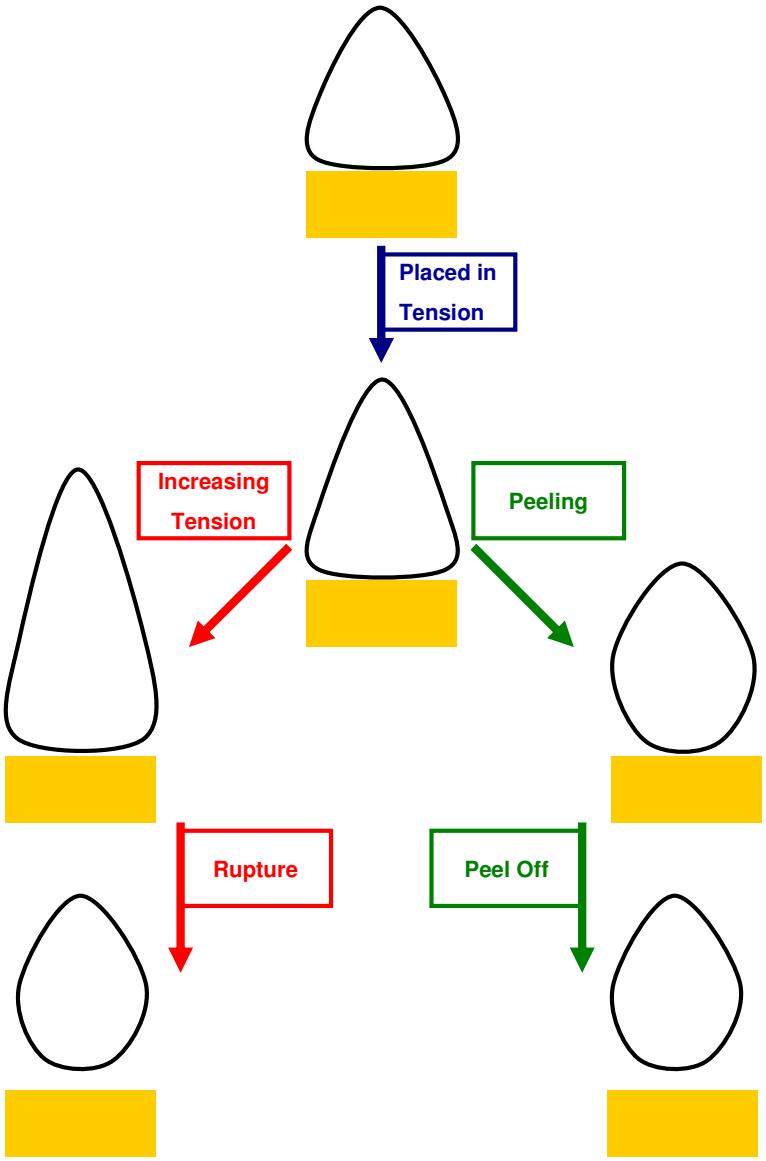

Figure 7.22. Illustration of the difference between rupture and peeling of a loop. After contact, the loop is put into tension. From this point, there are two pathways. The left pathway shows increasing tension in the system, but the contact area remains the same. The tension in the system overcomes the adhesive forces and the loop is released from the surface and returns to its regular conformation. The right pathway shows that as tension is placed in the system, the loop peels from the surface. The tension in the system is released both from peeling and by the loop returning to its regular conformation. As the surface continues to move away, the loop is peeled off the surface.

CHAPTER 8

CONCLUSIONS AND RECOMMENDATIONS

8.1 Conclusions

The primary goal of this work was measuring the adhesive and mechanical properties of carbon nanostructures in contact with chemically modified surfaces. The specific aims of this investigation were: 1) deconvolute mechanical and adhesive forces acting on the carbon nanostructures; 2) quantify the tribological properties, i.e. rupture, friction, and/or peeling, of carbon nanotubes on chemically modified surfaces; 3) quantify the mechanical properties of the carbon nanostructures. All three aims were successfully achieved.

The use of multi-parameter force spectroscopy to interrogate the complex adhesive and mechanical dynamics of carbon nanostructures has been well demonstrated. By varying the extent of compression, the static coefficient of friction was calculated. Additionally, a new method of determining the elastic modulus of carbon nanotubes in tension by measuring the change in frequency was presented. The calculated results are in good agreement with previous literature. The complex mechanical behavior of carbon nanoloops was also investigated. Both peeling and rupture were observed to occur. An elastica model to interpret the results is currently being developed, which should serve to quantify the results.

In addition, the results presented in Chapter 6 clearly call into question any force spectroscopic conclusions that use amplitude of a fixed frequency for interpretation. The results presented show that even weakly interacting mechanical systems are not damping. Instead, the resonance frequency increases because the stiffness of the system has increased. Most of this work using dynamic force spectroscopy has been built off the

paper by Cleveland et al.[118] The authors clearly state the following assumptions in their derivations: the resonance frequency does not change; the steady state motion of the cantilever is sinusoidal; the damping effects on the cantilever remain unchanged during experimentation. The results presented for each of the different nanostructures used in this investigation clearly show that the resonance frequency does change. The system is far from steady state while the scanner extends or retracts. As such, the conclusions offered by Cleveland et al. should be left to the field of phase imaging, where the amplitude and frequency remain at fixed values through a feedback loop. It is this author's strong recommendation that any future force spectroscopic methods of mechanical systems be performed using MPFS.

8.2 Future Directions of Research

The methods and models presented herein are not limited to carbon nanostructures. One of the potential applications is other nanofibers. Work in this area was initiated with electrospun polymer fibers, as detailed in Appendix B. The investigation was cut short with the graduation and subsequent departures of the collaborators. Individual fibers can be attached to an AFM by using a micromanipulator to position the fiber on a flattened AFM tip. The fiber could be attached using an epoxy or by depositing material on top of it, e.g. ion beam induced deposition. Effectively, this would create two cantilevers: the AFM cantilever and the fiber cantilever. The fiber could be brought into contact at the edge of a plateau. A schematic of the experimental setup is shown in Figure 8.1. The elastic modulus of the fiber could be determined using MPFS by varying the length of the fiber spanning between the AFM tip and plateau. The slope of the deflection curve is related to the ratio of the spring constant of the fiber and the cantilever. Changes in effective length of the nanofiber can also affect the frequency response of the system. MPFS is more than capable of measuring those changes, and allowing the investigator to use the data to estimate the spring constant and elastic

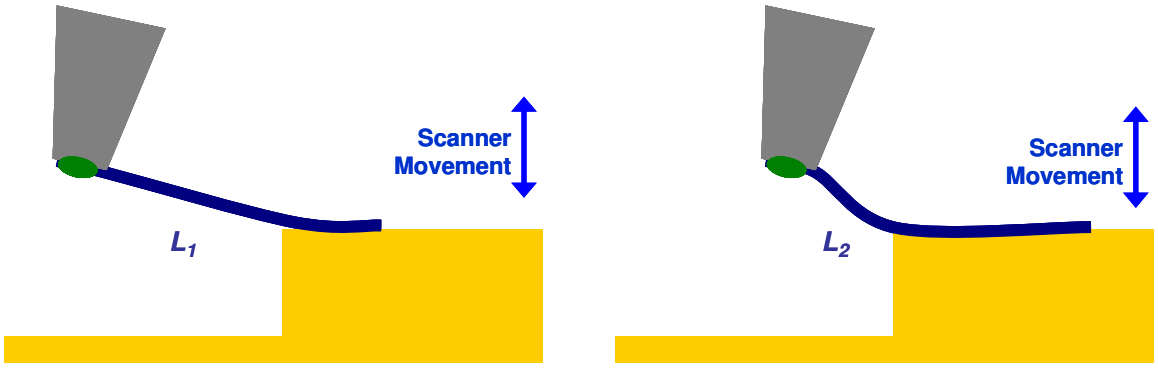

Figure 8.1. Schematic of experimental setup for measuring the mechanical and adhesive properties of any nanofiber. The nanofiber is fixed to a flattened AFM tip. By changing the length of the nanofiber between the AFM tip and the plateau, the contributions from the bending of the nanofiber could easily be deconvoluted. This would also change the amount of fiber in contact with the surface.

modulus of the nanofiber.

Measurements of adhesion can be made while varying the length of the nanofiber. The theory of peeling states that the amount in contact has no affect on the force required to peel a fixed area. This experimental setup would test that assumption. If peeling does occur, then the force per unit length required to peel would not be dependent on the length in contact. The duration that force occurs would be dependent on the length in contact. Conversely, if peeling does not occur, then according to JKR theory of adhesion, the contact area does matter. In this case, the magnitude of the measured force required to pull the fiber off the surface would increase with increasing length in contact. This experimental setup is designed to determine the force of adhesion per unit area whether the nanofiber peels or ruptures from the surface. Numerous interfaces could be interrogated by using nanofibers of varying composition and by changing the surface chemistry on the plateau.

A completely separate method of interrogating the adhesive properties per unit area could be accomplished by using alternating diblock copolymers as the probe molecule. Either isotactic or syndiotactic copolymers are acceptable, so long as the tacticity is well defined. These diblock copolymers can be synthesized with known lengths of each block, each with differing surface affinities. There are several synthetic routes to achieve this, including the so-called "click chemistry,"[358] reversible addition–fragmentation chain transfer (RAFT) polymerization,[359] or DNA.[360, 361] The greatest disadvantage of the first two methods lies in their separation. Gel permeation chromatography is the best method to separate polymers, but small differences in size are difficult to resolve. The separation of DNA, on the other hand, is straightforward using gel electrophoresis. Differences in length of a few bases can easily be resolved. The work by Herrmann and coworkers to create DNA diblock copolymers with a polydispersity approaching unity is very promising.[360-366] Their primary focus has been on the creation of DNA micelles, so the number of repeating units in their copolymers is

low. Their synthetic methods could be scaled up to make longer chains that would be more useful for investigating adhesion.

An even simpler method of synthesis of a DNA containing diblock copolymer is presented in Figure 8.2. Each end of the DNA is modified with different terminal chemistries. The simplest DNA to start with is single stranded DNA that is comprised of one base, e.g. thymine. Poly(thymine) has no secondary structure and, as a result, has uniform interactions with the surface. The other block unit can be any polymer that can be made in well defined blocks, e.g. poly(ethylene glycol) (PEG). The polymer would need to be modified with complementary end groups for reaction with the modified DNA. Polymerization proceeds via coupling reactions between the NHS and amine termini as well as between the thiol and maleimide termini. The addition of a chain-terminating molecule to the reaction increases the dispersity of the product, favoring shorter diblock copolymers. Products of varying number of repeating units should be separable by gel electrophoresis. Immersion of a gold-coated AFM probe into a solution containing the copolymer of the desired size should result in the immobilization of the polymer onto the tip. By using a specially designed cantilever with a single 70 nm diameter spot of gold near the apex of the tip, a single molecule with a thiol end group will bind to the probe tip. [74, 367, 368] The binding affinity of the thiol to the gold selects only the product with the thiol end group. This synthetic method uses commercially available compounds and takes full advantage the electrostatic property of DNA to separate the products by the number of DNA blocks in the molecule.

The main advantage of using DNA for force spectroscopic investigations is the numerous possibilities of surface interactions: van der Waals, polarity, hydrogen bonding, and electrostatics. By changing the ionic strength, pH, polarity, composition of the solution, and the surface chemistry, all of the intermolecular forces can be interrogated for both the DNA and the PEG blocks. A conceptual picture of using electrostatics to favor DNA binding to the surface is presented in Figure 8.3.

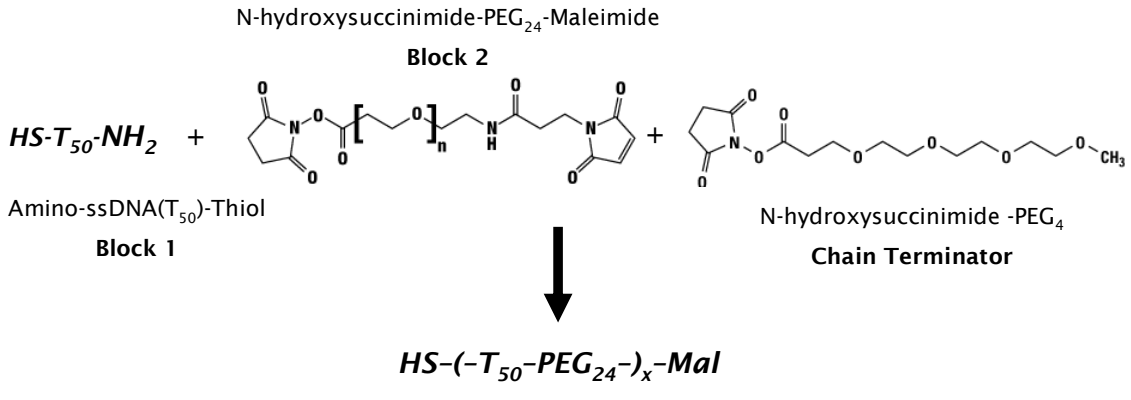

Figure 8.2. Reaction scheme to produce a diblock copolymer of DNA and PEG blocks. The reactants are mixed together, creating a large distribution of products. The amino and N-hydroxysuccinimide (NHS) end group react preferentially. The thiol and maleimide (Mal) end groups react preferentially. The first four products are non-terminating, and can continue to react to form longer chains. If the reaction is left to proceed until the reactive end groups are mostly consumed (~24 hr), the bottom two products are highly favored. The product in green is a loop of the diblock copolymer. The product in blue is the ideal final product, but any of the thiol-terminated products could be used as long as the number of repeating units is greater than two. The ratio of the chain-terminating group can be altered to adjust the probability of the lengths produced from the reaction.

The second advantage of this scheme is the production of blocks with known lengths. Again, by knowing the length in contact, the force per unit area can be estimated using either JKR or peeling theory. Currently the majority of research assumes desorption of a polymer occurs through rupture or friction.[40, 69, 138, 167, 369-372] The proposed use of a diblock copolymer is well suited to test these assumptions and investigate peeling. The force curve response will be able to distinguish between the peeling and friction, as friction should be unrelated to the length in contact. The length of the DNA and PEG blocks can be changed. By varying the length, the contact area will change. For the JKR model, this will increase the measured force. This should have no affect on friction. For peeling, the magnitude of the force should not change. Instead, the duration over which the force is measured should increase.

Finally, the chemical identity of the blocks can be changed. There are numerous options for the polymer block. The only limitation is that each block must be mono-disperse. For the DNA block, a progression is suggested. The above discussion focus on single stranded poly(thymine) because of the control it offers. The next step should use ssDNA that has multiple bases, e.g. poly(GGTCTAACTC). Other options could be made as long as the ssDNA does not self-dimerize or have any secondary structure. The data provided from this DNA should determine if the identity of the bases affects the measured forces. Depending upon the results, a third step would to be to use dsDNA. The ssDNA example from the second step, poly(GGTCTAACTC) could be used for this step after hybridization with its complement. This pair does form hetero-dimers where bases are left unmatched. This deficiency will always exist when using repeating segments of DNA. The drawback can be overcome by designing monomer units that contain a greater number of base pairs. This increases the probability that complete hybridization occurs. Collectively, this is a parametric study of the adhesive interactions of DNA and polymers with chemically modified surfaces.

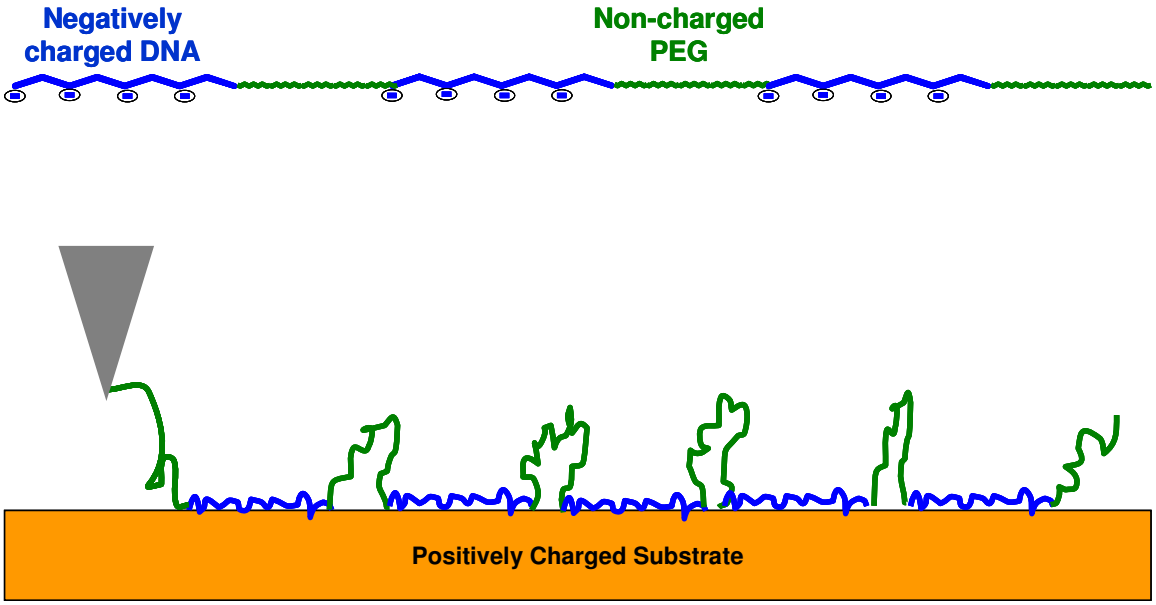

Figure 8.3. Illustration of a potential binding scenario of a DNA-PEG diblock copolymer. In this scenario, the electrostatic binding of DNA is favored by using a positively charged surface, and the solvation of the PEG is favored by using an appropriate solvent. The adhered portion of the diblock copolymer can either peel from the surface or rupture.

Recalling from Chapter 2, the angle of peeling significantly affects the measured peeling force. Kuhner et al. have shown that translocation of the AFM tip before the polymer is desorbed can result in very different force curves.[69] They attribute the changes of angle to friction and desorption, completely ignoring the real possibility of peeling. In their experiments, the polymers were comprised of only one type of monomer unit. This disadvantage to this method is that the angle must be estimated from the distance traveled by the AFM probe. There is no indication from their data that the angle is well known. Instead, they fit angle *and* an assumed rupture length *and* coefficient of friction to their data.

If the polymer peels during translocation of the probe, then the pull off angle has changed. As discussed in Chapter 6, the angle at which the forces are applied significantly affects the behavior of the molecule. The large advantage of the diblock copolymer proposed herein is the known lengths of each block. For any peeling angle, the length of the block in contact is the same, assuming that the conditions favor binding of one block over the other, e.g. electrostatics. By repeating the measurements at different unknown angles, the peeling angle alone can be determined from the force curve by comparing the measured forces. This provides a self-consistency check on the results. Alteration of the peeling angle can be accomplished by translocation of the cantilever or by using angled shims. The experiments using the diblock copolymer provide the necessary parameters to investigate all three major theories for modeling desorption: rupture, friction, and peeling. Additionally, the experiments serve as an excellent method to test the assumptions for each of the desorption theories.

The largest disadvantage of the above experimental method is that it must be performed in solution. MPFS has very poor amplitude resolution because of viscous damping of the cantilever. It may be possible to perform the experiments using static force spectroscopy, but performing the experiments using MPFS would allow for better monitoring of the conditions of the system as the molecule is pulled from the surface.

When a cantilever is placed in solution, the amplitude of thermal resonance frequency is damped by the viscous solutions and the quality factor decreases substantially. Tracking changes in resonance frequency becomes very difficult. If the noise floor could be significantly reduced, then MPFS may be capable of resolving changes in frequency in fluid. Improvements must be made to the MPFS instrumentation for it to become a fully viable force spectroscopic technique.

This amplitude resolution problem exists because MPFS is currently performed using a commercial AFM detection scheme. The vertical deflection signal of the position sensitive detector used in this study has a voltage range of ±2.5 V with a bit resolution of 76 μV. For a typical AFM cantilever, this voltage range equates to approximately ±350 nm of deflection 5 pm bit resolution. The limit of detection for a peak-to-peak oscillation is 15pm. Not surprisingly, the white noise floor occurs at 5 pm of amplitude in MPFS data. The large deflection range and bit resolution were designed for force spectroscopy in which large displacements occur. For small displacements, such a large range is unnecessary. If the range can be decreased, then the noise floor, i.e. the least significant bit, can be reduced. A costly solution is to increase the bit resolution of the analog-to-digital converter (ADC). The ADC used in this investigation is 16-bit. Using a 24-bit ADC would result in a least significant bit of 0.3 μV. If this change were to occur, it is reasonable to conclude that a PSD with better output resolution would also be required. If the PSD had an output resolution of 50 μV, there would be no significant gain by using an ADC with a higher bit resolution.

A less costly alternative would be to increase the path length of the laser after it reflects off the end of the cantilever. For a discrete displacement of the cantilever, the displacement of the laser spot at the PSD increases with increasing path length. The resolution of a PSD is also directly related to the intensity of the incident light. Increasing the intensity of the laser light may prevent any loss of resolution over longer path lengths. The final issue created by a longer path is the diffusion of the laser spot.

The laser used in this investigation is a diode laser, whose light is not collimated. The ideal solution to this problem would have a fiber optic capped with a collimating lens deliver the light right above the cantilever.

Without advances in the detection method for MPFS, its use as a force spectroscopic technique is limited to fluids with low viscous damping (i.e. air or vacuum). Even so, the applicability of MPFS is still broad. The ability to study nanomechanics without performing the experiments in an SEM is very advantageous and opens up the possibility of studying adhesive and mechanical properties on a wide array of nano-objects.

APPENDIX A

CUSTOM SOURCE CODE FOR DATA ANALYSIS

This appendix contains custom code written by the author to process and analyze different sets of data encountered throughout this investigation.

A.1 Batch Extraction for Dynamic Force Spectroscopy Files

This code, written in Visual Basic 6.0, converts raw data files containing both the deflection-distance and oscillation amplitude-distance curves from Veeco's NanoScope software (v5.31) into a comma separated variable (.csv) file format for ease of analysis in Excel™. This program was written to mimic the export to ASCII option from the NanoScope software with two much needed improvements: batch processing allowing multiple files to be extracted with a single command and .csv file extensions allowing Excel™ to open the files without any import steps.

FC DataExtractor 1024x2.exe

frmFVDE (FC DataExtractor 1024x2)

```
'Written by Kane Barker 01-13-2009
'
'Extracts all Nanoscope Tapping Mode Force Curve files, so long as
they
'   are 1024 data points and have Cantilever Deflection (CH 1)
'   and Oscillation Amplitude (CH 2)
'This program is to serve as an analog to using the Nanoscope
software to
'   manually export the data (in Volts) without the header

Option Explicit
Public strFileNames As Variant

Private Sub cmdExtract_Click()
Dim i As Integer
    'Sends each file the extraction module
    For i = 1 To UBound(strFileNames)
      Call DataExtractMacro(strFileNames(i))
    Next i
    'Resets defaults of program
    frmFVDE.cmdLoadFile.Caption = "Load File(s)..."
    List1.Clear
    frmFVDE.ProgressBar1.Visible = True
End Sub
```

```
'Below is code modified from Brian Matumbura found at
www.freevbcode.com
'It allows for batch processing
Private Sub cmdLoadFile_Click()
  Dim i As Integer
  'Obtains file list from GetFiles function
  strFileNames = Split(GetFiles, vbNullChar)
  'If only one file was selected, this places it in the correct
format
  'Note:  This only works if the file name is conventional:
[initials][6# date].[file#]
  If UBound(strFileNames, 1) = LBound(strFileNames, 1) Then
      strFileNames = Split(strFileNames(0) & vbNullChar &
Right(strFileNames(0), 12), vbNullChar)
  End If
  With List1
    'Adds files to list to show user which files have been
succesfully loaded
    If UBound(strFileNames) > 0 Then
      .Clear
      'Path is stored in index 0 of strFileNames, the files are in
index 1 to i
      Label1.Caption = "Files selected from: " & strFileNames(0)
      For i = 1 To UBound(strFileNames)
        .AddItem strFileNames(i)
      Next i
    'Let's user know if no files have been selected
    Else
      .AddItem "(No files selected)"
    End If
  End With
  cmdLoadFile.Caption = "File(s) Loaded!"
End Sub

Public Function GetFiles(Optional ByVal sTitle As String = "Open
files...") As String
  ' sTitle: Optional Title of Dialog
  Dim sFilenames As String
  Dim cdlOpen As Object
  On Error GoTo ProcError
  ' Get the desired name using the common dialog
  Set cdlOpen = CreateObject("MSComDlg.CommonDialog")
  ' set up the file open dialog file types
  With cdlOpen
    ' setting CancelError means the control will
    ' raise an error if the user clicks Cancel
    .CancelError = True
    .Filter = "All Files (*.*)|*.*"
    .FilterIndex = 1
    .DialogTitle = sTitle
    .MaxFileSize = &H7FFF ' 32KB filename buffer
    ' set up Common Dialog flags
    .Flags = cdlOFNHideReadOnly Or cdlOFNPathMustExist Or
cdlOFNLongNames Or cdlOFNAllowMultiselect Or cdlOFNExplorer
    .ShowOpen
    ' Adds the selected file(s) to the array
    sFilenames = .FileName
  End With
ProcExit:
  GetFiles = sFilenames
  Set cdlOpen = Nothing
  Exit Function
ProcError:
```

```
  If Err.Number = &H7FF3 Then Resume Next 'Cancel selected -
Ignore
  MsgBox Err.Description & "(" & Err.Number & ")", vbExclamation,
"Open error"
  sFilenames = ""
  Resume ProcExit
End Function
```

Module1 (FC DataExtractor 1024x2)

```
'Modified by Kane Barker From Original DataExtractor by Jeff
Boyles , 1/14/2009
Sub DataExtractMacro(datafile As Variant)

'Nominal Values for 1024x2 FC with 1024x2 Osc Amp
'Only works for Version 5.31 (because that's the only version
that
'   I had access to at the time (and had 1024 points)
'\Data offset: ?     <--Calculates from header
'\Data length: 4096

Dim zscanbyte(1 To 2048) As String
Dim binbyte(1 To 2048, 1 To 2) As String
Dim bintemp(1 To 2048, 1 To 2) As Integer
Dim header(1 To 500) As String
Dim DataOffset As String
Dim Zsens As String
Dim RampSize As String
Dim OffsetTrue As String
Dim SensTrue As String
Dim RampTrue As String
Dim temp As String
Dim datafile2 As String

frmFVDE.ProgressBar1.Min = 1
frmFVDE.ProgressBar1.Max = 8
frmFVDE.ProgressBar1.Visible = True
frmFVDE.ProgressBar1.Value = frmFVDE.ProgressBar1.Min

' Open file as text and get the header info
Open datafile For Input As #1

' Stores header text
    k = 1
    OffsetTrue = "\Data offset"
    SensTrue = "\@Sens. Zsca"
    RampTrue = "\@4:Ramp siz"
    Do Until EOF(1)
        Line Input #1, header(k)
        ' Searches for Header values, and then defines them for
use
        temp = Mid(header(k), 1, 12)
          If temp = OffsetTrue Then
            DataOffset = Mid(header(k), 15, 6)
          ElseIf temp = SensTrue Then
            Zsens = Mid(header(k), 18, 6)
          ElseIf temp = RampTrue Then
            RampSize = Mid(header(k), 52, 9)
```

```
          End If

          k = k + 1
        DoEvents
    Loop
Close #1
frmFVDE.ProgressBar1.Value = 2

'Stores the Z position calculated from header, assuming 1024
points
For i = 1 To 1024
    zscanbyte(i) = (i - 1) * RampSize * Zsens / 1024
    k = i + 1024
    zscanbyte(k) = (i - 1) * RampSize * Zsens / 1024
Next i

' Open file as Binary and get the data
Open datafile For Binary As #1
' Transposes and stores Force Curve Data
    j = 1
    For i = 1 To 2048
            Get #1, i * 2 - 1 + DataOffset - 4096, bintemp(i, j)
            binbyte(i, j) = CStr(bintemp(i, j))
            'In Tapping Mode, FC Data is stored using a 15-bit
conversion over a
            'FIXED 2.5 Volts.  This converts the bit value to
defl. voltage
            binbyte(i, j) = 2.5 * binbyte(i, j) / 32768
            DoEvents
    Next i
   frmFVDE.ProgressBar1.Value = 3
' Transposes and stores Oscillation Amplitude Data
    j = 2
    For i = 1 To 2048
            Get #1, i * 2 - 1 + DataOffset, bintemp(i, j)
            binbyte(i, j) = CStr(bintemp(i, j))
            'In Tapping Mode, OA Data is stored using a 16-bit
conversion over
            'NOMINAL 2.5 Volts.  This converts the bit value to
amp. voltage
            binbyte(i, j) = 2.5 * binbyte(i, j) / 65536
            DoEvents
    Next i
   frmFVDE.ProgressBar1.Value = 4
Close #1

'Stores data
    'Opens and renames file for printing the extracted data to a
.csv format
    datafile2 = Mid(datafile, 1, 8) & "_" & Mid(datafile, 10, 3)
& ".csv"
    Open datafile2 For Output As #1
    ' Prints header text
        'For i = 1 To k
            'Print #1, header(i)
            'DoEvents
        'Next i
```

```
        frmFVDE.ProgressBar1.Value = 5
    ' Prints column headers for data
        Print #1, "Calculated Z (nm),"; "TM Deflect. (V),";
"Amplitude (V)";
        Print #1,
        Print #1, "Extend Data";
        Print #1,
    ' Prints Approach Data Curves Inverted for Correct Order
        For i = 1 To 1024
            Print #1, zscanbyte(i); ",";
            For j = 1 To 2
                k = -1 * (i - 1025)
                Print #1, binbyte(k, j); ",";
                DoEvents
            Next j
            Print #1,
        Next i
        Print #1,
        Print #1, "Retract Data";
        Print #1,
        frmFVDE.ProgressBar1.Value = 7
    ' Prints Retract data for Version 5.31
        For i = 1025 To 2048
            Print #1, zscanbyte(i); ",";
            For j = 1 To 2
                Print #1, binbyte(i, j); ",";
                DoEvents
            Next j
            Print #1,
        Next i
        frmFVDE.ProgressBar1.Value = 8
    Close #1

'Call MsgBox("Data Extracted", vbOKOnly, "Success!")
frmFVDE.ProgressBar1.Visible = False
frmFVDE.ProgressBar1.Value = frmFVDE.ProgressBar1.Min

End Sub
```

A.2 Batch Extraction Program for Force Volume Files

These programs are based on a program written by Jeffrey Boyles that was limited in its use. The previous program only worked for Nanoscope software version 4.23. The programs presented below work with both versions of the Nanoscope software encountered in this investigation. The previous program required that force volume (FV) data be acquired with very specific user settings in the Nanoscope software. These specific settings are not referenced or explained by the previous author. The new

programs use information contained within the FV file header to determine the specific settings during data extraction.

Force volume data exists in two forms: 16x16 FV files and 32x32 FV files. Because the post-processing analysis is performed in Excel™, there are limitations in the number of columns available, i.e. 256. For 16x16 FV files, 256 columns are sufficient, but for 32x32 FV files, the data needs to be parsed into four different files that can then be analyzed. This requires the results to be reintegrated after analysis.

The code is written in Visual Basic 6.0 and is capable of extracting files in batch for both versions of the NanoScope software used with the NanoScope IIIa controller, v4.23 and v5.31.

A.2.1 FV Data Extractor for 16x16 FV Files

FV DataExtractor 16x16.exe

frmFVDE (FV DataExtractor 16x16)

```
'Written by Kane Barker 06-25-2007
'Extracts all Nanoscope Force Volume files, so long as they are
'  16x16 and 512x2

Option Explicit
Public strFileNames As Variant

Private Sub cmdExtract_Click()
Dim i As Integer
    'Sends each file the extraction module
    For i = 1 To UBound(strFileNames)
      Call DataExtractMacro(strFileNames(i))
    Next i
    'Resets defaults of program
    frmFVDE.cmdLoadFile.Caption = "Load File(s)..."
    List1.Clear
    frmFVDE.ProgressBar1.Visible = True
End Sub

'Below is code modified from Brian Matumbura found at
www.freevbcode.com
'It allows for batch processing
Private Sub cmdLoadFile_Click()
  Dim i As Integer
  'Obtains file list from GetFiles function
  strFileNames = Split(GetFiles, vbNullChar)
  'If only one file was selected, this places it in the correct
format
```

```
  'Note:  This only works if the file name is conventional:
[initials][6# date].[file#]
  If UBound(strFileNames, 1) = LBound(strFileNames, 1) Then
      strFileNames = Split(strFileNames(0) & vbNullChar &
Right(strFileNames(0), 12), vbNullChar)
  End If
  With List1
    'Adds files to list to show user which files have been
succesfully loaded
    If UBound(strFileNames) > 0 Then
      .Clear
      'Path is stored in index 0 of strFileNames, the files are
in index 1 to i
      Label1.Caption = "Files selected from: " & strFileNames(0)
      For i = 1 To UBound(strFileNames)
        .AddItem strFileNames(i)
      Next i
    'Let's user know if no files have been selected
    Else
      .AddItem "(No files selected)"
    End If
  End With
  cmdLoadFile.Caption = "File(s) Loaded!"
End Sub

Public Function GetFiles(Optional ByVal sTitle As String = "Open
files...") As String
  ' sTitle: Optional Title of Dialog
  Dim sFilenames As String
  Dim cdlOpen As Object
  On Error GoTo ProcError
  ' Get the desired name using the common dialog
  Set cdlOpen = CreateObject("MSComDlg.CommonDialog")
  ' set up the file open dialog file types
  With cdlOpen
    ' setting CancelError means the control will
    ' raise an error if the user clicks Cancel
    .CancelError = True
    .Filter = "All Files (*.*)|*.*"
    .FilterIndex = 1
    .DialogTitle = sTitle
    .MaxFileSize = &H7FFF ' 32KB filename buffer
    ' set up Common Dialog flags
    .Flags = cdlOFNHideReadOnly Or cdlOFNPathMustExist Or
cdlOFNLongNames Or cdlOFNAllowMultiselect Or cdlOFNExplorer
    .ShowOpen
    ' Adds the selected file(s) to the array
    sFilenames = .FileName
  End With
ProcExit:
  GetFiles = sFilenames
  Set cdlOpen = Nothing
  Exit Function
ProcError:
  If Err.Number = &H7FF3 Then Resume Next 'Cancel selected -
Ignore
```

```
  MsgBox Err.Description & "(" & Err.Number & ")", vbExclamation,
"Open error"
  sFilenames = ""
  Resume ProcExit
End Function
```

Module1 (FV DataExtractor 16x16)

```
'Copied and Modified by Kane Barker From Original DataExtractor
by Jeff Boyles , 6/25/2007
Sub DataExtractMacro(datafile As Variant)

'Nominal Values for 16x16 FVol and 512x2 FCurve
'\*Force image list
'\Data offset: ?     <--Calculates from header
'\Data length: 524288

Dim binbyte(1 To 1024, 1 To 256) As Integer
Dim header(1 To 500) As String
Dim DataOffset As String
Dim OffsetTrue As String
Dim temp As String
Dim version531 As String
Dim version423 As String

frmFVDE.ProgressBar1.Min = 1
frmFVDE.ProgressBar1.Max = 8
frmFVDE.ProgressBar1.Visible = True
frmFVDE.ProgressBar1.Value = frmFVDE.ProgressBar1.Min

' Open file as text and get the header info
Open datafile For Input As #1

' Stores header text
    k = 1
    z = 0
    OffsetTrue = "\Data offset"
    version531 = "531"
    version423 = "423"
    Do Until EOF(1)
        Line Input #1, header(k)
        ' Searches for \DataOffset, and then defines it
        temp = Mid(header(k), 1, 12)
          If temp = OffsetTrue Then
            DataOffset = Mid(header(k), 15, 6)
          End If
        'Compares versions to setup correct file placement
        temp = Mid(header(k), 14, 3)
          If temp = version531 Then
            z = 1
          ElseIf temp = version423 Then
            z = 2
          End If
          k = k + 1
        DoEvents
    Loop
Close #1
```

```
frmFVDE.ProgressBar1.Value = 2

' Open file as Binary and get the data
Open datafile For Binary As #1
' Transposes and stores first set of Curves
    For i = 1 To 512
        For j = 1 To 256
            Get #1, i * 2 + j * 2048 + DataOffset - 2049,
binbyte(i, j)
            DoEvents
        Next j
    Next i
   frmFVDE.ProgressBar1.Value = 3
' Transposes and stores second set of Curves
    For i = 513 To 1024
        For j = 1 To 256
            Get #1, i * 2 + j * 2048 + DataOffset - 2049,
binbyte(i, j)
            DoEvents
        Next j
    Next i
   frmFVDE.ProgressBar1.Value = 4
Close #1

'Upon version change from 4.23 to 5.31, the order of the force
curve data changed
'For 4.23, the data is stored retract and then approach
'For 5.31, the data is stored approach and then retract

'Stores data for version 5.31
If z = 1 Then
    'Opens and renames file for printing the extracted data
    Open datafile & "Extracted" For Output As #1
    ' Prints header text
        For i = 1 To k
            Print #1, header(i)
            DoEvents
        Next i
        frmFVDE.ProgressBar1.Value = 5
    ' Prints column headers for data
        Print #1,
        For i = 1 To 256
            Print #1, "#"; i; ",";
            DoEvents
        Next i
        Print #1,
        For i = 1 To 256
            Print #1, "retract"; ",";
            DoEvents
        Next i
        Print #1,
        frmFVDE.ProgressBar1.Value = 6
    ' Prints Retract Curve data for Version 5.31
        For i = 513 To 1024
            For j = 1 To 256
                Print #1, binbyte(i, j); ",";
                DoEvents
```

```
            Next j
            Print #1,
        Next i
        Print #1,
        Print #1,
        frmFVDE.ProgressBar1.Value = 7
    ' Prints ApproachCurve data for Version 5.31
        For i = 1 To 256
            Print #1, "approach"; ",";
            DoEvents
        Next i
        Print #1,
        For i = 1 To 512
            For j = 1 To 256
                Print #1, binbyte(i, j); ",";
                DoEvents
            Next j
            Print #1,
        Next i
        frmFVDE.ProgressBar1.Value = 8
    Close #1

'Stores data for version 4.23
ElseIf z = 2 Then
 'Opens and renames file for printing the extracted data
    Open datafile & "Extracted" For Output As #1
    ' Prints header text
        For i = 1 To k
            Print #1, header(i)
            DoEvents
        Next i
        frmFVDE.ProgressBar1.Value = 5
    ' Prints column headers for data
        Print #1,
        For i = 1 To 256
            Print #1, "#"; i; ",";
            DoEvents
        Next i
        Print #1,
        For i = 1 To 256
            Print #1, "retract"; ",";
            DoEvents
        Next i
        Print #1,
        frmFVDE.ProgressBar1.Value = 6
    ' Prints Retract Curve data for Version 4.23
        For i = 1 To 512
            For j = 1 To 256
                Print #1, binbyte(i, j); ",";
                DoEvents
            Next j
            Print #1,
        Next i
        Print #1,
        Print #1,
        frmFVDE.ProgressBar1.Value = 7
    ' Prints ApproachCurve data for Version 4.23
```

```
        For i = 1 To 256
            Print #1, "approach"; ",";
            DoEvents
        Next i
        Print #1,
        For i = 513 To 1024
            For j = 1 To 256
                Print #1, binbyte(i, j); ",";
                DoEvents
            Next j
            Print #1,
        Next i
        frmFVDE.ProgressBar1.Value = 8
    Close #1

'If neither version 5.31 or 4.23 were used, then the extraction
ends
'I, Kane, only had access to ver5.31 and 4.23, so I couldn't
determine how other versions stored force curve data
'Next User will need to determine how other versions behave
ElseIf z = 0 Then
    Call MsgBox("Incompatible Version of Nanoscope Software!",
vbOKOnly, "ERROR")
    Exit Sub
End If

'Call MsgBox("Data Extracted", vbOKOnly, "Success!")
frmFVDE.ProgressBar1.Visible = False
frmFVDE.ProgressBar1.Value = frmFVDE.ProgressBar1.Min

End Sub
```

A.2.2 FV Data Extractor for 32x32 FV Files

FV DataExtractor 32x32.exe

frmFVDE (FV DataExtractor 32x32)

```
'Written by Kane Barker 06-25-2007
'Extracts Nanoscope Force Volume files (32x32 and 512x2) into
four different files

Option Explicit
Public strFileNames As Variant

Private Sub cmdExtract_Click()
Dim i As Integer
    'Sends each file to be extracted
    For i = 1 To UBound(strFileNames)
      Call DataExtractMacro(strFileNames(i))
    Next i
    'Resets defaults of program
    frmFVDE.cmdLoadFile.Caption = "Load File(s)..."
    List1.Clear
    frmFVDE.ProgressBar1.Visible = False
```

```
End Sub

'Below is code modified from Brian Matumbura found at
www.freevbcode.com
'It allows for batch processing
Private Sub cmdLoadFile_Click()
  Dim i As Integer
  Dim temp As Variant
  strFileNames = Split(GetFiles, vbNullChar)
  'Corrects format if only one file was selected
  If UBound(strFileNames, 1) = LBound(strFileNames, 1) Then
      strFileNames = Split(strFileNames(0) & vbNullChar &
Right(strFileNames(0), 12), vbNullChar)
  End If
  'Adds files to List for user to see
  With List1
    If UBound(strFileNames) > 0 Then
      .Clear
      'Path is stored in index 0 of array files in index 1 to
i...
      Label1.Caption = "Files selected from: " & strFileNames(0)
      For i = 1 To UBound(strFileNames)
        .AddItem strFileNames(i)
      Next i
    'Let's user know if no files were selected
    Else
      .AddItem "(No files selected)"
    End If
  End With
  cmdLoadFile.Caption = "File(s) Loaded!"
End Sub

Public Function GetFiles(Optional ByVal sTitle As String = "Open
files...") As String
  ' sTitle: Optional Title of Dialog
  Dim sFilenames As String
  Dim cdlOpen As Object
  On Error GoTo ProcError
  ' Get the desired name using the common dialog
  Set cdlOpen = CreateObject("MSComDlg.CommonDialog")
  ' set up the file open dialog file types
  With cdlOpen
    ' setting CancelError means the control will raise an error
if the user clicks Cancel
    .CancelError = True
    .Filter = "All Files (*.*)|*.*"
    .FilterIndex = 1
    .DialogTitle = sTitle
    .MaxFileSize = &H7FFF ' 32KB filename buffer
    ' set up Common Dialog flags
    .Flags = cdlOFNHideReadOnly Or cdlOFNPathMustExist Or
cdlOFNLongNames Or cdlOFNAllowMultiselect Or cdlOFNExplorer
    .ShowOpen
    sFilenames = .FileName
  End With
ProcExit:
  GetFiles = sFilenames
```

```
  Set cdlOpen = Nothing
  Exit Function
ProcError:
  If Err.Number = &H7FF3 Then Resume Next 'Cancel selected -
Ignore
  MsgBox Err.Description & "(" & Err.Number & ")", vbExclamation,
"Open error"
  sFilenames = ""
  Resume ProcExit
End Function
```

Module1 (FV DataExtractor 32x32)

```
'Heavily modifiedfFrom DataExtractor by Jeff Boyles
Sub DataExtractMacro(datafile As Variant)

'Nominal Values for 16x16 FVol and 512x2 FCurve
'\*Force image list
'\Data offset: ?     <--Calculates while searching header
'\Data length: 2097152

Dim binbyte1(1 To 1024, 1 To 256) As Integer
Dim binbyte2(1 To 1024, 1 To 256) As Integer
Dim binbyte3(1 To 1024, 1 To 256) As Integer
Dim binbyte4(1 To 1024, 1 To 256) As Integer
Dim i, j, k, x, y, z As Integer
Dim header(1 To 500) As String
Dim DataOffset As String
Dim OffsetTrue As String
Dim temp As String
Dim version531 As String
Dim version423 As String

frmFVDE.ProgressBar1.Min = 1
frmFVDE.ProgressBar1.Max = 25
frmFVDE.ProgressBar1.Visible = True
frmFVDE.ProgressBar1.Value = frmFVDE.ProgressBar1.Min

' Open file as text and get the header info
Open datafile For Input As #1
' Stores header text
    k = 1
    q = 0
    OffsetTrue = "\Data offset"
    version531 = "531"
    version423 = "423"
    Do Until EOF(1)
        Line Input #1, header(k)
        ' Searches for DataOffset value, and defines it
        temp = Mid(header(k), 1, 12)
          If temp = OffsetTrue Then
            DataOffset = Mid(header(k), 15, 6)
          End If
        'Compares versions to setup correct file placement
        temp = Mid(header(k), 14, 3)
          If temp = version531 Then
            q = 1
```

```
          ElseIf temp = version423 Then
            q = 2
          End If
          k = k + 1
        DoEvents
    Loop
Close #1
frmFVDE.ProgressBar1.Value = 2

'Data is extracted in four 16x16 blocks as follows:
' 1   |   2
' ---------
' 3   |   4
'This allows for easy manipulation with previously existing Excel
macros

' Opens file as Binary to get the data for block #1
Open datafile For Binary As #1
' Transposes and stores first set of Curves
    For i = 1 To 512
        j = 1
        For y = 1 To 481
            For z = 1 To 16
                Get #1, i * 2 + (y + z - 1) * 2048 + DataOffset -
2049, binbyte1(i, j)
                j = j + 1
                DoEvents
            Next z
            y = y + 31
        Next y
    Next i
   frmFVDE.ProgressBar1.Value = 3
' Transposes and stores second set of Curves
    For i = 513 To 1024
        j = 1
        For y = 1 To 481
            For z = 1 To 16
                Get #1, i * 2 + (y + z - 1) * 2048 + DataOffset -
2049, binbyte1(i, j)
                DoEvents
                j = j + 1
            Next z
            y = y + 31
        Next y
    Next i
   frmFVDE.ProgressBar1.Value = 4
Close #1

' Opens file as Binary to get the data for block #2
Open datafile For Binary As #2
' Transposes and stores first set of Curves
    For i = 1 To 512
        j = 1
        For y = 17 To 497
            For z = 1 To 16
                Get #2, i * 2 + (y + z - 1) * 2048 + DataOffset -
2049, binbyte2(i, j)
```

```
                DoEvents
                j = j + 1
            Next z
            y = y + 31
        Next y
    Next i
   frmFVDE.ProgressBar1.Value = 5
' Transposes and stores second set of Curves
    For i = 513 To 1024
        j = 1
        For y = 17 To 497
            For z = 1 To 16
                Get #2, i * 2 + (y + z - 1) * 2048 + DataOffset -
2049, binbyte2(i, j)
                DoEvents
                j = j + 1
            Next z
            y = y + 31
        Next y
    Next i
   frmFVDE.ProgressBar1.Value = 6
Close #2

' Opens file as Binary to get the data for block #3
Open datafile For Binary As #3
' Transposes and stores first set of Curves
    For i = 1 To 512
        j = 1
        For y = 513 To 993
            For z = 1 To 16
                Get #3, i * 2 + (y + z - 1) * 2048 + DataOffset -
2049, binbyte3(i, j)
                DoEvents
                j = j + 1
            Next z
            y = y + 31
        Next y
    Next i
   frmFVDE.ProgressBar1.Value = 7
' Transposes and stores second set of Curves
    For i = 513 To 1024
        j = 1
        For y = 513 To 993
            For z = 1 To 16
                Get #3, i * 2 + (y + z - 1) * 2048 + DataOffset -
2049, binbyte3(i, j)
                DoEvents
                j = j + 1
            Next z
            y = y + 31
        Next y
    Next i
   frmFVDE.ProgressBar1.Value = 8
Close #3

' Opens file as Binary to get the data for block #4
Open datafile For Binary As #4
```

```
' Transposes and stores first set of Curves
    For i = 1 To 512
        j = 1
        For y = 529 To 1009
            For z = 1 To 16
                Get #4, i * 2 + (y + z - 1) * 2048 + DataOffset -
2049, binbyte4(i, j)
                DoEvents
                j = j + 1
            Next z
            y = y + 31
        Next y
    Next i
   frmFVDE.ProgressBar1.Value = 9
' Transposes and stores second set of Curves
    For i = 513 To 1024
        j = 1
        For y = 529 To 1009
            For z = 1 To 16
                Get #4, i * 2 + (y + z - 1) * 2048 + DataOffset -
2049, binbyte4(i, j)
                DoEvents
                j = j + 1
            Next z
            y = y + 31
        Next y
    Next i
   frmFVDE.ProgressBar1.Value = 10
Close #4

'Upon version change from 4.23 to 5.31, the order of the force
curve data changed
'For 4.23, the data is stored retract and then approach
'For 5.31, the data is stored approach and then retract

'Stores data for version 5.31
If q = 1 Then
    'Opens file and renames according to block for printing
    Open datafile & "Ext_1" For Output As #1
    ' Prints header text
        For i = 1 To k
            Print #1, header(i)
            DoEvents
        Next i
        frmFVDE.ProgressBar1.Value = 11
    ' Prints column headers for data
        Print #1,
        For i = 1 To 256
            Print #1, "#"; i; ",";
            DoEvents
        Next i
        Print #1,
        For i = 1 To 256
            Print #1, "retract"; ",";
            DoEvents
        Next i
        Print #1,
```

```
    frmFVDE.ProgressBar1.Value = 12
' Prints Retract Curve data
    For i = 513 To 1024
        For j = 1 To 256
            Print #1, binbyte1(i, j); ",";
            DoEvents
        Next j
        Print #1,
    Next i
    Print #1,
    Print #1,
    frmFVDE.ProgressBar1.Value = 13
' Prints Approach Curve data
    For i = 1 To 256
        Print #1, "approach"; ",";
        DoEvents
    Next i
    Print #1,
    For i = 1 To 512
        For j = 1 To 256
            Print #1, binbyte1(i, j); ",";
            DoEvents
        Next j
        Print #1,
    Next i
    frmFVDE.ProgressBar1.Value = 13
Close #1

Open datafile & "Ext_2" For Output As #2
'  Prints header text
    For i = 1 To k
        Print #2, header(i)
        DoEvents
    Next i
    frmFVDE.ProgressBar1.Value = 14
' Prints headers for column data
    Print #2,
    For i = 1 To 256
        Print #2, "#"; i; ",";
        DoEvents
    Next i
    Print #2,
    For i = 1 To 256
        Print #2, "retract"; ",";
        DoEvents
    Next i
    Print #2,
    frmFVDE.ProgressBar1.Value = 15
' Prints Retract Curve data
    For i = 513 To 1024
        For j = 1 To 256
            Print #2, binbyte2(i, j); ",";
            DoEvents
        Next j
        Print #2,
    Next i
    Print #2,
```

```
    Print #2,
    frmFVDE.ProgressBar1.Value = 16
' Prints Approach Curve data
    For i = 1 To 256
        Print #2, "approach"; ",";
        DoEvents
    Next i
    Print #2,
    For i = 1 To 512
        For j = 1 To 256
            Print #2, binbyte2(i, j); ",";
            DoEvents
        Next j
        Print #2,
    Next i
    frmFVDE.ProgressBar1.Value = 17
Close #2

Open datafile & "Ext_3" For Output As #3
' Prints header text
    For i = 1 To k
        Print #3, header(i)
        DoEvents
    Next i
    frmFVDE.ProgressBar1.Value = 18
' headers for data
    Print #3,
    For i = 1 To 256
        Print #3, "#"; i; ",";
        DoEvents
    Next i
    Print #3,
    For i = 1 To 256
        Print #3, "retract"; ",";
        DoEvents
    Next i
    Print #3,
    frmFVDE.ProgressBar1.Value = 19
' Retract Curves
    For i = 513 To 1024
        For j = 1 To 256
            Print #3, binbyte3(i, j); ",";
            DoEvents
        Next j
        Print #3,
    Next i
    Print #3,
    Print #3,
    frmFVDE.ProgressBar1.Value = 20
' Approach
    For i = 1 To 256
        Print #3, "approach"; ",";
        DoEvents
    Next i
    Print #3,
    For i = 1 To 512
        For j = 1 To 256
```

```
                Print #3, binbyte3(i, j); ",";
                DoEvents
            Next j
            Print #3,
        Next i
        frmFVDE.ProgressBar1.Value = 21
    Close #3

    Open datafile & "Ext_4" For Output As #4
    ' header text
        For i = 1 To k
            Print #4, header(i)
            DoEvents
        Next i
        frmFVDE.ProgressBar1.Value = 22
    ' headers for data
        Print #4,
        For i = 1 To 256
            Print #4, "#"; i; ",";
            DoEvents
        Next i
        Print #4,
        For i = 1 To 256
            Print #4, "retract"; ",";
            DoEvents
        Next i
        Print #4,
        frmFVDE.ProgressBar1.Value = 23
    ' Retract Curves
        For i = 513 To 1024
            For j = 1 To 256
                Print #4, binbyte4(i, j); ",";
                DoEvents
            Next j
            Print #4,
        Next i
        Print #4,
        Print #4,
        frmFVDE.ProgressBar1.Value = 24
    ' Approach
        For i = 1 To 256
            Print #4, "approach"; ",";
            DoEvents
        Next i
        Print #4,
        For i = 1 To 512
            For j = 1 To 256
                Print #4, binbyte4(i, j); ",";
                DoEvents
            Next j
            Print #4,
        Next i
        frmFVDE.ProgressBar1.Value = 25
    Close #4

'Stores data for version 4.23
ElseIf z = 2 Then
```

```
'Opens file and renames according to block for printing
Open datafile & "Ext_1" For Output As #1
' Prints header text
    For i = 1 To k
        Print #1, header(i)
        DoEvents
    Next i
    frmFVDE.ProgressBar1.Value = 11
' Prints column headers for data
    Print #1,
    For i = 1 To 256
        Print #1, "#"; i; ",";
        DoEvents
    Next i
    Print #1,
    For i = 1 To 256
        Print #1, "retract"; ",";
        DoEvents
    Next i
    Print #1,
    frmFVDE.ProgressBar1.Value = 12
' Prints Retract Curve data
    For i = 1 To 512
        For j = 1 To 256
            Print #1, binbyte1(i, j); ",";
            DoEvents
        Next j
        Print #1,
    Next i
    Print #1,
    Print #1,
    frmFVDE.ProgressBar1.Value = 13
' Prints Approach Curve data
    For i = 1 To 256
        Print #1, "approach"; ",";
        DoEvents
    Next i
    Print #1,
    For i = 513 To 1024
        For j = 1 To 256
            Print #1, binbyte1(i, j); ",";
            DoEvents
        Next j
        Print #1,
    Next i
    frmFVDE.ProgressBar1.Value = 13
Close #1

Open datafile & "Ext_2" For Output As #2
'  Prints header text
    For i = 1 To k
        Print #2, header(i)
        DoEvents
    Next i
    frmFVDE.ProgressBar1.Value = 14
' Prints headers for column data
    Print #2,
```

```
    For i = 1 To 256
        Print #2, "#"; i; ",";
        DoEvents
    Next i
    Print #2,
    For i = 1 To 256
        Print #2, "retract"; ",";
        DoEvents
    Next i
    Print #2,
    frmFVDE.ProgressBar1.Value = 15
' Prints Retract Curve data
    For i = 1 To 512
        For j = 1 To 256
            Print #2, binbyte2(i, j); ",";
            DoEvents
        Next j
        Print #2,
    Next i
    Print #2,
    Print #2,
    frmFVDE.ProgressBar1.Value = 16
' Prints Approach Curve data
    For i = 1 To 256
        Print #2, "approach"; ",";
        DoEvents
    Next i
    Print #2,
    For i = 513 To 1024
        For j = 1 To 256
            Print #2, binbyte2(i, j); ",";
            DoEvents
        Next j
        Print #2,
    Next i
    frmFVDE.ProgressBar1.Value = 17
Close #2

Open datafile & "Ext_3" For Output As #3
' Prints header text
    For i = 1 To k
        Print #3, header(i)
        DoEvents
    Next i
    frmFVDE.ProgressBar1.Value = 18
' headers for data
    Print #3,
    For i = 1 To 256
        Print #3, "#"; i; ",";
        DoEvents
    Next i
    Print #3,
    For i = 1 To 256
        Print #3, "retract"; ",";
        DoEvents
    Next i
    Print #3,
```

```
    frmFVDE.ProgressBar1.Value = 19
' Retract Curves
    For i = 1 To 512
        For j = 1 To 256
            Print #3, binbyte3(i, j); ",";
            DoEvents
        Next j
        Print #3,
    Next i
    Print #3,
    Print #3,
    frmFVDE.ProgressBar1.Value = 20
' Approach
    For i = 1 To 256
        Print #3, "approach"; ",";
        DoEvents
    Next i
    Print #3,
    For i = 513 To 1024
        For j = 1 To 256
            Print #3, binbyte3(i, j); ",";
            DoEvents
        Next j
        Print #3,
    Next i
    frmFVDE.ProgressBar1.Value = 21
Close #3

Open datafile & "Ext_4" For Output As #4
' header text
    For i = 1 To k
        Print #4, header(i)
        DoEvents
    Next i
    frmFVDE.ProgressBar1.Value = 22
' headers for data
    Print #4,
    For i = 1 To 256
        Print #4, "#"; i; ",";
        DoEvents
    Next i
    Print #4,
    For i = 1 To 256
        Print #4, "retract"; ",";
        DoEvents
    Next i
    Print #4,
    frmFVDE.ProgressBar1.Value = 23
' Retract Curves
    For i = 1 To 512
        For j = 1 To 256
            Print #4, binbyte4(i, j); ",";
            DoEvents
        Next j
        Print #4,
    Next i
    Print #4,
```

```
        Print #4,
        frmFVDE.ProgressBar1.Value = 24
    ' Approach
        For i = 1 To 256
            Print #4, "approach"; ",";
            DoEvents
        Next i
        Print #4,
        For i = 513 To 1024
            For j = 1 To 256
                Print #4, binbyte4(i, j); ",";
                DoEvents
            Next j
            Print #4,
        Next i
        frmFVDE.ProgressBar1.Value = 25
    Close #4

'If neither version 5.31 or 4.23 were used, then the extraction
ends
'I, Kane, only had access to ver5.31 and 4.23, so I couldn't
determine how other versions stored force curve data
'Next User will need to determine how other versions behave
ElseIf q = 0 Then
    Call MsgBox("Incompatible Version of Nanoscope Software!",
vbOKOnly, "ERROR")
    Exit Sub
End If

'Call MsgBox("Data Extracted", vbOKOnly, "Success!")
frmFVDE.ProgressBar1.Visible = False
frmFVDE.ProgressBar1.Value = frmFVDE.ProgressBar1.Min

End Sub
```

A.3 Matlab™ Code for Calculating the Spring Constant of a Cantilever Using the Equipartition Theorem

This program was written to correctly fit the equipartition theorem to the thermal resonance data of any AFM cantilever. This program fits a small, user-defined range for the white noise and then user-defined ranges for the 1/*f* noise. The user is then given the opportunity to verify the fit of the noise to the PSD data. The user then selects the appropriate window for fitting a Lorentzian model for simple harmonic oscillators to the data. The code uses the mathematical relationship between the base amplitude, the peak amplitude at the resonance frequency, and the amplitude scaling factor so that only one

value is adjusted by the user: the amplitude scaling factor. Once the initial parameters are set, the program outputs figures that compare the fit with the raw data for both a window around the resonance peak and the full PSD range.

kb_thermalfit.m

```
%The program is designed to fit WF data to the equipartition
method.
%Previous methods tried fitting data to 1/f, white noise and SHO
in one fit
%This program fits 1/f and white noise, then fits that combined
with SHO
%This program also corrects the error in summing all three, as
Hutter & Boechoffer clearly state that application of the
equipartition method should only include SHO (i.e. noise should
be subtracted)
%The goal of this program is to allow fitting of all spring
constants
%This program is not yet optimized to fit WF from compression
studies

%Program by Kane Barker, Geogia Tech, October 2008

clear;
clc;
format long e;

%Asks User to select the previously processed WF Matlab file
(from kb1 or jb1)
%and then loads it into the workspace:  WF HM SM bdwth dtime freq
wft
[fname,pname]=uigetfile('*.mat','Load Matlab WF data');
if fname==0;return;end;
disp(fname)
load([pname,fname]);

%Loads detector sensitivity, then corrects for 0.825 Gain from
base to
%Nanoscope Controller and converts from V/nm to V/m
sensitivity=input('Enter the detector sensitivity (V/nm): ','s');
sensitivity=str2double(sensitivity);
sens=1.21e9*sensitivity;

%Loads Pre-Amp gain; if no pre-amp was used, gain is 1
gain=input('Enter the gain: ','s');
gain=str2double(gain);

%Converts WF data from dB to m*Hz^-0.5
WF_SI=(sqrt(2)*10.^((WF)./20))/sens;
fkHz=freq./1000;
fstep=fkHz(2,1);

%Asks User to select ranges for noise fitting range
clc;
```

```
disp('The following will be used to fit background noise white
noise.');
disp('The best approximation for white noise is far from
resonance and 1/f contributions, e.g. 395 kHz.');
whnoise=input('Enter the central value for a 6 kHz zone for white
noise (kHz): ');
%Sets bounds for 6 kHz zone
    l_lim=floor(((whnoise-3)-rem(whnoise,fstep))/fstep+1);
    u_lim=ceil(((whnoise+3)-rem(whnoise,fstep))/fstep+1);
    %Stores value of white noise for first waterfall
    %As of right now, only the first waterfall is fit
    C0=mean(WF_SI(l_lim:u_lim,1));
%Fitting zones should include three low freq zones (1/f)
%Preallocation of variables
freq_ns=zeros(1,size(freq,2));
fkHz_ns=zeros(1,size(fkHz,2));
WF_SI_ns=zeros(1,size(WF_SI,2));
disp('The following will be used to fit background noise to the
1/f component.');
disp('It is highly recommended that the three ranges are low in
frequency, but avoid any resonance peaks, e.g. 4, 12, 20 kHz.');
for i=1:3
    hold off;
    plot(fkHz,WF(:,1));
    xlabel('Frequency (kHz)');
    title('Waterfall');
    ylabel('dB');
    fnoise=input('Enter the central value for a 6 kHz zone to
help fit 1/f noise (kHz): ');
    %Sets bounds for 6 kHz zone
    l_lim=floor(((fnoise-3)-rem(fnoise,fstep))/fstep+1);
    u_lim=ceil(((fnoise+3)-rem(fnoise,fstep))/fstep+1);
    %Moves data of interest into temp arrays
    freq_tmp(:,:,i)=freq(l_lim:u_lim,:);
    fkHz_tmp(:,:,i)=fkHz(l_lim:u_lim,:);
    WF_SI_tmp(:,:,i)=WF_SI(l_lim:u_lim,:);
    %Concatenates each temp array into arrays for noise fit
    freq_ns=[freq_ns;freq_tmp(:,:,i)];
    fkHz_ns=[fkHz_ns;freq_tmp(:,:,i)];
    WF_SI_ns=[WF_SI_ns;WF_SI_tmp(:,:,i)];
end

%Removes extra row created during preallocation/concatenation
freq_ns=freq_ns(2:size(freq_ns,1),:);
fkHz_ns=fkHz_ns(2:size(fkHz_ns,1),:);
WF_SI_ns=WF_SI_ns(2:size(WF_SI_ns,1),:);

%Normalizes Amplitude data for curve fitting
WF_SI_ns(:,1)=WF_SI_ns(:,1)/C0;

%Sets the initial guesses and bounds of the fitting routine
NOISE_init=[1, 1.5];
lb=[1e-14,1.0];
ub=[1e5,2.0];
options = optimset('maxiter',1000,'TolX',1e-15,'tolfun',1e-
15,'maxfunevals',3000,'tolcon',1e-15,'display','off');
```

```
%Performs the optimization
[NOISE,resnorm,void,exitflag] =
lsqcurvefit(@kb_thermalfit_noise,NOISE_init,freq_ns,WF_SI_ns(:,1)
,lb,ub,options,1);
if exitflag<0
    figure
    a=get(0,'screensize');
    set(gcf,'position',[10+a(1),10+a(2),a(3)-100,a(4)-100])
    plot([-1,1],[0,1],'color','red')
    text(0,0.75,'\bf\fontsize{20}WARNING: OPTIMIZATION TERMINATED
UNSUCESSFULLY','horizontalalignment','center')
    text(0,0.5,'\bf\fontsize{20}CHECK RESULTS
CAREFULLY','horizontalalignment','center')
    text(0,0.2,'\bf\fontsize{15}TRY TO GET INITIAL GUESSES CLOSER
TO CURVE','horizontalalignment','center','color','b')
    if exitflag==0
        text(0,0.15,'\bf\fontsize{15}AND/OR INCREASE NUMBER OF
FUNCTION CALLS','horizontalalignment','center','color','b')
    end
    axis off
    set(gcf,'color','red')
    return
end

%Rescales data
WF_SI_ns(:,1)=WF_SI_ns(:,1)*C0;
NOISE(1)=NOISE(1)*C0;

%Saves output parameters for later use
C1=NOISE(1);
C2=NOISE(2);

%Plots noise fit to compare with data
WF_ns_fit=zeros(length(freq),1);
for i=1:length(freq)
    WF_ns_fit(i,1)=C0+(C1./(freq(i,1).^C2));
end
semilogy(freq_ns,WF_SI_ns(:,1),'r.');
hold on
semilogy(freq,WF_ns_fit(:,1),'b');
hold off

%Verifies with user if fit is adequate
clc;
disp('Check plot for fit.  If this is unnacceptable, break
(Ctrl+c) the program and vary the fitting inputs.');
disp('Otherwise press any key to continue.');
pause;

    %Program now moves into fitting SHO with noise parameters
%Asks User to input SHO fitting range
plot(fkHz,WF(:,1));
xlabel('Frequency (kHz)');
title('Waterfall');
ylabel('dB');
clc;
```

```
disp('The following will be used to fit the WF data to SHO and
previous noise fit');
fmin=input('Enter the lower frequency limit (kHz): ');
fmax=input('Enter the upper frequency limit (kHz): ');

%Reduces data sets to fitting range
lowlim=floor((fmin-rem(fmin,fstep))/fstep+1);
uplim=ceil((fmax-rem(fmax,fstep))/fstep+1);
freq_red=freq(lowlim:uplim,:);
fkHz_red=fkHz(lowlim:uplim,:);
WF_red=WF(lowlim:uplim,:);
WF_SI_red=WF_SI(lowlim:uplim,:);

plot(fkHz_red,WF_red(:,1));
xlabel('Frequency (kHz)');
title('Waterfall reduced for Fitting');
ylabel('dB?');

%Fail/check for user inputs
verify=input('These values will be used as bounds for the fitting
routine.  Are they correct? (y/n)?  ','s');
    while verify~='y'
        clc;
        disp('The following will be for fitting the WF data to
SHO');
        fmin=input('Enter the lower frequency limit (kHz): ');
        fmax=input('Enter the upper frequency limit (kHz): ');
        lowlim=floor((fmin-rem(fmin,fstep))/fstep+1);
        uplim=ceil((fmax-rem(fmax,fstep))/fstep+1);
        freq_red=fkhz(lowlim:uplim,:);
        WF_red=WF(lowlim:uplim,:);
        WF_SI_red=WF_SI(lowlim:uplim,:);
        plot(fkHz_red,WF_red(:,1));
        xlabel('Frequency (kHz)');
        title('Waterfall reduced for Fitting');
        ylabel('dB?');
        verify=input('These values will be used as bounds for the
fitting routine.  Are they correct? (y/n)?  ','s');
    end

%User now goes through steps to set initial fitting parameters
clc;
G_init=input('Enter a first approximation for gamma: ');
%Stores max amplitude from data
peak_amp=max(WF_SI_red(:,1));
%Loactes resonance frequency from max amplitude
imax=find(WF_SI_red(:,1)==peak_amp);
ResFreq_init=freq_red(imax,1);
%Calculates noise value of amplitude
Noise_resfreq=(C0-(C1/(ResFreq_init^C2)));
%Uses covariance of gamma and base amplitude for SHO to set
initial base amplitude
Amp_init=(peak_amp-Noise_resfreq)/G_init;

%Creates fit based on initial guesses
WF_SI_init=zeros(length(freq_red),1);
for i=1:length(freq_red)
```

```
    WF_SI_init(i,1)=(C0-
Amp_init)+(C1/(freq_red(i,1)^C2))+Amp_init*ResFreq_init^2*((ResFr
eq_init^2-
(freq_red(i,1)^2))^2+(((ResFreq_init^2)*((freq_red(i,1)^2)))/G_in
it^2))^-.5;
end

%Plots for comparison
semilogy(freq_red,WF_SI_red(:,1),'r.');
hold on
semilogy(freq_red,WF_SI_init(:,1),'b');
hold off

%User must adjust gamma guess so that initial guess is a better
fit
verify=input('These values will be used as bounds for the SHO
fitting routine.  Are they close enough? (y/n)?  ','s');
    while verify~='y'
        G_init=input('Enter an adjusted approximation for gamma:
');
        peak_amp=max(WF_SI_red(:,1));
        imax=find(WF_SI_red(:,1)==peak_amp);
        ResFreq_init=freq_red(imax,1);
        Noise_resfreq=(C0-(C1/(ResFreq_init^C2)));
        Amp_init=(peak_amp-Noise_resfreq)/G_init;
        for i=1:length(freq_red)
            WF_SI_init(i,1)=(C0-
Amp_init)+(C1/(freq_red(i,1)^C2))+Amp_init*ResFreq_init^2*((ResFr
eq_init^2-
(freq_red(i,1)^2))^2+(((ResFreq_init^2)*((freq_red(i,1)^2)))/G_in
it^2))^-.5;
        end
        semilogy(freq_red,WF_SI_red(:,1),'r.');
        hold on
        semilogy(freq_red,WF_SI_init(:,1),'b');
        hold off
        verify=input('These values will be used as bounds for the
SHO fitting routine.  Are they close enough? (y/n)?  ','s');
    end

%Normalizes Amplitude data for curve fitting
WF_SI_red(:,1)=(WF_SI_red(:,1))/C0;

%Sets the initial guesses and bounds of the fitting routine.
SHO_init=[peak_amp/C0,ResFreq_init,G_init];
lb=[SHO_init(1)*.99,ResFreq_init*.95,G_init*.1];
ub=[SHO_init(1)*1.01,ResFreq_init*1.05,G_init*5];
options = optimset('maxiter',100,'TolX',1e-30,'tolfun',1e-
30,'maxfunevals',3000,'tolcon',1e-30,'display','off');

%Performs the optimization
[SHO,resnorm,void,exitflag] =
lsqcurvefit(@kb_thermalfit_sho,SHO_init,freq_red,WF_SI_red(:,1),l
b,ub,options,1,C1/C0,C2);
if exitflag<0
    figure
    a=get(0,'screensize');
```

```
    set(gcf,'position',[10+a(1),10+a(2),a(3)-100,a(4)-100])
    plot([-1,1],[0,1],'color','red')
    text(0,0.75,'\bf\fontsize{20}WARNING: OPTIMIZATION TERMINATED
UNSUCESSFULLY','horizontalalignment','center')
    text(0,0.5,'\bf\fontsize{20}CHECK RESULTS
CAREFULLY','horizontalalignment','center')
    text(0,0.2,'\bf\fontsize{15}TRY TO GET INITIAL GUESSES CLOSER
TO CURVE','horizontalalignment','center','color','b')
    if exitflag==0
        text(0,0.15,'\bf\fontsize{15}AND/OR INCREASE NUMBER OF
FUNCTION CALLS','horizontalalignment','center','color','b')
    end
    axis off
    set(gcf,'color','red')
    return
end

%Rescale the data
WF_SI_red(:,1)=WF_SI_red(:,1)*C0;
SHO(1)=SHO(1)*C0;
%SHO(3)=SHO(3)*SHO_init(1);
Ns_Res=(C0-(C1/(SHO(2).^C2)));
Bs_amp=(SHO(1)-Ns_Res)/SHO(3);

%Calculate the fitted data in the data_reduced range
for i=1:length(freq_red)
    WF_SHO_fit(i,1)=(C0-
Bs_amp)+(C1/(freq_red(i,1)^C2))+Bs_amp*SHO(2)^2*((SHO(2)^2-
(freq_red(i,1)^2))^2+(((SHO(2)^2)*((freq_red(i,1)^2)))/SHO(3)^2))
^-.5;
end

%Calculate the fitted data for full range
for i=1:length(freq)
    WF_SHO_fullfit(i,1)=(C0-
Bs_amp)+(C1/(freq(i,1)^C2))+Bs_amp*SHO(2)^2*((SHO(2)^2-
(freq(i,1)^2))^2+(((SHO(2)^2)*((freq(i,1)^2)))/SHO(3)^2))^-.5;
    SHO_LRAM(i,1)=(freq(10,1)-
freq(9,1))*(Bs_amp*SHO(2)^2*((SHO(2)^2-
(freq(i,1)^2))^2+(((SHO(2)^2)*((freq(i,1)^2)))/SHO(3)^2))^-
.5).^2;
end
%Integrates/sums fit data to simple harmonic oscillator ONLY
%This subtracts background noise components
tol=1e-30;
X2_1=quad(@SHO_summation,0.1,399999.9,tol,[],SHO);
X2_2=quadl(@SHO_summation,0.1,399999.9,tol,[],SHO);
X2_3=sum(SHO_LRAM(:,1));

%Boltzmann constant
k_b=1.38e-23;
%Typical temperature of AFM lab, Kelvin
T=295;

%Solves each integration method for spring constant; used to
check validity
%of integration methods
```

```
k1=(k_b*T*(gain^2))/(0.75*X2_1);
k2=(k_b*T*(gain^2))/(0.75*X2_2);
k3=(k_b*T*(gain^2))/(0.75*X2_3);

%Sets critical parameters to easily accessible variables
K=[k1,k2,k3];
Gamma=SHO(3);
Qf=SHO(3)/sqrt(3);
Amp_base=Bs_amp;
PeakFreq=SHO(2);

semilogy(freq_red,WF_SI_red(:,1),'r.');
hold on
semilogy(freq_red,WF_SHO_fit,'b');
hold off
xlabel('\bf\fontsize{12}Frequency (Hz)')
ylabel('\bf\fontsize{12}Amplitude (m-Hz^{-1/2})')
title('\bf\fontsize{16}Reduced Thermal Spectra Fit')
patch(freq_red(1,1),0,'white');
patch(freq_red(1,1),0,'white');
patch(freq_red(1,1),0,'white');
patch(freq_red(1,1),0,'white');
patch(freq_red(1,1),0,'white');
legend('Sensitivity-Scaled Amplitude','OPTIMIZED MODEL',...
    ['Amplitude = ',num2str(SHO(1)/SHO(3)),' m-Hz^{-1/2}'],...
    ['f_{res} = ',num2str(SHO(2)),' Hz'],['Gamma =
',num2str(SHO(3))],['{\itk} = ',num2str(k1),' N/m'],...
    ['\midResiduals\mid = ',num2str(resnorm)]);

clc;
disp('Adjust plot to save as a picture.');
disp('Press any key to continue.');
pause;

%Will save same folder as original data
save1=input('Save data as? ','s');
save
([pname,save1],'K','Gamma','Qf','Amp_base','PeakFreq','C0','C1','
C2','freq*','WF*','SHO');
saveas (gcf, [pname,save1], 'tiffn');

semilogy(freq,WF_SI(:,1),'r.');
hold on
semilogy(freq,WF_SHO_fullfit,'b');
hold off
xlabel('\bf\fontsize{12}Frequency (Hz)')
ylabel('\bf\fontsize{12}Amplitude (m-Hz^{-1/2})')
title('\bf\fontsize{16}Reduced Thermal Spectra Fit')
patch(freq_red(1,1),0,'white');
patch(freq_red(1,1),0,'white');
patch(freq_red(1,1),0,'white');
patch(freq_red(1,1),0,'white');
patch(freq_red(1,1),0,'white');
legend('Sensitivity-Scaled Amplitude','OPTIMIZED MODEL',...
    ['Amplitude = ',num2str(SHO(1)/SHO(3)),' m-Hz^{-1/2}'],...
    ['f_{res} = ',num2str(SHO(2)),' Hz'],['Gamma =
',num2str(SHO(3))],['{\itk} = ',num2str(k1),' N/m'],...
```

```
    ['\midResiduals\mid = ',num2str(resnorm)]);

clc;
disp('Adjust plot to save as a picture.');
disp('Press any key to continue.');
pause;

saveas (gcf, [pname,save1,'full'], 'tiffn');
```

kb_thermalfit_noise.m

```
%Function for thermal noise fit to determine beam parameters
%NOTES: c0=white noise (C0), noise(1)=1/f constant (C1),
noise(2)=exponent of 1/f (C2)

function F = kb_thermalfit_noise(noise,freq_ns,c0)

    F=c0+(noise(1)./(freq_ns.^noise(2)));
```

kb_thermalfit_sho.m

```
%Objective function for thermal noise fit to determine noise
background
%NOTES: c0=white noise, c1=1/f constant, c2=exponent of 1/f,
    %sho(1)=peak amplitude of resonance frequency, sho(2)=
resonance
    %frequency, sho(3)=Gamma (i.e. amplitude scaling factor)
%Base amplitude is fit by using the covariance between gamma and
base
%amplitude, that is that gamma times base amplitude equals max
amplitude at
%the resonance frequency (minus the noise at the res freq)
%This method should help ensure that a correct base amplitude is
fit,
%ignoring the magnitude of difference between C0 and the base
amplitude

function F = kb_thermalfit_sho(sho,freq_red,c0,c1,c2)

%Commented out: initially tried fitting data by subtracting noise
from data--obvious errors
    %F=sho(1)*sho(2)*((sho(2)^2-
(freq_red.^2)).^2+(((sho(2)^2)*((freq_red.^2)))/sho(3)^2)).^(-
.5);

    F=(c0-((sho(1)-(c0-
(c1/(sho(2)^c2))))/sho(3)))+(c1./(freq_red.^c2))+((sho(1)-(c0-
(c1/(sho(2)^c2))))/sho(3))*sho(2)^2*((sho(2)^2-
(freq_red.^2)).^2+(((sho(2)^2)*((freq_red.^2)))/sho(3)^2)).^(-
.5);
```

SHO_summation.m

```
%Function for summing thermal fit to determine beam parameters
%NOTES: sho(1)=Max Amp at Res Freq, sho(2)=Res Freq,
sho(3)=Amplitude scaling factor
```

```
function P=SHO_summation(x,sho)

    P=((sho(1)/sho(3))*sho(2)^2*((sho(2)^2-
(x.^2)).^2+(((sho(2)^2)*((x.^2)))/sho(3)^2)).^(-.5)).^2;
```

APPENDIX B

MECHANICAL PROPERTIES OF ELECTROSPUN FIBERS

This appendix contains a description of work performed to investigate the elastic modulus of electrospun poly(methyl methacrylate), PMMA, fibers. This work was done in collaboration with Matija Crne (Georgia Institute of Technology, May 2009), who supplied the electrospun fibers.

B.1 Introduction

Nanoindentation is commonly used to evaluate the modulus of a variety of materials, including fibers.[320, 374-376] This method uses an AFM tip to apply a load sufficient to deform the sample. The elastic modulus of the sample can be calculated from the applied load versus deformation displacement using the Hertz theory of contact mechanics. Although this method may appear straight forward, several experimental parameters have to be addressed. Nanoindentation, by definition, only measures the local elastic modulus. Nanoindentation experiments must be carried out at many different locations for the results to be a statistically valid sample. The physical and mechanical parameters of the AFM probe also contribute to the accuracy of this method. To accurately know the applied load, the spring constant of the cantilever must be accurately measured. Proper interpretation of the displacement from deformation requires that the geometry of the AFM tip be well characterized and unchanging over the duration of the experiments. As Clifford and Seah point out, these accumulated uncertainties can lead to gross inaccuracies in the measured values of the elastic modulus.[320] Their work also shows the limits of nanoindentation: less than half of the samples they measured using the nanoindentation method returned comparable values to those determined with bulk techniques.

Another common method for measuring the elastic modulus of a fiber involves deformation displacement of the fiber suspended over a gap.[325] The elastic modulus is calculated from the applied load versus change in deflection of the suspended fiber, i.e. bridge, using Euler-Bernoulli beam theory. This method has several different experimental designs for creating nanoscale bridges. Two of the more common are to lay down many fibers over a substrate with mesopores[233, 300, 311, 377] or small trenches.[290, 310, 324, 334-336, 378-381] With either substrate, some fibers cross over the gaps, and the AFM is used to push on several different points of the bridge. Euler-Bernoulli beam theory is applied to interpret the results. The commonly used solution of this theory operates under the assumption that the applied load is a point source with respect to the length of the beam and that the fiber is fixed on both ends. In many instances, the fiber was not anchored to the substrate other than through adhesive interactions between the fiber and substrate.[300, 324, 334-336] These authors applied a solution of the Euler-Bernoulli beam theory to interpret the data, even though this solution of the theory assumes that the fiber is clamped on both ends. When the fiber is not clamped in place, then the bridge has some rotational freedom. In this situation, alternative solutions to the Euler-Bernoulli beam theory, such as pinned-pinned or simply supported, should be applied to interpret the results.[325] Also, if the force required to bend the bridge is enough to cause the fiber to slip free from the adhesion, the bridge can sink down into the trench. A completely different model is required to calculate the elastic modulus. This is especially problematic when the substrate has a high density of mesopores[300, 377] or small plateaus for the fiber to adhere to.[334, 336]

Another problem with these methods is the convolution of local deformation of the fiber with the overall bending of the bridge. This rises from the use of sharp AFM tips which can indent the local area of the fiber.[290] A sharp AFM tip also only makes contact with a portion of bridge, so it is possible that shearing forces could be convoluted within the force response.[382] Contact between a sharp AFM tip and the fiber may not

occur at the apex of the fiber. It is possible that the AFM tip makes contact with the side of the fiber. This would result in horizontal forces being applied to the bridge. Several groups have tried to overcome these limitations by flattening the AFM tip.[335, 378] This reduces the amount of indentation, but also changes the area of the applied load. The applied load from a flattened AFM tip is not point source, even though the authors applied models that assumed point sources. The approach in this investigation of a PMMA fiber is designed to address all of the concerns for the bridge method, ensuring the validity of the results.

B.2 Results

Silicon substrates with trenches etched into the surface, as described in Chapter 4.6, are used as substrates. A nano-fiber/tube/rod (henceforth nanofiber) is placed onto the substrate so that a portion of the nanofiber forms a bridge over a trench. In this experiment, the nanofibers are electrospun PMMA fibers. The nanofibers are clamped onto the surface by depositing platinum using focused ion beam (FIB) deposition, as seen in Figure B.1. A modified AFM tip was fabricated by milling with FIB; the process is demonstrated in Figure B.2. The tips were milled to be hemi-cylindrical at the point of contact with the fiber. The dimensions of the hemi-cylinder are 50 nm radius of curvature and 1 μm long. The advantage of a hemi-cylindrical tip over a sharp tip is that local deformation at contact with a nanofiber is minimized. The sculpted AFM tip is then brought into contact at several different points along the span of the nanofiber; force volume imaging mode was used to record the force curves as a function of position, apparent in Figure B.3. The value of the slope as a function of the distance across the span of the fiber was extracted from this data. The spring constant of the fiber-cantilever system was determined by comparing the slope of the deflection of the cantilever, i.e. the sensitivity, on both the fiber and a hard surface, as described in Chapter 4.3. Figure B.4 displays a comparison between two deflection-distance curves taken from the FV image

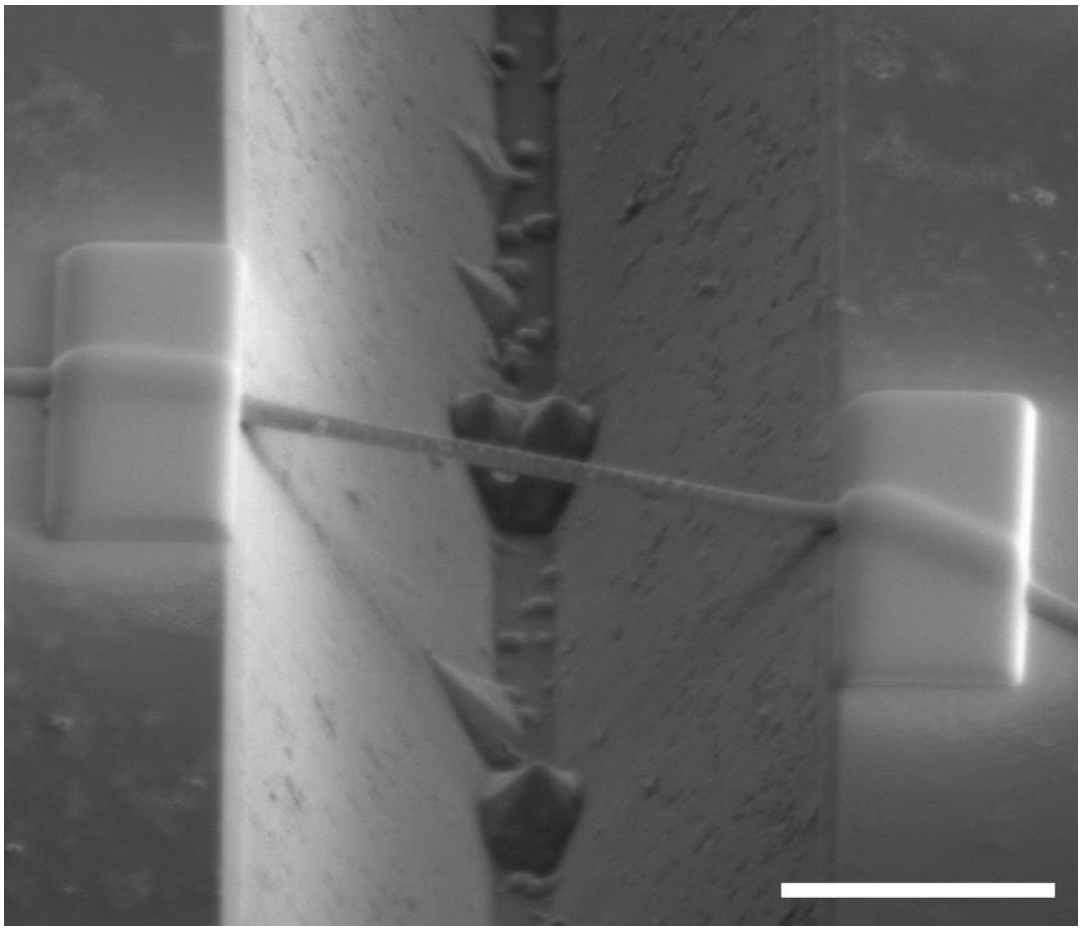

Figure B.1. SEM image of a PMMA nanofiber spanning a silicon trench. The fiber is held in place by platinum over layers that were deposited by ion beam induced deposition. Careful use of the focused ion beam ensured that the ion beam never interacted with the suspended portion of the fiber, thereby preventing any damage to the suspended fiber. The scale bar represents five micrometers.

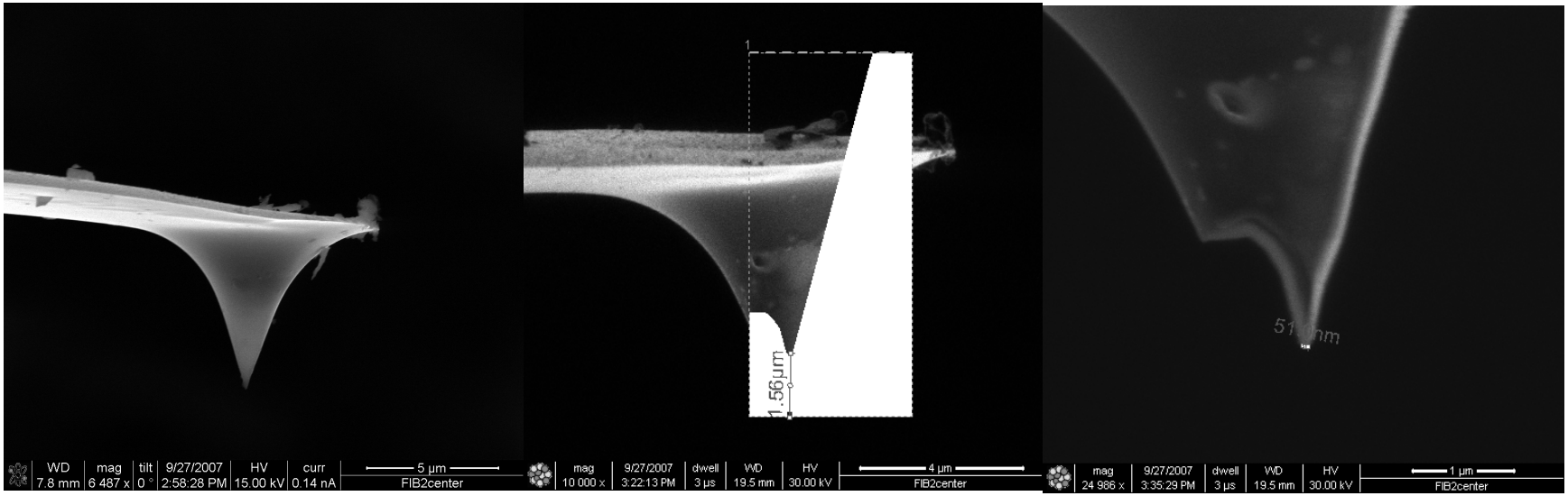

Figure B.2. SEM images of an AFM tip before, during, and after focused ion beam milling. A regular AFM tip (left image) was patterned for milling from the side (center) in such a way as to provide a curved tip (right) after the milling is complete. The AFM tip is shaped as a hemi-cylinder that is 1 um long into the plane of the paper with a radius of curvature of 50 nm.

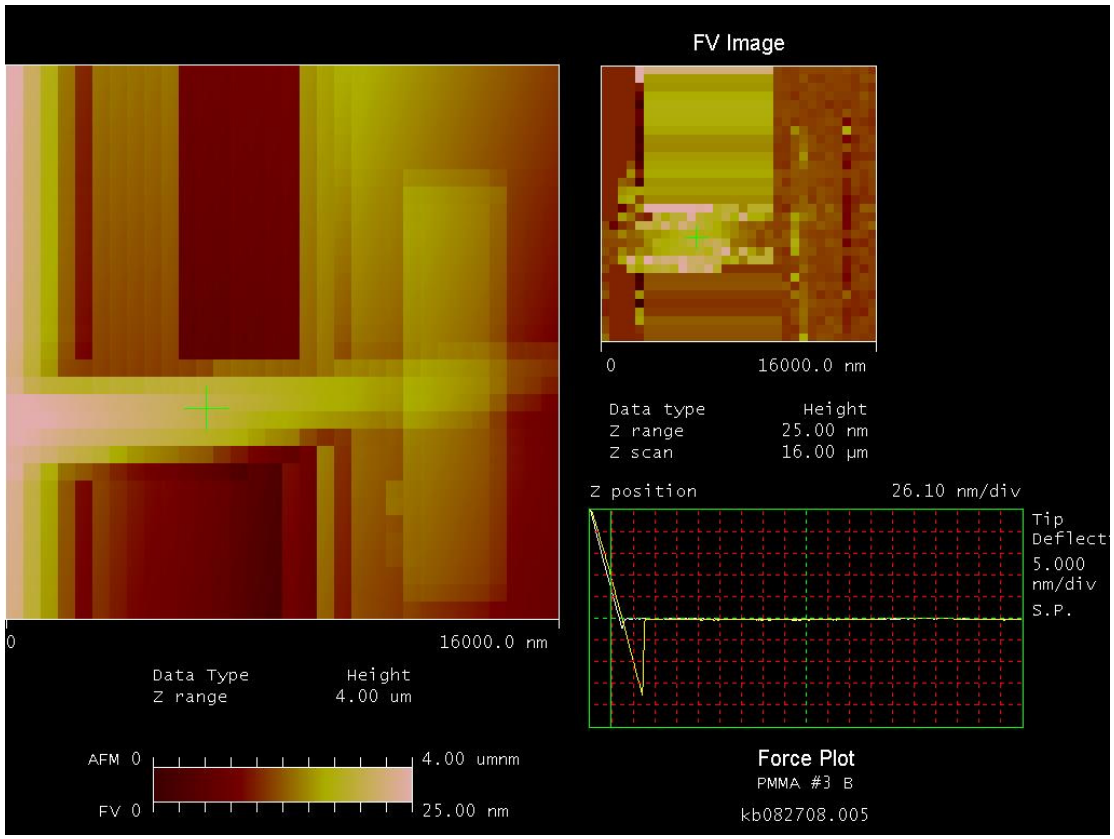

Figure B.3. A highly pixelated force volume image of a nanofiber spanning a silicon trench. The nanofiber, trench, and deposited pad can clearly be distinguished. The force volume image contains height information and the force-distance curves at each pixel.

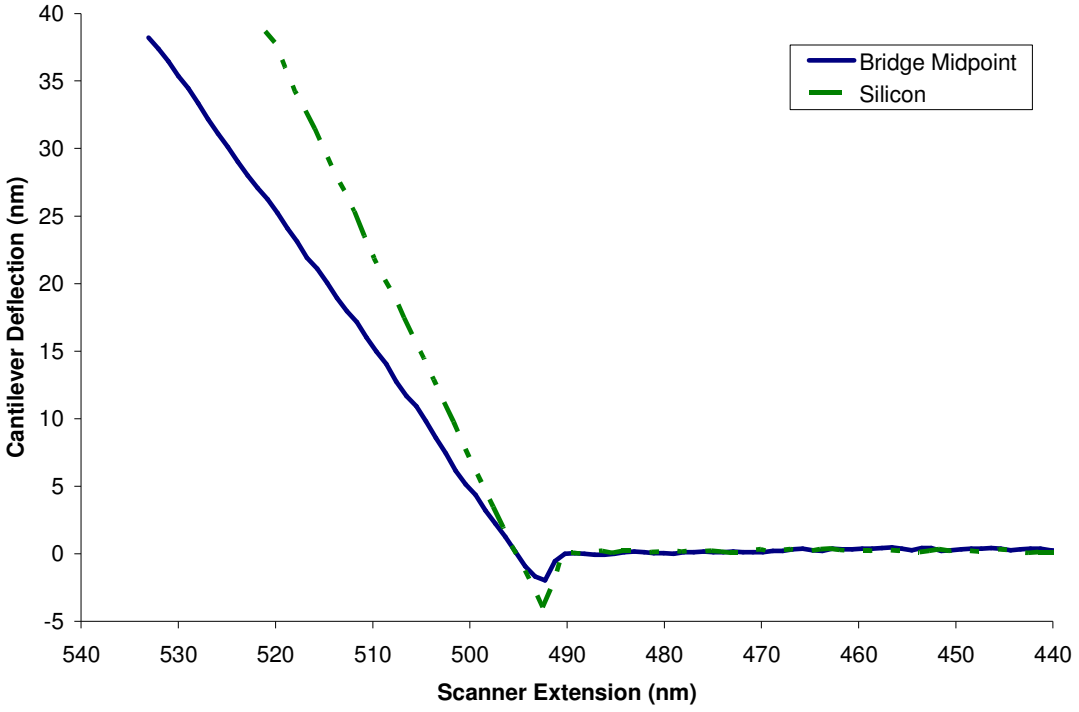

Figure B.4. Deflection-distance curves from two different points from Figure B.3. Both graphs were recorded during scanner extension. The hard contact with the silicon surface (green dashed line) results in a stiff response and steep slope in the deflection-distance curve. Contact with a fiber bridge (blue solid line) results in convolution of the bridge and cantilever bending, which results in a reduced slope.

in Figure B.3.

Once the spring constant of the nanofiber at each location along the span of the fiber is known, the elastic modulus of the fiber can be calculated from the solution of the Euler-Bernoulli beam equation using clamped-clamped boundary conditions,

$$E = \frac{k_{fiber}}{3I}\left[\frac{(L-x)x}{L^3}\right]^3, \qquad \text{Equation B.1}$$

where E is the elastic modulus, k_{fiber} is the spring constant of the fiber, I is the area moment of inertia, L is the length of the fiber bridge, and x is the location of the applied load with reference to a fixed end of the fiber. There are four critical assumptions made in applying this theory to the results. 1) The clamped-clamped boundary condition is an accurate description of the fiber because both ends of the fiber are clamped in place. 2) The applied load to the fiber is modeled as a point source. The geometry of the milled tip is that of a hemi-cylinder. When two cylinders come into contact (i.e. our milled tip and the nanofiber), they form a point contact. 3) Local deformation is negligible. Localized fiber deformation or indentation is reduced because the tip is a cylinder with a radius of curvature of 50 nm, and not a sharp AFM tip, which typically has a radius of curvature less than 10 nm. This does not eliminate deformation, but the increased contact area decreases the pressure that leads to deformation. 4) The model also assumes that the only source of deformation is from the vertical bending of the fiber bridge. The length of the cylinder (1.0 µm) was made so that is was wider than the fiber, reducing any horizontal forces that could cause lateral movement of the fiber bridge. The model used to interpret the results of this investigation was carefully chosen to accurately describe the system.

Using Equation B.1 with the data from the force volume images, the elastic modulus of three electrospun PMMA fibers was calculated to be 2.1 GPa with a standard deviation of 0.6 GPa among the fibers and repeated experiments.

B.3 Discussion

The results, unfortunately, are filled with uncertainty. The spring constant of the fiber bridge was an order of magnitude greater than the spring constant of the AFM cantilever. Based solely on experimental design, the inherent uncertainty from the ratio of the two spring constants is 25%.[172] Matching the spring constants of the cantilever and fiber bridge improves certainty and provides the most sensitivity to changes in the slope of the force-distance curve. There are several approaches to bring the ratio of the spring constants towards unity: increasing the width of the trench, decreasing the diameter of the fiber, or using a cantilever with a higher spring constant.

The high pixelation from force volume imaging left a large uncertainty (±500 nm) in the location of the span for each pixel. This could be improved by increasing the X-Y resolution of the FV image. The newest version of the NanoScope software can achieve much higher X-Y resolution.

Even though this work sought to correct many of the assumptions made in literature, it remains incomplete because of the limitations of the tools used to perform the experiments. Further experiments could not be conducted because of the departure of the collaborator. Future work could easily overcome these limitations, and the technique presented herein could be applied to a host of nano-fibers/tubes/rods.

REFERENCES

[1] Nitzan, A.; Ratner, M. A., Electron transport in molecular wire junctions. *Science* **2003,** 300, (5624), 1384-1389.

[2] Tans, S. J.; Verschueren, A. R. M.; Dekker, C., Room-temperature transistor based on a single carbon nanotube. *Nature* **1998,** 393, (6680), 49-52.

[3] Reed, M. A.; Zhou, C.; Muller, C. J.; Burgin, T. P.; Tour, J. M., Conductance of a molecular junction. *Science* **1997,** 278, (5336), 252-254.

[4] Park, H.; Park, J.; Lim, A. K. L.; Anderson, E. H.; Alivisatos, A. P.; McEuen, P. L., Nanomechanical oscillations in a single-C-60 transistor. *Nature* **2000,** 407, (6800), 57-60.

[5] Drexler, K. E., *Nanosystems: Molecular Machinery, Manufacturing, and Computation*. John Wiley & Sons, Inc.: New York, 1992; p 556.

[6] Binnig, G.; Quate, C. F.; Gerber, C., Atomic Force Microscope. *Phys. Rev. Lett.* **1986,** 56, (9), 930-933.

[7] Oberhauser, A. F.; Hansma, P. K.; Carrion-Vazquez, M.; Fernandez, J. M., Stepwise unfolding of titin under force-clamp atomic force microscopy. *Proc. Natl. Acad. Sci. U. S. A.* **2001,** 98, (2), 468-472.

[8] Carrion-Vazquez, M.; Oberhauser, A. F.; Fowler, S. B.; Marszalek, P. E.; Broedel, S. E.; Clarke, J.; Fernandez, J. M., Mechanical and chemical unfolding of a single protein: A comparison. *Proc. Natl. Acad. Sci. U. S. A.* **1999,** 96, (7), 3694-3699.

[9] Cooke, R., Actomyosin interaction in striated muscle. *Physiol. Rev.* **1997,** 77, (3), 671-697.

[10] Kellermayer, M. S. Z.; Smith, S. B.; Granzier, H. L.; Bustamante, C., Folding-unfolding transitions in single titin molecules characterized with laser tweezers. *Science* **1997,** 276, (5315), 1112-1116.

[11] Kasianowicz, J. J.; Brandin, E.; Branton, D.; Deamer, D. W., Characterization of individual polynucleotide molecules using a membrane channel. *Proc. Natl. Acad. Sci. U. S. A.* **1996,** 93, (24), 13770-13773.

[12] Ha, T.; Enderle, T.; Ogletree, D. F.; Chemla, D. S.; Selvin, P. R.; Weiss, S., Probing the interaction between two single molecules: Fluorescence resonance energy transfer between a single donor and a single acceptor. *Proc. Natl. Acad. Sci. U. S. A.* **1996,** 93, (13), 6264-6268.

[13] Lee, G. U.; Chrisey, L. A.; Colton, R. J., Direct Measurement of the Forces between Complementary Strands of DNA. *Science* **1994,** 266, (5186), 771-773.

[14] Kaelble, D. H., *Physical Chemistry of Adhesion*. 1971; p 507 pp.

[15] Mammen, M.; Choi, S. K.; Whitesides, G. M., Polyvalent interactions in biological systems: Implications for design and use of multivalent ligands and inhibitors. *Angewandte Chemie-International Edition* **1998,** 37, (20), 2755-2794.

[16] Whitesides, G. M.; Mathias, J. P.; Seto, C. T., Molecular Self-Assembly and Nanochemistry - a Chemical Strategy for the Synthesis of Nanostructures. *Science* **1991,** 254, (5036), 1312-1319.

[17] Cappella, B.; Dietler, G., Force-distance curves by atomic force microscopy. *Surf. Sci. Rep.* **1999,** 34, (1-3), 1-104.

[18] Subramoney, S., Novel nanocarbons - Structure, properties, and potential applications. *Adv. Mater.* **1998,** 10, (15), 1157-+.

[19] Terrones, M.; Hsu, W. K.; Kroto, H. W.; Walton, D. R. M., Nanotubes: A revolution in materials science and electronics. In *Fullerenes and Related Structures*, 1999; Vol. 199, pp 189-234.

[20] Ajayan, P. M.; Zhou, O. Z., Applications of carbon nanotubes. In *Carbon Nanotubes*, 2001; Vol. 80, pp 391-425.

[21] Dresselhaus, M. S.; Dresselhaus, G.; Avouris, P., *Carbon Nanotubes Synthesis, Structure, Properties, and Applications*. 2001; p 447.

[22] Baughman, R. H.; Zakhidov, A. A.; de Heer, W. A., Carbon nanotubes-the route toward applications. *Science* **2002,** 297, (5582), 787-792.

[23] Dai, H. J., Carbon nanotubes: opportunities and challenges. *Surf. Sci.* **2002,** 500, (1-3), 218-241.

[24] Terrones, M., Science and technology of the twenty-first century: Synthesis, properties and applications of carbon nanotubes. *Annu. Rev. Mater. Res.* **2003,** 33, 419-501.

[25] Popov, V. N., Carbon nanotubes: properties and application. *Materials Science & Engineering R-Reports* **2004,** 43, (3), 61-102.

[26] Yogeswaran, U.; Chen, S. M., Recent trends in the application of carbon nanotubes-polymer composite modified electrodes for biosensors: A review. *Anal. Lett.* **2008,** 41, (2), 210-243.

[27] Poggi, M. A.; Boyles, J. S.; Bottomley, L. A.; McFarland, A. W.; Colton, J. S.; Nguyen, C. V.; Stevens, R. M.; Lillehei, P. T., Measuring the Compression of a Carbon Nanospring. *Nano Lett.* **2004,** 4, (6), 1009-1016.

[28] Poggi, M. A. Interfacial and Mechanical Properties of Carbon Nanotubes: A Force Spectroscopy Study. Doctoral, Georgia Institute of Technology, Atlanta, 2004.

[29] Binning, G.; Rohrer, H.; Gerber, C.; Weibel, E., Surface Studies by Scanning Tunneling Microscopy. *Phys. Rev. Lett.* **1982,** 49, (1), 57-61.

[30] Binnig, G.; Gerber, C.; Stoll, E.; Albrecht, T. R.; Quate, C. F., Atomic Resolution with Atomic Force Microscope. *Surf. Sci.* **1987,** 189, 1-6.

[31] Quate, C. F., The Afm as a Tool for Surface Imaging. *Surf. Sci.* **1994,** 299, (1-3), 980-995.

[32] Butt, H. J.; Wolff, E. K.; Gould, S. A. C.; Northern, B. D.; Peterson, C. M.; Hansma, P. K., Imaging Cells with the Atomic Force Microscope. *Journal of Structural Biology* **1990,** 105, (1-3), 54-61.

[33] Lal, R.; John, S. A., Biological Applications of Atomic-Force Microscopy. *Am. J. Physiol.* **1994,** 266, (1), C1-&.

[34] Woolley, A. T.; Li Cheung, C.; Hafner, J. H.; Lieber, C. M., Structural biology with carbon nanotube AFM probes. *Chem. Biol.* **2000,** 7, (11), R193-R204.

[35] Dague, E.; Alsteens, D.; Latge, J.-P.; Verbelen, C.; Raze, D.; Baulard, A. R.; Dufrene, Y. F., Chemical Force Microscopy of Single Live Cells. *Nano Lett.* **2007,** 7, (10), 3026-3030.

[36] Muller, D. J., AFM: a nanotool in membrane biology. *Biochemistry* **2008,** 47, (31), 7986-7998.

[37] Radmacher, M.; Tillmann, R. W.; Fritz, M.; Gaub, H. E., From Molecules to Cells - Imaging Soft Samples with the Atomic Force Microscope. *Science* **1992,** 257, (5078), 1900-1905.

[38] Hinterdorfer, P.; Baumgartner, W.; Gruber, H. J.; Schilcher, K.; Schindler, H., Detection and localization of individual antibody-antigen recognition events by atomic force microscopy. *Proc. Natl. Acad. Sci. U. S. A.* **1996,** 93, (8), 3477-3481.

[39] Fisher, T. E.; Oberhauser, A. F.; Carrion-Vazquez, M.; Marszalek, P. E.; Fernandez, J. M., The study of protein mechanics with the atomic force microscope. *Trends Biochem. Sci.* **1999,** 24, (10), 379-384.

[40] Merkel, R.; Nassoy, P.; Leung, A.; Ritchie, K.; Evans, E., Energy landscapes of receptor-ligand bonds explored with dynamic force spectroscopy. *Nature* **1999,** 397, (6714), 50-53.

[41] Bustamante, C.; Smith, S. B.; Liphardt, J.; Smith, D., Single-molecule studies of DNA mechanics. *Curr. Opin. Struct. Biol.* **2000,** 10, (3), 279-285.

[42] Engel, A.; Muller, D. J., Observing single biomolecules at work with the atomic force microscope. *Nature Structural Biology* **2000,** 7, (9), 715-718.

[43] Fisher, T. E.; Marszalek, P. E.; Fernandez, J. M., Stretching single molecules into novel conformations using the atomic force microscope. *Nature Structural Biology* **2000,** 7, (9), 719-724.

[44] Zlatanova, J.; Lindsay, S. M.; Leuba, S. H., Single molecule force spectroscopy in biology using the atomic force microscope. *Prog. Biophys. & Molec. Biol.* **2000,** 74, (1-2), 37-61.

[45] Ando, T.; Kodera, N.; Takai, E.; Maruyama, D.; Saito, K.; Toda, A., A high-speed atomic force microscope for studying biological macromolecules. *Proc. Natl. Acad. Sci. U. S. A.* **2001,** 98, (22), 12468-12472.

[46] Oberhauser, A. F.; Badilla-Fernandez, C.; Carrion-Vazquez, M.; Fernandez, J. M., The mechanical hierarchies of fibronectin observed with single-molecule AFM. *J. Mol. Biol.* **2002,** 319, (2), 433-447.

[47] Davis, J., J.; Coleman, K., S.; Azamian, B., R.; Bagshaw, C., B.; Green, M., L. H., Chemical and biochemical sensing with modified single walled carbon nanotubes. *Chemistry* **2003,** 9, (16), 3732-9.

[48] Chang, Y. C.; Chang, C. S.; Wang, D. C.; Lee, M.-H.; Wang, T.-F.; Wu, M.-Y.; Fu, T.-Y.; Tsong, T. T., Nanoscale imaging of biomolecules by controlled carbon nanotube probes. *Jpn. J. Appl. Phys.* **2004,** 43, (7B), 4517-4520.

[49] Toledocrow, R.; Yang, P. C.; Chen, Y.; Vaeziravani, M., Near-Field Differential Scanning Optical Microscope with Atomic Force Regulation. *Appl. Phys. Lett.* **1992,** 60, (24), 2957-2959.

[50] Zenhausern, F.; Oboyle, M. P.; Wickramasinghe, H. K., Apertureless near-Field Optical Microscope. *Appl. Phys. Lett.* **1994,** 65, (13), 1623-1625.

[51] Knoll, B.; Keilmann, F., Near-field probing of vibrational absorption for chemical microscopy. *Nature* **1999,** 399, (6732), 134-137.

[52] Manne, S.; Hansma, P. K.; Massie, J.; Elings, V. B.; Gewirth, A. A., Atomic-Resolution Electrochemistry with the Atomic Force Microscope - Copper Deposition on Gold. *Science* **1991,** 251, (4990), 183-186.

[53] Manne, S.; Massie, J.; Elings, V. B.; Hansma, P. K.; Gewirth, A. A., Electrochemistry on a Gold Surface Observed with the Atomic Force Microscope. *Journal of Vacuum Science & Technology B* **1991,** 9, (2), 950-954.

[54] Macpherson, J. V.; Unwin, P. R., Combined scanning electrochemical-atomic force microscopy. *Anal. Chem.* **2000,** 72, (2), 276-285.

[55] Kranz, C.; Friedbacher, G.; Mizaikoff, B., Integrating an ultramicroelectrode in an AFM cantilever: Combined technology for enhanced information. *Anal. Chem.* **2001,** 73, (11), 2491-+.

[56] Majumdar, A.; Oden, P. I.; Carrejo, J. P.; Nagahara, L. A.; Graham, J. J.; Alexander, J., Nanometer-Scale Lithography Using the Atomic Force Microscope. *Appl. Phys. Lett.* **1992,** 61, (19), 2293-2295.

[57] Piner, R. D.; Zhu, J.; Xu, F.; Hong, S. H.; Mirkin, C. A., "Dip-pen" nanolithography. *Science* **1999,** 283, (5402), 661-663.

[58] Vettiger, P.; Despont, M.; Drechsler, U.; Durig, U.; Haberle, W.; Lutwyche, M. I.; Rothuizen, H. E.; Stutz, R.; Widmer, R.; Binnig, G. K., The "Millipede" - More than one thousand tips for future AFM data storage. *Ibm Journal of Research and Development* **2000,** 44, (3), 323-340.

[59] Butt, H. J., Measuring Electrostatic, Vanderwaals, and Hydration Forces in Electrolyte-Solutions with an Atomic Force Microscope. *Biophys. J.* **1991,** 60, (6), 1438-1444.

[60] Rabinovich, Y. I.; Yoon, R. H., Use of Atomic-Force Microscope for the Measurements of Hydrophobic Forces between Silanated Silica Plate and Glass Sphere. *Langmuir* **1994,** 10, (6), 1903-1909.

[61] Boland, T.; Ratner, B. D., Direct Measurement of Hydrogen-Bonding in DNA Nucleotide Bases by Atomic-Force Microscopy. *Proc. Natl. Acad. Sci. U. S. A.* **1995,** 92, (12), 5297-5301.

[62] Magonov, S. N.; Reneker, D. H., Characterization of polymer surfaces with atomic force microscopy. *Annu. Rev. Mater. Sci.* **1997,** 27, 175-222.

[63] Stowe, T. D.; Yasumura, K.; Kenny, T. W.; Botkin, D.; Wago, K.; Rugar, D., Attonewton force detection using ultrathin silicon cantilevers. *Appl. Phys. Lett.* **1997,** 71, (2), 288-290.

[64] Wong, S. S.; Woolley, A. T.; Odom, T. W.; Huang, J.-L.; Kim, P.; Vezenov, D. V.; Lieber, C. M., Single-walled carbon nanotube probes for high-resolution nanostructure imaging. *Appl. Phys. Lett.* **1998,** 73, (23), 3465-3467.

[65] Schoenherr, H.; Hruska, Z.; Vancso, G. J., Toward High Resolution Mapping of Functional Group Distributions at Surface-Treated Polymers by AFM Using Modified Tips. *Macromolecules* **2000,** 33, (12), 4532-4537.

[66] Hugel, T.; Seitz, M., The study of molecular interactions by AFM force spectroscopy. *Macromol. Rapid Commun.* **2001,** 22, (13), 989-1016.

[67] Ishikawa, M.; Yoshimura, M.; Ueda, K., A study of friction by carbon nanotube tip. *Appl. Surf. Sci.* **2002,** 188, 456-459.

[68] Liu, H.; Bhushan, B., Investigation of nanotribological properties of self-assembled monolayers with alkyl and biphenyl spacer chains (Invited). *Ultramicroscopy* **2002,** 91, (1-4), 185-202.

[69] Kuhner, F.; Erdmann, M.; Sonnenberg, L.; Serr, A.; Morfill, J.; Gaub, H. E., Friction of single polymers at surfaces. *Langmuir* **2006,** 22, (26), 11180-11186.

[70] Seo, Y.; Jhe, W., Atomic force microscopy and spectroscopy. *Reports on Progress in Physics* **2008,** 71, (1).

[71] Strus, M. C.; Zalamea, L.; Raman, A.; Pipes, R. B.; Nguyen, C. V.; Stach, E. A., Peeling Force Spectroscopy: Exposing the Adhesive Nanomechanics of One-Dimensional Nanostructures. *Nano Lett.* **2008,** 8, (2), 544-550.

[72] Albrecht, T. R.; Akamine, S.; Carver, T. E.; Quate, C. F., Microfabrication of Cantilever Styli for the Atomic Force Microscope. *Journal of Vacuum Science & Technology a-Vacuum Surfaces and Films* **1990,** 8, (4), 3386-3396.

[73] Rief, M.; Oesterhelt, F.; Heymann, B.; Gaub, H. E., Single molecule force spectroscopy on polysaccharides by atomic force microscopy. *Science* **1997,** 275, (5304), 1295-1297.

[74] Brotherson, B.; Bottomley, L. A.; Ludovice, P.; Deng, Y. L., Cationic polyacrylamide conformation on mica studied by single molecule "pulling" with scanning probe microscopy. *Macromolecules* **2007,** 40, (13), 4561-4567.

[75] Yenilmez, E.; Wang, Q.; Chen, R. J.; Wang, D.; Dai, H., Wafer scale production of carbon nanotube scanning probe tips for atomic force microscopy. *Appl. Phys. Lett.* **2002,** 80, (12), 2225-2227.

[76] Gan, Y., Invited Review Article: A review of techniques for attaching micro- and nanoparticles to a probe's tip for surface force and near-field optical measurements. *Rev. Sci. Instrum.* **2007,** 78, (8), 081101-8.

[77] Tortonese, M.; Barrett, R. C.; Quate, C. F., Atomic Resolution with an Atomic Force Microscope Using Piezoresistive Detection. *Appl. Phys. Lett.* **1993,** 62, (8), 834-836.

[78] Minne, S. C.; Manalis, S. R.; Quate, C. F., Parallel atomic force microscopy using cantilevers with integrated piezoresistive sensors and integrated piezoelectric actuators. *Appl. Phys. Lett.* **1995,** 67, (26), 3918-3920.

[79] Linnemann, R.; Gotszalk, T.; Hadjiiski, L.; Rangelow, I. W., Characterization of a Cantilever with an Integrated Deflection Sensor. *Thin Solid Films* **1995,** 264, (2), 159-164.

[80] Alexander, S.; Hellemans, L.; Marti, O.; Schneir, J.; Elings, V.; Hansma, P. K.; Longmire, M.; Gurley, J., An Atomic-Resolution Atomic-Force Microscope Implemented Using an Optical-Lever. *J. Appl. Phys.* **1989,** 65, (1), 164-167.

[81] Meyer, G.; Amer, N. M., Simultaneous Measurement of Lateral and Normal Forces with an Optical-Beam-Deflection Atomic Force Microscope. *Appl. Phys. Lett.* **1990,** 57, (20), 2089-2091.

[82] Erlandsson, R.; Wigren, R.; Olsson, L., A Scanning Force Microscope Designed for Applied Surface Studies. *Microscopy Microanalysis Microstructures* **1990,** 1, (5-6), 471-480.

[83] Overney, R. M.; Meyer, E.; Frommer, J.; Brodbeck, D.; Luthi, R.; Howald, L.; Guntherodt, H. J.; Fujihira, M.; Takano, H.; Gotoh, Y., Friction Measurements on Phase-Separated Thin-Films with a Modified Atomic Force Microscope. *Nature* **1992,** 359, (6391), 133-135.

[84] Houston, J. E.; Kim, H. I., Adhesion, Friction, and Mechanical Properties of Functionalized Alkanethiol Self-Assembled Monolayers. *Acc. Chem. Res.* **2002,** 35, (7), 547-553.

[85] Salmeron, M., Observing friction at work. *Chemtech* **1998,** 28, (9), 17-23.

[86] Carpick, R. W.; Salmeron, M., Scratching the surface: Fundamental investigations of tribology with atomic force microscopy. *Chemical Reviews* **1997,** 97, (4), 1163-1194.

[87] Maivald, P.; Butt, H. J.; Gould, S. A. C.; Prater, C. B.; Drake, B.; Gurley, J. A.; Elings, V. B.; Hansma, P. K., Using force modulation to image surface elasticities with the atomic force microscope. In 1991; p 103.

[88] Anczykowski, B.; Kruger, D.; Babcock, K. L.; Fuchs, H., Basic properties of dynamic force spectroscopy with the scanning force microscope in experiment and simulation. *Ultramicroscopy* **1996,** 66, (3-4), 251-259.

[89] Ishida, N.; Inoue, T.; Miyahara, M.; Higashitani, K., Nano bubbles on a hydrophobic surface in water observed by tapping-mode atomic force microscopy. *Langmuir* **2000,** 16, (16), 6377-6380.

[90] Fritz, M.; Radmacher, M.; Cleveland, J. P.; Allersma, M. W.; Stewart, R. J.; Gieselmann, R.; Janmey, P.; Schmidt, C. F.; Hansma, P. K., Imaging Globular and Filamentous Proteins in Physiological Buffer Solutions with Tapping Mode Atomic-Force Microscopy. *Langmuir* **1995,** 11, (9), 3529-3535.

[91] Radmacher, M.; Fritz, M.; Hansma, P. K., Imaging Soft Samples with the Atomic-Force Microscope - Gelatin in Water and Propanol. *Biophys. J.* **1995,** 69, (1), 264-270.

[92] Putman, C. A. J.; Vanderwerf, K. O.; Degrooth, B. G.; Vanhulst, N. F.; Greve, J., Viscoelasticity of Living Cells Allows High-Resolution Imaging by Tapping Mode Atomic-Force Microscopy. *Biophys. J.* **1994,** 67, (4), 1749-1753.

[93] Shibataseki, T.; Watanabe, W.; Masai, J., Imaging of Cell with Atomic-Force Microscopy Operated at a Tapping Mode. *Journal of Vacuum Science & Technology B* **1994,** 12, (3), 1530-1534.

[94] Putman, C. A. J.; Vanderwerf, K. O.; Degrooth, B. G.; Vanhulst, N. F.; Greve, J., Tapping Mode Atomic-Force Microscopy in Liquid. *Appl. Phys. Lett.* **1994,** 64, (18), 2454-2456.

[95] Umemura, K.; Arakawa, H.; Ikai, A., High-Resolution Images of Cell-Surface Using a Tapping-Mode Atomic-Force Microscope. *Japanese Journal of Applied Physics Part 2-Letters* **1993,** 32, (11B), L1711-L1714.

[96] Zhong, Q.; Inniss, D.; Kjoller, K.; Elings, V. B., Fractured Polymer Silica Fiber Surface Studied by Tapping Mode Atomic-Force Microscopy. *Surf. Sci.* **1993,** 290, (1-2), L688-L692.

[97] Camesano, T. A.; Natan, M. J.; Logan, B. E., Observation of changes in bacterial cell morphology using tapping mode atomic force microscopy. *Langmuir* **2000,** 16, (10), 4563-4572.

[98] Hansma, H. G.; Kim, K. J.; Laney, D. E.; Garcia, R. A.; Argaman, M.; Allen, M. J.; Parsons, S. M., Properties of biomolecules measured from atomic force microscope images: A review. *Journal of Structural Biology* **1997,** 119, (2), 99-108.

[99] Leclere, P.; Hennebicq, E.; Calderone, A.; Brocorens, P.; Grimsdale, A. C.; Mullen, K.; Bredas, J. L.; Lazzaroni, R., Supramolecular organization in block copolymers containing a conjugated segment: a joint AFM/molecular modeling study. *Prog. Polym. Sci.* **2003,** 28, (1), 55-81.

[100] Viville, P.; Deffieux, A.; Schappacher, M.; Bredas, J. L.; Lazzaroni, R., Surface organization of single hyperbranched polymer molecules, as studied by atomic force microscopy. *Materials Science & Engineering C-Biomimetic and Supramolecular Systems* **2001,** 15, (1-2), 311-314.

[101] Leclere, P.; Rasmont, A.; Bredas, J. L.; Jerome, R.; Aime, J. P.; Lazzaroni, R., Phase-separated microstructures in "all-acrylic" thermoplastic elastomers. *Macromol. Symp.* **2001,** 167, 117-137.

[102] Rasmont, A.; Leclere, P.; Doneux, C.; Lambin, G.; Tong, J. D.; Jerome, R.; Bredas, J. L.; Lazzaroni, R., Microphase separation at the surface of block copolymers, as studied with atomic force microscopy. *Colloids and Surfaces B-Biointerfaces* **2000,** 19, (4), 381-395.

[103] Leclere, P.; Lazzaroni, R.; Bredas, J. L.; Yu, J. M.; Dubois, P.; Jerome, R., Microdomain morphology analysis of block copolymers by atomic force microscopy with phase detection imaging. *Langmuir* **1996,** 12, (18), 4317-4320.

[104] Beake, B. D.; Brewer, N. J.; Leggett, G. J., Scanning force microscopy of polyester: surface structure and adhesive properties. *Macromol. Symp.* **2001,** 167, (Recent Advances in Scanning Probe Microscopy of Polymers), 101-115.

[105] Raghavan, D.; Gu, X.; Nguyen, T.; VanLandingham, M.; Karim, A., Mapping polymer heterogeneity using atomic force microscopy phase imaging and nanoscale indentation. *Macromolecules* **2000,** 33, (7), 2573-2583.

[106] Butt, H. J.; Cappella, B.; Kappl, M., Force measurements with the atomic force microscope: Technique, interpretation and applications. *Surf. Sci. Rep.* **2005,** 59, (1-6), 1-152.

[107] Leite, F. L.; Herrmann, P. S. P., Application of atomic force spectroscopy (AFS) to studies of adhesion phenomena: a review. *J. Adhes. Sci. Technol.* **2005,** 19, (3-5), 365-405.

[108] Burnham, N. A.; Colton, R. J.; Pollock, H. M., Interpretation of force curves in force microscopy. *Nanotechnology* **1993,** 4, (2), 64-80.

[109] Burnham, N. A.; Colton, R. J., Measuring the Nanomechanical Properties and Surface Forces of Materials Using an Atomic Force Microscope. *Journal of Vacuum Science & Technology* **1989,** 7, (4), 2906-2913.

[110] Noy, A.; Frisbie, C. D.; Rozsnyai, L. F.; Wrighton, M. S.; Lieber, C. M., Chemical Force Microscopy: Exploiting Chemically-Modified Tips To Quantify Adhesion, Friction, and Functional Group Distributions in Molecular Assemblies. *J. Am. Chem. Soc.* **1995,** 117, (30), 7943-51.

[111] Noy, A.; Vezenov, D. V.; Lieber, C. M., Chemical force microscopy. *Annu. Rev. Mater. Sci.* **1997,** 27, 381-421.

[112] Duwez, A. S.; Nysten, B., Mapping Aging Effects on Polymer Surfaces: Specific Detection of Additives by Chemical Force Microscopy. *Langmuir* **2001,** 17, (26), 8287-8292.

[113] Poggi, M. A.; Lillehei, P. T.; Bottomley, L. A., Chemical Force Microscopy on Single-Walled Carbon Nanotube Paper. *Chem. Mater.* **2005,** 17, (17), 4289-4295.

[114] Friddle, R. W.; Lemieux, M. C.; Cicero, G.; Artyukhin, A. B.; Tsukruk, V. V.; Grossman, J. C.; Galli, G.; Noy, A., Single functional group interactions with individual carbon nanotubes. *Nat. Nanotechnol.* **2007,** 2, (11), 692-697.

[115] Tsukruk, V. V.; Bliznyuk, V. N., Adhesive and Friction Forces between Chemically Modified Silicon and Silicon Nitride Surfaces. *Langmuir* **1998,** 14, 446-455.

[116] Burnham, N. A.; Behrend, O. P.; Oulevey, F.; Gremaud, G.; Gallo, P. J.; Gourdon, D.; Dupas, E.; Kulik, A. J.; Pollock, H. M.; Briggs, G. A. D., How does a tip tap? *Nanotechnology* **1997,** 8, (2), 67-75.

[117] Giessibl, F. J., Forces and frequency shifts in atomic-resolution dynamic-force microscopy. *Phys. Rev. B* **1997,** 56, (24), 16010-16015.

[118] Cleveland, J. P.; Anczykowski, B.; Schmid, A. E.; Elings, V. B., Energy dissipation in tapping-mode atomic force microscopy. *Appl. Phys. Lett.* **1998,** 72, (20), 2613-2615.

[119] Sader, J. E.; Larson, I.; Mulvaney, P.; White, L. R., Method for the calibration of atomic force microscope cantilevers. *Rev. Sci. Instrum.* **1995,** 66, (7), 3789-98.

[120] Hutter, J. L.; Bechhoefer, J., Calibration of atomic-force microscope tips. *Rev. Sci. Instrum.* **1993,** 64, (7), 1868-73.

[121] Tamayo, J.; Garcia, R., Relationship between phase shift and energy dissipation in tapping-mode scanning force microscopy. *Appl. Phys. Lett.* **1998,** 73, (20), 2926-2928.

[122] Garcia, R.; San Paulo, A., Attractive and repulsive tip-sample interaction regimes in tapping-mode atomic force microscopy. *Phys. Rev. B* **1999,** 60, (7), 4961-4967.

[123] Bar, G.; Brandsch, R.; Bruch, M.; Delineau, L.; Whangbo, M. H., Examination of the relationship between phase shift and energy dissipation in tapping mode atomic force microscopy by frequency-sweep and force-probe measurements. *Surf. Sci.* **2000,** 444, (1-3), L11-L16.

[124] Lee, S. I.; Howell, S. W.; Raman, A.; Reifenberger, R., Nonlinear dynamics of microcantilevers in tapping mode atomic force microscopy. A comparison

between theory and experiment. *Phys. Rev. B: Condens. Matter Mater. Phys.* **2002,** 66, (11), 115409/1-115409/10.

[125] Lee, S. I.; Howell, S. W.; Raman, A.; Reifenberger, R., Nonlinear dynamic perspectives on dynamic force microscopy. *Ultramicroscopy* **2003,** 97, (1-4), 185-198.

[126] Holscher, H., Theory of phase-modulation atomic force microscopy with constant-oscillation amplitude. *J. Appl. Phys.* **2008,** 103, (6).

[127] Holscher, H.; Anczykowski, B., Quantitative measurement of tip-sample forces by dynamic force spectroscopy in ambient conditions. *Surf. Sci.* **2005,** 579, (1), 21-26.

[128] Sader, J. E.; Jarvis, S. P., Accurate formulas for interaction force and energy in frequency modulation force spectroscopy. *Appl. Phys. Lett.* **2004,** 84, (10), 1801-1803.

[129] Holscher, H.; Gotsmann, B.; Schirmeisen, A., Dynamic force spectroscopy using the frequency modulation technique with constant excitation. *Phys. Rev. B: Condens. Matter Mater. Phys.* **2003,** 68, (15), 153401/1-153401/4.

[130] Strunz, T.; Oroszlan, K.; Schafer, R.; Guntherodt, H. J., Dynamic force spectroscopy of single DNA molecules. *Proc. Natl. Acad. Sci. U. S. A.* **1999,** 96, (20), 11277-11282.

[131] Heymann, B.; Grubmuller, H., Dynamic force spectroscopy of molecular adhesion bonds. *Phys. Rev. Lett.* **2000,** 84, (26), 6126-6129.

[132] Humphris, A. D. L.; Antognozzi, M.; McMaster, T. J.; Miles, M. J., Transverse Dynamic Force Spectroscopy: A Novel Approach to Determining the Complex Stiffness of a Single Molecule. *Langmuir* **2002,** 18, (5), 1729-1733.

[133] Dudko, O. K.; Filippov, A. E.; Klafter, J.; Urbakh, M., Beyond the conventional description of dynamic force spectroscopy of adhesion bonds. *Proc. Natl. Acad. Sci. U. S. A.* **2003,** 100, (20), 11378-11381.

[134] Zou, S.; Korczagin, I.; Hempenius, M. A.; Schoenherr, H.; Vancso, G. J., Single molecule force spectroscopy of smart poly(ferrocenylsilane) macromolecules:

Towards highly controlled redox-driven single chain motors. *Polymer* **2006,** 47, (7), 2483-2492.

[135] Friedsam, C.; Wehle, A. K.; Kuhner, F.; Gaub, H. E., Dynamic single-molecule force spectroscopy: bond rupture analysis with variable spacer length. *Journal of Physics-Condensed Matter* **2003,** 15, (18), S1709-S1723.

[136] Vancso, G. J., Feeling the force of supramolecular bonds in polymers. *Angew. Chem., Int. Ed.* **2007,** 46, (21), 3794-3796.

[137] Bhushan, B.; Ling, X., Adhesion and friction between individual carbon nanotubes measured using force-versus-distance curves in atomic force microscopy. *Phys. Rev. B* **2008,** 78, (4).

[138] Evans, E., Probing the relation between force - Lifetime - and chemistry in single molecular bonds. *Annu. Rev. Biophys. Biomol. Struct.* **2001,** 30, 105-128.

[139] Sugimoto, Y.; Pou, P.; Abe, M.; Jelinek, P.; Perez, R.; Morita, S.; Custance, O., Chemical identification of individual surface atoms by atomic force microscopy. *Nature* **2007,** 446, (7131), 64-67.

[140] Schmutz, J. E.; Holscher, H.; Ebeling, D.; Schafer, M. M.; Anczykowski, B. In *Mapping the tip-sample interactions on DPPC and DNA by dynamic force spectroscopy under ambient conditions*, 2007; 2007; pp 875-881.

[141] Holscher, H.; Schirmeisen, A., Dynamic force microscopy and spectroscopy. In *Advances in Imaging and Electron Physics, Vol 135*, 2005; Vol. 135, pp 41-101.

[142] Rief, M.; Pascual, J.; Saraste, M.; Gaub, H. E., Single Molecule Force Spectroscopy of Spectrin Repeats: Low Unfolding Forces in Helix Bundles. *J. Mol. Biol.* **1999,** 286, (2), 553-561.

[143] Rief, M.; Gautel, M.; Oesterhelt, F.; Fernandez, J. M.; Gaub, H. E., Reversible unfolding of individual titin immunoglobulin domains by AFM. *Science* **1997,** 276, (5315), 1109-1112.

[144] Bhushan, B.; Ling, X.; Jungen, A.; Hierold, C., Adhesion and friction of a multiwalled carbon nanotube sliding against single-walled carbon nanotube. *Phys. Rev. B: Condens. Matter Mater. Phys.* **2008,** 77, (16), 165428/1-165428/12.

[145] Jiang, A. N.; Gao, S.; Wei, X. L.; Liang, X. L.; Chen, Q., Amplitude Response of Multiwalled Carbon Nanotube Probe with Controlled Length during Tapping Mode Atomic Force Microscopy. *J. Phys. Chem. C* **2008,** 112, (40), 15631-15636.

[146] Johnson, K. L.; Kendall, K.; Roberts, A. D., Surface energy and the contact of elastic solid. *Proceedings of the Royal Society of London, Series A: Mathematical, Physical and Engineering Sciences* **1971,** 324, (1558), 301-13.

[147] Derjaguin, B. V.; Muller, V. M.; Toporov, Y. P., Effect of Contact Deformations on Adhesion of Particles. *J. Colloid Interface Sci.* **1975,** 53, (2), 314-326.

[148] Breslauer, E.; Troczynski, T., Experimental determination of the peel adhesion strength for metallic foils. *J. Adhes. Sci. Technol.* **1998,** 12, (4), 367-382.

[149] Kaelble, D. H., Theory and analysis of peel adhesion: bond stresses and distributions. *Transactions of the Society of Rheology* **1960,** 4, 45-73.

[150] Kaelble, D. H., Peel adhesion-microfracture mechanics of inter facia unbonding of polymers. *Transactions of the Society of Rheology* **1965,** 9, (2), 135-63.

[151] Kaelble, D. H., Peel adhesion: influence of surface energies and adhesive rheology. *J. Adhes.* **1969,** 1, (April), 102-23.

[152] Kaelble, D. H., Rheology of adhesion. *Journal of Macromolecular Science, Reviews in Macromolecular Chemistry* **1971,** 6, (1), 85-112.

[153] Kaelble, D. H., Interfacial morphology and mechanical properties of A-B-A triblock copolymers. *Transactions of the Society of Rheology* **1971,** 15, (2), 235-60.

[154] Kaelble, D. H., Theory and analysis of peel adhesion: adhesive thickness effects. *J. Adhes.* **1992,** 37, (1-3), 205-14.

[155] Kaelble, D. H., New theory and analysis of peel adhesion. *Proceedings of the Annual Meeting of the Adhesion Society* **1998,** 21st, 350.

[156] Kaelble, D. H.; Reylek, R. S., Peel adhesion: rate dependence of micro-fracture processes. *J. Adhes.* **1969,** 1, (April), 124-35.

[157] Bikerman, J. J., *The Science of Adhesive Joints. 2nd ed*. 1968; p 349 pp.

[158] Houwink, R.; Editor, *Adhesion and Adhesives, Vol 2: Applications. 2nd ed*. 1967; p 590 pp.

[159] Kinloch, A. J.; Williams, J. G., The mechanics of peel tests. *Adhesion Science and Engineering* **2002,** 1, (Mechanics of Adhesion), 273-301.

[160] Shi, X. H.; Yong, K.; Zhao, Y. P.; Gao, H. J., Molecular dynamics simulation of peeling a DNA molecule on substrate. *Acta Mechanica Sinica* **2005,** 21, (3), 249-256.

[161] Coffin, D. W.; Carlsson, L. A.; Pipes, R. B., On the separation of carbon nanotubes. *Composites Science and Technology* **2006,** 66, (9), 1132-1140.

[162] Sasaki, N.; Toyoda, A.; Saitoh, H.; Itamura, N.; Ohyama, M.; Miura, K., Theoretical simulation of atomic-scale peeling of single-walled carbon nanotube from graphite surface. *e-J. Surf. Sci. Nanotechnol.* **2006,** 4, 133-137.

[163] Sasaki, N.; Toyoda, A.; Itamura, N.; Miura, K., Simulation of nanoscale peeling and adhesion of single-walled carbon nanotube on graphite surface. *e-J. Surf. Sci. Nanotechnol.* **2008,** 6, 72-78.

[164] Manohar, S.; Mantz, A. R.; Bancroft, K. E.; Hui, C. Y.; Jagota, A.; Vezenov, D. V., Peeling Single-Stranded DNA from Graphite Surface to Determine Oligonucleotide Binding Energy by Force Spectroscopy. *Nano Lett.* **2008,** 8, (12), 4365-4372.

[165] Ishikawa, M.; Harada, R.; Sasaki, N.; Miura, K., Visualization of nanoscale peeling of carbon nanotube on graphite. *Appl. Phys. Lett.* **2008,** 93, (8), 083122/1-083122/3.

[166] Strus, M. C.; Cano, C. I.; Pipes, R. B.; Nguyen, C.; Raman, A., Interfacial energy between carbon nanotubes and polymers measured from nanoscale peel tests in the atomic force microscope. *Composites Science and Technology* **2009,** 69, (10).

[167] Serr, A.; Netz, R. R., Pulling adsorbed polymers from surfaces with the AFM: stick vs. slip, peeling vs. gliding. *Europhys. Lett.* **2006,** 73, (2), 292-298.

[168] Cleveland, J. P.; Manne, S.; Bocek, D.; Hansma, P. K., A nondestructive method for determining the spring constant of cantilevers for scanning force microscopy. *Rev. Sci. Instrum.* **1993,** 64, (2), 403-5.

[169] Butt, H. J.; Jaschke, M., Calculation of Thermal Noise in Atomic-Force Microscopy. *Nanotechnology* **1995,** 6, (1), 1-7.

[170] Sader, J. E.; Chon, J. W. M.; Mulvaney, P., Calibration of rectangular atomic force microscope cantilevers. *Rev. Sci. Instrum.* **1999,** 70, (10), 3967-3969.

[171] Poggi, M. A.; McFarland, A. W.; Colton, J. S.; Bottomley, L. A., A Method for Calculating the Spring Constant of Atomic Force Microscopy Cantilevers with a Nonrectangular Cross Section. *Anal. Chem.* **2005,** 77, (4), 1192-1195.

[172] Gibson, C. T.; Watson, G. S.; Myhra, S., Determination of the spring constants of probes for force microscopy/spectroscopy. *Nanotechnology* **1996,** 7, 259-262.

[173] Torii, A.; Sasaki, M.; Hane, K.; Okuma, S., A method for determining the spring constant of cantilevers for atomic force microscopy. *Meas. Sci. Technol.* **1996,** 7, (2), 179-84.

[174] Clifford, C. A.; Seah, M. P., The determination of atomic force microscope cantilever spring constants via dimensional methods for nanomechanical analysis. *Nanotechnology* **2005,** 16, (9), 1666-1680.

[175] Burnham, N. A.; Chen, X.; Hodges, C. S.; Matei, G. A.; Thoreson, E. J.; Roberts, C. J.; Davies, M. C.; Tendler, S. J. B., Comparison of calibration methods for atomic-force microscopy cantilevers. *Nanotechnology* **2003,** 14, (1), 1-6.

[176] Iijima, S., Helical microtubules of graphitic carbon. *Nature* **1991,** 354, (6348), 56-58.

[177] White, C. T.; Robertson, D. H.; Mintmire, J. W., Helical and rotational symmetries of nanoscale graphitic tubules. *Phys. Rev. B* **1993,** 47, (9), 5485.

[178] Haijun, L.; Wanlin, G., Transversely isotropic elastic properties of single-walled carbon nanotubes by a rectangular beam model for the C[Single Bond]C bonds. In AIP: 2008; Vol. 103, p 103501.

[179] Mintmire, J. W.; Dunlap, B. I.; White, C. T., Are fullerene tubules metallic? *Phys. Rev. Lett.* **1992,** 68, (5), 631.

[180] Ruoff, R. S.; Lorents, D. C., Mechanical and thermal properties of carbon nanotubes. *Carbon* **1995,** 33, (7), 925-30.

[181] Ruoff, R. S.; Qian, D.; Liu, W. K., Mechanical properties of carbon nanotubes: theoretical predictions and experimental measurements. *C. R. Phys.* **2003,** 4, (9), 993-1008.

[182] Sears, A.; Batra, R. C., Macroscopic properties of carbon nanotubes from molecular-mechanics simulations. *Phys. Rev. B: Condens. Matter Mater. Phys.* **2004,** 69, (23), 235406/1-235406/10.

[183] Ebbesen, T. W.; Ajayan, P. M., Large-Scale Synthesis of Carbon Nanotubes. *Nature* **1992,** 358, (6383), 220-222.

[184] Kingston, C. T.; Simard, B., Fabrication of carbon nanotubes. *Anal. Lett.* **2003,** 36, (15), 3119-3145.

[185] Rakov, E. G., Methods for preparation of carbon nanotubes. *Usp. Khim.* **2000,** 69, (1), 41-59.

[186] Pillai, S. K.; Ray, S. S.; Moodley, M., Purification of Multi-Walled Carbon Nanotubes. *J. Nanosci. Nanotechnol.* **2008,** 8, (12), 6187-6207.

[187] Ding, R. G.; Lu, G. Q.; Yan, Z. F.; Wilson, M. A., Recent advances in the preparation and utilization of carbon nanotubes for hydrogen storage. *J. Nanosci. Nanotechnol.* **2001,** 1, (1), 7-29.

[188] Guo, T.; Nikolaev, P.; Rinzler, A. G.; Tomanek, D.; Colbert, D. T.; Smalley, R. E., Self-Assembly of Tubular Fullerenes. *J. Phys. Chem.* **1995,** 99, (27), 10694-10697.

[189] Guo, T.; Nikolaev, P.; Thess, A.; Colbert, D. T.; Smalley, R. E., Catalytic Growth of Single-Walled Nanotubes by Laser Vaporization. *Chem. Phys. Lett.* **1995,** 243, (1-2), 49-54.

[190] Tang, J.; Qin, L. C.; Sasaki, T.; Yudasaka, M.; Matsushita, A.; Iijima, S., Structure and property changes of single-walled carbon nanotubes under pressure. *Synth. Met.* **2001,** 121, (1-3), 1245-1246.

[191] Scott, C. D.; Arepalli, S.; Nikolaev, P.; Smalley, R. E., Growth mechanisms for single-wall carbon nanotubes in a laser-ablation process. *Applied Physics a-Materials Science & Processing* **2001,** 72, (5), 573-580.

[192] Puretzky, A. A.; Geohegan, D. B.; Fan, X.; Pennycook, S. J., Dynamics of single-wall carbon nanotube synthesis by laser vaporization. *Applied Physics a-Materials Science & Processing* **2000,** 70, (2), 153-160.

[193] Yudasaka, M.; Ichihashi, T.; Komatsu, T.; Iijima, S., Single-wall carbon nanotubes formed by a single laser-beam pulse. *Chem. Phys. Lett.* **1999,** 299, (1), 91-96.

[194] Yudasaka, M.; Komatsu, T.; Ichihashi, T.; Iijima, S., Single-wall carbon nanotube formation by laser ablation using double-targets of carbon and metal. *Chem. Phys. Lett.* **1997,** 278, (1-3), 102-106.

[195] Salvetat, J. P.; Bonard, J. M.; Thomson, N. H.; Kulik, A. J.; Forro, L.; Benoit, W.; Zuppiroli, L., Mechanical properties of carbon nanotubes. *Applied Physics A* **1999,** 69, 255-260.

[196] Ismail, A. F.; Goh, P. S.; Tee, J. C.; Sanip, S. M.; Aziz, M., A Review of Purification Techniques for Carbon Nanotubes. *NANO* **2008,** 3, (3), 127-143.

[197] José-Yacamán , M.; Mikiyoshida, M.; Rendon, L.; Santiesteban, J. G., Catalytic Growth of Carbon Microtubules with Fullerene Structure. *Appl. Phys. Lett.* **1993,** 62, (2), 202-204.

[198] José-Yacamán , M.; Mikiyoshida, M.; Rendon, L.; Santiesteban, J. G., Catalytic Growth of Carbon Microtubules with Fullerene Structure. *Appl. Phys. Lett.* **1993,** 62, (6), 657-659.

[199] Delzeit, L.; Nguyen, C. V.; Stevens, R. M.; Han, J.; Meyyappan, M., Growth of carbon nanotubes by thermal and plasma chemical vapour deposition processes and applications in microscopy. *Nanotechnology* **2002,** 13, (3), 280-284.

[200] Delzeit, L.; Nguyen, C. V.; Chen, B.; Stevens, R.; Cassell, A.; Han, J.; Meyyappan, M., Multiwalled Carbon Nanotubes by Chemical Vapor Deposition Using Multilayered Metal Catalysts. *J. Phys. Chem. B* **2002,** 106, (22), 5629-5635.

[201] Delzeit, L.; McAninch, I.; Matthews, K.; Ng, H. T.; Stevens, R.; Meyyappan, M., CVD growth of carbon nanotubes: Catalyst, growth, and structure. *Proc. - Electrochem. Soc.* **2003,** 2003-8, (Chemical Vapor Deposition XVI and EUROCVD 14, Volume 2), 1047-1055.

[202] Sato, H.; Hata, K., Growth of carbon nanotubes by plasma-enhanced chemical vapor deposition. *New Diamond Front. Carbon Technol.* **2006,** 16, (3), 163-176.

[203] Terranova, M. L.; Sessa, V.; Rossi, M., The world of carbon nanotubes: An overview of CVD growth methodologies. *Chem. Vap. Deposition* **2006,** 12, (6), 315-325.

[204] Dai, H. J., Nanotube growth and characterization. In *Carbon Nanotubes*, 2001; Vol. 80, pp 29-53.

[205] Li, Y. M.; Mann, D.; Rolandi, M.; Kim, W.; Ural, A.; Hung, S.; Javey, A.; Cao, J.; Wang, D. W.; Yenilmez, E.; Wang, Q.; Gibbons, J. F.; Nishi, Y.; Dai, H. J., Preferential growth of semiconducting single-walled carbon nanotubes by a plasma enhanced CVD method. *Nano Lett.* **2004,** 4, (2), 317-321.

[206] Bladh, K.; Falk, L. K. L.; Rohmund, F., On the iron-catalysed growth of single-walled carbon nanotubes and encapsulated metal particles in the gas phase. *Applied Physics a-Materials Science & Processing* **2000,** 70, (3), 317-322.

[207] Nikolaev, P.; Bronikowski, M. J.; Bradley, R. K.; Rohmund, F.; Colbert, D. T.; Smith, K. A.; Smalley, R. E., Gas-phase catalytic growth of single-walled carbon nanotubes from carbon monoxide. *Chem. Phys. Lett.* **1999,** 313, (1-2), 91-97.

[208] Cassell, A. M.; Raymakers, J. A.; Kong, J.; Dai, H. J., Large scale CVD synthesis of single-walled carbon nanotubes. *J. Phys. Chem. B* **1999,** 103, (31), 6484-6492.

[209] Cheng, H. M.; Li, F.; Sun, X.; Brown, S. D. M.; Pimenta, M. A.; Marucci, A.; Dresselhaus, G.; Dresselhaus, M. S., Bulk morphology and diameter distribution of single-walled carbon nanotubes synthesized by catalytic decomposition of hydrocarbons. *Chem. Phys. Lett.* **1998,** 289, (5-6), 602-610.

[210] Laurent, C.; Flahaut, E.; Peigney, A.; Rousset, A., Metal nanoparticles for the catalytic synthesis of carbon nanotubes. *New J. Chem.* **1998,** 22, (11), 1229-1237.

[211] Lewenstein, J. C.; Burgin, T. P.; Ribayrol, A.; Nagahara, L. A.; Tsui, R. K., High-Yield Selective Placement of Carbon Nanotubes on Pre-Patterned Electrodes. *Nano Lett.* **2002,** 2, (5), 443-446.

[212] Joselevich, E.; Dai, H. J.; Liu, J.; Hata, K.; Windle, A. H., Carbon nanotube synthesis and organization. In *Carbon Nanotubes*, 2008; Vol. 111, pp 101-164.

[213] Cheng, H. M.; Li, F.; Su, G.; Pan, H. Y.; He, L. L.; Sun, X.; Dresselhaus, M. S., Large-scale and low-cost synthesis of single-walled carbon nanotubes by the catalytic pyrolysis of hydrocarbons. *Appl. Phys. Lett.* **1998,** 72, (25), 3282-3284.

[214] Awasthi, K.; Srivastava, A.; Srivastava, O. N., Synthesis of carbon nanotubes. *J. Nanosci. Nanotechnol.* **2005,** 5, (10), 1616-1636.

[215] Huczko, A., Synthesis of aligned carbon nanotubes. *Applied Physics a-Materials Science & Processing* **2002,** 74, (5), 617-638.

[216] Zhu, H. W.; Xu, C. L.; Wu, D. H.; Wei, B. Q.; Vajtai, R.; Ajayan, P. M., Direct synthesis of long single-walled carbon nanotube strands. *Science* **2002,** 296, (5569), 884-886.

[217] Bernholc, J.; Roland, C.; Yakobson, B. I., Nanotubes. *Current Opinion in Solid State & Materials Science* **1997,** 2, (6), 706-715.

[218] Rakov, E. G., The chemistry and application of carbons nanotubes. *Usp. Khim.* **2001,** 70, (10), 934-973.

[219] Thostenson, E. T.; Ren, Z.; Chou, T. W., Advances in the science and technology of carbon nanotubes and their composites: a review. *Composites Science and Technology* **2001,** 61, (13), 1899-1912.

[220] Dai, H., Carbon Nanotubes: Synthesis, Integration, and Properties. *Acc. Chem. Res.* **2002,** 35, (12), 1035-1044.

[221] Liao, K.; Li, S., Interfacial characteristics of a carbon nanotube–polystyrene composite system. *Appl. Phys. Lett.* **2001,** 79, (25), 4225-4227.

[222] Star, A.; Stoddart, J. F.; Steuerman, D.; Diehl, M.; Boukai, A.; Wong, E. W.; Yang, X.; Chung, S.-W.; Choi, H.; Heath, J. R., Preparation and properties of polymer-wrapped single-walled carbon nanotubes. *Angew. Chem., Int. Ed.* **2001,** 40, (9), 1721-1725.

[223] Kumar, S.; Dang, T. D.; Arnold, F. E.; Bhattacharyya, A. R.; Min, B. G.; Zhang, X.; Vaia, R. A.; Park, C.; Adams, W. W.; Hauge, R. H.; Smalley, R. E.; Ramesh, S.; Willis, P. A., Synthesis, Structure, and Properties of PBO/SWNT Composites. *Macromolecules* **2002,** 35, (24), 9039-9043.

[224] Lau, A. K.-T.; Hui, D., The revolutionary creation of new advanced materials-carbon nanotube composites. *Composites, Part B: Engineering* **2002,** 33B, (4), 263-277.

[225] Antonucci, V.; Hsiao, K.-T.; Advani, S. G., Review of polymer composites with carbon nanotubes. *Advanced Polymeric Materials* **2003**, 397-437.

[226] Ding, W.; Eitan, A.; Fisher, F. T.; Chen, X.; Dikin, D. A.; Andrews, R.; Brinson, L. C.; Schadler, L. S.; Ruoff, R. S., Direct Observation of Polymer Sheathing in Carbon Nanotube-Polycarbonate Composites. *Nano Lett.* **2003**.

[227] Odegard, G. M.; Gates, T. S.; Wise, K. E.; Park, C.; Siochi, E. J., Constitutive modeling of nanotube-reinforced polymer composites. *Composites Science and Technology* **2003,** 63, (11), 1671-1687.

[228] Ounaies, Z.; Park, C.; Wise, K. E.; Siochi, E. J.; Harrison, J. S., Electrical properties of single wall carbon nanotube reinforced polyimide composites. *Composites Science and Technology* **2003,** 63, (11), 1637-1646.

[229] Peigney, A., Composite materials: Tougher ceramics with nanotubes. *Nat. Mater.* **2003,** 2, (1), 15-16.

[230] Zhu, J.; Kim, J.; Peng, H.; Margrave, J. L.; Khabashesku, V. N.; Barrera, E. V., Improving the Dispersion and Integration of Single-Walled Carbon Nanotubes in Epoxy Composites through Functionalization. *Nano Lett.* **2003**, ACS ASAP.

[231] Miyagawa, H.; Misra, M.; Mohanty, A. K., Mechanical properties of carbon nanotubes and their polymer nanocomposites. *J. Nanosci. Nanotechnol.* **2005,** 5, (10), 1593-1615.

[232] Bokobza, L., Multiwall carbon nanotube elastomeric composites: A review. *Polymer* **2007,** 48, (17), 4907-4920.

[233] Lee, S.-H.; Sigmund, W. M., Young's modulus studies of electrospun TiO2-carbon nanotubes. *Jom* **2007,** 59, (1), 30-33.

[234] Dai, H.; Hafner, J. H.; Rinzler, A. G.; Colbert, D. T.; Smalley, R. E., Nanotubes as nanoprobes in scanning probe microscopy. *Nature* **1996,** 384, (6605), 147-150.

[235] Moloni, K.; Buss, M. R.; Andres, R. P., Tapping mode scanning force microscopy in water using a carbon nanotube probe. *Ultramicroscopy* **1999,** 80, (4), 237-246.

[236] Collier, C. P., Carbon nanotube tips for scanning probe microscopy. *Carbon Nanotubes* **2006**, 295-313.

[237] Nguyen, C. V.; Stevens, R. M. D.; Barber, J.; Han, J.; Meyyappan, M.; Sanchez, M. I.; Larson, C.; Hinsberg, W. D., Carbon nanotube scanning probe for profiling of deep-ultraviolet and 193 nm photoresist patterns. *Appl. Phys. Lett.* **2002,** 81, (5), 901-903.

[238] Wong, S. S.; Harper, J. D.; Lansbury, P. T., Jr.; Lieber, C. M., Carbon Nanotube Tips: High-Resolution Probes for Imaging Biological Systems. *J. Am. Chem. Soc.* **1998,** 120, (3), 603-604.

[239] Wong, S. S.; Woolley, A. T.; Odom, T. W.; Huang, J. L.; Kim, P.; Vezenov, D. V.; Lieber, C. M., Single-walled carbon nanotube probes for high-resolution nanostructure imaging. *Appl. Phys. Lett.* **1998,** 73, (23), 3465-3467.

[240] Nguyen, C. V.; Chao, K.-J.; Stevens, R. M. D.; Delzeit, L.; Cassell, A.; Han, J.; Meyyappan, M., Carbon nanotube tip probes: Stability and lateral resolution in

scanning probe microscopy and application to surface science in semiconductors. *Nanotechnology* **2001,** 12, (3), 363-367.

[241] Snow, E. S.; Campbell, P. M.; Novak, J. P., Atomic force microscopy using single-wall C nanotube probes. *Journal of Vacuum Science and Technology B* **2002,** 20, (3), 822-827.

[242] Yang, S. I., Structural study using ultrahigh resolution carbon nanotube AFM probe tips. *J. Korean Chem. Soc.* **2005,** 49, (6), 517-520.

[243] Dedkov, G. V.; Rekhviashvili, S. S., Nanotubes and force interactions in an atomic force microscope. *Technical Physics* **1999,** 44, (8), 982-985.

[244] Guo, L.; Wang, R.; Xu, H.; Liang, J., Wear-resistance comparison of carbon nanotubes and conventional silicon - probes for atomic force microscopy. *Wear* **2005,** 258, (11-12), 1836-1839.

[245] Wong, S. S.; Joselevich, E.; Woolley, A. T.; Cheung, C. L.; Lieber, C. M., Covalently functionalized nanotubes as nanometer-sized probes in chemistry and biology. *Nature* **1998,** 394, (6688), 52-55.

[246] Wong, S. S.; Woolley, A. T.; Joselevich, E.; Cheung, C. L.; Lieber, C. M., Covalently-Functionalized Single-Walled Carbon Nanotube Probe Tips for Chemical Force Microscopy. *J. Am. Chem. Soc.* **1998,** 120, (33), 8557-8558.

[247] Hafner, J. H.; Cheung, C. L.; Woolley, A. T.; Lieber, C. M., Structural and functional imaging with carbon nanotube AFM probes. *Prog. Biophys. & Molec. Biol.* **2001,** 77, (1), 73-110.

[248] Guo, L. Q.; Wang, R.; Xu, H. M.; Liang, J., Measuring the adhesion forces of ligand-receptor bonds using functionalized carbon nanotube atomic force microscopic tips. *Chinese Journal of Analytical Chemistry* **2006,** 34, (3), 359-361.

[249] Azehara, H.; Kasanuma, Y.; Ide, K.; Hidaka, K.; Tokumoto, H., Distinct Chemical Contrast in Adhesion Force Images of Hydrophobic-Hydrophilic Patterned Surfaces Using Multiwalled Carbon Nanotube Probe Tips. *Jpn. J. Appl. Phys.* **2008,** 47, (5), 3594-3599.

[250] Stevens, R. M. D.; Frederick, N. A.; Smith, B. L.; Morse, D. E.; Stucky, G. D.; Hansma, P. K., Carbon nanotubes as probes for atomic force microscopy. *Nanotechnology* **2000,** 11, (1), 1-5.

[251] Hudspeth, Q. M.; Nagle, K. P.; Zhao, Y. P.; Karabacak, T.; Nguyen, C. V.; Meyyappan, M.; Wang, G. C.; Lu, T. M., How does a multiwalled carbon nanotube atomic force microscopy probe affect the determination of surface roughness statistics? *Surf. Sci.* **2002,** 515, (2-3), 453-461.

[252] Solares, S. D.; Esplandiu, M. J.; Goddard, W. A.; Collier, C. P., Mechanisms of single-walled carbon nanotube probe-sample multistability in tapping mode AFM imaging. *J. Phys. Chem. B* **2005,** 109, (23), 11493-11500.

[253] Strus, M. C.; Raman, A.; Han, C. S.; Nguyen, C. V., Imaging artefacts in atomic force microscopy with carbon nanotube tips. *Nanotechnology* **2005,** 16, (11), 2482-2492.

[254] Hafner, J. H.; Cheung, C. L.; Lieber, C. M., Direct Growth of Single-Walled Carbon Nanotube Scanning Probe Microscopy Tips. *J. Am. Chem. Soc.* **1999,** 121, (41), 9750-9751.

[255] Hafner, J. H.; Cheung, C. L.; Lieber, C. M., Growth of nanotubes for probe microscopy tips. *Nature* **1999,** 398, (6730), 761-762.

[256] Cheung, C. L.; Hafner, J. H.; Lieber, C. M., Carbon nanotube atomic force microscopy tips: direct growth by chemical vapor deposition and application to high-resolution imaging. *Proc. Natl. Acad. Sci. U. S. A.* **2000,** 97, (8), 3809-3813.

[257] Cheung, C. L.; Hafner, J. H.; Odom, T. W.; Kim, K.; Lieber, C. M., Growth and fabrication with single-walled carbon nanotube probe microscopy tips. *Appl. Phys. Lett.* **2000,** 76, (21), 3136-3138.

[258] Xu, Z. W.; Zhao, Q. L.; Sun, T.; Guo, L. Q.; Wang, R.; Dong, S., Welding method for fabricating carbon nanotube probe. *J. Mater. Process. Technol.* **2007,** 190, (1-3), 397-401.

[259] Stevens, R.; Nguyen, C.; Cassell, A.; Delzeit, L.; Meyyappan, M.; Han, J., Improved fabrication approach for carbon nanotube probe devices. *Appl. Phys. Lett.* **2000,** 77, (21), 3453-3455.

[260] Avouris, P.; Chen, Z. H.; Perebeinos, V., Carbon-based electronics. *Nat. Nanotechnol.* **2007,** 2, (10), 605-615.

[261] Avouris, P., Carbon nanotube electronics. *Chem. Phys.* **2002,** 281, (2-3), 429-445.

[262] Artukovic, E.; Kaempgen, M.; Hecht, D. S.; Roth, S.; GrUner, G., Transparent and flexible carbon nanotube transistors. *Nano Lett.* **2005,** 5, (4), 757-760.

[263] Wong, H. S. P., Beyond the conventional transistor. *Ibm Journal of Research and Development* **2002,** 46, (2-3), 133-168.

[264] Huang, Y.; Duan, X. F.; Cui, Y.; Lauhon, L. J.; Kim, K. H.; Lieber, C. M., Logic gates and computation from assembled nanowire building blocks. *Science* **2001,** 294, (5545), 1313-1317.

[265] Bachtold, A.; Hadley, P.; Nakanishi, T.; Dekker, C., Logic circuits with carbon nanotube transistors. *Science* **2001,** 294, (5545), 1317-1320.

[266] Yao, Z.; Postma, H. W. C.; Balents, L.; Dekker, C., Carbon nanotube intramolecular junctions. *Nature* **1999,** 402, (6759), 273-276.

[267] Martel, R.; Schmidt, T.; Shea, H. R.; Hertel, T.; Avouris, P., Single- and multi-wall carbon nanotube field-effect transistors. *Appl. Phys. Lett.* **1998,** 73, (17), 2447-2449.

[268] Niu, C. M.; Sichel, E. K.; Hoch, R.; Moy, D.; Tennent, H., High power electrochemical capacitors based on carbon nanotube electrodes. *Appl. Phys. Lett.* **1997,** 70, (11), 1480-1482.

[269] Rueckes, T.; Kim, K.; Joselevich, E.; Tseng, G. Y.; Cheung, C. L.; Lieber, C. M., Carbon nanotube-based nonvolatile random access memory for molecular computing. *Science* **2000,** 289, (5476), 94-97.

[270] Begtrup, G. E.; Gannett, W.; Yuzvinsky, T. D.; Crespi, V. H.; Zettl, A., Nanoscale Reversible Mass Transport for Archival Memory. *Nano Lett.* **2009,** 9, (5), 1835-1838.

[271] Lu, S. X.; Panchapakesan, B., Hybrid platinum/single-wall carbon nanotube nanowire actuators: metallic artificial muscles. *Nanotechnology* **2006,** 17, (3), 888-894.

[272] Vohrer, U.; Kolaric, I.; Haque, M. H.; Roth, S.; Detlaff-Weglikowska, U., Carbon nanotube sheets for the use as artificial muscles. *Carbon* **2004,** 42, (5-6), 1159-1164.

[273] Minett, A.; Fraysse, J.; Gang, G.; Kim, G. T.; Roth, S., Nanotube actuators for nanomechanics. *Current Applied Physics* **2002,** 2, (1), 61-64.

[274] Inganas, O.; Lundstrum, I., Materials science - Carbon nanotube muscles. *Science* **1999,** 284, (5418), 1281-1282.

[275] Baughman, R. H.; Cui, C. X.; Zakhidov, A. A.; Iqbal, Z.; Barisci, J. N.; Spinks, G. M.; Wallace, G. G.; Mazzoldi, A.; De Rossi, D.; Rinzler, A. G.; Jaschinski, O.; Roth, S.; Kertesz, M., Carbon nanotube actuators. *Science* **1999,** 284, (5418), 1340-1344.

[276] Dai, H.; Wong, E. W.; Lieber, C. M., Probing electrical transport in nanomaterials: conductivity of individual carbon nanotubes. *Science* **1996,** 272, (5261), 523-6.

[277] Bozovic, D.; Bockrath, M.; Hafner, J. H.; Lieber, C. M.; Park, H.; Tinkham, M., Electronic properties of mechanically induced kinks in single-walled carbon nanotubes. *Appl. Phys. Lett.* **2001,** 78, (23), 3693-3695.

[278] Wang, Z. L.; Gao, R. P.; Poncharal, P.; de Heer, W. A.; Da, Z. R.; Pan, Z. W., Mechanical and electrostatic properties of carbon nanotubes and nanowires. *Materials Science and Engineering C* **2001,** 16, 3-10.

[279] Kim, K. S.; Bae, D. J.; Kim, J. R.; Park, K. A.; Lim, S. C.; Kim, J.-J.; Choi, W. B.; Park, C. Y.; Lee, Y. H., Modification of electronic structures of a carbon nanotube by hydrogen functionalization. *Adv. Mater.* **2002,** 14, (24), 1818-1821.

[280] Pecchia, A.; Gheorghe, M.; Di Carlo, A.; Lugli, P., Modulation of the electronic transport properties of carbon nanotubes with adsorbed molecules. *Synth. Met.* **2003,** 138, (1-2), 89-93.

[281] Agrawal, S.; Raghuveer, M. S.; Li, H.; Ramanath, G., Defect-induced electrical conductivity increase in individual multiwalled carbon nanotubes. *Appl. Phys. Lett.* **2007,** 90, (19).

[282] Gomez-Navarro, C.; de Pablo, P. J.; Gomez-Herrero, J., Studying electrical transport in carbon nanotubes by conductance atomic force microscopy. *Journal of Materials Science-Materials in Electronics* **2006,** 17, (6), 475-482.

[283] Pop, E.; Mann, D.; Wang, Q.; Goodson, K.; Dai, H. J., Thermal conductance of an individual single-wall carbon nanotube above room temperature. *Nano Lett.* **2006,** 6, (1), 96-100.

[284] Dai, H. J.; Wong, E. W.; Lieber, C. M., Probing electrical transport in nanomaterials: Conductivity of individual carbon nanotubes. *Science* **1996,** 272, (5261), 523-526.

[285] Ebbesen, T. W.; Lezec, H. J.; Hiura, H.; Bennett, J. W.; Ghaemi, H. F.; Thio, T., Electrical conductivity of individual carbon nanotubes. *Nature* **1996,** 382, (6586), 54-56.

[286] Berger, C.; Yi, Y.; Wang, Z. L.; de Heer, W. A., Multiwalled carbon nanotubes are ballistic conductors at room temperature. *Applied Physics a-Materials Science & Processing* **2002,** 74, (3), 363-365.

[287] Poncharal, P.; Berger, C.; Yi, Y.; Wang, Z. L.; de Heer, W. A., Room temperature ballistic conduction in carbon nanotubes. *J. Phys. Chem. B* **2002,** 106, (47), 12104-12118.

[288] Poncharal, P.; Frank, S.; Wang, Z. L.; de Heer, W. A., Conductance quantization in multiwalled carbon nanotubes. *European Physical Journal D* **1999,** 9, (1-4), 77-79.

[289] Frank, S.; Poncharal, P.; Wang, Z. L.; de Heer, W. A., Carbon nanotube quantum resistors. *Science* **1998,** 280, (5370), 1744-1746.

[290] Tombler, T. W.; Zhou, C.; Alexseyev, L.; Kong, J.; Dai, H.; Jayanthi, C. S.; Tang, M.; Wu, S.-Y., Reversible electromechanical characteristics of carbon nanotubes under local-probe manipulation. *Nature* **2000,** 405, (6788), 769-772.

[291] Hong, S.; Myung, S., Nanotube electronics - A flexible approach to mobility. *Nat. Nanotechnol.* **2007,** 2, (4), 207-208.

[292] Cornwell, C. F.; Wille, L. T., Elastic properties of single-walled carbon nanotubes in compression. *Solid State Commun.* **1997,** 101, (8), 555-558.

[293] Falvo, M. R.; Clary, G. J.; Taylor, R. M., 2nd; Chi, V.; Brooks, F. P., Jr.; Washburn, S.; Superfine, R., Bending and buckling of carbon nanotubes under large strain. *Nature* **1997,** 389, (6651), 582-584.

[294] Lu, J. P., Elastic Properties of Carbon Nanotubes and Nanoropes. *Phys. Rev. Lett.* **1997,** 79, (7), 1297-1300.

[295] Wong, E. W.; Sheehan, P. E.; Lieber, C. M., Nanobeam mechanics: elasticity, strength, and toughness of nanorods and nanotubes. *Science* **1997,** 277, (5334), 1971-1975.

[296] Gao, G.; Cagin, T.; Goddard, W. A., III, Energetics, structure, mechanical and vibrational properties of single-walled carbon nanotubes. *Nanotechnology* **1998,** 9, (3), 184-191.

[297] Krishnan, A.; Dujardin, E.; Ebbesen, T. W.; Yianilos, P. N.; Treacy, M. M. J., Young's modulus of single-walled nanotubes. *Phys. Rev. B: Condens. Matter Mater. Phys.* **1998,** 58, (20), 14013-14019.

[298] Treacy, M. M. J.; Ebbesen, T. W.; Gibson, J. M., Exceptionally high Young's modulus observed for individual carbon nanotubes. *Nature* **1996,** 381, (6584), 678-680.

[299] Poncharal, P.; Wang, L.; Ugarte, D.; de Heer, W. A., Electrostatic deflections and electromechanical resonances of carbon nanotubes. *Science* **1999,** 283, (5407), 1513-1516.

[300] Salvetat, J.-P.; Briggs, G. A. D.; Bonard, J.-M.; Bacsa, R. R.; Kulik, A. J.; Stockli, T.; Burnham, N. A.; Forro, L., Elastic and Shear Moduli of Single-Walled Carbon Nanotube Ropes. *Phys. Rev. Lett.* **1999,** 82, (5), 944-947.

[301] Salvetat, J.-P.; Kulik, A. J.; Bonard, J.-M.; Briggs, G. A. D.; Stoeckli, T.; Metenier, K.; Bonnamy, S.; Beguin, F.; Burnham, N. A.; Forro, L., Elastic

modulus of ordered and disordered multiwalled carbon nanotubes. *Adv. Mater.* **1999,** 11, (2), 161-165.

[302] Yu, M.-F.; Files, B. S.; Arepalli, S.; Ruoff, R. S., Tensile loading of ropes of single wall carbon nanotubes and their mechanical properties. *Phys. Rev. Lett.* **2000,** 84, (24), 5552-5555.

[303] Yu, M.-F.; Lourie, O.; Dyer, M. J.; Moloni, K.; Kelly, T. F.; Ruoff, R. S., Strength and breaking mechanism of multiwalled carbon nanotubes under tensile load. *Science* **2000,** 287, (5453), 637-640.

[304] Chen, X.; Zhang, S.; Dikin, D. A.; Ding, W.; Ruoff, R. S.; Pan, L.; Nakayama, Y., Mechanics of a Carbon Nanocoil. *Nano Lett.* **2003,** 3, (9), 1299-1304.

[305] Falvo, M. R.; Clary, G.; Helser, A.; Paulson, S.; Taylor, R. M., II; Chi, V.; Brooks, F. P., Jr.; Washburn, S.; Superfine, R., Nanomanipulation experiments exploring frictional and mechanical properties of carbon nanotubes. *Microsc. Microanal.* **1998,** 4, (5), 504-512.

[306] Barber, J. R. T. Mechanical Compression of Coiled Carbon Nanotubes. Doctoral, Georgia Institute of Technology, Atlanta, 2009.

[307] Yu, M.-F.; Kowalewski, T.; Ruoff, R. S., Investigation of the Radial Deformability of Individual Carbon Nanotubes under Controlled Indentation Force. *Phys. Rev. Lett.* **2000,** 85, (7), 1456-1459.

[308] Demczyk, B. G.; Wang, Y. M.; Cumings, J.; Hetman, M.; Han, W.; Zettl, A.; Ritchie, R. O., Direct mechanical measurement of the tensile strength and elastic modulus of multiwalled carbon nanotubes. *Mater. Sci. Eng., A* **2002,** A334, (1-2), 173-178.

[309] Arroyo, M.; Belytschko, T., Nonlinear Mechanical Response and Rippling of Thick Multiwalled Carbon Nanotubes. *Phys. Rev. Lett.* **2003,** 91, (21), 215505/1-215505/4.

[310] Xiong, Q.; Duarte, N.; Tadigadapa, S.; Eklund, P. C., Force-Deflection Spectroscopy: A New Method to Determine the Young's Modulus of Nanofilaments. *Nano Lett.* **2006,** 6, (9), 1904-1909.

[311] Guhados, G.; Wan, W.; Sun, X.; Hutter, J. L., Simultaneous measurement of Young's and shear moduli of multiwalled carbon nanotubes using atomic force microscopy. *J. Appl. Phys.* **2007,** 101, (3), 033514/1-033514/5.

[312] Williams, P. A.; Papadakis, S. J.; Patel, A. M.; Falvo, M. R.; Washburn, S.; Superfine, R., Torsional Response and Stiffening of Individual Multiwalled Carbon Nanotubes. *Phys. Rev. Lett.* **2002,** 89, (25), 255502/1-255502/4.

[313] Yu, M.-F.; Dyer, M. J.; Ruoff, R. S., Structure and mechanical flexibility of carbon nanotube ribbons: An atomic-force microscopy study. *J. Appl. Phys.* **2001,** 89, (8), 4554-4557.

[314] Yu, M.-F.; Kowalewski, T.; Ruoff, R. S., Structural Analysis of Collapsed, and Twisted and Collapsed, Multiwalled Carbon Nanotubes by Atomic Force Microscopy. *Phys. Rev. Lett.* **2000,** 86, (1), 87-90.

[315] Poggi, M. A.; Bottomley, L. A.; Lillehei, P. T., Measuring the Adhesion Forces between Alkanethiol-Modified AFM Cantilevers and Single Walled Carbon Nanotubes. *Nano Lett.* **2004,** 4, (1), 61-64.

[316] Bhushan, B., Nanotribology and nanomechanics. *Wear* **2005,** 259, (Pt. 2), 1507-1531.

[317] Miura, K.; Takagi, T.; Kamiya, S.; Sahashi, T.; Yamauchi, M., Natural Rolling of Zigzag Multiwalled Carbon Nanotubes on Graphite. *Nano Lett.* **2001,** 1, (3), 161-163.

[318] Poggi, M. A.; Bottomley, L. A.; Lillehei, P. T., Scanning Probe Microscopy. *Anal. Chem.* **2002,** 74, (12), 2851-2862.

[319] Cooper, C. A.; Cohen, S. R.; Barber, A. H.; Wagner, H. D., Detachment of nanotubes from a polymer matrix. *Appl. Phys. Lett.* **2002,** 81, (20), 3873-3875.

[320] Clifford, C. A.; Seah, M. P., Quantification issues in the identification of nanoscale regions of homopolymers using modulus measurement via AFM nanoindentation. *Appl. Surf. Sci.* **2005,** 252, (5), 1915-1933.

[321] Johnson, K. L.; Sridhar, I., Adhesion between a spherical indenter and an elastic solid with a compliant elastic coating. *Journal of Physical Chemistry D* **2001,** 34, (5), 683-689.

[322] Eaton, P.; Fernandez Estarlich, F.; Ewen, R. J.; Nevell, T. G.; Smith, J. R.; Tsibouklis, J., Combined Nanoindentation and Adhesion Force Mapping Using the Atomic Force Microscope: Investigations of a Filled Polysiloxane Coating. *Langmuir* **2002,** 18, (25), 10011-10015.

[323] Eaton, P.; Smith, J. R.; Graham, P.; Smart, J. D.; Nevell, T. G.; Tsibouklis, J., Adhesion Force Mapping of Polymer Surfaces: Factors Influencing Force of Adhesion. *Langmuir* **2002,** 18, (8), 3387-3389.

[324] Shanmugham, S.; Jeong, J.; Alkhateeb, A.; Aston, D. E., Polymer Nanowire Elastic Moduli Measured with Digital Pulsed Force Mode AFM. *Langmuir* **2005,** 21, (22), 10214-10218.

[325] Withers, J. R.; Aston, D. E., Nanomechanical measurements with AFM in the elastic limit. *Adv. Colloid Interface Sci.* **2006,** 120, (1-3), 57-67.

[326] Shen, W.; Jiang, B.; Han, B. S.; Xie, S.-s., Investigation of the Radial Compression of Carbon Nanotubes with a Scanning Probe Microscope. *Phys. Rev. Lett.* **2000,** 84, (16), 3634-3637.

[327] Gaire, C.; Ye, D. X.; Lu, T. M.; Wang, G. C.; Picu, R. C., Deformation of amorphous silicon nanostructures subjected to monotonic and cyclic loading. *J. Mater. Res.* **2008,** 23, (2), 328-335.

[328] Buzio, R.; Bosca, A.; Krol, S.; Marchetto, D.; Valeri, S.; Valbusa, U., Deformation and Adhesion of Elastomer Poly(dimethylsiloxane) Colloidal AFM Probes. *Langmuir* **2007,** 23, (18), 9293-9302.

[329] Dedkov, G. V.; Dyshekov, M. B., Deformation of the contact region and adhesional friction between nanoprobe and surface. *Surf. Sci.* **2000,** 463, (2), 125-134.

[330] Shapiro, I. R.; Solares, S. D.; Esplandiu, M. J.; Wade, L. A.; Goddard, W. A.; Collier, C. P., Influence of Elastic Deformation on Single-Wall Carbon Nanotube Atomic Force Microscopy Probe Resolution. *J. Phys. Chem. B* **2004,** 108, (36), 13613-13618.

[331] Lee, S. I.; Howell, S. W.; Raman, A.; Reifenberger, R.; Nguyen, C. V.; Meyyappan, M., Nonlinear tapping dynamics of multi-walled carbon nanotube tipped atomic force microcantilevers. *Nanotechnology* **2004,** 15, 416–421.

[332] Kutana, A.; Giapis, K. P.; Chen, J. Y.; Collier, C. P., Amplitude response of single-wall carbon nanotube probes during tapping mode atomic force microscopy: Modeling and experiment. *Nano Lett.* **2006,** 6, (8), 1669-1673.

[333] Lee, S. I.; Howell, S. W.; Raman, A.; Reifenberger, R.; Nguyen, C. V.; Meyyappan, M., Complex dynamics of carbon nanotube probe tips. *Ultramicroscopy* **2005,** 103, (2), 95-102.

[334] Lee, K.; Lukic, B.; Magrez, A.; Seo, J. W.; Briggs, G. A. D.; Kulik, A. J.; Forro, L., Diameter-dependent elastic modulus supports the metastable-catalyst growth of carbon nanotubes. *Nano Lett.* **2007,** 7, (6), 1598-1602.

[335] Yang, L.; van der Werf, K. O.; Koopman, B. F. J. M.; Subramaniam, V.; Bennink, M. L.; Dijkstra, P. J.; Feijen, J., Micromechanical bending of single collagen fibrils using atomic force microscopy. *J. Biomed. Mater. Res., Part A* **2007,** 82A, (1), 160-168.

[336] Tan, E. P. S.; Lim, C. T., Physical properties of a single polymeric nanofiber. *Appl. Phys. Lett.* **2004,** 84, (9), 1603-1605.

[337] Karnovsky, I. A.; Lebed, O. I., *Formulas for Structural Dynamics: Tables, Graphs, and Solutions*. McGraw-Hill: New York, 2001; p 535.

[338] Karnovsky, I. A.; Lebed, O. I., *Free Vibrations of Beams and Frames*. McGraw-Hill: New York, 2004; p 280.

[339] Karnovsky, I. A.; Lebed, O. I., *Non-classical Vibrations of Arches and Beams*. McGraw-Hill: New York, 2004; p 239.

[340] Butt, H.; Jaschke, M., Calculation of thermal noise in atomic force microscopy. *Nanotechnology* **1995,** 6, 1-7.

[341] McFarland, A. W. Production and Analysis of Polymer Microcantilever Parts. Doctoral, Georgia Institute of Technology, Atlanta, 2004.

[342] Wagner, P.; Hegner, M.; Guentherodt, H.-J.; Semenza, G., Formation and in Situ Modification of Monolayers Chemisorbed on Ultraflat Template-Stripped Gold Surfaces. *Langmuir* **1995,** 11, (10), 3867-75.

[343] Hegner, M.; Wagner, P.; Semenza, G., Ultralarge atomically flat template-stripped gold surfaces for scanning probe microscopy. *Surf. Sci.* **1993,** 291, (1-2), 39-46.

[344] Ulman, A., Formation and structure of self-assembled monolayers. *Chemical Reviews* **1996,** 96, (4), 1533-1554.

[345] Laibinis, P. E.; Whitesides, G. M., Omega-Terminated Alkanethiolate Monolayers on Surfaces of Copper, Silver, and Gold Have Similar Wettabilities. *J. Am. Chem. Soc.* **1992,** 114, (6), 1990-1995.

[346] Bhushan, B.; Liu, H., Nanotribological properties and mechanisms of alkylthiol and biphenyl thiol self-assembled monolayers studied by AFM. *Phys. Rev. B: Condens. Matter Mater. Phys.* **2001,** 63, (24), 245412/1-245412/11.

[347] Mate, C. M., Nanotribology studies of carbon surfaces by force microscopy. *Wear* **1993,** 168, (1-2), 17-20.

[348] Carlotti, B.; Barker, K. M.; Barber, J. R.; Ferri, A. A.; Bottomley, L. A., Multi-Parameter Force Spectroscopy for Thin Film Meachanical Testing. *Langmuir* **2009**, (to be submitted).

[349] Giannotti, M. I.; Vancso, G. J., Interrogation of single synthetic polymer chains and polysaccharides by AFM-based force spectroscopy. *ChemPhysChem* **2007,** 8, (16), 2290-2307.

[350] Zou, S.; Hempenius, M. A.; Schoenherr, H.; Vancso, G. J., Force spectroscopy of individual stimulus-responsive poly(ferrocenyldimethylsilane) chains: towards a redox-driven macromolecular motor. *Macromol. Rapid Commun.* **2006,** 27, (2), 103-108.

[351] Helenius, J.; Heisenberg, C. P.; Gaub, H. E.; Muller, D. J., Single-cell force spectroscopy. *J. Cell Sci.* **2008,** 121, (11), 1785-1791.

[352] Poirier, G. E., Characterization of Organosulfur Molecular Monolayers on Au(111) using Scanning Tunneling Microscopy. *Chemical Reviews* **1997,** 97, (4), 1117-1127.

[353] Plaut, R. H.; Virgin, L. N., Three-dimensional postbuckling and vibration of vertical half-loop under self-weight. *International Journal of Solids and Structures* **2004,** 41, (18-19), 4975-4988.

[354] Woo, Y.; Plaut, R. H.; Dillard, D. A.; Coulthard, S. L., Experiments and inelastic analysis of the loop tack test for pressure-sensitive adhesives. *J. Adhes.* **2004,** 80, (3), 203-221.

[355] Qi, J.; Dillard, D. A.; Plaut, R. H.; Dillard, J. G., Experiments on contact of a loop with a substrate to measure work of adhesion. *J. Adhes.* **2003,** 79, (6), 559-579.

[356] Plaut, R. H.; Williams, N. L.; Dillard, D. A., Elastic analysis of the loop tack test for pressure sensitive adhesives. *J. Adhes.* **2001,** 76, (1), 37-53.

[357] Girifalco, L. A.; Hodak, M.; Lee, R. S., Carbon nanotubes, buckyballs, ropes, and a universal graphitic potential. *Phys. Rev. B: Condens. Matter Mater. Phys.* **2000,** 62, (19), 13104-13110.

[358] Kolb, H. C.; Finn, M. G.; Sharpless, K. B., Click chemistry: Diverse chemical function from a few good reactions. *Angewandte Chemie-International Edition* **2001,** 40, (11), 2004-+.

[359] Chiefari, J.; Chong, Y. K.; Ercole, F.; Krstina, J.; Jeffery, J.; Le, T. P. T.; Mayadunne, R. T. A.; Meijs, G. F.; Moad, C. L.; Moad, G.; Rizzardo, E.; Thang, S. H., Living Free-Radical Polymerization by Reversible Additionâ^'Fragmentation Chain Transfer: The RAFT Process. *Macromolecules* **1998,** 31, (16), 5559-5562.

[360] Safak, M.; Alemdaroglu, F. E.; Li, Y.; Ergen, E.; Hernnann, A., Polymerase chain reaction as an efficient tool for the preparation of block copolymers. *Adv. Mater.* **2007,** 19, (11), 1499-+.

[361] Alemdaroglu, F. E.; Safak, M.; Wang, J.; Berger, R.; Herrmann, A., DNA multiblock copolymers. *Chemical Communications* **2007**, (13), 1358-1359.

[362] Alemdaroglu, F. E.; Alemdaroglu, N. C.; Langguth, P.; Herrmann, A., DNA block copolymer micelles - A combinatorial tool for cancer Nanotechnology. *Adv. Mater.* **2008,** 20, (5), 899-+.

[363] Alemdaroglu, F. E.; Alemdaroglu, N. C.; Langguth, P.; Herrmann, A., Cellular uptake of DNA block copolymer micelles with different shapes. *Macromol. Rapid Commun.* **2008,** 29, (4), 326-329.

[364] Alemdaroglu, F. E.; Wang, J.; Borsch, M.; Berger, R.; Herrmann, A., Enzymatic control of the size of DNA block copolymer nanoparticles. *Angewandte Chemie-International Edition* **2008,** 47, (5), 974-976.

[365] Alemdaroglu, F. E.; Herrmann, A., DNA meets synthetic polymers - highly versatile hybrid materials. *Org. Biomol. Chem.* **2007,** 5, (9), 1311-1320.

[366] Ding, K.; Alemdaroglu, F. E.; Boersch, M.; Berger, R.; Herrmann, A., Engineering the structural properties of DNA block copolymer micelles by molecular recogntition. *Angewandte Chemie-International Edition* **2007,** 46, (7), 1172-1175.

[367] Brotherson, B.; Bottomley, L. A.; Ludovice, P.; Deng, Y. L., Salt effect on cationic polyacrylamide conformation on mica studied by single molecule "pulling" with scanning probe microscopy. *J. Phys. Chem. B* **2008,** 112, (40), 12686-12691.

[368] Brotherson, B.; Deng, Y. L., Site blocking effect on the conformation of adsorbed cationic polyacrylamide on a solid surface. *J. Colloid Interface Sci.* **2008,** 326, (2), 324-328.

[369] Evans, E., Energy landscapes of biomolecular adhesion and receptor anchoring at interfaces explored with dynamic force spectroscopy. *Faraday Discuss.* **1998,** 111, 1-16.

[370] Evans, E.; Kinoshita, K., Using force to probe single-molecule receptor-cytoskeletal anchoring beneath the surface of a living cell. In *Cell Mechanics*, 2007; Vol. 83, pp 373-396.

[371] Evans, E. A.; Calderwood, D. A., Forces and bond dynamics in cell adhesion. *Science* **2007,** 316, (5828), 1148-1153.

[372] Evans, E.; Wong, W. P.; Halvorsen, K.; Kinoshita, K., Using forward and reverse dynamic force spectroscopy to explore unfolding and refolding transitions in poly-protein domains. *Biophys. J.* **2007**, 1A-1A.

[373] Niyogi, S.; Hamon, M. A.; Hu, H.; Zhao, B.; Bhowmik, P.; Sen, R.; Itkis, M. E.; Haddon, R. C., Chemistry of Single-Walled Carbon Nanotubes. *Acc. Chem. Res.* **2002,** 35, 1105-1113.

[374] Belikov, S.; Magonov, S.; Erina, N.; Huang, L.; Su, C.; Rice, A.; Meyer, C.; Prater, C.; Ginzburg, V.; Meyers, G.; McIntyre, R.; Lakrout, H., Theoretical modelling and implementation of elastic modulus measurement at the nanoscale using atomic force microscope. *J. Phys.: Conf. Ser.* **2007,** 61, 1303-1307.

[375] Lee, H.; Mall, S.; Nalladega, V.; Sathish, S.; Roy, A.; Lafdi, K., Characterization of carbon nanofibre reinforced epoxy composite using nanoindentation and AFM/UFM techniques. *Polym. Polym. Compos.* **2006,** 14, (6), 549-562.

[376] Tan, E. P. S.; Lim, C. T., Nanoindentation study of nanofibers. *Appl. Phys. Lett.* **2005,** 87, (12), 123106/1-123106/3.

[377] Guzman, C.; Jeney, S.; Kreplak, L.; Kasas, S.; Kulik, A. J.; Aebi, U.; Forro, L., Exploring the Mechanical Properties of Single Vimentin Intermediate Filaments by Atomic Force Microscopy. *J. Mol. Biol.* **2006,** 360, (3), 623-630.

[378] Bellan, L. M.; Coates, G. W.; Craighead, H. G., Poly(dicyclopentadiene) submicron fibers produced by electrospinning. *Macromol. Rapid Commun.* **2006,** 27, (7), 511-515.

[379] Kaplan-Ashiri, I.; Cohen, S. R.; Apter, N.; Wang, Y.; Seifert, G.; Wagner, H. D.; Tenne, R., Microscopic Investigation of Shear in Multiwalled Nanotube Deformation. *J. Phys. Chem. C* **2007,** 111, (24), 8432-8436.

[380] Mai, W.; Wang, Z. L., Quantifying the elastic deformation behavior of bridged nanobelts. *Appl. Phys. Lett.* **2006,** 89, (7), 073112/1-073112/3.

[381] Tan, E. P. S.; Lim, C. T., Effects of annealing on the structural and mechanical properties of electro-spun polymeric nanofibres. *Nanotechnology* **2006,** 17, (10), 2649-2654.

[382] Chaudhry, H.; Findley, T., Physical properties of a single polymeric nanofiber. Comment. *Appl. Phys. Lett.* **2008,** 93, (16), 166101/1.